Understanding the magnetic field configuration in X-ray pulsars through spectroscopy and polarimetry

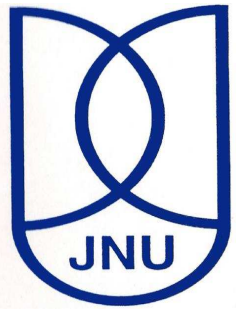

Varun

Under the supervision of

Prof. Biswajit Paul

Department of Astronomy & Astrophysics
Raman Research Institute,
Bangalore, India.

This dissertation is submitted for the degree of
Doctor of Philosophy
to Jawaharlal Nehru University,
New Delhi, India.

August 2019

To my family and friends.
And to an average person who wants to dream and achieve.

Declaration

I hereby declare that the work presented in this thesis titled, "**Understanding the magnetic field configuration in X-ray pulsars through spectroscopy and polarimetry**" is the result of the investigations carried out by me under the supervision of Prof. Biswajit Paul at the Astronomy and Astrophysics Group, Raman Research Institute, Bengaluru, India. I further declare that the work presented in this thesis has not been submitted for the award of any other degree or diploma of any other University or Institution. Keeping with the general practice, due acknowledgements have been made wherever the work described is based on other investigations. I have also run the thesis through the Turnitin software.

Prof. Biswajit Paul
Thesis Supervisor

Varun

Astronomy and Astrophysics
Raman Research Institute
Bengaluru - 560080

Certificate

This is to certify that the dissertation entitled "**Understanding the magnetic field configuration in X-ray pulsars through spectroscopy and polarimetry**" submitted by **Varun** for the award of the degree of Doctor of Philosophy to Jawaharlal Nehru University, is his original work. This has not been submitted or published for any other degree or qualification to any other university.

Prof. Ravi Subrahmanyan
Director

Prof. Biswajit Paul
Thesis Supervisor

Raman Research Institute,
Bengaluru 560 080
INDIA.

Acknowledgements

I want to thank the whole RRI for being my home and workplace for all these years. I really enjoyed the natural environment and relaxed work culture here. All the staff members are extremely helpful, prompt, and generous.

I thank my supervisor, Prof. Biswajit Paul for introducing me to the high energy instrumentation and observations. He has been very supportive and patient throughout this journey. He has always come to my aid at critical times. He has always been available for sending feedbacks and clarifying my doubts. I would also like to thank my thesis advisors Prof. Shiv Sethi and Dr. Ramesh Balasubramanyam, for their support, encouragement, and timely feedback. They have helped me grow as a researcher. I want to thank all the members of X-ray lab: Rishin Ji, GK Ji, Rajagopal Sir, Abhilash, Sandhya P., Pooja Verma. Rishin ji has been very helpful for all the guidance and help in my instrumentation work. It is amazing to work with him. GK Ji has been very a helpful and cheerful company in the lab. I thank Rajgopal sir for his help in the lab. During my experiments, Abhilash has been a great company from time to time.

I want to thank Vidya for treating me with love and affection. Her presence in the department always gave me a homely feeling. She has really been very helpful for planning all my national and international travels. She always kept me aware of all official procedures and suggested the best options. After Vidya was shifted to administration department, Harini has also been very helpful and prompt. I would like to thank Lakhmi amma, Hanmantappa, and Gangadhar their help in keeping my sitting place neat and clean. I have really become fond of tea and coffee made Lakshmi amma. I want to thank the computer department staff for technical support. Jacob, Krishnamurthy, and Sridhar have always been very prompt for any software and hardware related issues. Also, I would like to thank the administration staff for their help and quick response in handling all the official matters.

I want to thank my parents for their love and affections. Both of them have given me full freedom to pursue my life and have always been there for me. My father always allowed me to make independent decisions, and that has helped me to become fearless. My mother has been a great source of inspiration throughout my Ph.D. My wife Anjali is the most pleasant addition to my life during last one year. She really has been very accommodating and adjusting for my hectic working schedule.

I want to thank all the students in the department for their help and engaging discussions. I shared many memorable moments during our conversations on lunch or tea time. My batch mates Sourabh and Janakee were a cheerful company during the course work. I have shared many laughs with all my roommates in the department – Abir, Raj, Karam, Priyanka, Nazma, Naveen, Karthik, Hemanth, Sanhita, Saikat, and Angnibha. I am proud of being a member of "Noisy Corner" in the department.

I thanks all my seniors (Chandreyee, Nazma, Gayathri, Aru, Pragati, Nirmal) for sharing their knowledge with me. For general counseling on any matter, I have always reached to Nazma or Gayathri. I have learned a lot from Nirmal Iyer, who was a postdoc in the department. His curious nature and creativity really inspired me. Chandreyee has been really great collaborator. I thank my juniors Sanhita, Hemanth and Ashwin. I have gained a lot to confidence about my own abilities in my research field by discussing with them.

My time in RRI, would not have been a pleasant one without hostel friends. I thank Deepak, Raj, Nomaan, Rahul, Nancy, Amrita, Chaitra, Reena, and Anand for being such a great company of mutual interest and values. Spending time with them really kept my mood positive.

I would like to thanks all the members of RRI Cricket club for being an amazing company. Also, I learned some new sports after coming to Bengaluru. I thank my running, cycling, and swimming partners Nomaan and Raj. I leaned a lot, and had a great time with Simon in the Gym. I thanks Adit for teaching me tennis.

Table of contents

Abstract

Magnetic field plays an important role in the broadband emission of many astrophysical sources. The strength of this field whose presence leads to the observed polarization of radiation varies over an extraordinary range of about 20 orders of magnitude. Neutron stars have the most powerful magnetic field strength of 10^{12}-10^{15} G. One interesting manifestation of strong magnetic field is the cyclotron resonance scattering feature (CRSF) which is seen in the spectrum of these sources. In this thesis, we present the results of pulse phase variation of CRSF in two high mass X-ray binaries using *AstroSat*-LAXPC observations. We also present results of other types of isolated neutron stars from *AstroSat*-LAXPC observations. Another manifestation of the presence of a strong magnetic field is the polarization of high energy radiation. The measurement of high energy polarization has been limited or somewhat elusive so far. This is now set to become possible thanks to the renewed efforts in the past decade. *POLIX* is an X-ray polarimeter based on Thomson scattering. It can perform polarimetry of hard X-ray sources like accretion powered pulsars, black holes, blazars, supernova remnants etc. We present the results of two experiments, which are part of ongoing ground calibration of this instrument. We also present the experimental results for a new polarization measurement technique based on photo-electric interaction.

SYNOPSIS

Background and motivation

Neutron stars have powerful magnetic fields. The strongest magnetic field known in such objects is hundreds of millions of times stronger than any man-made magnet and quadrillions times more powerful than the field surrounding the earth. Strong magnetic fields in neutron stars have crucial contribution in properties of pulsed radiation from radio to gamma rays. This radiation bears signatures of field strength and its configuration. One important signature is polarization properties, which is only known for the radio pulsars. While expected X-ray polarization properties of different types of pulsars studies have been investigated theoretically, confirmation and validation can only be obtained with polarization measurements. Recent advancement in Thompson (Rishin and et al., 2010), Compton, and Photo-electron (Evangelista, 2017) based X-ray polarimetry technique has brought us closer to the day when such measurements will be done.

When a neutron star is in binary with a main sequence star, it can accrete matter from its companion. The strong magnetic field of NS in such a system can have a crucial contribution in the formation of the X-ray spectrum of these sources. Scattering cross-sections of photons are altered in the presence of a strong magnetic field. They acquire different dependencies depending on whether they escape parallel or perpendicular to the magnetic field (Becker, 1998). Two characteristic which should arise due to the magnetic field are the formation of cyclotron resonance scattering feature (CRSF) and polarization of the X-rays. The presence of CRSF was first theoretically predicted (Gnedin and Sunyaev, 1974) even before it was discovered observationally. The current census is more than 30 CRSF sources discovered with magnetic field ranging from $\sim 1 - 7 \times 10^{12}$G. Harmonics of the CRSFs are also seen in several sources : for example up to the fifth harmonic in 4U 0115+63 (Santangelo et al., 2000), two harmonics in V 0332+53 (Pottschmidt et al., 2005) and single harmonics in several sources like Vela X-1 (Kreykenbohm et al., 2002), A 0535+26 (Caballero et al., 2007)

and 4U 1538-52 (Rodes-Roca et al., 2009).

Inherently, the angular dependence of the CRSF cross-section is expected to result in variations of a few % in CRSF parameters with pulse phase. Physical parameters of the region like plasma temperature, optical depth, and geometry of region can also result in variations of CRSF parameters. Pulse phase dependence of CRSF thus provide crucial clues regarding these conditions across the pulse phase. It also provides clues on magnetic field configuration of the same (Maitra, 2017).

Research Methods

For carrying out a study on cyclotron lines, data from *AstroSat*-LAXPC along with its analysis software tools have been used. This instrument has a large effective area in broad energy band 3.0-80.0 keV and hence suited for the phase-resolved analysis of broad feature like CRSF in the spectrum. In addition to data from the performance verification and guaranteed time observations with *AstroSat*, we had 3 guest proposals accepted with *AstroSat* in 2016 and 2017. For the study of one source, we also used archival data from *XMM-Newton* and *RXTE* PCA space telescope. Archival data was obtained from *HEASARC* NASA's archive of high energy astrophysical data. *HEASARC* also provides data analysis tools that allow users to carry out several timing and spectral task effectively.

Polarization experiments were set in RRI's X-ray lab. Some of the equipments were built in mechanical engineering services (MES) workshop at RRI while others were either bought or designed and manufactured in collaboration with outside industries.

Thesis Outline

This thesis is divided into 7 chapters

Chapter 1: Introduction

Chapter 2: Description of the Instruments and Methods Used in the thesis

Chapter 3: Pulse Phase Variation Of Cyclotron Resonance Absorption Feature In HMXBs Using *AstroSat*-LAXPC

4U 1538–522 is a wind-fed persistent HMXB formed by a massive (17 $M_{\odot}$) B0Iab supergiant and a neutron star. The orbit of the binary system is almost edge-on, and is characterized by a period of 3.75 days, a low eccentricity of ~ 0.08, and a well defined X-ray eclipse lasting ~ 0.6 days. The persistent X-ray luminosity is estimated to be about 2×10^{36} erg/s for a distance of ~ 6.4 kpc. The system consists of a supergiant that under-fills its Roche Lobe and is similar to other wind fed systems like Vela X-1 and 4U 1907+09 exhibiting short time variability in terms of dips and flaring activity.

The neutron star is spinning with a period of $\sim$ 529 s. A CRSF at $\sim$ 20 keV was discovered by using a *Ginga* observation. An additional absorption feature was identified in the spectrum at $\sim$ 51 keV using *BeppoSAX* observations and was later confirmed as the first harmonic of the CRSF. Using X-ray observations from 1996-2012, it has been suggested that CRSF centroid energy has increased by $\sim$ 1.5 keV during this period.

4U 1907+09 is an HMXB comprising of a neutron star and an O8/O9 Ia supergiant star. It was discovered in the *UHURU* survey in 1971. X-ray flux modulation of $\sim$ 8.38 d is attributed to the orbital period of the binary. Companion has a mass loss rate of 7×10^{-6} $M_{\odot}$ yr^{-1}. The neutron star in 4U 1907+09 is pulsating with a periodicity of $\sim$ 437 s and it is known to show occasional quasi-periodic oscillations at a frequency of about 65 mHz. The light-curve of 4U 1907+09 is highly variable with dips and flares. Based on the long periods of quiescense similar to supergiant fast X-ray transients (SFXTs), it was classified as an intermediary between classical sgHMXBs and SFXTs. Pulse profile of 4U 1907+09 shows double peak upto 10 keV. In 10-20 keV pulse profiles exhibit a single peak with only a small secondary hump. Above 30 keV, there is no visible change in it's pulse profiles with energy. The CRSF for 4U 1907+09 at $\sim$ 19 keV was first discovered with *Ginga* and it's first harmonic was detected with *BeppoSAX*.

In this work cyclotron line studies of 4U 1538–522 were carried out with observation data from LAXPC instrument onboard *AstroSat*. Cyclotron Resonance Scattering Feature (CRSF) was detected at $\sim$ 22 keV which confirms the long term increase in the centroid energy of the CRSF observed between the 1996–2004 *RXTE* and 2012 *Suzaku* observations. It is one of the highest signal to noise ratio detection of CRSF for this source. Detailed pulse phase-resolved spectroscopy of continuum and CRSF was done. Significant variations are found in CRSF parameters, which implies physical parameters like plasma temperature, optical depth, and projections of different parts of accreting column changes significantly across the pulse phase. Also, pulse profile showed strong energy dependence, with a double-peaked profile in low energy range and a single-peaked profile in high energy range, the transition taking place around the cyclotron line energy of the source. The secondary peak (phase 0.6–1.0) decreases in strength until it disappears for energy $>$ 19 keV.

In this work, an in-depth pulse phase variation of spectral parameters of 4U 1907+09 has been studied along with energy dependence of pulse profile. The light curve con-

sisted of a flare at the beginning of the observation, followed by persistent emission. Pulse profiles are detected up to 60 keV. The amplitude and shape of secondary peak is energy dependent, with a marked difference below and above $\sim$ 16 keV. The amplitude of secondary peak goes down significantly in energy bands around CRSF. We have detected a cyclotron absorption line at $\sim$ 18.5 keV with high detection significance and performed a detailed pulse phase resolved-spectral analysis. The cyclotron line parameters show dependence on the spin phase of the neutron star. Cyclotron parameters are found to be same for luminosity change by a factor of 2.6.

Chapter 4: *AstroSat*-LAXPC Observations Of Some Isolated Neutron Stars
In addition to accretion powered pulsars, we have also investigated two other types of X-ray pulsars with *AstroSat* observations: 1) Rotation Powered Pulsars 2) Magnetars.

The Crab nebula is a remnant of a supernova explosion in 1054 AD. Crab nebula is the brightest sources in the sky at photon energies $\geq$ 30 keV. Crab nebula is the brightest sources in the sky at photon energies $\geq$ 30 keV. In the center of the nebula, there is a high magnetic field neutron star with a spin period of $\sim$ 33 ms, which was discovered in 1968 (Staelin and Reifenstein, 1968). The pulsar is slowing down at a rate of $\dot{P} = 4.2 \times 10^{-13}$ ss^{-1} (Manchester et al., 2005).

PSR B1509-58 was first discovered in X-rays with *Einstein* observatory. Its spin period was found to be 150 ms. It is embedded in a bright supernova remnant MSH 15-52. Radio pulsations were detected subsequently and a large period derivative of $\sim 1.5 \times 10^{-12}$ ss^{-1} was also confirmed. This implies a dipole field of B = 1.5×10^{13} G. The radio pulse profile show a sharp peak, while the X-ray profile has a single, broad and asymmetric peak and lags the radio peak by about one quarter of cycle. Using 11 years of radio timing observations, the detailed spin-down evolution suggests the characteristic age of 1700 years. The distance is 5.2 ± 1.5 kpc estimated from HI measurement.

The magnetar 1E 1048.1-5937 is relatively active, often showing X-ray bursts and unstable timing behavior. Its spin period is 6.46 s, and the spin inferred surface magnetic field strength is B = 4×10^{14} G. In quiescence, it shows a spectrum which is well described with a blackbody plus power-law model having a kT $\sim$ 0.6 keV and $\Gamma \sim 2.9$. The distance to the source is estimated to be 9 kpc.

1E 2259+586 was the first anomalous X-ray pulsar (AXP) to be discovered and also played a key role in the identification of AXPs as magnetars when it exhibited a series of over 80 X-ray bursts in 2002. The spin period of 1E 2259+586 is P = 6.98 s with a spin-down rate of $\dot{P} = 0.05 \times 10^{-11} ss^{-1}$. This implies a surface magnetic field of 0.59×10^{14} G, which is toward the lower end of typical range of magnetar magnetic fields and the characteristic age is estimated to be 230 kyr. It is located near the center of SNR CTB, which is known for its half shell morphology in both radio and X-rays. It is at a distance of 4.0 ± 0.9 kpc.

Rotation powered pulsars and magnetars are very faint in X-ray except when they are bursting. In this work, we have developed data analysis method to handle these faint sources with *AstroSat*-LAXPC. LAXPC detector has 7 anodes arranged into 5 layers each with 1024 channels. We can extract spectra from different layers separately. From different layer spectra, we can decide about the right configuration of channels and layers for timing and spectroscopy can be done. A Source which has comparable flux to these sources are mostly detected in top 2 layers. We have detected a spin period of 151.85 ms for PSR B1509-58. Pulsations are detected up to 60 keV for this source. Emission profile consists of a very broad single peak whose shape does not change with energy. Another idea we have developed in this work is the extraction of different types of spectra.

Different types of spectra give us a consistency check on spectral parameters of the model. For spectroscopy of PSR B1509-58, we have used off pulse emission as a background spectrum and on pulse emission to source spectrum. Hence obtained spectra of PSR B1509-58 is found to be well fitted with a model of absorbed power-law in 3.0-25 keV band.

We detected pulsations of 6.46 s for 1E 1048.1-593. Emission profile has a single peak. Pulsations are detected only in soft energy band up to 7.0 keV. For 1E 2259+586, we detected pulsations of 6.98 s. The pulse profile of this source is double-peaked. For this source also, pulsations are detected up to 7.0 keV. Data from both sources was found unsuitable for spectroscopy.

Chapter 5: A Hydrogen Like Iron Line in HMXB Pulsar IGR J16320-4751 and Pulse Phase Dependence of Its Neutral Iron Emission Line

IGR J16320-4751 was detected with *INTEGRAL* in 2003 and identified with *ASCA* source AXJ1631.9-4751 detected in 1994. It is an HMXB consisting of an O8I optical counterpart and a neutron star. It shows periodic intensity modulation at 8.96 days, which is considered to be its orbital period. The spin period of neutron star in this system is $\sim$ 1300 s. It is located at a distance of $\sim$ 3.5 kpc and has an average X-ray luminosity of 3×10^{35} ergs s^{-1} in 17-60 keV energy band. Other than orbital modulation, light curves of IGR J16320-4751 show variability at various time scales, from seconds-minutes to days-months. The pulse fraction is found to be constant with energy in the *XMM-Newton* and *INTEGRAL* energy bands. The X-ray spectrum of this source is similar to other highly absorbed HMXBs, consisting of a power-law, prominent iron emission lines along with large absorption column (N_H $\simeq 2 - 5 \times 10^{23} cm^{-2}$). Inspite of large column density, the spectrum also shows a soft excess below $\sim$ 3 keV, which can be best explained with a black body of $\sim$ 0.07 keV. The absorption (N_H) and line emission (EW of Fe K_α) are correlated with each other, as expected from a system with the absorbing material also yielding fluorescence lines.

In this work, we report on results from multiple observations of the High Mass X-ray Binary (HMXB) pulsar IGR 16320-4751 with *XMM-Newton*-Newton and *RXTE* PCA. Using *XMM-Newton* and *RXTE* observations spanning about one binary orbit each, we investigate the pulse profiles and spectral variations in the system. The pulsar shows pulse profile variations on a day to day time scale, thereby making it difficult to determine an orbital solution for the binary. The X-ray spectrum shows signatures of multiple Fe emission lines. We find the presence of a hydrogen like iron line in the spectrum. We also find that pulse fraction in iron line energy band pulse profiles is surprisingly comparable to lower and higher energy range pulse profiles. A pulsating iron line flux indicates the presence of a complex and asymmetric medium surrounding the binary system. A soft excess component is seen in three of the *XMM-Newton* observations.

Chapter 6: Experimental X-ray polarimetric activities

In this work, we report on experiments conducted to establish the proof of concept for simple photo-electron polarimeter. We have used a proportional counter with closely spaced wires, interleaved as two sets of anodes. This technique does not require X-ray focusing optics, very high pointing accuracy, or spin of the satellite. This technique is therefore suitable for a small X-ray polarimetry mission. Photo-electron track made along wires are likely to produce signal in a single anode whereas tracks perpendicular

to wires will produce signal in both anodes almost equally. For any track direction in between, there is a splitting of charges in a ratio somewhere in between depending upon orientation of track with respect to two anodes. The first challenge is to establish the charge division concept. For this we used radioactive sources (unpolarized) Cd and Fe which emit X-rays of $\sim$ 23 keV and $\sim$ 6.0 keV respectively. For Cd charge division is seen at 200, 400 and 700 Torr gas pressure in detector due to large charge tracks. For Fe charge division is seen at 200 Torr. However, at higher gas pressure photo-electron track length is smaller than anode spacing and hence charge division is not seen. The second step is to distinguish between ratio histograms patterns for photons of different polarization angle. The ratio of events when the charge is divided between two events was found to be different for photons with different polarization angle.

POLIX is an X-ray Polarimeter for astronomical observation in the energy band of 5-30 keV. It is made of proportional counter based X-ray detectors, a scatterer and a collimator. Scatterer is made of low atomic mass material which causes the Thomson scattering of incoming X-rays, a process sensitive to the polarization of the X-rays. A Collimator had been made so as to avoid or reduce the number of other bright X-ray sources in its field of view. In addition, the dead area between cells and mass of collimator has to be minimized. These requirements are met with a collimator made of tapered hexagonal cells with a flat top angular response. This flat top response helps in mitigating any small pointing error of the satellite. Space based astronomy is a challenging field. An instrument has to be thoroughly understood and well calibrated before it is launched and astronomical observations are made. In the case of Thompson polarimeter we have to calibrate the flat top and overall angular response for payload rotation with misalignment with respect to collimator axis. Secondly Modulation curve which is used to infer the polarization properties, might be affected by other sources in field of view in addition to target on-axis source. This effect needs to be well understood and taken into account during observations. In this work, we present construction and development on two calibration experiments: 1. To measure the parameters of the flat top response of collimator with hexagonal cells. 2. Understanding and estimating the contribution of off-axis non polarized sources to the modulation curve.

Chapter 7: Summary and Future Works

List of Publications

- Probing the Cyclotron line characteristics of 4U 1538–522 using *AstroSat*-LAXPC

  Varun, Pragati Pradhan, Chandreyee Maitra, Harsha Raichur, Biswajit Paul

  Mon. Not. Ro. Astron. Soc.: Letters, Volume 484, Issue 1, March 2019, Pages L1–L6

  `https://academic.oup.com/mnrasl/article-abstract/484/1/L1/5245189`

- Pulse Phase Variation of the Cyclotron Line in HMXB 4U 1907+09 with *AstroSat*-LAXPC

  Varun, Chandreyee Maitra, Pragati Pradhan, Harsha Raichur, Biswajit Paul

  The Astrophysical Journal, Volume 880, Number 1,25 July 2019, Page 61

  `https://doi.org/10.3847/1538-4357/ab2763`

- A Hydrogen Like Iron Line in HMXB Pulsar IGR J16320-4751 and Pulse Phase Dependence of Its Neutral Iron Emission Line

  Varun, Nirmal Iyer, Biswajit Paul

  In preparation.

  Other Publication:

- Thermonuclear X-ray bursts in rapid succession in 4U 1636–536 with *AstroSat*-LAXPC

  Aru Beri, Biswajit Paul, J S Yadav, H M Antia, P C Agrawal, R. K Manchanda, Dhiraj Dedhia, Jai Verdhan Chauhan, Mayukh Pahari, Ranjeev Misra, Tilak Katoch, P. Madhwani, Parag Shah, Varun, Sujay Mate

  Mon. Not. Ro. Astron. Soc.: Volume 482, Issue 4, February 2019, Pages 4397–4407

  `https://doi.org/10.1093/mnras/sty2975`

List of figures

List of tables

Chapter 1

Introduction

"Light brings us the news of the Universe. Coming to us from the Sun and the stars it tells us of their existence, their positions, their movements, their constituents and many other matters of interest".

—**William Bragg**.

1.1 Introduction

The messages of the universe come to us in the form of electromagnetic radiation. Most of our understanding of the universe has come by measuring the strength and direction of radiation at different wavelengths. But the electromagnetic waves are transverse in nature and direction of the instantaneous electric (or magnetic) field is perpendicular to its direction of propagation. This fundamental property of the electromagnetic wave is called polarization. The most intense astronomical radiation that we receive on earth is the sunlight. Most of this radiation is randomly polarized. Probably, this was the reason human did not notice this characteristic of electromagnetic radiation for a very long. Polarization of electromagnetic radiation was observed by Malus in 1808 while looking through a calcite crystal at the setting sun. He noticed that the relative intensity of light changed as he rotated the crystal. The sunlight can become polarized due to scattering. Halo of the moon at night and rainbow after rain are natural examples of polarization by scattering. Light rays from rainbows are highly polarized (up to 95%). The unique design of their eyes allows bees to detect the polarization of light. This ability helps them to search for nectar. Figure 1.1 gives us interesting and funny insight into group discussion in a typical beehive.

Astrophysical sources are large aggregates of particles (plasma or atoms or molecules) with violent internal motions. The radiation from such sources is expected to be ran-

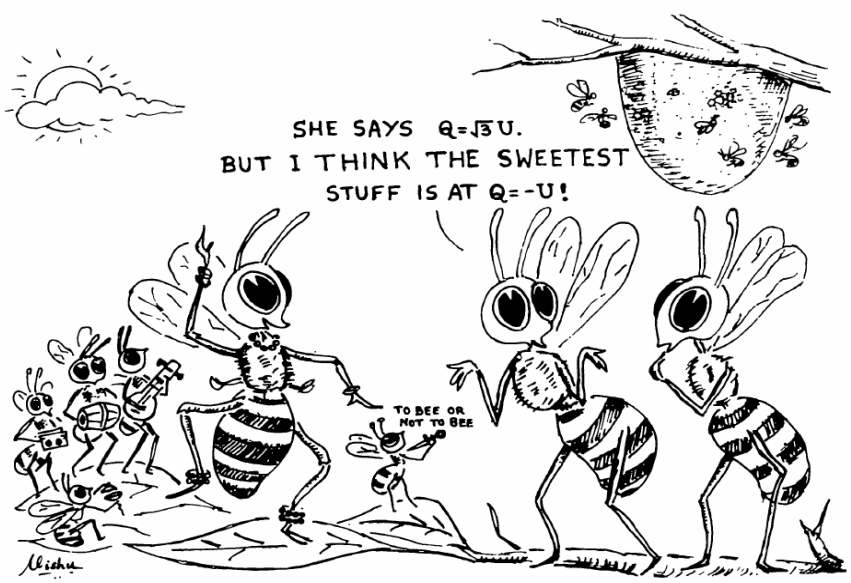

Fig. 1.1 A Cartoon representing the ability of bees to recognize polarization and how it plays crucial role in their survival. Figure credit: Radhakrishnan (1989).

domly polarised. For the radiation to have a net polatisation there must be something to break the symmetry and lead to a preferred direction of polarization. One such agent is scattering which leads to the modification of the symmetry of incident radiation by inherent anisotropy of radiation distribution after scattering. In all the cases mentioned above it is the Rayleigh scattering of optical light. Interactions of radiation with atoms Thomson/Compton scattering also leads to polarization of incident radiation. Another symmetry breaking agent is magnetic field. Magnetic field leads to polarization of radiation via synchrotron emission. Magnetic field varies over an extraordinary range of about 20 orders of magnitude in astrophysical sources. Some sources like radio galaxies Virgo A, Cygnus A, and Centaurus A have very feeble magnetic field of the order of microgauss. In the interstellar medium we have atomic and molecular clouds with fields of the order of microgauss. In the radiation belts of Jupiter the field strength is order of 1 Gauss. Even sun has a magnetic field strength of about $\sim$ Gauss. On the other hand, stellar compact objects like white dwarfs and neutron stars have very strong magnetic field. The magnetic fields found in white dwarfs ranges from thousand to billion Gauss. Neutron star have even more stronger magnetic field in range 10^{11}-10^{15} Gauss. Hence, we should be getting polarized radiation in abundances from these astrophysical sources. Polarized radiation comes to us across the electromagnetic band.

Polarization studies of astrophysical sources in optical and radio astronomy has been going on for some time now. On the other hand, polarization studies of astrophysical sources in high energy is yet to take off. This is a notoriously difficult area of research, compounded by the combination of low flux levels of high energy sources, poor efficiency of interaction processes known for making polarimeters of high energy radiation, high background rates and instrumental artifacts. In this thesis I have worked on a new technique to measure X-ray polarization. This technique is based on the photo-electron interaction of X-rays. We have done experiments to demonstrate the feasibility of distinguishing between incoming photons with different polarization angles. Along with the development of new techniques, there are renewed efforts to measure X-ray polarization of high energy astrophysical sources based using space based polarimeters. India is set to take important step in this field with the launch of its indigenous X-ray polarimeter (*POLIX*) by Indian Space Research Organization (ISRO). It will be the first dedicated X-ray polarimeter mission in the world. This X-ray polarimeter is based on Thompson Scattering of X-ray photons and being developed at Raman Research Institute (RRI). I have worked on calibration experiments of this polarimeter to characterise its collimator and study the effect of presence of an off axis unpolarized X-ray source in the the field of view of instrument.

Apart from polarization of radiation the presence of a strong magnetic field has another interesting effect in accretion powered pulsars which is imprinted on their spectra. In these X-ray sources, energy levels of electrons are quantized due to presence of strong field which can interact with photons of only certain energy values. Hence, some of interacting photons with these energies are scattered by the electrons and are absent from continuum spectra and is manifested as an absorption feature known as cyclotron line. Study of these features has become a vital tool to understand magnetic field configuration and accretion geometry of these sources. I have studied this feature in two HMXBs using data from *AstroSat*-LAXPC. *AstroSat* is India's first dedicated space based observatory with multiwavelength capability from UV to all the way up to hard X-ray.

1.2 Cyclotron Resonance Scattering Feature

Cyclotron resonance scattering feature (CRSF) is a line like broad absorption feature in high energy spectra of X-ray pulsars. Also known as cyclotron line, this feature has been observed at energies 10-100 keV for various sources. Cyclotron lines are manifestation of quantum electrodynamics process at work in astrophysical sources. In

electrodynamics, electron makes helical trajectories in the presence of the magnetic field. The magnetic field strength of earth is ~ 1 G and strongest humanmade magnets have a magnetic field strength of $\sim 10^6$ G. At these magnetic fields strengths classical electrodynamics is applicable, and electrons have continuous energy levels in the presence of magnetic field. Pulsars are however extreme objects with magnetic field strengths $\sim 10^{11} - 10^{13}$ G. One special class of pulsars called magnetars, even have magnetic field strengths $\sim 10^{14} - 10^{15}$ G. There is certain limit of the magnetic field for a particle beyond which problem of its motion needs to take care of relativistic quantum effects. This is called critical field at which particle its cyclotron energy equals its rest mass energy. For electrons, $B_{crit} = \frac{m^2c^3}{e\hbar} = 44 \times 10^{12}$ G. Detailed calculations have shown that beyond B_{crit}, electron's perpendicular momenta (and hence energies) are quantized in discrete Landau levels. This is given as

$$\frac{p_\perp}{mec} = n\frac{B}{B_{crit}} \tag{1.1}$$

Pulsars emit photons in a broad and continuous energy band. These photons can interact with electrons at their discrete energy levels only, and photons with energy in between do not interact. In other words, scattering cross-section at these energy is very high. Scattering cross-section of a pulsar with magnetic field 1.69×10^{12} is shown in Figure 1.2. Photons of these energies might be missing in the line of sight of observer and hence may be observed as absorption feature in the source energy spectrum. The energy at which this absorption is seen in the spectrum is given by

$$E_n = (m_e c^2)\frac{\sqrt{1 + 2n\frac{B}{B_{crit}}\sin^2\theta} - 1}{\sin^2\theta} \times \frac{1}{1+z} \tag{1.2}$$

Where
$m_e \equiv$ Mass of electron
$c \equiv$ Velocity of light
$\theta \equiv$ Angle between direction of incident photon and magnetic field
$z \equiv$ Gravitational redshift at the surface of the pulsar

The same physics is valid for other charged particles. However their lines will be seen in different energy band, and the separation between them will be different due their masses. For example, proton cyclotron lines are expected to be in the range a few eV to 100 eV for similar magnetic field strength.

The research on cyclotron lines in X-ray binaries is an emerging sub-field of X-ray astronomy. It is a very active area of research in observations and theoretical modeling.

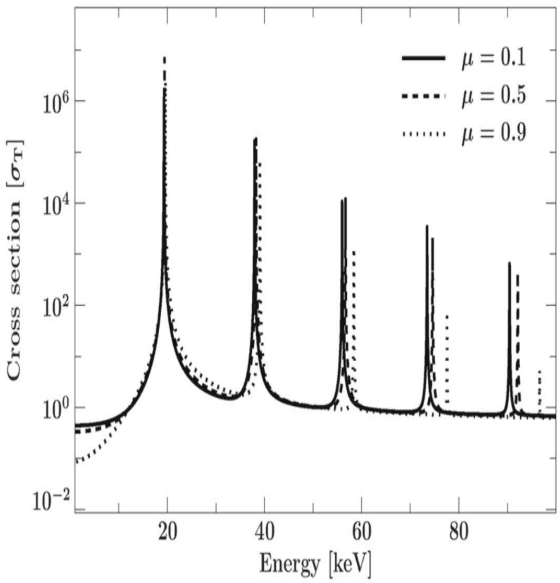

Fig. 1.2 Resonant Scattering photons with electron in presence of strong magnetic field strength. Figure shows cross sections for three viewing angles $\mu = \cos\theta = 0.1$,0.5, and 0.9 represented by solid,dashed, and dotted lines respectively. Figure credit: Schwarm et al. (2017).

The observations are detecting cyclotron lines in many new sources and theoretical works are focused on modeling the change in cyclotron line energy on different time scales, the relationship between cyclotron line parameters with luminosity, and several other interesting related problem. In short, cyclotron line research has become probe to understand the accretion physics in X-ray binaries.

The first cyclotron line was discovered in spectrum of High mass binary Her X-1 using a balloon experiment (Truemper et al., 1978) which provided first direct measurement of Neutron star's magnetic field strength. Initially, there was an ambiguity about the cyclotron line in Her X-1 to be an emission feature at ~ 53 keV or an absorption feature at ~ 40 keV (See Figure 1.3). Later detailed calculations of radiative transfer in the presence of magnetic field showed that it should be an absorption feature at ~ 40 keV. Within few years, another cyclotron line along with its fundamental and harmonics was detected in 4U 0115+63 (White et al., 1983). At present, there are five cyclotron lines (one fundamental and four harmonics) known in this source (Heindl et al., 2004). In early years of space-based astronomy, cyclotron lines were discovered from observations with pioneering satellite *Ginga*. After that many instruments with broad energy coverage and moderate spectral resolution like *RXTE*, *BeppoSAX*, *INTEGRAL* were used to study these features. More recently, *Suzaku*, *NuSTAR*, *As-*

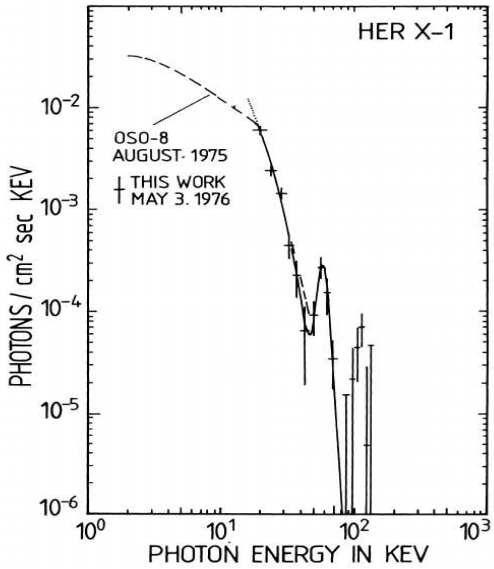

Fig. 1.3 Discovery of cyclotron line in energy spectrum of Her X-1. Observation was done using a balloon experiment. Figure credit: Truemper et al. (1978).

troSat are providing valuable information regarding cyclotron lines in pulsar systems. In the last 43 years since the discovery of first electron cyclotron line, they have been detected in $\sim$ 35 sources. Also, proton cyclotron line have been found in the spectra of isolated neutron star in energy range 0.1-1.0 keV using soft X-ray observations of *XMM-Newton* and *Chandra* (Haberl, 2007).

There are many scientific implications of studying cyclotron lines in binary pulsars. Measurement of centroid energy of the cyclotron line gives direct estimate of magnetic field strength of a neutron star. It can tell us more about physics of extreme environment near to neutron star by calculating ratios of observed value of fundamental and its harmonics. It has been seen that many sources show anharmonic spacing between fundamental and its harmonics. A ratio < 2 can be explained by relativistic corrections as in 4U 0115+63 (Santangelo et al., 2000) and > 2 by superposition of many lines as in Vela X-1 (Kreykenbohm et al., 2002). The shape of the CRSF itself is of great importance. It is generally fitted with a Gaussian or Lorentzian profile in spectra modeling. However, complex CRSF shapes have been observed in many pulsars like Cep X-4 (Fürst et al., 2015) and X Persei (Maitra et al., 2017). Even theoretical works have predicted complex CRSF shapes which includes the presence of line wings in the fundamental (Nishimura, 2008). Complex shapes are expected for low luminosity pulsars due to distortion of the magnetic field near the base of accretion mound due to the effects of local instabilities (Mukherjee and Bhattacharya, 2012) or variation

of Doppler boost with changing luminosity (Mushtukov et al., 2015a). Variations of CRSF line energy with luminosity can tell us about type of the accretion regime in sources. It depends upon whether its shows a positive, negative or no correlation of CRSF energy with luminosity. Theoretical studies have suggested that such correlations can be seen depending on whether a source is in sub-critical or super-critical regime (Becker et al., 2012). The critical luminosity is given by

$$\begin{aligned} L_{\rm crt} &= 1.49\times10^{37}{\rm erg\,s^{-1}}\left(\frac{\Lambda}{0.1}\right)^{-7/5} w^{-28/15} \\ &\times\left(\frac{M}{1.4\,{\rm M_\odot}}\right)^{29/30}\left(\frac{R}{10\,{\rm km}}\right)^{1/10}\left(\frac{B_{\rm surf}}{10^{12}\,{\rm G}}\right)^{16/15} \end{aligned} \tag{1.3}$$

$M \equiv$ Mass to the neutron star.
$R \equiv$ Radius of the neutron star.
$B \equiv$ Magnetic field strength of neutron star.
w characterizes the shape of the photon spectrum inside the column.
Λ characterizes the mode of accretion.

Sources in the super-critical regime show a negative correlation whereas sources in the sub-critical regime show positive correlation between the cyclotron line energy and luminosity. Long term changes in cyclotron line can be indication of geometrical change in line forming region or change in configuration of the magnetic field at poles due to the process of continued accretion. Finally, all CRSF parameters can change as a function of the pulse phase. This is indication of the change in physical parameters like plasma temperature, optical depth, etc. of the region around the neutron star. Projections of different parts of accretion mound with different properties results in variations of CRSF parameters with pulse phase.

1.3 Recent significant results in cyclotron line research

- **Evolution of cyclotron energy in Her X-1** : Her X-1 has been a source of interest for astronomers since in CRSF field research from past $\sim$ 40 years. It was the first source in which this feature was discovered. Since then it has been astronomer's favorite target of study in many electromagnetic bands. In the

hard X-ray band (> 10 keV), this source has been studied by many instruments like *Ginga*, *BeppoSAX*, *RXTE*, *INTEGRAL*, *Suzaku*, *NuSTAR* and *AstroSat*. Taking all the values of cyclotron line and their uncertainties on face value, it was found to be constant at $\sim$ 35 keV before 1991 then it suddenly increased to 45 keV between 1991-1994 and an apparent decay after that. However, a comparison of values derived from observation of different instruments needs to be corrected for systematic uncertainties due to calibration and different data analysis methods. Much of the decay of cyclotron line energy between 1994-2007 was found to be an artifact (Staubert et al., 2007). Instead, they found that cyclotron energy has a positive correlation with X-ray luminosity. When cyclotron line energy was normalized with the correct flux value, the time dependence vanished. However, by adding more measurements (2005-2012), it has been established that cyclotron energy in this source has decreased by $\sim$ 5 keV over the past 20 years (Staubert et al., 2014). The latest observation by *NuSTAR* in 2015 has further strengthened this result (Staubert et al., 2016). This study has separated the flux dependence from time dependence. Such change in cyclotron energy over a few tens of years reflects a local phenomenon in the accretion mound rather than change in the magnetic field strength. A change in magnetic field strength will happen at timescale of million years (Bhattacharya et al., 1992; Geppert and Urpin, 1994). A change in cyclotron energy at short timescales can be caused by the geometric displacement of the CRSF region to a larger distance from neutron star surface and hence a smaller magnetic field strength in the line producing region. Another possible explanation is that accreted material in the accretion column could drag field lines radially out and hence reduces the effective field strength where resonant scattering takes place.

- **Luminosity dependent variation of cyclotron line parameters** : X-ray luminosity of pulsar binaries is known to be variable. The CRSF parameters of these systems are seen to be varying with luminosity. CRSF line energy E_{cyc} dependence on X-ray luminosity L_X has been observed for many sources. Cyclotron line width and depth can also vary with L_X. A negative correlation was seen in transient source V 0332+53 by *Ginga* observation (Makishima et al., 1990). A second source with a confirmed negative E_{cyc}/L_X correlation is SMC X-2 (Jaisawal and Naik, 2016). Positive E_{cyc}/L_X correlation has been seen in many sources: Her X-1 (Staubert et al., 2007), Vela X-1 (Fuerst et al., 2014; La Parola et al., 2016), A 0535+26 (Klochkov et al., 2011; Sartore et al., 2015), GX 304-1 (Malacaria et al., 2015), Cep X-4 (Vybornov et al., 2017). V 0332+53

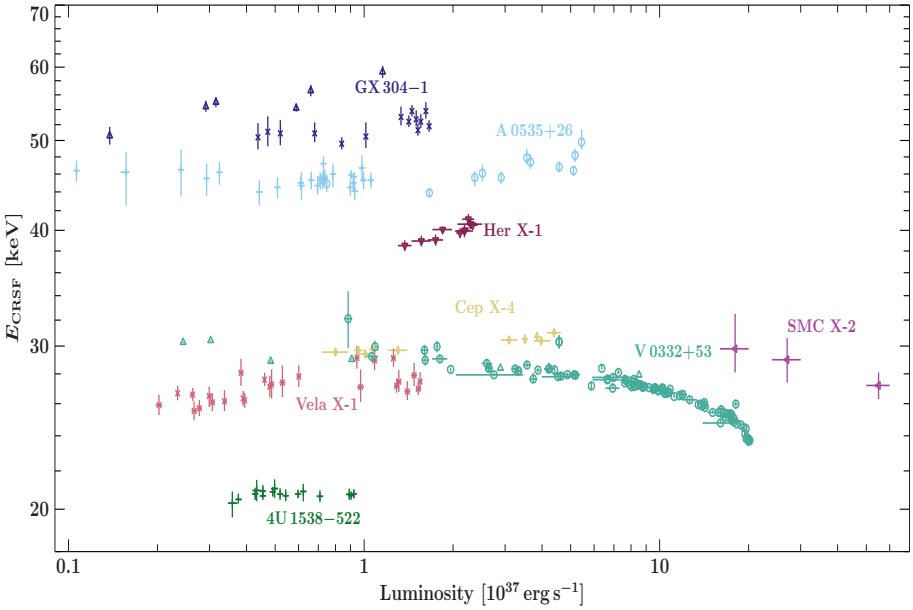

Fig. 1.4 Established luminosity dependence of E_{cyc} for various sources. A bimodal distribution is seen among all the sources along with some exception. Figure credit: Staubert et al. (2019).

also show positive correlation at very low luminosity at the end of outburst (Doroshenko et al., 2017). In GX 304-1 and Cep X-4, a flattening of linear correlation is seen at high luminosities (Rothschild et al., 2017; Vybornov et al., 2017). A comprehensive picture of E_{cyc}/L_X behavior is shown in Figure 1.4. Some indication of positive correlation of width and depth of cyclotron line has also been found (see table 8 of (Staubert et al., 2019)).

These two types of correlation can be understood in terms of two types of accretion modes separated by L_{crit} (critical luminosity) (Becker et al., 2012). Sources above and below L_{crit} are in super-critical and sub-critical luminosity state. L_{crit} depends upon the shape of photon spectrum inside the accretion column, whether a source is wind accretor or disk accretor and surface magnetic field of NS. In super-critical accretion mode, a radiative shock is formed in accretion column. This radiative shock decelerates the infalling material. Hence, an increase in accretion rate results with increased height of line forming region and vice versa. In sub-critical accretion mode, no radiative shock is formed, and matter falls on to the surface of the Neutron star. The deceleration of infalling matter is achieved through Coloumb interaction. An increased accretion rate leads to the smaller line forming region and vice versa.

Some other alternate efforts have tried to explain the bimodal distribution of luminosity dependence of E_{cyc}. For Example, CRSF line might be produced by Doppler-shift of radiative plasma whose movement depends on accretion rate (Nishimura, 2011, 2014). Luminosity dependence of E_{cyc} can be explained by combining change of height and the area of accretion mound with changes in emission profile (Mushtukov et al., 2015b). This approach also explains both positive and negative correlations. Another idea explains the observed positive correlation by producing CRSF line from the radiation reflected from the NS surface in accretion column with radiation dominated shock (Poutanen et al., 2013).

- **Detection of multiple cyclotron harmonics in 4U 0115+63** : High mass X-ray binary system 4U 0115+63 was one of the earliest cyclotron line pulsar. It has a very low energy fundamental line which make it a very good candidate for multiple harmonics to be observed with current class of broad band instruments. It is a very intriguing source in CRSF studies as it validates this phenomenon by showing multiple harmonics of the cyclotron line in its X-ray spectrum. It was first discovered in a sky survey conducted by *UHURU* satellite in 1972 (Giacconi et al., 1977). It is very active transient source, and 15 outburst have been reported in it since its discovery (Boldin et al., 2013). These are very luminous type-II X-ray outbursts during which multiple cyclotron lines are seen in it (Ferrigno et al., 2009; Giacconi et al., 1977). In *BeppoSAX* observation of outburst in 1999, four absorption feature were seen in pulse phase resolved spectra at a phase near the descending edge of the main peak of pulse profile. These were identified as one fundamental and three harmonics of cyclotron line at 12.74, 24.16, 35.74 and 49.5 keV having ratios of centroid energy with respect to the first to be $1 : (1.9) : (2.8) : (3.9)$. These ratios are significantly different from the classical values $1 : 2 : 3 : 4$. Theoretical modeling of CRSF have shown that excess of "shoulder" photons, below the fundamental (Isenberg et al., 1998) causes line energy of fundamental to appear high and hence ratios comes out to be smaller than expected. Equivalent widths of higher harmonics are found to be larger than that of the fundamental. At these energies two-photon processes have higher cross sections compared to one photon processes (Alexander and Meszaros, 1991). Due to these processes a photon with energy $E \sim 2E_c$ is scattered into to two photons at $E \sim E_c$. Hence photons at the fundamental cyclotron line are replenished at the cost of photons at higher harmonics. The net result is that the spectral line at higher harmonics will be significantly

deeper. In *RXTE* observation of 1999 outburst, five lines (Fundamental and four harmonics) were detected in one of phase resolved spectra (Heindl et al., 2004). These results emphasized that phase resolved spectroscopy of these features holds greater potential than phase averaged spectrum. Variations of CRSF parameters are averaged out in the phase averaged spectrum. These variations could be due to presence of multipole component of the magnetic field or an offset of dipole field with respect to center of star. X-ray observatories with broad energy coverage and very high effective area in whole band are very useful for phase resolved spectroscopy of these features.

- **Pulse phase variation of cyclotron parameter**

  Neutron stars in binary systems are rotating objects in the sky. Their rotation axis is generally tilted with respect to their magnetic axis. Emission towards an observer from such an object varies as a function of its rotation phase due to this misalignment. Model component for CSRF has three parameters for its line energy, width and depth. A few % of variation in CRSF parameters is due to angular dependence of cross section. Physical parameters (geometrical view of accretion column, plasma temperature and optical depth) or magnetic field may also change with pulsar rotation phase. Thus phase resolved spectroscopy of CRSF can provide better understanding on geometrical structure and magnetic field structure of pulsars. Pulse phase resolved studies have played very crucial role in the development of CRSF research. First of all, the presence of harmonics was was first noticed in phase resolved spectra than phase averaged spectrum for may sources like Her X-1 (Enoto et al., 2008; Klochkov et al., 2008), 4U 0115+63 (Robba et al., 2001), etc. Using this technique, it has been observed that ratio of second harmonic to fundamental energy varies across the phase for Vela X-1 (Maitra and Paul, 2013a). Pulse phase resolved spectroscopy of all three parameter have been performed for many sources, for example Vela X-1 (Maitra and Paul, 2013a), 4U 1538-522 (Hemphill et al., 2014; Varun et al., 2019), Cen X-3 (Suchy et al., 2008) A0535+26, 4U 1907+09, XTE J1946+274 (Maitra and Paul, 2013b), etc. The phase resolved variation of parameters show complex and different patterns for different sources. These patterns are interpreted differently for each sources invoking different conditions. However, there is serious need for comprehensive scheme of theoretical modeling.

  Several complicated processes needs to be considered for a sensible interpretation of observational patterns of CRSR phase variations. To begin with, gravity

near the NS surface is very strong and effects of gravitational light bending needs to be included (Leahy, 2003). Due to this, a particular viewing angle gets contributions from multiple emission regions. Another effect is the presence of multipolar magnetic field or magnetic field with sharp gradients. Then effect of different types beaming patterns also needs to be considered. "Pencil" and "Fan" are two types of beaming pattern considered in pulsars depending on the source luminosity. Some times a combination of both can be present in a pulsar. Source luminosity determines which type of beam is emitted. The theoretical modeling should give us readymade templates for phase variations of cyclotron parameters given the source physical conditions. Then we will be able to understand these extreme environments in more details.

- **Formation mechanism of cyclotron lines**

  Cyclotron lines observed in pulsar systems tend to be different than any other atomic or ionic absorption lines. These lines are considerably broader and their shape also tend to be more complex. Some authors have tried to explain these lines by solving radiative transfer in slab or cylindrical geometries with uniform physical conditions (Araya and Harding, 1999; Nagel, 1981a,b). Cyclotron lines observed in X-ray pulsars are much broader and shallower than predicted by these theoretical works. Recently, some authors have tried to model accretion column with a series of regions on top of each other, having different physical properties like temperature, density and magnetic field varying with height. Properties of effective cyclotron line emerging from accretion column or mound is the superposition of cyclotron line emerging from different parts (Nishimura, 2008, 2005). Two types of accretion mound geometries are considered depending upon whether source luminosity is higher or smaller than critical luminosity ($L_* \sim 10^{37}$ erg s^{-1}). The systems with $L > L^*$ tend to have extended accretion mounds and are modeled by a cylindrical geometry. On other hand, the systems with $L < L^*$ accretion happens directly on the surface of neutron star surface and are modeled by slab geometry of accretion. This model shows that superposition of narrow and deep lines from individual domains with different peak energies results into effective broad and shallow cyclotron line. The fundamental line profile has asymmetric shape that is shallower towards lower energies than towards higher energies. Further, the shape of fundamental line can be more complex as it is due to the superposition of large number of individual line with absorption like feature in center and two wings in sides. On the other hand, shape of harmonics is simple but asymmetric. This type of modeling has been

considerably successful in explaining properties of cyclotron lines like complex nature of fundamental line, change in line parameters (energy, depth and width), deviation of ratio of harmonics and fundamentals from expected value, luminosity dependence of line energy, etc. Results of this model has been used to explain some enigmatic features in some well known sources. The observed increase of energy and depth of cyclotron line with time, together with decrease of its width in V0332+52 (Mowlavi et al., 2006) are consistent with model predictions for this system. In 4U 0115+63, dependence of line energy (while its depth is almost constant) with luminosity can be explained using this model. The complex shape of fundamental line as seen in V0332+53 (Pottschmidt et al., 2005) and 4U 0115+63 (Heindl et al., 1999) can be explained naturally in this model as superposition of photon densities coming from different segments of accretion column with cylindrical geometry resulting in a double absorption feature for fundamental line. However, harmonic lines are much simpler than the fundamental even in the case of cylindrical geometry. This complicated shape of fundamental line makes it harder to detect fundamental than harmonics as seen in Vela X-1 and A0535+26. This also make ratio of harmonics to fundamental to deviate from expected value as seen in Vela X-1 (Kreykenbohm et al., 1999).

1.4 Polarimetry in high energy astrophysics

Since its birth in 1960s, X-ray astronomy has given significant contribution to our understanding of universe thanks to fantastic advancements in timing, spectroscopy and imaging with pioneering instruments like Rossi X-ray Timing explorer (RXTE), Chandra and XMM-Newton. Polarimetry in high energy started in early phase of X-ray astronomy with polarimeters on board OSO-8 (Novick, 1975; Weisskopf et al., 1976) and ARIEL-5 satellites (Gowen et al., 1977). A few observations were made with these polarimeters. The measurement of polarization of CRAB Nebula (Weisskopf et al., 1978b) and upper limits on polarization degree for CYG X-1 (Weisskopf et al., 1977) and Sco X-1 (Weisskopf et al., 1978a) we obtained from these observations. The advent of X-ray optics gave significant improvements in imaging and spectroscopy. Polarimeters based on classical techniques like Bragg diffraction and Thomson scattering along with collimators required rotation of satellite for measurements. Also, X-ray polarimeters requires a large number of photons and therefore, very long durations are required. Due to these differences polarimeters could not be assembled along with satellite dedicated to other techniques. As a result, polarimetry has been an almost

unexplored field of high energy astrophysics until recently. Although some polarization measurements were made using balloon-borne experiments.

1.5 Science Prospects of Polarimetry in High Energy

In recent years, dedicated efforts are being made to open this window of astronomy due to its promise to solve some unresolved issues. Polarisation measurements are suggested to be a good method to investigate acceleration processes due to magnetic reconnections in solar flares and in strong magnetic fields of Neutron stars and White dwarfs. Polarization measurements can give more details about the geometrical structures in astrophysical sources like accretion disks, accretion column, molecular torus and ionization cones by measuring polarization of radiation. Radiation in these structures gets polarized by scattering from asymmetric regions. Polarisation measurements also has potential to understand fundamental physics in extreme regimes of strong gravitational and magnetic fields not accessible on lab experiments on earth. Finally, it can test some predictions of physical theories like quantum electrodynamics (QED) and quantum gravity. Astrophysical sources are readymade test beds for testing these processes and theories. Below is list sources which can be observed by upcoming space mission for polarization measurements.

- **Accretion powered pulsars:** In accretion powered pulsars, the accreted matter is a plasma in a strong magnetic field. The scattering of radiation with magnetized plasma can lead to strong polarization. The radiation propagates as ordinary and extraordinary modes in the presence of a strong magnetic field. These two orthogonal modes of radiation have different opacity in the magnetized plasma. The ordinary mode propagates parallel and extraordinary mode propagate perpendicular to the magnetic field. This difference in opacities for the two modes leads to birefringence for the propagating photons and thus strong polarization of the outgoing radiation. The degree of polarization is strongly dependent on the geometry of the emission region, the spin phase, and also varies with the energy (Meszaros et al., 1988). For some suitable orientations, the degree of polarization can reach up to 70 %. The polarization of photons parallel to the magnetic field ("pencil beam") is expected to be the weakest at the maximum of flux amplitude. For the photons perpendicular to the field ("fan beam"), the polarization is expected to be the strongest at the maximum of flux

amplitude. Thus, the pulse phase-resolved polarimetry can help us get insight about the geometry of the emission region and radiation pattern model in the accreting pulsars.

- **Galactic Black Hole Binary:** In high-soft state of Black hole, the emission from accretion disk component is the brightest component of X-ray spectrum. Gravity is very strong in the innermost region of the disk. Although General relativity has been tested in weak field limit, there are some predictions of GR in strong field limit which have not been tested yet. Innermost regions of accretion disk are suitable for testing strong gravity effects. The strong gravitational field in the innermost regions changes the polarization properties of X-ray emission (Krawczynski, 2012). These effects have a dependence on mass and spin of black hole and also show variation with energy. Combining polarimetric measurements with the timing and spectroscopic data, it will be possible to understand the spin rate of the black hole and its effect on inner structure of the accretion disk. In the low-hard state of black hole, X-ray polarization measurements will allow us to study the reflection of X-rays from the accretion disk, its extent and relation with the geometry of the disk.

- **Rotation powered pulsars:** This class of objects have been studied in radio, optical and X-ray wavelengths via timing and spectroscopic observations. One question that has not been answered so far is about the origin of X-rays. Pulsar emission models suggest that X-ray are originated either on polar caps or at outer gap of the pulsar magnetosphere. Recent observations of Crab pulsar above 25 Gev by Cherenkov detectors seems to prefer polar cap model (Aliu et al., 2008) but this observation had a small signal to noise ratio. X-ray polarization measurements will allow us to make a clear distinction between these pulsar emission models.

- **Supernova Remnants:** X-ray emission from supernova remnants has two possible contribution – thermal emission from shock heated high temperature gas and synchrotron emission from relativistic electrons accelerated by the shock. Synchrotron emission has been thought to dominate emission from some of these remnants, and in some specific regions of some supernova remnants. In particular, remnants that are significantly energised by the wind from an embedded pulsar are expected to radiate mainly via the synchrotron mechanism. Measurements of X-ray polarization can confirm synchrotron mechanism as the dominant emission process in such cases. Comparison of the angle of polarization with op-

tical/radio data can tell us about population distribution of electrons responsible production of photons in the entire electromagnetic band. Further imaging polarimetry can be used to localise the the regions of synchrotron emission and measure the strength and orientation of magnetic field at different emission sites (Vink, 2012).

- **Blazars:** The spectral energy distribution in blazars, shows two characteristic emission peaks. The second characteristic peak can be either due to synchrotron-self Compton (Celotti and Matt, 1994) or due to inverse compton of seed photons (Poutanen, 1994). This problem can not be solved via spectroscopic studies. Both these models give rise to different degree of polarization. Hence, the polarization studies of these objects can help us distinguish between these two alternative scenario for blazars emission.

- **Solar Flares:** Solar flares are produced due to magnetic reconnection and subsequent acceleration of particle in the corona of the Sun (Brown, 1971). Similar phenomenon happens in other stars too which are at larger distance and hence much fainter. Sun being closer gives the gives us much brighter signal. Hence, study of solar flares can give us a good understanding of behavior of this class of sources. In hard X-rays (above 20 keV), the emission from solar flare is dominated by the non-thermal emission with a polarization degree as high as 40% (Zharkova et al., 2010). Below 10 keV, the emission is mostly thermal but this thermal emission can also be polarized due to possible anisotropy in the electron distribution function (Emslie and Brown, 1980). Polarization measurement of soft X-rays gives us the possibility to find out the anisotropy in electron distribution and study the acceleration mechanism of solar corona at the same time using hard X-rays. Study of solar flares is also important for space weather studies.

- **Millisecond Pulsars:** A pulsar with rotational period in range of about 1-10 milliseconds is called millisecond pulsar (MSP). These are very old binary systems where Neutron star has been spun up by accreting matter from companion. For these systems emission from accretion shock and accretion disk gives different degree of polarization (Sazonov and Sunyaev, 2001; Viironen and Poutanen, 2004). Phase resolved X-ray polarimetry allows us to test which model gives more appropriate description of emission from these systems. It can also provide the geometrical parameters, such as the orbital and magnetic inclination. Usually millisecond pulsars are very faint in quiescence but can undergo outburst

for few hours to days. During these outbursts these systems are active in X-rays and can give us useful information about these systems.

1.6 Recent measurement of X-ray Polarization from astrophysical sources

High energy astrophysics community has made new effort to open this window. Some new measurements have been made using balloon experiments and space based instruments. An intense activity of theoretical modelling has started again. Some new mission are being planned dedicated to X-ray polarization measurements. Here I present a brief summary of interesting results in X-ray polarization in last few years. These results have given specific insights into the understanding related to astrophysical sources which could not be gained with other type of studies. The impact of these results are quite remarkable despite poor statistics and low confidence level.

- **The pulse phase resolved polarization of Crab:** The Crab pulsar is a typical example of a young, rapidly spinning, strongly magnetized neutron star that generates broadband electromagnetic radiation by accelerating charged particles its magnetosphere. It is very bright in X-rays and the flux density and spectrum are known to be constant, with the exception of the pulsar itself. Crab is the only pulsar for which X-ray polarization has been measured with high significance so far. This observation dates almost 50 years back. Recently, a new measurement of X-ray polarization from the Crab pulsar and nebula was done in the 100-380 keV band using the Cadmium-Zinc-Telluride Imager (CZTI) on-board Indian astronomy satellite *AstroSat* (Vadawale et al., 2018). Crab was observed 21 times with a total exposure time of ~ 800 ks. Crab has a phase averaged polarization of $32.7 \pm 5.8\%$. The measured polarization angle is $143.5 \pm 2.8^{\circ}$ eastwards from the celestial north. For the off-pulse region the measured polarization fraction and polarization angle are $39.0 \pm 10\%$ and $140.9 \pm 3.7^{\circ}$, respectively. A pulse phase resolved analysis showed that polarization fraction and angle show a large variation across the pulse phase as shown in Figure 1.5. Polarization fraction is found to be stronger in off-pulse region than at two peaks. Polarization fraction also show a dip at phase 0 along with a swing in polarization angle. There are two significant implication of these observations in comparison with optical polarization behavior (Słowikowska et al., 2009). X-ray polarization behavior show a noticeable variation of polarization in the off-pulse region. This indicates that

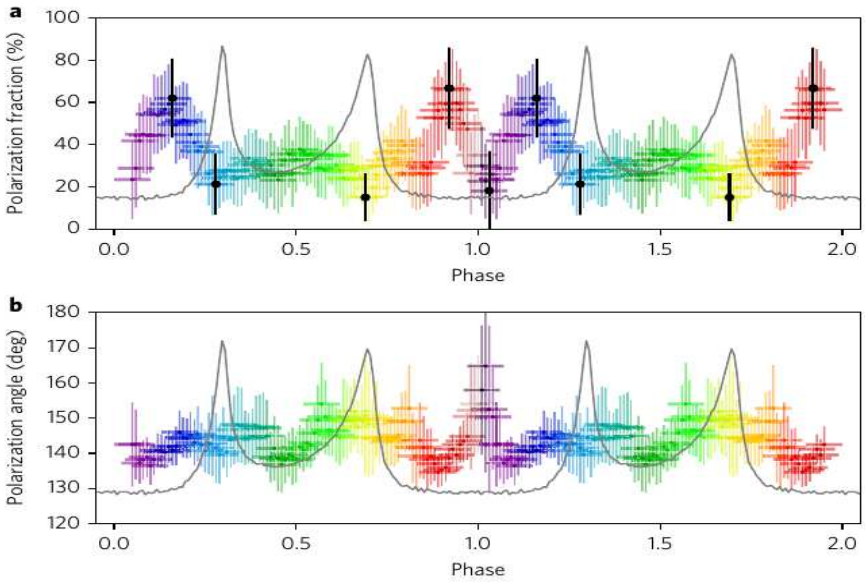

Fig. 1.5 Pulse phase resolved polarization behavior of Total Crab emission. Top and bottom panel shows polarization fraction and angle variation pattern. Pulse profile of crab pulsar is overlaid in gray colored line. Figure credit: Vadawale et al. (2018)

.

a significant fraction of the off-pulse emission in hard X-rays might be produced in the pulsar itself. Second, two emission peaks show different behavior in terms of pulsar properties. This is in contrast with behavior seen at optical band.

- **Accretion geometry of Cyg X-1**: Cyg X-1 is a Black Hole Binary (BHB) system in which a stellar mass black hole is closely orbiting a companion star. Black hole is accreting material from the companion which forms an accretion disk, corona and a jet. As the matter is accreted, it emits X-ray due to the release of gravitational potential energy. Cyg X-1 was observed between 12-18 July 2016 by PoGO+ polarimeter which is a balloon experiment (Chauvin et al., 2018). Source was in its hard state during the observation. Figure 1.6 shows the results of measurement form this observation. The polarization fraction of Cyg X-1 of hard X-rays (19-181 keV) was found to be $< 8.6\%$ (upper limit at 90% confidence level) and polarization angle is found to be aligned with jet axis (PA $= 154 \pm 31^{\circ}$). This is consistent with radio measurements where this was found to be $158 \pm 5^{\circ}$ (Stirling et al., 2001).

  Two competing models describe the disk-corona geometry for the hard spectral state of BHB (Fabian et al., 2012; Makishima et al., 2008). The first is "lamp-post" corona model in which corona is small and is located on the rotation axis

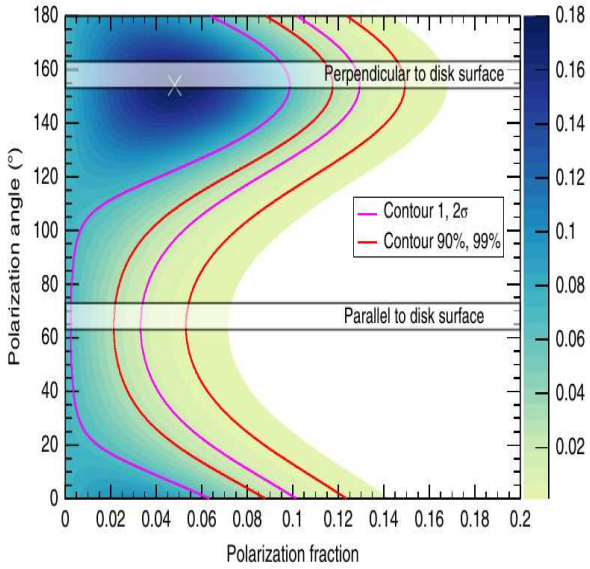

Fig. 1.6 PoGo+ measurement of polarization fraction and angle for Cyg X-1. Posterior density and credibility regions are shown. White cross corresponds to maximum posterior density. Figure credit: Chauvin et al. (2018).

of black hole, close to the event horizon. In this model secondary emission is strongly affected by strong gravitational field of black hole. Second model is "extended corona model" in which corona has a spherical distribution around the black hole and accretion disk is truncated before the innermost stable circular orbit. Both these models are shown in Figure 1.7. In the lamp-post corona model, the secondary reflected emission is emitted very near to the black hole and results into large pulse fraction up to $\sim 15\%$ and polarization angle (PA) not perpendicular to the accretion disk surface (Dovčiak et al., 2011, 2012). In the extended corona model, a low pulse fraction of 2-5% is predicted along with a PA perpendicular to the disk surface. Hence PoGO+ polarization measurement reveals that the accretion corona to be an extended in agreement with second model or it might be located far form the black hole.

This measurement has two interesting implications. First, the BHB emission in hard state comes far away in disk and not affected by strong gravitational field and black hole spin. Hence, spin parameter will be difficult to determine in the hard state by using secondary emission. Second, the transition from soft to hard can be a result of shrinking of corona structure and subsequent expansion accretion disk beyond the innermost stable circular orbit.

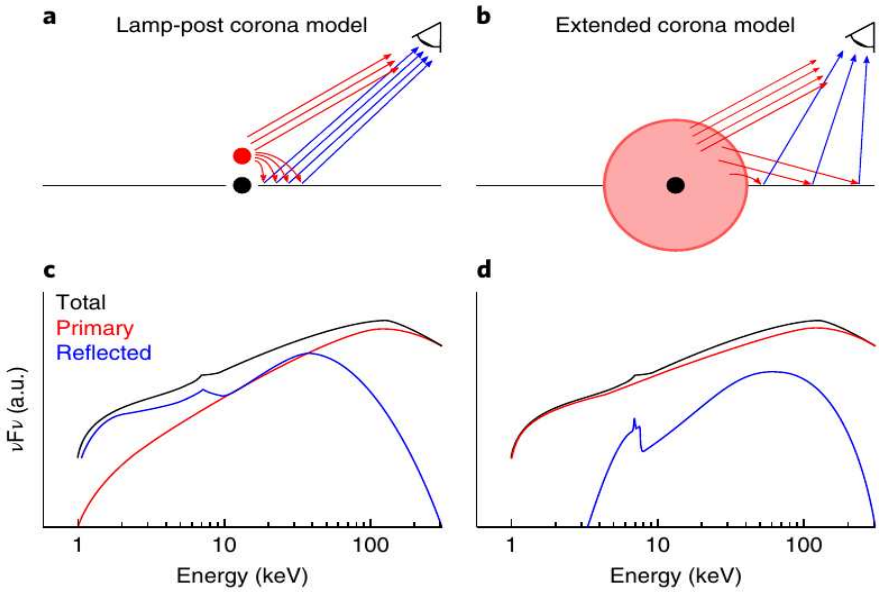

Fig. 1.7 Geometrical description two models of X-ray emission of hard spectral state of BHB. Black hole is shown as a black point, accretion disk is the horizontal black line, and the corona in red color. The primary and secondary emission is shown with red and blue rays respectively. Primary, second and total spectrum emitted from in case of these models is shown in bottom panels. Figure credit: Chauvin et al. (2018).

- **Polarization measurement of GRBs:** Gamma-ray bursts (GRB) are explosive cosmological events which occur during the formation of the stellar mass compact objects (Mészáros, 2006). Most of the burst energy is released during first few seconds to a few minutes time duration along with launch of highly relativistic jet from the central object. This is known as the prompt emission phase (Piran, 2004). When the outflowing material hits the surrounding material, it heats the material. This happens on longer timescale and is known as the afterglow phase. The prompt emission contains most important information about the intrinsic properties of outflowing plasma and the central engine, as it occurs close the the burst site.

  The CZT Imager (CZTI) on-board *AstroSat* works in 20-200 keV band and becomes an open detector above 100 keV (Rao et al., 2016). The CZTI also has polarization detection capabilities in 100-380 keV (Vadawale et al., 2015). Thus, the CZTI provides good spectroscopic and polarization capabilities for studying GRBs. The first GRB detected by Astrosat CZTI, GRB 151006A was found to high polarization fraction of 77% and 94% (at 1σ significance) for prompt and afterglow phases respectively (Basak et al., 2017). A larger sample of GRBs from

one year of CZTI operation gave polarization measurement at higher significance level. All the 11 GBRs observed showed clear polarization signal with $\geq 3\sigma$ significance for 4 GRBS and ~ 2.5 sigma for another 3 GRBs (see Table 2. of Chattopadhyay et al. (2017)). GRB 171010A, a very bright GRBs with fluence $10^{-4} ergs^{-1}$ was also studied with CZTI (Chand et al., 2019). During the prompt phase it had a low but time variable polarization. It is difficult to rule out various emission models with the current sample of polarization measurements. However, with a proven polarization measurement capabilities with rapidly growing sample promises an era of polarization detection.

1.7 Measuring X-ray Polarization

A photon is a discrete packet of electric and magnetic fields which are perpendicular to each other and to the direction of propagation. The polarization describes the configuration of these fields. All photons are polarized individually. However, a source is polarized if the polarization of different photons have same or similar. If the individual photon polarization are uncorrelated, then the source is unpolarized or poorly polarization.

X-ray polarization cannot be measured directly. All the present X-ray measurements are done indirectly by converting the polarization information into intensity (Novick, 1975). X-rays first undergo interaction and gets distributed anisotropically into various directions. The distribution pattern depends upon the type of interaction. The histogram of X-rays counts collected as a function of angle is called modulation curve. An sample modulation curve is shown in Figure 1.8. In general, the modulation curve can be fitted with analytical function given by

$$C(\eta) = A + B\cos^2(\eta - \phi) \tag{1.4}$$

Where
$\phi \equiv$ Polarization angle.
A $\equiv$ Unpolarized component of the intensity.
B $\equiv$ Maximum polarized intensity.

The Modulation amplitude is, $a = (C_{max} - C_{min})/(C_{max} + C_{min}) = B/(2A + B)$. If the modulation curve is given, a and ϕ can be obtained from it.

This description assumes an ideal polarimeter which means that there is no modulation for unpolarized source. In this case the modulation amplitude is equal to polarization degree. Most polarimeter show some modulation for unpolarized radiation. For a polarimeter, the modulation factor, μ is defined as the modulation amplitude measured for 100% polarized radiation. This a property depends upon the working of polarimeter and energy or spatial distribution of incoming photons. Background count b, also affects the modulation curve. In practice, the polarization degree of a source measured from a polarimeter with a given μ is

$$P = \frac{a}{\mu}\frac{r+b}{r}. \tag{1.5}$$

Where r is source count rate, a is modulation amplitude which is measure from modulation curve.

The X-ray polarization levels predicted for the astronomical objects are often quite low. The polarization fraction P, is a non-negative quantity. Due to statistical fluctuations, any particular measurement of P will also give a small value. Thus instrumental or systematic errors are a serious concern as non-polarized source can be confused to have small polarization. The sensitivity of a polarimeter is defined in terms of "Minimum Detectable Polarization" (MDP) (Novick et al., 1977). The MDP is a measure of confidence of its measurement. It is the largest fluctuation expected with a probability of 1% for an unpolarized source. Equivalently, the MDP is the smallest polarization that can be detected with 99% confidence. The MDP is defined as

$$\text{MDP} = \frac{4.29}{\mu r}\sqrt{\frac{r+b}{T}} = \frac{4.29}{\mu}\frac{1}{\sqrt{N}}\sqrt{1+\frac{b}{r}}, \tag{1.6}$$

where T is the observation duration and $N = rT$ is the total number of source counts.

1.8 Upcoming High energy polarization missions:

- **Indian X-ray Polarimeter (POLIX)**: India is set to enter in the field of X-ray polarization with the launch of an indigenous space mission. A Thomson X-ray polarimeter has been approved for a small mission by Indian Space Research Organization (ISRO). It can perform polarimetry of hard X-ray sources like accretion powered pulsars, black holes, blazars etc. It also has moderate spectral and good timing capabilities. The instrument has a simple design which does not require X-ray optics. The instrument has a very large photon collection area

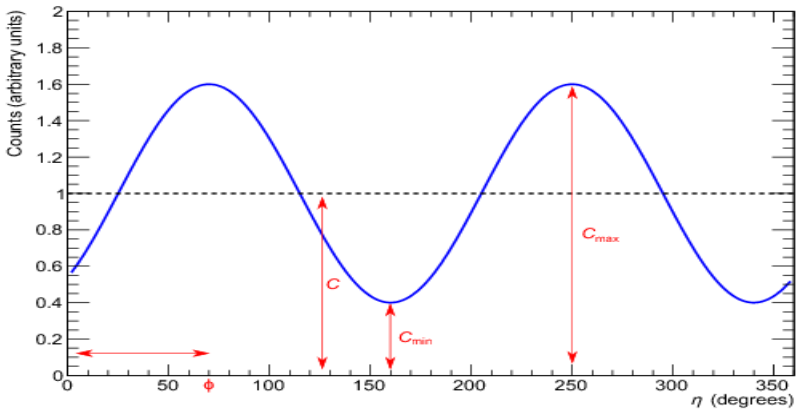

Fig. 1.8 Modulation Curve: Detector count rate versus angle for a linearly polarized radiation.

in 8-30 keV energy band. Some cosmic sources like accreting X-ray pulsars are brightest in this energy band as they are absorbed at lower energies. There are about 50 bright X-ray sources for which a Minimum detectable polarization of 2-3% can achieved with this instrument.

The basic configuration of the instrument consists of a collimator, a scatterer and X-ray detectors surrounding the detector as shown in Figure 1.9. The collimator restricts the field of view to a small part of the sky, $3° \times 3°$ so that there is only one bright X-ray source in the field of view for most of the observations. The scatterer is made of a low atomic mass material, Lithium and/or Beryllium which causes Thomson scattering of the incoming X-rays, a process that is sensitive to polarization of the X-rays. The scattered X-rays are absorbed and detected in a set of X-ray proportional counters surrounding the scatterer. The whole instrument is rotated around the viewing axis, thus providing azimuthal distribution of the scattering of X-rays in each element of the detectors, which enables X-ray polarization measurement.

- **Imaging X-ray Polarimeter Explorer (IXPE)**: IXPE is space based telescope which will measure the polarization of X-rays from galactic and extra-galactic sources. IXPE was proposed for a NASA mission in January, 2017 for a small satellite program to be launched in mid 2021. It can perform polarimetry of X-ray sources along with imaging, spectroscopy and timing. This will be the first mission to perform all four types of study with a single instrument. Many galactic sources produce polarized radiations, like Neutron star (isolated and bi-

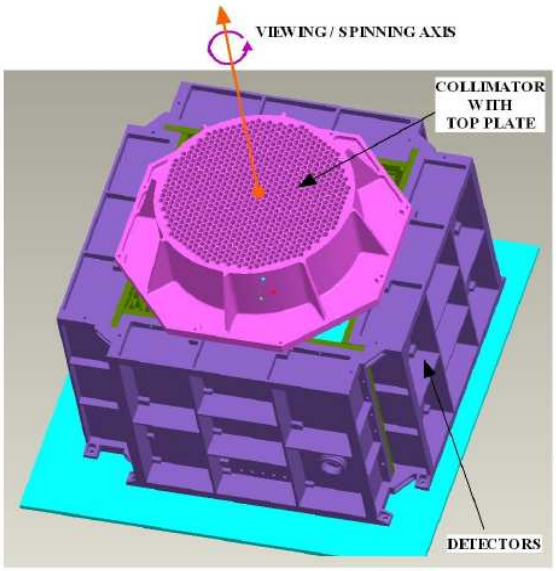

Fig. 1.9 Mechanical design of Thomson X-ray polarimeter. Figure cradit: Rishin P. V.

nary), black holes, supernova remnants (and pulsar wind nebula associated with them) and micro-quasars. Extra-galactic objects, especially blazars can also be studied. Studying the polarization reveals the physics of these objects and can provide insights into the extreme environments where they are created.

Chapter 2

Description of the Instruments and Methods Used in the thesis

2.1 Scientific Instruments Used for Data Analysis

Astronomers use four types of measurements, namely timing, spectroscopy, imaging and polarimetry of electromagnetic waves to understand the cosmic sources. A particular instrument might be capable of doing all or some of these measurements. X-ray instruments used in different space missions have different capabilities, for example, LAXPC on board *AstroSat* has very good timing and moderate spectroscopy but no imaging capabilities. On the other hand, ACIS on *Chandra* is very good imaging and spectroscopic instrument but its timing capabilities are poor compared to LAXPC. Generally, astronomers choose to observe a particular source with some astrophysical phenomenon in their minds which determines the choice of instrument. Observations from multiple instruments can become useful in some cases.

Progress in any branch of science depends on the new discoveries which is closely linked with the development of new technology. X-ray astronomy has come a long way since its birth in the 1960s, from the discovery of high energy radiation from the sun and other types of cosmic sources to the current era of fast timing, high resolution spectroscopy, and arcsec angular resolution imaging. Next milestone will be the addition of high energy polarimetry and its assimilation with other techniques. Astronomical community has taken this challenge with renewed efforts in instrumentation design boosted by some new results in observations and theoretical modeling.

Our work in this thesis is partly motivated in the direction of high energy polarimetry with experiments to study the possibility of making a new large area polarization measurement technique, onground calibration of a polarimeter mission. Along with

the developmental work towards X-ray polarimetry instrumentation, we have also analysed data from pulsars to study their cyclotron lines. These lines give us a good understanding of magnetic field configuration in pulsars which will be probed in more detail by polarization observations by upcoming missions. Pulsar data were mainly obtained through observation proposals in the various cycle of guest opportunity of India's *AstroSat* mission. The central point of investigation in these proposals was the study of cyclotron lines with LAXPC which is ideal for this purpose due to its high effective area in broad energy band. Some of the pulsar data were obtained from performance verification cycle of *AstroSat*. In the next subsection I give a description of scientific mission and specific instrument used in this thesis.

2.1.1 *AstroSat*

AstroSat is India's first dedicated multi-wavelength space observatory. It is a collaborative mission of leading astronomy research institutes of India - Tata Institute of Fundamental Research (TIFR), Indian Institute of Astrophysics (IIA), Inter-university Center for Astronomy and Astrophysics (IUCAA), Raman Research Institute (RRI) and various centers of Indian Space Research Organisation (ISRO). These institutes have contributed to payload development and software support for this mission. Some parts of the payloads have also been developed in collaboration with Canadian Space Agency (CSA) and University of Leiscester (UoL), UK. The spacecraft control center at Mission Operations Complex (MOX) of ISRO Telemetry, Tracking and Command Network (ISTRAC), Bengaluru manages the satellite during its entire mission life. The mission was launched on 28 September 2015 into near-Earth (650 km) orbit inclined at an angle 6° to the equator. The expected operating life time of the satellite will be more than five years. *AstroSat* has five dedicated scientific instruments. These are the Ultra-Violet Imaging Telescope (UVIT) (Subramaniam et al., 2016; Tandon et al., 2017), Soft X-ray Telescope (SXT) (Singh and et al., 2017), Large Area X-ray Proportional Counter (LAXPC) (Agrawal et al., 2017; Antia et al., 2017), Cadmium–Zinc–Telluride Imager (CZTI) (Bhalerao et al., 2017; Vadawale et al., 2016) and Scanning Sky Monitor (SSM) (Ramadevi et al., 2017). The first four instruments are co-aligned so as to point to the same source. UVIT is a focusing telescope with two identical units, covering optical to Far-UV bands. SXT has an X-ray CCD detector with conical foil mirrors, covering the energy range 0.3-8.0 keV having an effective area about 120 cm^2 at 1 keV. Three LAXPC units cover medium to hard energy range from 3.0-80.0 keV. CZTI is coded-mask imager, covering 10-150 keV energy band with a field of 6°. Figure 2.1 is a schematic view of *AstroSat* showing all instruments on board. This

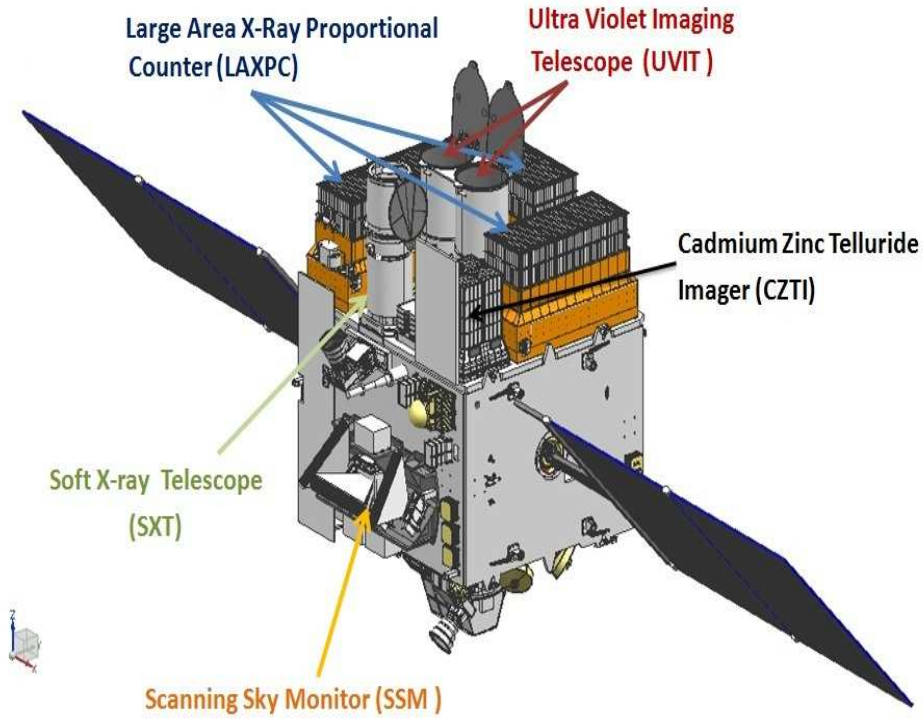

Fig. 2.1 Schematic view of all instruments on board *AstroSat*. Four instruments — UVIT, SXT, LAXPC, and CZTI are co-aligned. They have fixed pointing. SSM is placed on a rotating platform to scan the available sky once every six hours. Figure credit: ISRO.

broad coverage of electromagnetic band enables the simultaneous multi-wavelength observations of various astronomical sources with a single satellite. Multi-wavelength observations of *AstroSat* can be further extended with co-ordinated observations using other spacecraft and ground-based observations. Both individual studies of specific sources of interest and surveys can be conducted with this telescope.

2.1.1.1 LAXPC

The Large Area X-ray Proportional Counter (LAXPC) is one of the major instruments on *AstroSat*. It consists of three Proportional Counters viz., LXP10, LXP20 and LXP30, each filled with Xenon-Methane gas at 2 atmospheric pressure. The LAXPC detectors have a collimator with a field of view of about $1^\circ \times 1^\circ$. The detectors are similar to the Proportional Counter Array (PCA) on the Rossi X-ray Timing Explorer (*RXTE*). The main differences are the high gas pressure and larger depth of the detector, which gives a larger effective area at higher energies (> 15 keV). Three

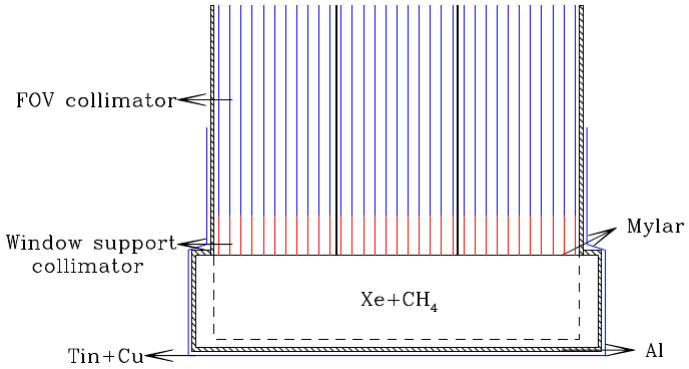

Fig. 2.2 The schematic view of one LAXPC detector including collimator and shield. Area between dashed line shows active volume of the detector. Figure credit: Antia et al. (2017).

LAXPC detectors are identical but independent of each other. This arrangement gives a large photon collecting area and continuity of scientific observations in case performance of any of the detector degrades. The geometric area of each proportional counter is $\sim 100 \times 36$ cm^2 (Antia et al., 2017) with a slightly different effective area for three different instruments. Each detector has five anode layers, each consisting of 12 anode cells of size $100 \times 3 \times 3$ cm^3. The top two layers are divided into two parts with alternate cells connected. There are seven main anodes—A1 and A2 in the top layer, A3 and A4 in the second layer from the top, and A5, A6, and A7 in the remaining three layers. The large detection volume (15 cm depth) of the LAXPCs results in detection efficiency greater than 50%, in 3-80 keV band. The detectors have a time resolution of 10 μs. They have moderate spectral capabilities, for example, around 20 keV the energy resolution of the detectors is 10%–15%, while the combined effective area of the three detectors is about 6000 cm^2. The broadband nature of the instrument with high time resolution capability makes it ideal to perform a detailed timing and spectral studies of HMXB pulsars and especially cyclotron lines and Quasi-Periodic Oscillations (QPO)(Paul, 2013).

The LAXPC detectors have two main modes of operation — event analysis (EA) mode and fast counter (FC) mode. In the EA mode, the timing of each event is recorded along with information about the anode ID where it is recorded as well as the pulse amplitude (channel number). In this mode, the detectors have a time resolution of 10 μs and a dead-time of about 42 μs. Another difference of LAXPC is that the EA mode, which is similar to good Xenon mode, can be used for any source whereas for PCA, the good xenon mode could not be used for very bright sources due to data volume/telemetry limitations. The EA mode is another difference of *AstroSat-*

LAXPC compared to *RXTE*-PCA. In the FC mode, the detector has a very low dead of ~ 10 μs. This allows the recording of much higer count rates and thus is very useful for the flaring sources. In this mode, counts from only top layers are recorded with a fixed bin time of 160 μs.

2.1.2 *XMM-Newton*

X-ray multi-mirror (*XMM-Newton*), also known as the High Throughput X-ray Spectroscopy Mission is an X-ray space observatory launched by the European Space Agency in December 1999. This telescope has a Wolter I type multi-mirror assembly (Egle et al., 2004a,b) which focuses X-rays on a platform called focal plane assembly where X-ray instruments are kept. Among these instruments are three European Photon Imaging Cameras (EPIC) and two Reflection Grating Spectrometers (RGS). It also carries an optical monitor (OM), designed to provide simultaneous observations alongside the spacecraft's X-ray instruments. Figure 2.3 shows a schematic view of *XMM-Newton* showing all its subsystems. The EPIC instrument is the primary instrument onboard *XMM-Newton* which consists of two MOS-CCD (Strüder et al., 2001) cameras and a single pn-CCD (Turner et al., 2001) camera with a field of view of $30'$ and high energy sensitivity in 0.15-50.0 keV band. RGSs are secondary system on the spacecraft, composed of two focal plane cameras. Their associated reflection gratings are attached to the mirror systems. Reflection gratings allow 50% of the incoming X-ray to pass undisturbed to EPIC system, while the other 50% are reflected onto its spectrometers. RGS system with very high resolution in 0.35-2.50 keV range can detect the presence of elements like carbon, nitrogen, oxygen, neon, magnesium, silicon and iron. OM is a 30 cm Ritchey-Chrétien an optical/ultraviolet telescope which is sensitive between 170 and 650 nanometers in a $17^{'}\times17'$ field of view. *XMM-Newton* is a pioneering instrument in investigating galactic and extra-galactic sources, performing narrow and broad spectroscopy, and performing the simultaneous imaging of objects in both X-ray and optical wavelengths.

2.1.2.1 EPIC PN

EPIC comprises a set of three X-ray CCD cameras. Two of the cameras which contain MOS-CCD arrays are known as MOS-camera. They are installed behind the X-ray telescopes that are equipped with the gratings of the RGS, receiving half of the unabsorbed X-ray flux. The EPIC instrument at the focus of the third X-ray telescope with an unobstructed beam is made of pn CCDs and is referred to as the PN-camera.

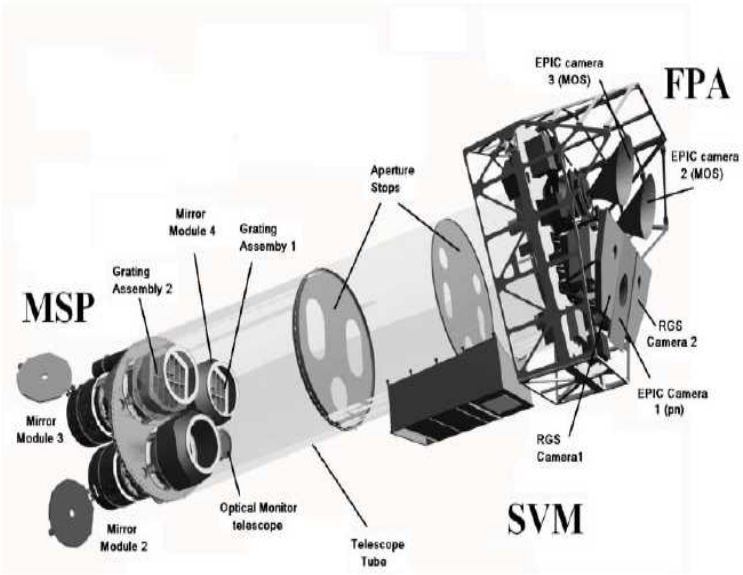

Fig. 2.3 A schematic view of *XMM-Newton*. The mirror assembly is shown in the lower left. X-ray instruments along with their supporting systems like heat radiators, electronics etc. are shown in top right. Optical Monitor telescope is hidden behind the mirror 2 module. Image Credit: ESA

The PN-camera is made of twelve 3 x 1 cm^2 pn-CCDs on a single wafer. Twelve CCDs are divided into four individual quadrants each having three pn-CCD subunits with a format 200 x 64 pixels operated in parallel. It has a total effective size of 6 $\times$ 6 cm^2. The telescope has a large effective area ($\sim$ 1000 cm^2) and good spectral resolution ($\Delta E/E \sim$ 20-50) in its nominal energy range (0.15-15 keV). Several observation modes are possible to adjust the performance of the instrument based on the observation requirement. The full frame and window modes are imaging modes. In the full frame mode all pixels of CCD are read out and thus full FOV is covered. In Large Window mode, only half of the area in all 12 CCDs is read out, whereas in Small Window mode only a part of CCD number 4 is used to collect data. In the Timing mode, spatial information is maintained only in one dimension, along the column axis. Along the row direction, spatial information is lost due to continuous shifting and collapsing of rows to be read out at high speed.

2.1.3 *RXTE*

The Rossi X-ray Timing Explorer (*RXTE*) was launched on December 30, 1995, and remained operational till the beginning of 2012. It was developed, built, tested and operated by NASA's Goddard Space Flight Center (GSFC). Two instruments onboard

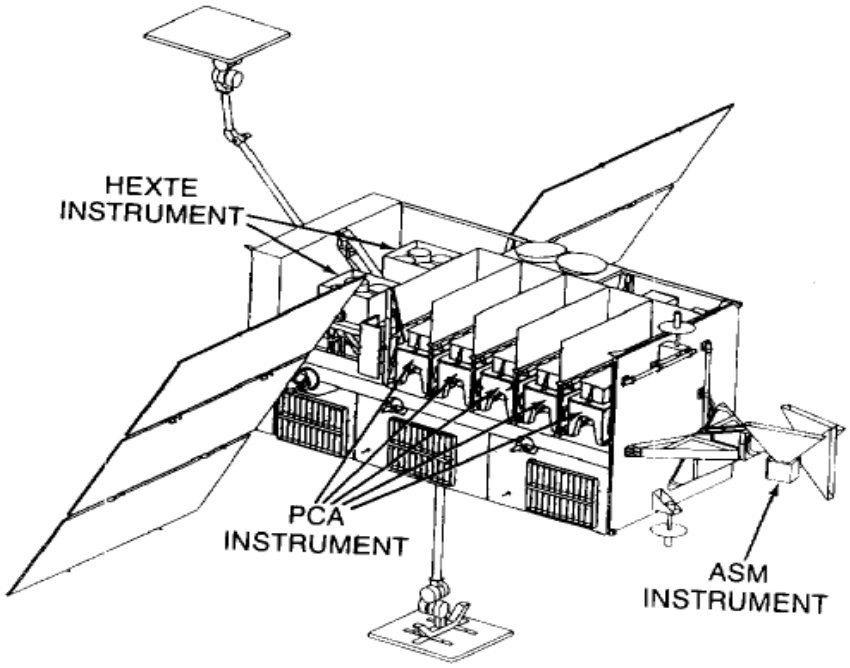

Fig. 2.4 A schematic view of *RXTE* with all its instruments PCA, HEXTE, ASM and other supporting subsystems. Image credit: NASA/GSFC

RXTE covered a wide energy range from 3 to 250 keV with a moderate spectral resolution, but had excellent timing capability. It could observe timing variations from microseconds to months time scale. Two co-aligned instruments on board were the Proportional Counter Array - PCA (Jahoda et al., 1996; Zhang et al., 1993) that covered the energy range from 3 to 60 keV and the High Energy X-ray Timing Experiment - HEXTE (Rothschild et al., 1998) which covered the higher energy range of 18–250 keV. The field of view of both the instruments was collimated to ~ 1 degree, and hence provided a low background. In addition to the pointing instruments, *RXTE* was also equipped with a small 1D coded mask All Sky Monitor - ASM (Levine et al., 1996) that scanned about 80 % of the sky in every revolution. It continuously monitored the sky to detect numerous transient sources for which follow-up pointing observations could be carried with the main instruments on board *RXTE* and also other X-ray mission. Figure 2.4 shows a schematic view of RXTE with all the instruments onboard. *RXTE* provided great insight into the fast-moving high-energy worlds of black holes, neutron stars, and AGNs.

2.1.3.1 PCA

PCA on board *RXTE* was composed of 5 Proportional Counter Units (PCUs) with a total photon collection area of 6500 cm^2 in the 3-60 keV range. Each detector had a hexagonal collimator made of beryllium copper with a field of view of 1°. Detectors were filled with Xenon gas at 1 atmosphere pressure. It had a good sensitivity, up to 1 mCrab, which was useful to detect faint sources. PCA covered a broad spectral range with moderate spectral resolution. The energy resolution was about 18% at 6 keV. The peak effective area was 6000 cm^2 in the 3-6 keV range, which fell rapidly above 15 keV. It had an excellent time resolution of one microsecond, which was best timing resolution achieved for any X-ray observatory. This made it ideal to study short time variability.

2.1.4 *Swift*

Swift is a multi-wavelength observatory, developed in collaboration between Goddard Space Flight Center (GFSC) and an international consortium of United States, United Kingdom, and Italy, and was launched on November 20, 2004. The primary goal of this mission is to observer GRBs and afterglows in the gamma-ray, X-Ray, ultraviolet and optical energy bands. It has three scientific instruments: the Burst Alert telescope (BAT) (Krimm et al., 2013), the X-ray Telescope (XRT)(Burrows et al., 2004), and

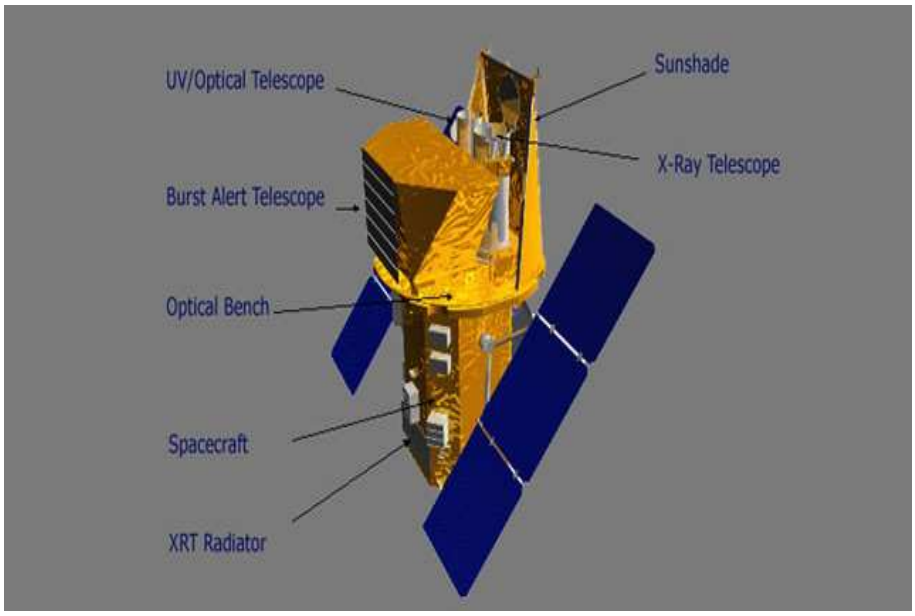

Fig. 2.5 A schematic view of *Swift* along with three scientific instruments and supporting systems on board. Image credit: NASA.

the Ultra-Violet/Optical Telescope (UVOT) (Breeveld et al., 2005). Figure 2.5 shows the schematic view of *Swift* with all the scientific instruments. BAT is the primary instrument on-board Swift to detect the GRBs with a few arcmin accuracy. Once the BAT locates a GRB, the spacecraft quickly re-orients to make observation of the burst position with XRT and UVOT. The BAT is a hard X-ray detector made of CdZnTe detectors and with a coded-aperture mask. The XRT uses a single MOS-CCD similar to those used in *XMM-Newton* which is placed at the focus of X-ray optics arrangement of Wolter Type I. The telescope can make X-ray images and perform timing and spectroscopy in the energy range 0.2-10.0 keV. The UVOT provides a sub-arcsecond position accuracy and very good optical/ultra-violet photometry through lenticulars filters and low resolution spectra (170-650 nm) through the use of optical and UV grisms. Along with GRB detections, *Swift*-BAT has carried out sensitive all-sky survey of low-energy gamma-rays. In the time between GRB events, *Swift*-XRT and UVOT are available for other types of scientific observations.

2.1.4.1 BAT

The BAT uses a coded-aperture mask of lead, 1 meter above the plane of CdZnTe hard X-ray detector. The coded mask aperture is a plate with a pre-determined pattern of transparent and opaque areas for the incoming photons. In other words, a coded mask

is a pinhole camera with not just one but many holes. A coded mask is placed over a position sensitive detector whose spatial resolution is matched to the spacing between the mask elements. The incoming photons cast a shadow on the detector plane and this shadow convolved with the pattern of mask elements gives us the information about the direction and intensity of incoming photons. The coded-aperture mask gives it a large field of view, covering a one-third of the sky at any instant. The operating energy range of BAT It operating energy range is 15-150 keV. It locates the position of each event with an accuracy of 1-4$'$ within 15 seconds. BAT detectors almost 100 GRBs every year. Apart from GRB discoveries, it also detects the outbursts in the known X-ray sources and continuously monitors the $\sim$ 1000 known transient and bright persistent X-ray sources. All these sources which are part of BAT catalog are tracked whether they are currently active or not.

2.1.5 A Special Collimator with Flat Top Angular Response for *POLIX*.

POLIX (Paul et al., 2016; Rishin and et al., 2010) is an X-ray polarimeter based on the Thomson scattering technique. Its operating in energy range is 10-30 keV, which can be extended for very bright sources. Astronomical sources like accreting X-ray pulsars are suitable candidates for this mission as they are brightest in this energy band. *POLIX* consists of a collimator, a scatterer and four X-ray detectors arranged in a rectangular configuration as shown in 2.6. The collimator restricts the field of view (FOV) to a small part of the sky. The scatterer is made of high purity beryllium. The scattered X-rays are detected in either of the surrounding detectors after the interaction. The whole instrument is rotated around the viewing axis. Rotation of instrument gives the azimuthal distribution of the scattering of X-rays in each of the four detectors.

A collimator is used to restrict the Field Of View (FOV) of *POLIX* to ensure only one bright X-ray sources in FOV for 50 bright source which are primary targets for this mission. While a small FOV is preferred for avoiding contamination from other sources, one has to optimize the collimator mass and dead areas between two adjacent holes in the collimator. A collimator with rectangular or hexagonal holes is better than circular holes under these considerations. Hexagonal shape is preferred in this case as it provides additional an advantage to determine the effects of a secondary source in the FOV. The effect of a secondary source is well studied and calibrated in advance. Another improvement made in the mechanical design of this collimator is

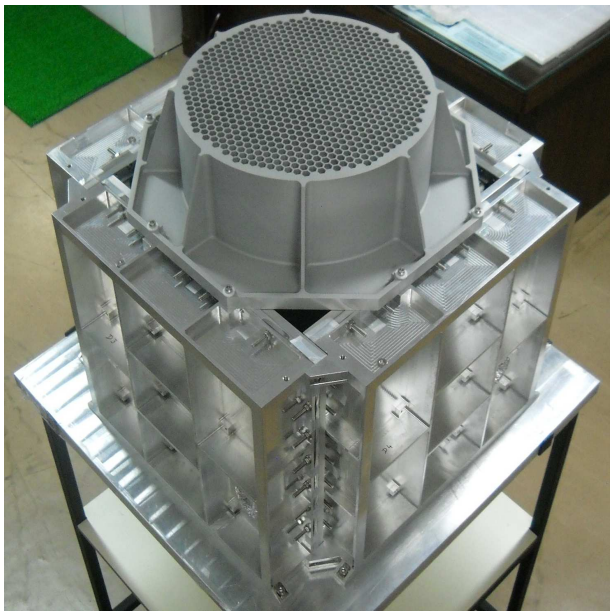

Fig. 2.6 Arial view of *POLIX* assembly in the lab. A collimator is seen on top of four detectors. Only two can be seen completely from this angle. A scatterer is kept at the base, beneath the collimator. Figure credit: Rishin P. V.

that the hexagonal holes are slightly tapered. This gives a flat top angular response upto 0.2° degrees from the center of the FOV. It helps in mitigating a pointing error of the satellite up to 0.1°. In the course of this thesis, we have done two calibration exercises, which involve the collimator. First is the study of collimator throughput as a function of off-axis angle and second is the azimuthal intensity modulation of off-axis sources within the field of view.

2.1.6 Photo-electron Polarization Measurement Technique

Photo-electric interaction of X-ray photons is a relatively new technique to built X-ray polarimeters (Costa et al., 2001). In this interaction, the electron emitted after the interaction is most likely to be ejected in the direction of the electric field of the incoming photon. This ejected photo-electron leaves a track of secondary electron-ion pairs. We are using proportional counter detectors with closely spaced wires, with two sets of interleaved anodes to measure the direction of these charge tracks. Charges deposited in the two anodes depends upon the polarization of incoming photons. The effectiveness of capturing polarization signature with this technique can be optimized by using a suitable separation between adjacent anodes, suitable gas mixtures, and gas pressures. The other polarimeters based on photo-electron technique along with

X-ray focusing optics, designed for relatively large spacecrafts are very sensitive, but they have a very small geometric area. On the other hand, the prototype photo-electron detector can be used to develop a large area X-ray polarimeter, which can be accommodated on relatively small satellite.

2.2 Data Analysis Methods

X-ray observations of cosmic sources cannot be done from the earth as these radiations are absorbed by the atmosphere. X-ray detectors must be taken to high altitude for this purpose. Earlier astronomers also used balloons or sounding rockets for this purpose, but these methods are less preferred in current times. These days X-ray astronomy is mostly done by sending scientific instruments into earth orbit on an artificial satellite. This gives an advantage of long uninterrupted observations and long usage of science instruments. Due to this, X-ray observatory like *RXTE*, *XMM-Newton*, and *Chandra* have far outlived their expected operational life. Initially, the observation data is stored on the satellite and later data is sent to the ground station using radio communication. This data is in the form of event mode, which means all the information like energy, arrival time, direction, and polarization of incoming photons is stored. Satellite orbital parameter should be taken into account for further data extraction from event mode into user products. The data is stored in a digital format called Flexible Image Transport System (FITS). The data used in this thesis was retrieved mainly from Indian Space Science Data Center (ISSDC) which is the primary data center for the payload archives of Indian space science missions. Some of the data were obtained from the High Energy Astrophysics Science Archive Research Center (HEASARC), which is the primary archive for astronomical data from all current and past space missions launched by NASA. The raw level1 event data from ISSDC was further processed using LAXPC Level1 to Level2 data processing guide[1] at Payload Operation Center (POC) at Raman Research Institute (RRI). Further timing and spectroscopy products were extracted using LAXPC data reduction guide for users[2]. Light curve and spectrum hence created were analyzed using HEASOFT software. General FITS file manipulation (create, examine, and modify) was done with FTOOLS package. The various tasks in HEASOFT software use the default graphics plotting package called QDP/PLT[3].

[1] http://www.rri.res.in/~rripoc/POC.html
[2] http://www.rri.res.in/~rripoc/LAXPC_user.html
[3] https://heasarc.gsfc.nasa.gov/ftools/others/qdp/node3.html

2.2.1 Timing Analysis

Timing analysis allows astronomers to study the dynamic properties of an object. The target of timing studies include accretion flows, pulsations, eclipses, and accretion disk instabilities as well as the instabilities in compact and non-compact stellar systems. Timing analysis involves recording photon count rate as a function of time which is known as "light curve". The photons are usually collected in a particular energy band. We have analysed light curves of binary and isolated pulsars in this thesis. Timing analysis of these pulsars was done to search for periodic signals, find their spin periods, create pulse profiles and pulse profiles in different energy band. The timing analysis was done using timing analysis software "XRONOS". The description of the specific tools of XRONOS used in our analysis is given below.

2.2.1.1 lcurve

This tool helps to visualise the source intensity variations in an observation. The input format is FITS using the BINTABLE extension. Both the binned data format and event data format are allowed for input. User can screen the data by using windows of time, phase, intensity and exposure. User can plot maximum of 4 light curves at a time. User can rebin the light curve with a binsize larger than that in the input file of light curve. This tool can also show the ratio of count rates from two light curves if they cover the same time duration. This is known as Hardness ratio or color, which tells us if there is any change in the spectra during an observation. For multiple time series, a color-color plot can also be created wherever possible. It is also possible to save the output of `lcurve` in a FITS file.

2.2.1.2 powspec

This tool calculates a Power Density Spectrum (PDS) of input light curve. The PDS is either computed by Fast Fourier Transform (FFT) or a direct slow Fourier algorithm by using parameter "fast" of the tool. The input file format is FITS using a BINTABLE extension. The power spectrum can be created for different intervals of a light curve or from the whole light curve. Different normalization can be used for the power spectrum by changing the parameter "normalization". Power spectrum can be visualised with different types of binning using the parameter "rebin" ($= 0$ for no rebinning, > 1 for constant binning, and $<$ geometric binning).

2.2.1.3 efsearch

There are several astrophysical phenomenon, which can give rise periodic signals in astronomical sources. Periodicity can be attributed to change in brightness as in case of binary pulsars and pulsating stars or change in position as the motion of neutron star in orbit around its companion in a binary. The tool `efsearch` finds the period in a light curve by folding it at different trial periods. For each trial period, the folded light curve is fitted to a constant and the χ^2 is calculated. At the correct period, the pulse profile is fully recovered giving a larger χ^2 whereas for incorrect trial period, the pulses are folded with varying phases resulting in a nearly constant profile and hence a low value of the χ^2. The maximum χ^2 corresponds to the most likely period value in given range of periods. The search can be done in different intervals of light curve as well as in full light curve. The error bars for the χ^2 represent the standard deviation of the relevant χ^2 distribution rescaled by the value of χ^2 for each period divided by N-1, where N is the number of phase bins.

2.2.1.4 efold

In the case of accretion-powered pulsars, the X-ray light curve contains a periodic signature corresponding to pulsar rotation. A light-curve containing periodic signal can be stacked with this period, and count rate can be averaged. This is known as folding a light curve and gives us an averaged count at each spin phase of the pulsar. This folded profile represents an averaged emission pattern of the pulsed component of total emission in the system. The `efold` tool creates the folded profile from an input light curve for a given period value and number of phases in the period. It can process up to four light curves at a time produce four pulse profiles at a time. Folded light curves from different intervals can be averaged in one or more frames. The error bars are calculated after averaging folded light curves from different intervals in a frame, either using the standard deviation of mean values of each phase bin or propagating the error in each phase.

2.2.2 Spectral Analysis

There are three main software package available for X-ray spectral analysis, `XSPEC`, `ISIS`, and `Sherpa`. In this thesis, I have used `XSPEC` (Arnaud, 1996), which is included in NASA's general software package HEASOFT for X-ray analysis. `XSPEC` uses χ^2 minimization for determining the best fit spectral models and the parameter values. Uncertainties in the fit parameter are generally found by freezing the parameter of

interest along a range of values and fitting the remaining parameters until the fit statistic exceeds the best-fit statistic by an amount corresponding to the desired confidence limit. One may also compute confidence contours by stepping one or more parameters over grids of two parameter values and fitting the remaining free parameters. These are more computationally demanding than uncertainty calculations for single parameters, but give a better picture of the χ^2 landscape around the best-fit parameters. These contour plots are important in spectral analysis of HMXB system as spectral parameters of the continuum may be artificially correlated with the parameters of cyclotron lines. The fitting algorithm can also fall into local minima and fail to find the global best-fit set of parameters. These uncertainty calculations and confidence contours allow one to shake up the fit and find the best-fit model.

The primary goal of spectral analysis is to infer the actual physical parameters behind the phenomenon that produces the observed spectrum. The spectra of HMXB pulsars are produced by a combination of many physical processes. This makes the theoretical modeling of pulsar spectra to be quite difficult. Consequently, spectra of these objects are generally fitted with empirical models. The complete model generally consists of many components which may have a simple mathematical form (constants, powerlaws, Gaussians, etc.) or highly complex form. The general form the multicomponent spectral model for accretion-powered pulsars takes the form

Total Model = (Absorption*f + Partial Absorption*(1-f))*(Continuum Model * Cyclotron line + Emission Line + Emission Line)

In the next subsection, I give an overview of models component used in the thesis for continuum spectra, cyclotron line, and other features.

2.2.2.1 Powerlaw with High Energy Cutoff Model

The basic shape of the continuum is a powerlaw multiplied by some form of exponential cut-off. The simplest form of this cutoff is `highecut` (White et al., 1983). This model is used in combination with the `powerlaw` model. This model has few free parameters and hence fast in implementing. A combined analytical form of both component becomes:

$$I(E) = KE^{-\Gamma} \times \begin{cases} 1 & E<E_{cut} \\ exp\left(\frac{E_{cut}-E}{E_{fold}}\right) & E\geq E_{cut} \end{cases}$$

The photon energy E is in keV. The normalization K is photon flux at 1 keV. Although this model fits the spectra of many sources fairly well, the piecewise exponential can produce an artifact which looks like an absorption feature around the cut-off energy. This issue is crucial in systems having a cyclotron line in their spectrum. In such cases, a correlation between E_{cut} and E_{cyc} should be investigated.

2.2.2.2 Negative and Positive Powerlaw Exponential Model

This model consists of negative and positive powerlaws with a common exponential cutoff. This model approximates a photon number spectrum for an unsaturated thermal Comptonization in plasma (Makishima et al., 1999). The analytical form of this model is given by

$$I(E) = (A_n E^{-\Gamma 1} + A_p E^{+\Gamma 2}) exp\left(-\frac{E}{kT}\right)$$

Where A_n, A_p, $\Gamma 1$, $\Gamma 2$ are positive parameters, and k is the Boltzmann constant. The index for positive powerlaw is fixed at 2.0, and the negative powerlaw is dominant at low energies. At high energies more contribution comes from positive powerlaw which gives it a concave curvature on a log-log plot.

2.2.2.3 compTT Model

This model is based on the theory of spectral formation in thermal X-ray sources, including the effects of Comptonization and Klein-Nishina corrections (Titarchuk, 1994; Titarchuk and Hua, 1995; Titarchuk and Lyubarskij, 1995). The analytical calculations of the source spectrum is case dependent (optically thick or thin plasma) and has five parameters which represents redshift, plasma temperature, optical depth of the plasma cloud, injected soft photon spectrum temperature and parameter β. The parameter β is not a free parameter in the model. It depends upon the geometry parameter which can be set to be spherical or disk type. For modeling the spectra of accretion-powered pulsars, this parameter is kept ≥ 1 which applies to a spherical geometry. Although it is not a correct approximation for the accretion column geometry, this is the closest to the expected conical/cylindrical geometry.

2.2.2.4 Powerlaw with a Smoothed High Energy Cutoff (NEWHCUT) Model

This model is a modification of high energy cutoff model, smoothed around the cutoff energy. Analytical form of model (Burderi et al., 2000) is given by:

$$I(E) = \begin{cases} NE^{-\Gamma} & \text{if } E \leq E_{cut} - \triangle E \\ AE^3{+}BE^2{+}CE{+}D & \text{if } E_{cut} - \triangle E \leq E \leq E_{cut} + \triangle E \\ NE^{-\Gamma} exp(\frac{E-E_{cut}}{E_{fold}}) & \text{if } E \geq E_{cut} + \triangle E \end{cases}$$

The constants A, B, C and D are calculated assuming the continuity of the function I(E) and its derivative in the range of $E_{cut} - \triangle E$ and $E_{cut} + \triangle E$ (Burderi et al., 2000).

2.2.2.5 Powerlaw with a Fermi-Dirac Cutoff (FDCUT) Model

This model is a powerlaw with a form of exponential that resembles with the Fermi Dirac function. The analytical form of model (Tanaka, 1986) is given by

$$I(E) = \begin{cases} NE^{-\Gamma} & \text{if } E \leq E_c \\ \frac{NE^{-\Gamma}}{exp(\frac{E_c - E}{E_f})} & \text{if } E \geq E_c \end{cases}$$

where Γ is the powerlaw photon index, E_c is cutoff energy and E_f is folding energy of exponential roll over.

2.2.2.6 Gaussian Absorption Line Model

This component is used for modeling the cyclotron line in HMXB pulsar. It is a multiplicative component in `XSPEC`. It has a simple form and fits the cyclotron line in many source very will, with few exception (Fürst et al., 2015). The analytical form of the model is given by

$$I(E) = exp\left(-\left(\frac{d}{\sqrt{2\pi}\sigma}\right) exp\left(-\frac{(E - E_{cyc})^2}{2\sigma^2}\right)\right)$$

where E_{cyc} is the line center, σ is line width and d is line depth. The optical depth at line center is $\frac{d}{\sqrt{2\pi}\sigma}$.

2.2.2.7 Photoelectric Absorption Model

A continuum emission is subjected to absorption by interstellar medium in the line of sight. This is more prominent at low energies. There are many model for accounting this absorption. The main difference in these models is abundance constituent of the interstellar medium. I have used `phabs` in this thesis. It is a multiplicative model in `XSPEC`. Its analytical form is given by

$$I(E) = exp\,(-n_H \sigma(E))$$

where $\sigma(E)$ is photo-electric cross-section (NOT including Thomson scattering) and n_H is equivalent hydrogen column (in units of 10^{22} atoms cm^{-2}). This model uses angr (Anders and Grevesse, 1989) table of `XSPEC` for abundances.

2.2.2.8 Gaussian Line Profile

The spectra of accretion-powered pulsar show many emission lines below 10 keV. Iron line at $\sim$ 6.5 keV is generally seen in many sources and modeled by gaussian line profile. It is a multiplicative model in `XSPEC`. The analytical form is given by

$$I(E) = K \frac{1}{\sigma\sqrt{2\pi}} exp\left(-\frac{(E - E_l)^2}{2\sigma^2}\right)$$

where E_l is line energy in keV, σ is line width in keV, and K is normalization in units of photons $cm^{-2}s^{-1}$.

Chapter 3

Pulse Phase Variation Of Cyclotron Resonance Absorption Feature In HMXBs Using *AstroSat*-LAXPC[1][2][3]

3.1 Effect Of High Magnetic Field On Accretion And High Energy Radiation

The neutron stars in HMXBs have magnetic fields that are of the order of 10^{12} G. The accreted material is channeled along the magnetic field lines at relatively large distances from the compact object, leading to the formation of extended accretion columns. The exact details of how the magnetic field affects the accretion flow is still a topic of investigation (Becker et al., 2012). It is generally expected that the inflowing material is directed towards the magnetic poles of the neutron star where two hot spots are formed. The gravitational potential energy of the inflowing material is first converted into kinetic energy and then released as X-rays due to shocks and dissipations into the accretion column and on the hot spots (Basko and Sunyaev, 1975). The emitted X-ray radiation is broadband in nature and is generated by multiple and interdependent processes near the neutron star surface. In the accreting X-ray pulsars, the hard X-rays are produced by inverse Compton scattering of soft X-ray photons by high energy electrons. The strong magnetic fields of neutron stars in HMXBs play a crucial role in the generated X-ray radiation. Due to the non-spherical nature of the

[1]Most of the results presented here have been published by me as first author in these two journal papers:

[2] https://academic.oup.com/mnrasl/article-abstract/484/1/L1/5245189

[3]https://doi.org/10.3847/1538-4357/ab2763

emission region, and the scattering cross sections which are altered by the magnetic fields, different emission beam patterns are produced: the fan-beam type emission at high accretion rates, and the pencil-beam type emission at low accretion rates. The distinction between the high and low accretion rate regimes is believed to be determined by the critical luminosity, which also depends on the magnetic field of the neutron star (Basko and Sunyaev, 1976; Becker et al., 2012; Mushtukov et al., 2015a).

3.2 Formation Of CRSF And Variation In Its Parameters

Cyclotron Resonance Scattering Feature (CRSF) is usually seen in absorption against the continuum spectrum in many HMXBs. CRSFs are formed by cyclotron resonant scattering of the X-ray photons in the presence of the strong magnetic field of the neutron star. The centroid energy of the CRSF is related to the magnetic field given by the "12-B-12" rule given by

$$E_{\rm cyc} = \frac{11.57\,{\rm keV}}{1+z} \times B_{12} \tag{3.1}$$

where B_{12} is the magnetic field in units of 10^{12} G and z is the gravitational redshift in the scattering region for neutron star. The CRSF parameters also provide important information on the line forming region like the plasma temperature and the optical depth of the line forming region. Most importantly, it provides crucial clues on the geometry of the line forming region: the emission beam pattern, and the magnetic field configuration of the neutron star (Maitra, 2017).

The CRSF properties of X-ray pulsars are found to be variable for different reasons (Maitra, 2017). The CRSF line energy evolves with time in sources like Her X-1 (Staubert et al., 2017) and 4U 1538–522 (Hemphill et al., 2019). Line energy also shows dependence on X-ray luminosity, for example, in V0332+53 (Doroshenko et al., 2017). An unvarying or weakly varying CRSF over a large luminosity range, as seen in 1A 0535+262 (Caballero et al., 2007; Sartore et al., 2015) is also of interest. CRSF parameters in most sources show large variation with spin phase, for example, A0535+26, XTE J1946+274, and 4U 1907+09 (Maitra and Paul, 2013a; Rivers et al., 2010). Accurate measurement of the CRSF also depends on broad band spectral coverage, and it is important to model the underlying continuum well. It is therefore of interest to study the CRSF with different instruments at different epochs, and intensity states of

the sources.

The LAXPC instrument on *AstroSat* with its moderate energy resolution and high effective area, is very good for the study of CRSF. We wrote two guest observation proposals on 4U 1907+09 and 4U 1538–522 to study their timing and spectral properties. The detection of CRSF and its pulse phase variation using LAXPC data was a key objective of these observations proposals.

3.3 4U 1907+09

4U 1907+09 is an HMXB system discovered in the *UHURU* survey (Giacconi et al., 1971). The companion is a O8/O9 Ia supergiant with a mass loss rate of 7×10^{-6} $M_\odot$ yr^{-1} (Cox et al., 2005; Schwartz et al., 1980; van Kerkwijk et al., 1989), a small fraction of which is accreted by the neutron star. X-ray flux modulation in 4U 1907+09 with a stable period of $\sim$ 8.38 d is attributed to the orbital period of the binary (Marshall and Ricketts, 1980), which is also corroborated from the orbital pulse arrival modulation measurements (in 't Zand et al., 1998). The X-ray emission from 4U 1907+09 shows clear pulsations with a periodicity of $\sim$ 437 s (Makishima et al., 1984), and it is known to show occasional quasi-periodic oscillations at a frequency of about 65 mHz (in 't Zand et al., 1998; Mukerjee et al., 2001). Though 4U 1907+09 was initially found to have a nearly constant spin-down (Baykal et al., 2001), later observations (Baykal et al., 2006) showed variation in the spin-down rate and multiple torque reversals (Fritz et al., 2006). Period measurements with *INTEGRAL* and *RXTE* exhibit short term fluctuations in pulse frequency over the long term spin-change rates, which are consistent with the random walk model (Şahiner et al., 1977). A Cyclotron Resonance Scattering Feature (CRSF) at 19 keV was first discovered with *Ginga* (Makishima and Mihara, 1992; Makishima et al., 1999) and its first harmonic was detected with *BeppoSAX* (Cusumano et al., 1998). The CRSF was further investigated with different instruments like *RXTE* (Fritz et al., 2006; Inam et al.), *INTEGRAL* (Hemphill et al., 2013) and *Suzaku* (Maitra and Paul, 2013a; Rivers et al., 2010).

3.4 4U 1538–522

4U 1538–522 is a wind-fed persistent X-ray binary formed by a massive (17 $M_\odot$) B0Iab supergiant (Reynolds et al., 1992) and a neutron star. At the time of its discovery,

the neutron star had a spin period of $\sim$ 528 s (Becker et al., 1977) and it was in spin down phase for more than a decade. Since then the source underwent two torque reversals, in 1988 (Rubin et al., 1997) and 2009 (Hemphill et al., 2013). The spin period is currently $\sim$ 527 s. The orbit of the binary system has a high inclination (67°) (Falanga et al., 2015), and has an orbital period of 3.75 days with an X-ray eclipse lasting $\sim$ 0.6 days (Becker et al., 1977; Mukherjee et al., 2006). However, shape of the orbit is still unknown for this system. Some authors have determined the orbit to be circular (Makishima et al., 1987; van Kerkwijk et al., 1995) whereas others have found an eccentricity of 0.17-0.18 (Clark, 2000; Mukherjee et al., 2006). Rawls et al. (2011) have used both circular and elliptical orbit parameters for mass determination of the neutron star from optical light curves and radial velocity measurements. The system consists of a supergiant donor that under-fills its Roche Lobe and is similar to other wind fed systems like Vela X-1 and 4U 1907+09 exhibiting short time variability in terms of dips and flaring activity. The persistent X-ray luminosity is estimated to be about 2×10^{36} erg/s for a distance of $\sim$ 6.4 kpc (Becker et al., 1977).
The X-ray spectrum is typical of an accreting HMXB pulsar with a power-law feature and an exponential turnover. A CRSF at $\sim$ 20 keV was discovered by Clark et al. (1990) using a *Ginga* observation. An additional absorption feature was identified in the spectrum at $\sim$ 51 keV using *BeppoSAX* observations (Robba et al., 2001), and was later confirmed as the first harmonic of the CRSF by Rodes-Roca et al. (2009). Hemphill et al. (2014) reported the results of a phase-resolved analysis of the CRSF fundamental in 4U 1538–522 for the first time using a *Suzaku* observation. Noticeable variations in the CRSF parameters were observed. However, the pattern of variation could not be probed in detail as the parameters had large error bars associated with them, due to statistical limitations of the data. Hemphill et al. (2016) reported that CRSF energy of 4U 1538–522 has increased by $\sim$ 1.5 keV between 1996 and 2012. Further measurements of cyclotron line energy are required to confirm that this increase is secular.

3.5 Observations

The Large Area X-ray Proportional Counter (LAXPC) onboard *AstroSat* (Agrawal, 2006; Antia et al., 2017) consists of three identical Proportional Counters viz., LXP10, LXP20, and LXP30, with seven anodes arranged into five layers, and each filled with Xe gas at 2 atmosphere pressure. The geometric area of each proportional counter

Table 3.1 Summary of Observations of two sources used in the study

Source Name	Obs ID	Start Date	End Date	Exposure (ks)	P_{spin} (sec)
4U 1907+09	A03_105T01_9000001268	04-06-2017	05-06-2017	46.7	~ 440
4U 1538–522	A02_198T01_9000001376	12-07-2017	13-07-2017	45.9	~ 530

is $\sim 100 \times 36$ cm^2 (Antia et al., 2017) with a slightly different effective area for three different instruments. The broadband nature of the instrument with high time resolution capability makes it ideal for performing a detailed timing and spectral studies of HMXB pulsars and especially study CRSFs (Paul, 2013). 4U 1907+09 was observed on the 4th and 5th of June 2017 for a total of 18 *AstroSat* orbits using the LAXPC instrument in the third cycle of guest observations. This observation was carried out at 0.5 orbital phase away from the peak of the orbital intensity profile. In the *Swift*-BAT light curve, the source intensity at this orbital phase is $\sim 1/3$ of the peak intensity. We have obtained a total of ~ 47 ks on-source data from this observation. 4U 1538–522 was observed with *AstroSat* on 12th and 13th July 2017. We have obtained a total of ~ 46 ks on-source data from this observation. The details of observations of both the observations are given in Table 3.1. In this chapter, we report the results of the analysis using LAXPC data of both these sources taken in the event analysis (EA) mode. Data files were reduced with Level1 to Level2 data processing guide[4] version 1. Level1 products were processed to reduce Level2 products from which we can produce light curves and spectral files. Further handling of light curves and spectra was done using tools in HEASOFT software suite, version 6.19. The time intervals when the source is occulted by earth and the satellite is passing through the South Atlantic Anomaly (SAA) region have been removed for the creation of light curves, and spectral files. Average of the count rates during earth occultation, and the spectra acquired during earth occultation with the satellite being outside the SAA are used as background count rate and spectra in subsequent sections.

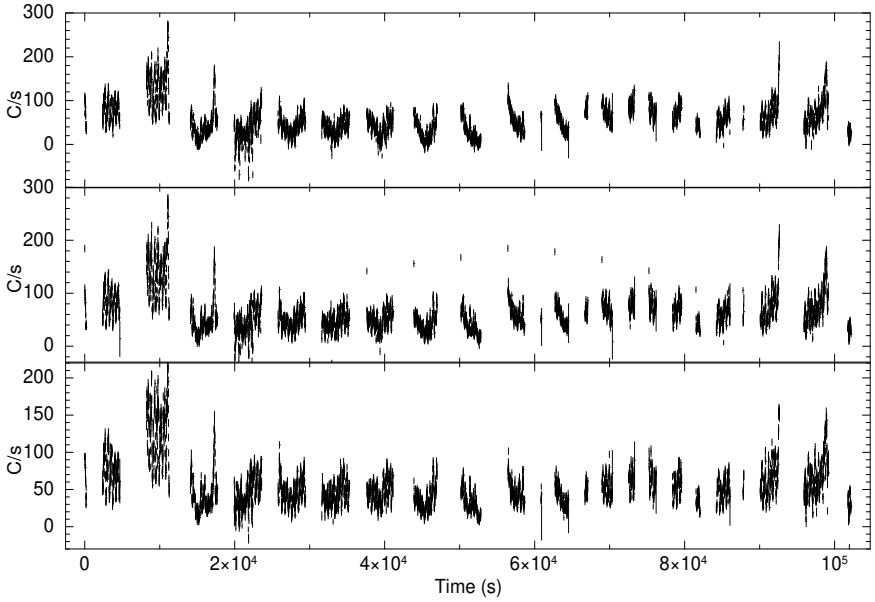

Fig. 3.1 Light curves of 4U 1907+09 from the *AstroSat* observation with the LAXPC. Top, middle and bottom panels show data from the 3 detectors LXP10, LXP20 and LXP30 respectively with a bin size of 10 s. Flaring is seen at the beginning of the observation.

3.6 Data Analysis

3.6.1 Timing Analysis

3.6.1.1 Timing Analysis Of 4U 1907+09

A single merged light curve was created with a bin time of 10 ms after eliminating all overlaps between adjacent data downloaded in different orbits. A background light curve was created using time windows during which the source was occulted by the earth. The average background rate was subtracted from the source light curves. The light curves from all three detectors in the 3.0-80.0 keV energy band are shown in Figure 3.1 with a bin size of 10 s after subtracting an average background count rate for each detector. LXP10, LXP20, and LXP30 have an average source count rate of 54, 61 and 54 per sec respectively. At the beginning of the observation, the source showed a higher count rate for $\sim 1/10$ of the observation, followed by a lower count rate for the rest of the observation. We carried out a periodicity search on the summed and barycentered light curve with the FTOOL `efsearch` and obtained a period of 442.33 $\pm$ 0.07 s (see Figure 3.2). The pulse profiles created using this spin period from the

[4]http://www.rri.res.in/~rripoc/POC.html

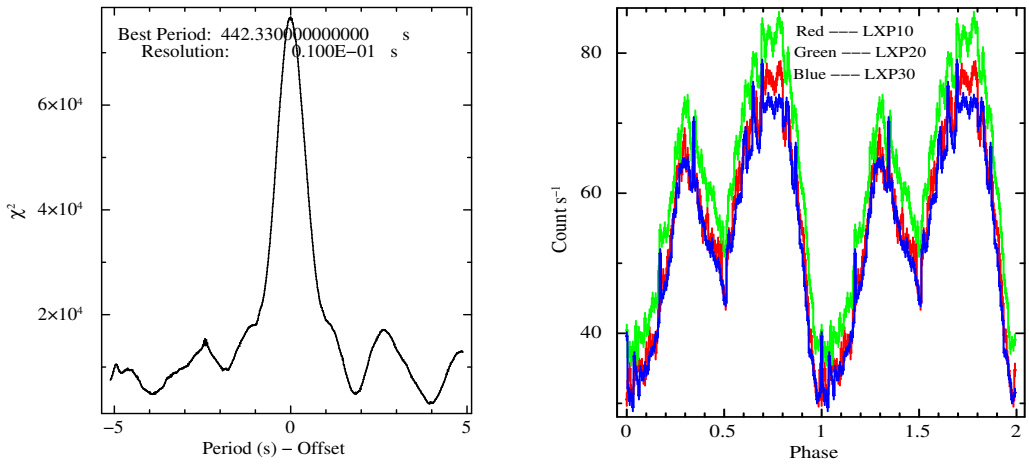

Fig. 3.2 Left: The results of pulse period search in the light curves of 4U 1907+09 from combined data of 3 detectors. The χ^2 for different trial pulse periods is shown. Right: The pulse profiles of 4U 1907+09 folded with the best period obtained in period search. Pulse profiles from three detectors – LXP10 (red), LXP20 (green), LXP30 (blue) are overlaid.

3 LAXPC detectors in the energy band 3.0-80.0 keV are shown in Figure 3.2. Pulse profiles from all detectors show an identical double-peaked shape. The first peak is smaller than the second peak. We did not perform orbital correction on the photon arrival time as there are large error bars on most of the orbital parameters of this source (in 't Zand et al., 1998). However, we checked whether a period derivative term should be included for the timing analysis. The period search was carried out for a wide range of period derivatives, and it was seen that the data is consistent with zero period derivative. Hence, all subsequent analysis was performed with the above-mentioned pulse period and a zero period derivative.

The emission pattern of many pulsars in the hard X-rays band is different from their emission pattern in soft X-rays, which is also affected by absorption. The large effective area of LAXPC allows us to carry out timing analysis in a broad range of 3.0-80.0 keV. In order to investigate the emission pattern at various energies we created energy resolved pulse profiles in 7 energy bands: 3.5-8.0 keV, 8.0-16.0 keV, 16.0-19.0 keV, 19.0-22.0 keV, 22.0-40.0 keV, 40.0-60.0 keV and 60.0-80 keV. Two energy bands 16.0-19.0 keV and 19.0-22.0 keV are chosen in the CRSF energy range of 4U 1907+09. Figure 3.3 shows the energy resolved pulse profiles created with combined data of 3 detectors. Pulse profiles have two peaks with a small peak preceding a higher and broader primary peak. Pulse profiles up to 40 keV are created with 128 phase bins and with 32 phase bins in last two energy bands. Pulsations are detected up to 60 keV. The amplitude and shape of the secondary peak have a strong energy dependence

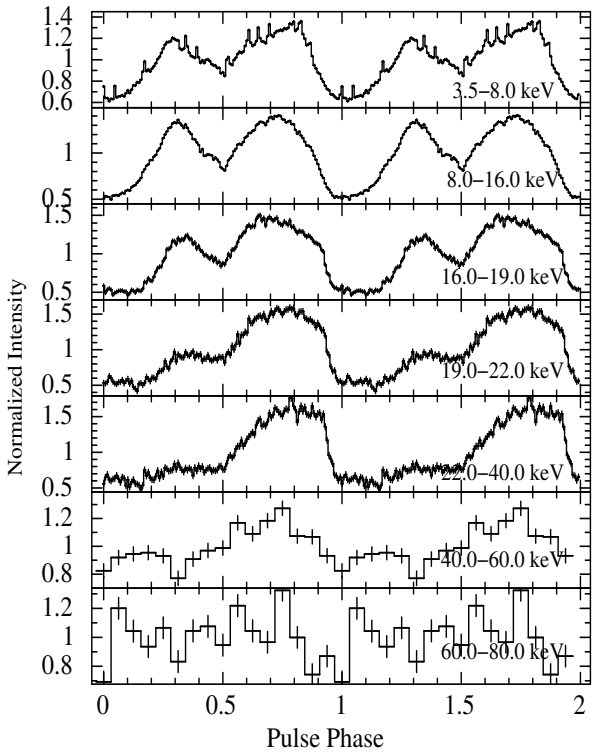

Fig. 3.3 The energy resolved pulse profiles of 4U 1907+09 created from combined data of 3 detectors. 3rd and 4th panels from the top are from 2 bands adjacent to the CRSF Energy. Pulse profiles in top 5 panels are created with 128 phase bins and in bottom two panels with 32 phase bins.

with a marked decrease in pulse fraction above the CRSF energy. Pulse fraction of the main peak increases from 38% in 3.5-8.0 keV to 58% 19.0-22.0 keV band. In the 22.0-40.0 keV band, it remains the same at 57%, and in 40.0-60.0 keV band, it drops to 25%.

3.6.1.2 Timing Analysis Of 4U 1538–522

For the timing analysis, light curves from the entire observation were extracted with a bin size of 10 ms. Barycenter correction was applied to light curve using tool `as1bary`[5] along with online tool *AstroSat* orbit file generator[6]. We have not done orbital correction on the photon arrival time as there is ambiguity about the orbital parameters of this source. Figure 3.4 shows the light curves binned at 10 s for LXP10, LXP20, and LXP30 with average source count rates of 89, 80, and 76 c/s respectively. Pulsations are clearly seen in the light curves of all the three detectors. We used the

[5]http://astrosat-ssc.iucaa.in/?q=data_and_analysis
[6]http://astrosat-ssc.iucaa.in:8080/orbitgen/

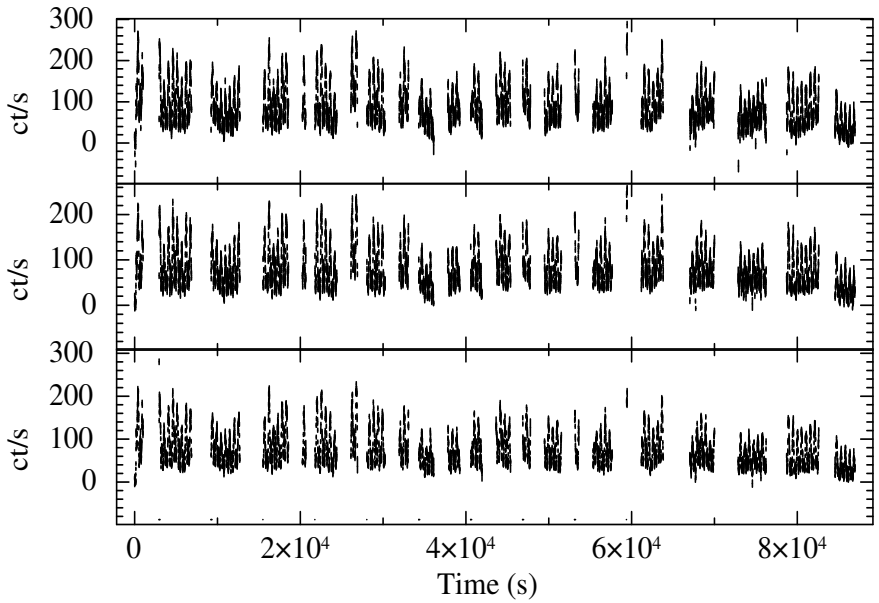

Fig. 3.4 Light curves of 4U 1538–522 in energy band 3.0-80.0 keV from 3 LAXPC detectors – From top to bottom LXP10, LXP20, LXP30. Data gaps corresponds to times when satellite is passing through SAA, or the source is occulted by earth.

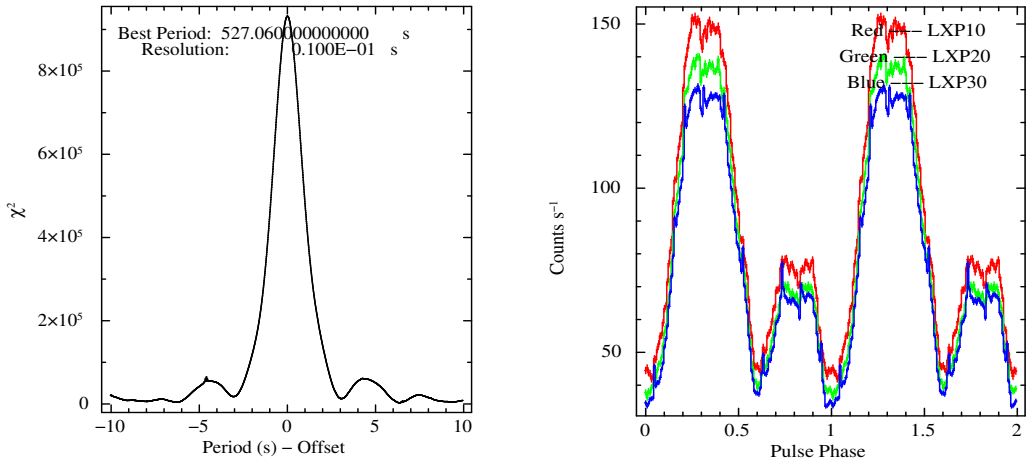

Fig. 3.5 Left: The results of pulse period search in the light curves of 4U 1538–522 from combined data of 3 detectors. The χ^2 for different trial pulse periods is shown. Right: X-ray Pulse profiles of 4U 1538–522 created from light curves folded with best period is divided in 128 phase bins. Pulse profiles from three detectors – LXP10 (red), LXP20 (green), LXP30 (blue) are overlaid.

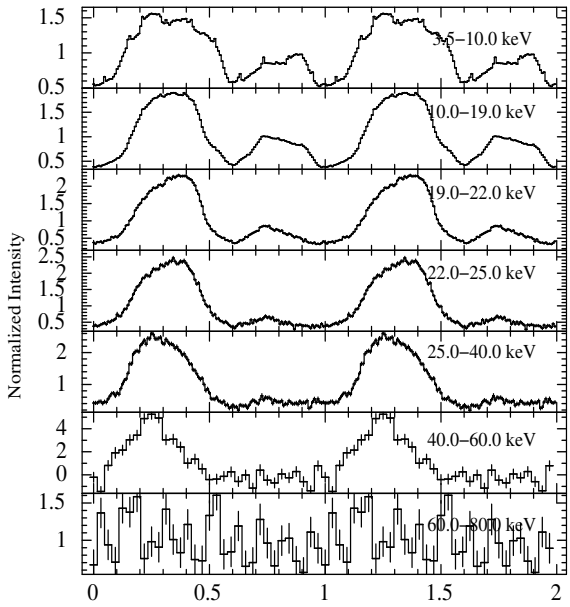

Fig. 3.6 Energy resolved pulse profiles of 4U 1538–522 from light curves of data added from 3 detectors. The 3.0-80.0 keV energy band has been divided into 7 finer energy bands. Pulse profiles in top 5 panels are created with 128 phase bins and in bottom two panels with 32 phase bins.

pulse folding and χ^2-maximization method to determine the pulse period of the pulsar using the FTOOL `efsearch`. Pulsations were detected at 527.06 ± 0.11 s using all the three detectors. Figure 3.5 shows the results of period search using added light curves from 3 detectors and background subtracted pulse profiles from all the detectors integrated in the energy range of 3.0–80.0 keV. Pulse profiles show a double-peaked structure with a primary and secondary peak. To investigate the energy dependence of the same, we extracted pulse profiles in seven energy bands from 3 to 80 keV, selecting two energy bands (19.0-22.0 and 22.0-25.0 keV) around cyclotron absorption feature as shown in Figure 3.6. The pulse profiles are double peaked and exhibit significant evolution with energy. The secondary peak (phase 0.6–1.0) decreases in strength until it disappears for energy > 19 keV. The primary peak also becomes narrower with energy with pulse fraction increasing from 48% to $\sim$ 98% (for 40.0-60.0 keV). Pulse fraction in band for the low energy side of CRSF line center (19.0-22.0 keV) is higher (74%) than to higher energy side (22.0-25.0 keV) where its value is 70%. Pulsations are detected up to $\sim$ 60 keV. In 60-80 keV energy band pulsations are not detected due to poor statistics in data. The pattern of evolution of the pulse profiles with energy are consistent with the results from *Ginga* (Clark et al., 1990), *BeppoSAX* (Robba et al., 2001), and *Suzaku* (Hemphill et al., 2014).

3.6.2 Spectral Analysis

3.6.2.1 Background Spectra And Response Matrix Files For Spectral Analysis

Spectra were created from all channels which encompass the 3.0-80.0 keV energy band of the LAXPC detectors. Background spectra were extracted from data acquired in time intervals when the source was occulted by the earth. Most of the X-ray photons of energy greater than 34 keV produce double events in LAXPC as an X-ray fluorescence photon emitted from the Xenon atoms is detected in a different part of detector. LAXPC detectors have different response matrices depending on the types of events taken to create the spectrum (single or double or all). The response matrix also depends on the gain in the detector, which is variable. To determine this, we first estimated the relative gain of each LAXPC detector during both observations and selected a response matrix accordingly. This was done by creating a spectrum of K-fluorescence photons from the double events. K-events spectrum[7] can be used as a gain calibrator as these photons are mono-energetic. Once the channels corresponding to the energy of these photons is determined, we compare it with their nominal values determined at the ground to get relative gain for our observations. Significant gain variations were found for LXP20 during these observations. As a result, not all of the double events were registered in the double event spectral window of this unit, which is preset for each detector irrespective of the gain variability. LXP30 data has large uncertainties in its quantum efficiency and energy response due to gas leakage and thus was not used for spectral analysis. Therefore, for the spectral analysis, only LXP10 data was used.

3.6.2.2 Models For Continuum Spectra

In HMXB pulsars, the continuum emission can be interpreted as arising from comptonization of soft X-rays in the plasma above the neutron star surface. The most commonly used spectral models for HMXB pulsars are high energy cutoff power-law (`XSPEC` model HIGHECUT), a combination of two negative and positive power laws with exponential cutoff (NPEX Makishima et al., 1999), and a thermal Comptonization model (CompTT Titarchuk, 1994). Other local models are power-law with Fermi-Dirac cutoff (FDCUT Tanaka, 1986) and a smooth high energy cutoff model (NEWHCUT Burderi et al., 2000). A careful modeling of the broadband continuum spectrum is crucial for

[7]http://www.rri.res.in/~rripoc/laxpc_gain.html

Table 3.2 Best-fit parameters of the pulse phase-averaged spectrum of 4U 1907+09 from the *AstroSat* observation. The errors correspond to 90% confidence limits.

Parameter	NEWHCUT	HIGHECUT
Γ	0.81 ± 0.04	0.84 ± 0.04
E_{cut} (keV)	12.0 ± 0.9	11.6 ± 0.4
E_{fold} (keV)	11.86 ± 0.48	12.42 ± 0.37
E_{CRSF} (keV)	18.5 ± 0.2	18.5 ± 0.2
σ_{CRSF} (keV)	2.4 ± 0.4	2.1 ± 0.3
τ_{CRSF}	2.48 ± 0.56	2.09 ± 0.30
$Fe_{K\alpha}$ eqwidth (eV)	216 ± 24	209 ± 52
$Fe_{K\beta}$ eqwidth (eV)	148 ± 45	159 ± 45
Flux[a] (4-40 keV)	6.21 ± 0.06	6.21 ± 0.04
χ^2_ν/d.o.f	0.94/288 (3.81/291 without GABS)	0.94/288 (3.58/291 without GABS)

[a] In units of 10^{-10} erg cm^{-2} s^{-1}

obtaining consistent and physically reliable parameters for the CRSF (see, for example, Müller et al., 2013).

3.6.2.3 Phase Average Spectrum Of 4U 1907+09

Different continuum models have been used in the past to fit the spectra of 4U 1907+09 from different instruments. We fitted the phase-averaged energy spectra with all the five continuum models mentioned above, available as a standard or local package in `XSPEC` (Dorman and Arnaud, 2001). `XSPEC` version 12.9.0 was used for spectral fitting. The spectrum was fitted in the energy range of 4.0-40.0 keV. Energy ranges lower and higher than this were neglected due to limited statistics. We added a systematic error of 1% in the energy band of 4.0-10.0 keV and 0.5% in the band of 10.0-40.0 keV using the tool `GRPPHA`. The background subtracted spectrum was fitted with all the parameters of the continuum model kept free except the absorption column density. The column density is not constrained well with LAXPC spectrum above 4.0 keV and was therefore fixed at 1.5×10^{22} atoms cm^{-2} (Maitra and Paul, 2013a). We have used angr (Anders and Grevesse, 1989) table of `XSPEC` for abundances. Iron Kα and Kβ lines were detected and modeled as Gaussians with their energy centers fixed at 6.4 keV and 7.1 keV respectively. The line widths were also fixed at 0.1 keV. Separate spectral fits to the continuum with the continuum models mentioned above showed a deep negative feature in the residuals around 19 keV with a width of about 2.5 keV. This is the CRSF feature already known in 4U 1907+09 and was modeled with

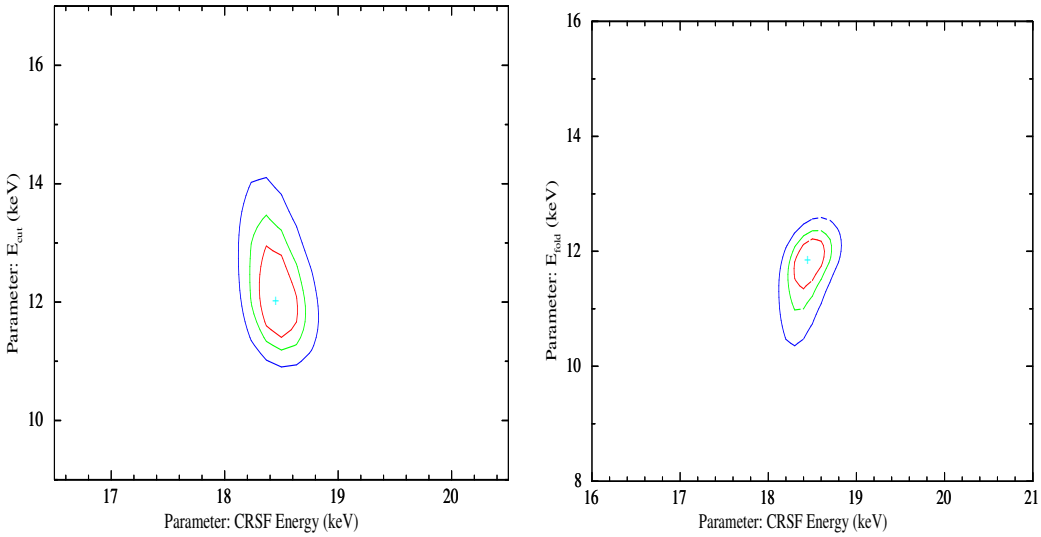

Fig. 3.7 χ^2 contour plots of continuum parameters and CRSF energy created from the phase averaged spectrum of 4U 1907+09. The central cross in light blue color represent the best fitted parameter values. Red, green and dark blue represent the contours of parameter values at 1σ, 2σ and 3σ deviations from the best fit.

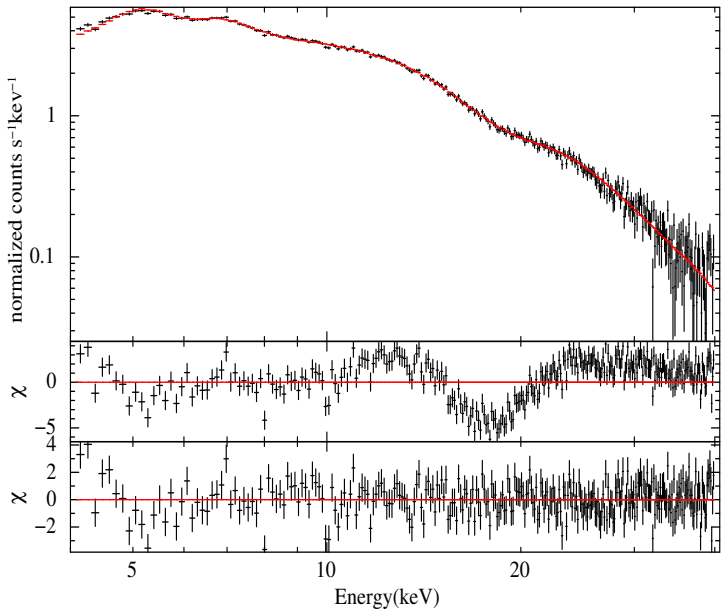

Fig. 3.8 The pulse phase-averaged spectrum of 4U 1907+09 along with the best fit NEWHCUT model and residuals to the fit without and with a CRSF component in the model.

a Gaussian absorption profile (GABS model in XSPEC). Among the five continuum models used, the HIGHECUT and the NEWHCUT model gave comparable fits, and both better compared to the remaining models. The best fit parameter values and fit statistics for these two models fitted to LXP10 spectrum are given in Table 3.2. To check any correlation between the CRSF and the continuum parameters, we have created contour plots of χ^2 for several combinations of parameters in the HIGHECUT and NEWHCUT models and no dependencies were found. For phase-resolved spectroscopy, we found that the continuum and CRSF parameters in some pulse phases were better constrained with the NEWHCUT model compared to the HIGHECUT model. Therefore, only NEWHCUT model is considered for further spectral analysis of this source. NEWHCUT model is a modification of the high energy cutoff model, smoothed around the cutoff energy. Functional form of this model was given in Burderi et al. (2000). The constants in this model are calculated internally assuming the continuity of the intensity function and its derivative in the range of $E_C \pm \Delta E$. This model has been used (Jaisawal and Naik, 2015; Maitra et al., 2018, 2017) extensively for broad band spectra of many accreting pulsars with cyclotron line and ΔE is usually kept constant at 5.0 keV. To be consistent with the literature, we have also fixed it to 5.0 keV. Figure 3.8 shows the LXP10 spectrum along with the best fit NEWHCUT model and the residuals before and after including the CRSF component, thus clearly showing the presence of the absorption feature. Using a CRSF component in the model improves χ^2 from 1108 (for 291 degrees of freedom) to 271 for the addition of three parameters. The line is detected with more than 8σ significance. We looked for any correlation between the CRSF and continuum parameters by creating contour plots in XSPEC for all possible combinations of parameters. The contour plots for CRSF energy and continuum parameters in Figure 3.7 shows that there is no correlation between them. Similarly, for other parameters no correlations were found. The photon index of ~ 0.8, Cutoff energy of ~ 12 keV and E-folding energy of about 12 keV are all well within the range for accretion powered high magnetic field pulsars. The CRSF feature is at ~ 18.5 keV with a width of 2.4 keV and depth of 2.48 keV. The equivalent width of iron Kα and Kβ are found to be ~ 220 eV and ~ 150 eV respectively.

3.6.2.4 Phase Average Spectrum Of 4U 1538–522

We fit the spectra of 4U 1538–522 with all the above-mentioned models. We found that two models FDCUT and NEWHCUT provided better fits to the continuum spectrum compared to other models in terms of the absence of residuals and the reduced

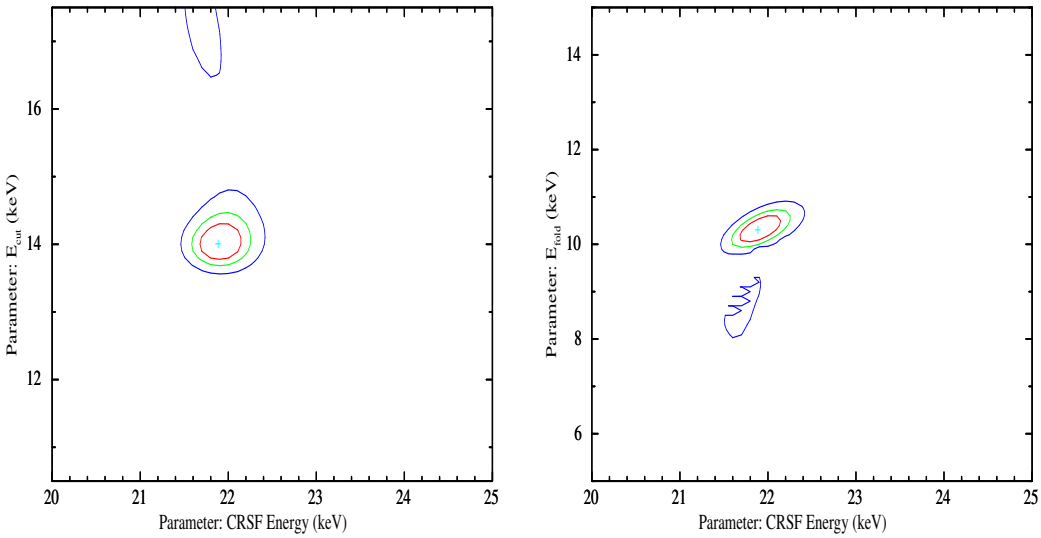

Fig. 3.9 χ^2 contour plots of continuum parameters and CRSF energy created from the phase averaged spectrum of 4U 1538–522. The central cross in light blue color represent the best fitted parameter values. Red, green and dark blue represent the contours of parameter values at 1σ, 2σ and 3σ deviations from the best fit.

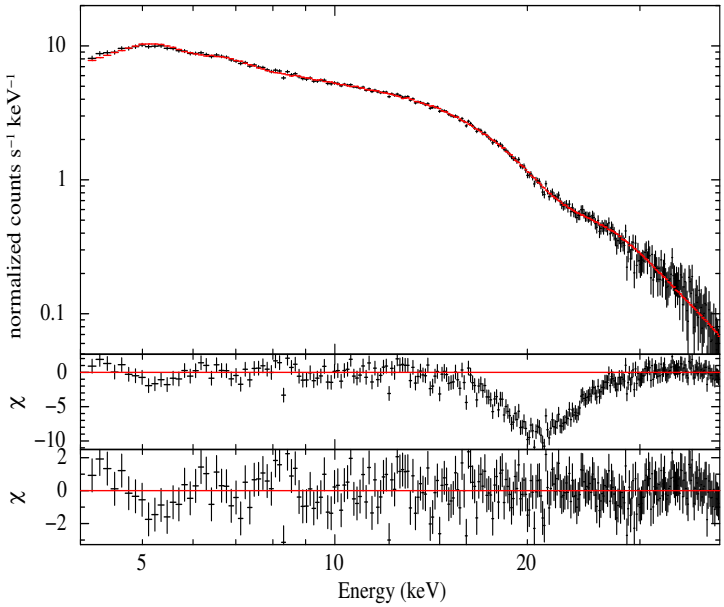

Fig. 3.10 Pulse-phase-averaged spectrum of 4U 1538–522 along with best fit model using LXP10 data. Top panel shows data (Black) and model (Red). Middle panel shows residuals when model does not contain component for CRSF. Bottom panel show residues when CRSF component is included in the model.

χ^2 values. A uniform systematic error across the entire energy band gave large contributions to the χ^2 in the 4.0-10.0 keV range without any structures in the residuals in that energy range. To reduce the χ^2, we have therefore added a systematic error of 1% in energy band 4.0-10.0 keV and 0.5% in 10.0-40.0 keV to the spectra using the tool `GRPPHA`. The fit parameters were found to be largely the same if the same systematics was used across the full band, albeit with a poorer spectral fit. A narrow and deep absorption feature at $\sim$ 22 keV was observed in the residuals, coincident with the CRSF known in this source. The feature was modeled with a Gaussian absorption feature (`XSPEC` model GABS). A Fe Kα line was also detected at 6.4 keV and was modeled by a Gaussian emission line. For the final spectral model, a power-law modified by NEWHCUT and a GABS absorption line for the CRSF was adopted. This is because the CRSF is better constrained in the NEWHCUT model compared to the FDCUT. Using NEWHCUT as continuum and GABS as CRSF we obtain a fit with χ^2 of 277.59 for 276 dof. When a fit is done without GABS component, we get a much poorer fit with χ^2 of 937.53 for 279 dof. This makes it one of the highest signal to noise ratio detection of CRSF for this source. To strengthen the reliability of the CRSF parameters, we performed a contour analysis in `XSPEC` and found that CRSF energy is not correlated with continuum parameters of the NEWHCUT model (see Figure 3.9). Similar analysis of CRSF width and depth with continuum parameters shows that no correlation is present between them. Figure 3.10 shows the phase-averaged spectrum with the best-fit model and the residuals with and without adding the CRSF component. The best-fit spectral parameters are reported in Table 3.3.

3.6.2.5 Pulse Phase-Resolved Spectral Analysis Of 4U 1907+09

As mentioned earlier, the pulse profile of 4U 1907+09 shows significant energy dependence. Morphology of pulse profile changes from being double-peaked between 3.5-22.0 keV to single peaked beyond the CRSF. Such a sharp change in pulse profile with energy indicates a significant spectral change with the pulse phase. To investigate this, we carried out a pulse phase-resolved spectral analysis. This was done by creating spectra in 10 independent phase bins, each of width 0.1. We also extracted spectra with overlapping bins of phase width 0.1 each sliding with a phase interval of 0.02. We refer to this as sliding phase-resolved spectroscopy. However, all the 50 spectra in sliding phase-resolved spectroscopy are not statistically independent. Effectively it is a set of five different phase-resolved analyses, each with ten independent bins. The same background spectrum and response matrix file, as in case of the phase-averaged

Table 3.3 Best fitting phase-averaged spectral parameters of 4U 1538–522. Errors quoted are for 90% confidence range.

Parameters	NEWHCUT	FDCUT
Γ	0.96 ± 0.02	0.87 ± 0.03
E_{cut} (keV)	14.0± 0.3	24.0± 2
E_{fold} (keV)	10.3± 0.3	5.0± 0.5
E_{CRSF} (keV)	21.9± 0.2	22.7± 0.3
σ_{CRSF} (keV)	2.3± 0.3	3.5± 0.3
τ_{CRSF}	2.9± 0.4	8±1
$Fe_{K\alpha}$ (keV)	6.45± 0.09	6.40±0.09
$Fe_{K\alpha}$ EQW (keV)	0.21± 0.03	0.21±0.03
Flux [a] (4.0-40.0 keV)	1.102± 0.006	1.10± 0.01
Reduced χ^2/d.o.f With CRSF	1.00/276	1.16/276
Reduced χ^2/d.of Without CRSF	3.36/279	6.29/279

[a] - Observed flux in units of 10^{-9} erg cm^{-2} s^{-1} in the mentioned energy band.

spectrum were used for phase-resolved analysis. The spectra were also fitted in the same energy range as the phase-averaged spectrum. The absorption column density and Fe line centers along with their width were frozen as in the case of the phase-averaged spectrum. Also, as the width of the CRSF could not be well constrained with the phase-resolved spectra, it was fixed to its phase-averaged value. We would like to mention here that since the CRSF energy is later found to be somewhat variable with the pulse phase, line width measured from the phase-averaged spectrum is perhaps broader than the intrinsic line width in phase resolved-spectra. The pulse phase variation of the continuum and the CRSF parameters obtained with the NEWHCUT model are shown in Figure 3.11 with error bars. The upper and lower limits of the parameters obtained from the sliding phase-resolved spectroscopy are shown in Figure 3.11 with shaded regions. The 4.0-40.0 keV flux at different pulse phases is shown in the top panel for comparison with the pulse profile. The ratio of two phase-resolved spectra with respect to the phase averaged spectrum are shown in Figure 3.12, highlighting the strong pulse phase dependence of the X-ray spectrum of 4U 1907+09. The spectrum at phase 0.59-0.69 is harder compared to the spectrum at phase 0.27-0.37, while the depth of CRSF is smaller in the former. All the Continuum parameters show significant variation with pulse phase. The photon index shows a double-peaked profile that is shifted in phase with respect to the pulse profile. Near the peak of emission profile the photon index decreases indicating a hard spectrum at that phase.

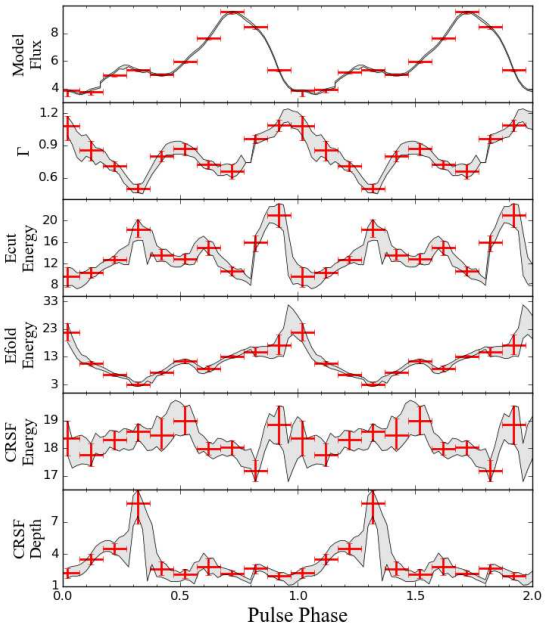

Fig. 3.11 Variation of spectral parameters of 4U 1907+09 with pulse phase is shown here. At top is flux measured in 4.0-40.0 keV band. The results from independent phase bins are shown in red and results from the sliding phase spectroscopy are shown as bounds on the parameters as shaded region. In the top panel is flux measured in units of 10^{-10} erg cm^{-2} s^{-1}.

Near the minimum of emission profile, the photon index is maximum, which means spectrum is comparatively soft in these phases. Hardening of the spectrum at the pulse peak and vice versa is consistent with increasing pulse fraction with energy. E_{cut} and E_{fold} parameters show some variation during most phases, both these parameters peak near the end of the primary peak in the pulse profile. The CRSF parameters also show significant variations with pulse phase. CRSF energy E_{cyc} shows about 12% variation around the mean value, with it being lowest at the main peak of the pulse. Strength of the CRSF is nearly constant except during the rise of the secondary peak. At phase 0.3, the CRSF strength is larger by a factor of ~ 3 compared to its value in the phase-averaged spectrum. The result of sliding phase-resolved spectroscopy agrees with independent phase bin spectroscopy. The sliding phase analysis also shows that the variation of cyclotron line parameters is insensitive to the choice of phase zero.

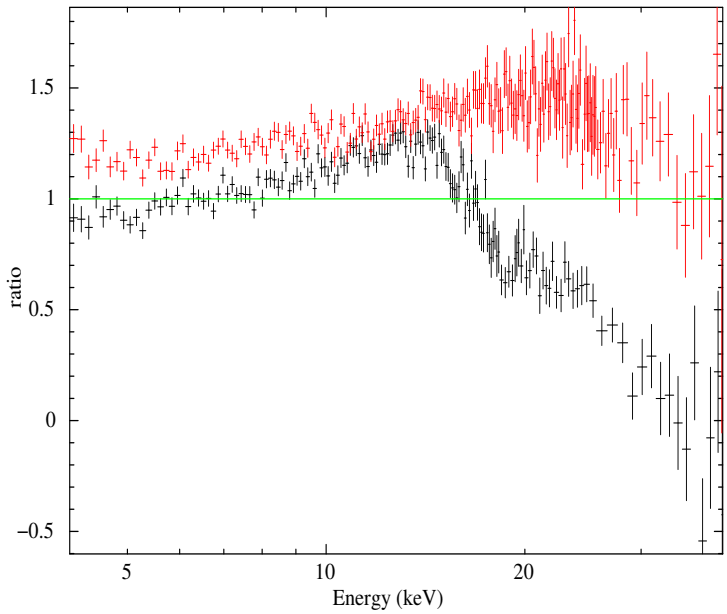

Fig. 3.12 The ratio of two phase resolved spectra of 4U 1907+09 with the phase average spectrum. Ratio of spectrum from phase 0.27-0.37 and phase-averaged spectra is shown in black, while same is shown for phase 0.59-0.69 in red. These two phases are chosen to demonstrate a high contrast.

3.6.2.6 Pulse Phase-Resolved Spectral Analysis Of 4U 1538–522

To probe the changes in the continuum and the CRSF parameters with the rotational phase of the pulsar, spectra were extracted from 10 independent pulse phase bins. The same background spectra and response file as in case of phase-averaged spectral analysis were used. Figure 3.13 shows the results of the phase-resolved spectral analysis of the continuum and CRSF parameters. We also performed a sliding phase-resolved analysis for this source as in the case of 4U 1907+09. The upper and lower limits of the parameters obtained from the sliding phase resolved spectroscopy are shown in Figure 3.13 with shaded regions. The spectrum is harder at the primary (phase 0.2-0.4) and secondary pulse peaks (phase 0.7-0.8) with lower values of Γ and corresponding increase in E_{cut} and E_{fold} energies. The secondary peak is softer in general than the primary peak and is consistent with the energy dependence of the pulse profiles seen in Fig. 3.6. The CRSF parameters show significant energy dependence with the phase as also observed in earlier works (Clark et al., 1990; Hemphill et al., 2014). The variation of all the CRSF parameters is however probed in detail for the first time, especially the CRSF depth. In Figure 3.14, we highlight the strong pulse phase dependence of the X-ray spectrum. The ratio of two of the pulse phase-resolved spectra are shown here. The spectrum at phase 0.3-0.4 (shown in red) is harder than

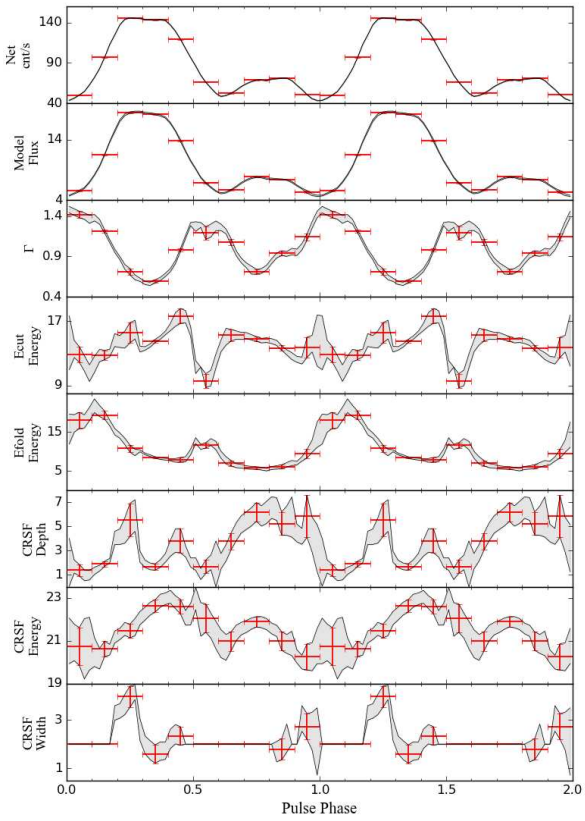

Fig. 3.13 The phase variation of the continuum and CRSF parameters of 4U 1538–522. Results from the independent phase bins are shown in red and from the sliding phase bins are shown as bound to the parameters as shaded region.

the phase- averaged spectrum whereas at phase 0.7-0.8 (shown in black) it is softer with a strong CRSF feature around 22 keV. The CRSF energy (E_{cyc}) is correlated with the pulse profile and rises to $\sim$ 23 keV near the peak of the primary peak (phase 0.4-0.5). This is consistent with that seen in earlier works (Clark et al., 1990; Hemphill et al., 2014). The overall variation in the CRSF energy measured from independent bins is 13 %(20.00-23.02 keV). The CRSF is deeper near the secondary peak (phase 0.65-0.95) than the primary peak (phase 0.2-0.3), and lot of variation is detected near the primary pulse. It was not possible to constrain the CRSF width at the rise (phase 0.0-0.2) of the primary peak and during secondary peak (phase 0.5-0.8) and was frozen to the phase-averaged value $\sim$ 2.0 keV instead for these phases. The overall pattern implies a complex pulse phase dependence of the CRSF parameters, which are evident, especially from the sliding phase-resolved spectroscopy. The parameter variations are consistent with that obtained from the independent phase bins.

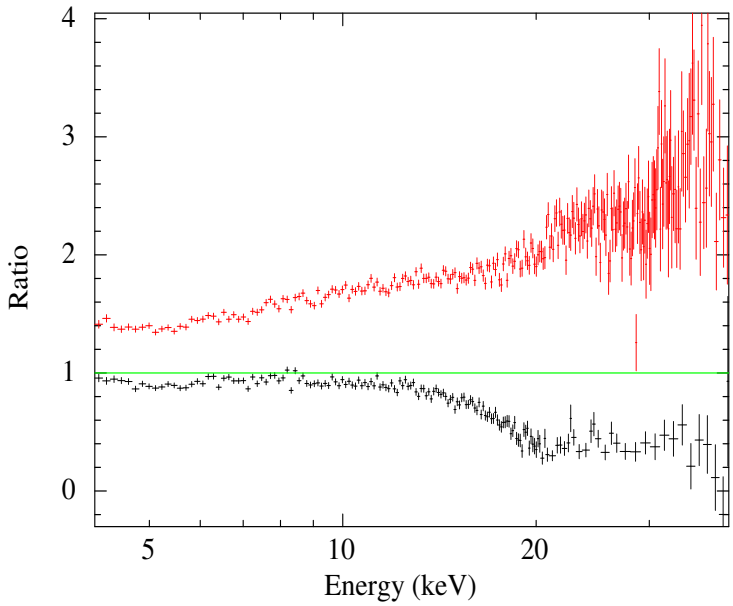

Fig. 3.14 Ratio of the spectrum of 4U 1538–522 during pulse phase 0.3-0.4 and its phase averaged spectrum is shown in red, while the same for phase 0.7-0.8 is shown in black. The spectrum is softer during phase 0.7-0.8 with a deep CRSF.

3.6.2.7 Intensity Resolved Spectral Analysis Of 4U 1907+09

At the beginning of the *AstroSat* observation of 4U 1907+09, the intensity was seen to be higher than later in the observation as seen in Figure 3.1. We performed an intensity dependent spectroscopy from this observation by considering the first two orbit data as high luminosity and rest of observation as low luminosity. We fitted both spectra with the NEWHCUT model, and the best-fit parameters are given in Table 3.4. The parameters in high and low luminosity states are in agreement within error bars.

3.7 Discussion On The Results

In this chapter, we have presented the results from timing analysis, pulse phase-averaged spectroscopy, and pulse phase-resolved spectroscopy of two HMXB pulsars 4U 1907+09 and 4U 1538–522 with *AstroSat*-LAXPC. For 4U 1907+09, we have also performed an intensity-resolved spectral analysis. These are early results on the cyclotron lines in accretion-powered pulsars with *AstroSat*, especially with pulse phase-resolved spectroscopy. In this section, we give a discussion on the implication of our results.

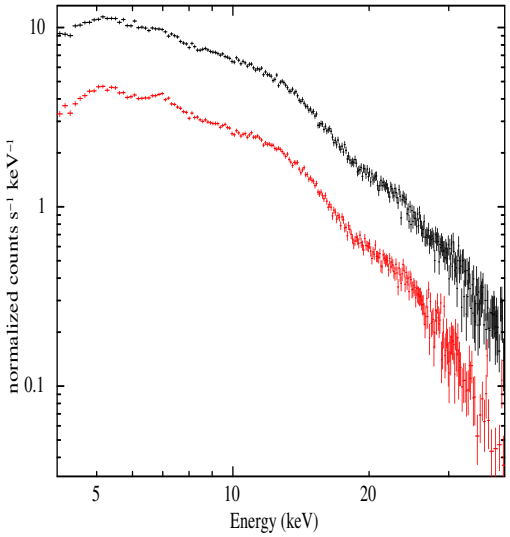

Fig. 3.15 Two spectra of 4U 1907+09 at different intensities during its *AstroSat* observation. Black is the spectrum during higher intensity in first $\sim$ 10 ks of observations. Red is the spectrum of data during the rest of the observation.

Table 3.4 The best-fit spectral parameters of 4U 1907+09 from intensity dependent spectroscopy with the same model as used with phase averaged spectrum. The errors correspond to 90% confidence limits.

Parameter	High Luminosity	Low Luminosity
Γ	0.82 ± 0.04	0.80 ± 0.04
E_{cut} (keV)	11.40 ± 0.87	13.6 ± 1.7
E_{fold} (keV)	13.42 ± 0.58	10.2 ± 1.2
E_{cyc}	18.71 ± 0.32	18.29 ± 0.26
σ (keV)	2.71 ± 0.54	2.74 ± 0.53
Strength	2.64 ± 0.73	3.3 ± 1.3
$Flux^a$ (4.0-40.0 keV)	13.4 ± 0.1	5.13 ± 0.06

[a] In units of 10^{-10} erg cm^{-2} s^{-1}

3.7.1 4U 1907+09

3.7.1.1 Energy Dependence Of The Pulse Profile And Period Evolution

As is known in 4U 1907+09, the LAXPC observations also show strong energy dependence of the pulse profile, the two peaks were varying differently with energy. *Suzaku* observations (Rivers et al., 2010) showed a pulse profile with two peaks of comparable amplitude at lower energies and the secondary peak to be much weaker at higher energy. Energy resolved pulse profiles from the LAXPC observation agree with these findings, and we have probed the pulse profile variations further around the cyclotron line energy. We have found that the secondary peak becomes weaker near cyclotron energy (energy bands of 16.0-19.0 keV and 19.0-22.0 keV) and the pulse fraction of primary peak increases from 38 % in 3.5-8.0 keV band to 58 % in 22.0-40.0 keV and then it drops to 25 % in 40.0-60.0 keV range. A change in pulse shape or pulse fraction near the cyclotron line energy has been seen in several pulsars like 1A 1118–61, A 0535+26, XTE J1946+274 (Maitra and Paul, 2014) and V 0332+53 (Tsygankov et al., 2006). Being at the lower end of luminosity for the persistent HMXB pulsars, a pencil beam pattern is expected in 4U 1907+09, with the two pulse peaks being produced from the two magnetic poles. The two pulse peaks are not separated by a phase of 0.5, which indicates either a non-dipole field geometry of the neutron star or a complex beaming profile (a combination of pencil and fan beam geometry) from at least one of the poles. Additionally, the different energy dependence of the two pulse peaks indicates a significant difference in the energy dependence of the beaming pattern in the two magnetic poles in 4U 1907+09.

Although we have not carried out photon arrival time correction for the orbital motion, if the nominal values of the orbital parameters determined from the *RXTE*-PCA observations are used (in 't Zand et al., 1998), the current LAXPC observation of 4U 1907+09 is done at an orbital phase of 0.18 after $T_{\pi/2}$, corresponding to a line of sight velocity of -119 km s^{-1}, and a Doppler-shift corrected pulse period of 442.51 seconds. Along with the historical data (Şahiner et al., 1977), it indicates a continued slow down of the pulsar.

3.7.1.2 The CRSF And A Possible Weak Luminosity Dependence

X-ray emission processes in accreting pulsars and the behavior of matter in strong magnetic fields determine the characteristics of their CRSF properties. The CRSF in this source was earlier investigated with several different instruments, most notably

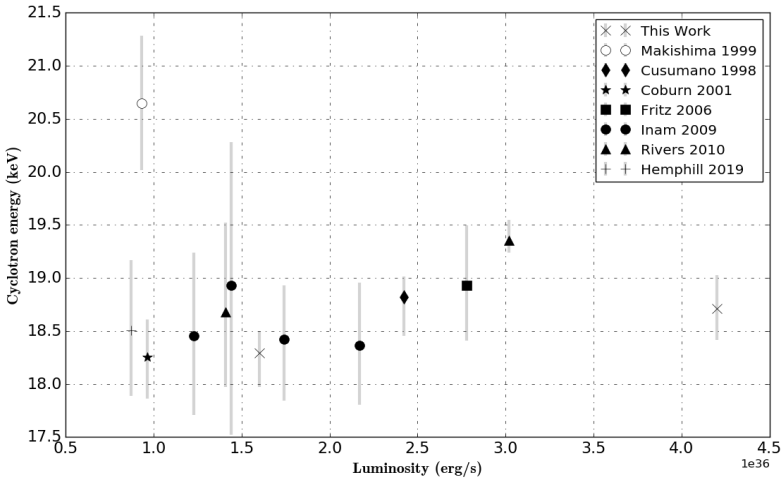

Fig. 3.16 The relationship of CRSF energy of 4U 1907+09 with its luminosity is shown. The measurement of CRSF energy at two luminosities in *AstroSat* observation is shown along with some previous measurements with different X-ray telescopes.

with two *Suzaku* observations which were analyzed differently (Maitra and Paul, 2013a, 2014; Rivers et al., 2010). It should be noted that the broad band *Suzaku* spectrum is obtained with two sets of instruments, XIS (0.7-10 keV) and PIN (15-80 keV), and the relative normalization of the two instruments is often derived from each spectral fit. It is also to be noted that the CRSF feature in 4U 1907+09 is close to the energy threshold of PIN detectors. The present measurements are carried out with a single instrument covering a broad band. The low and high energy thresholds of LAXPC are a factor of a few from the CRSF energy, giving a clear detection of the feature with a single instrument. Overall, the CRSF parameters determined from the LAXPC spectrum are in agreement with the previous measurements (Cusumano et al., 1998; Hemphill et al., 2013; Maitra and Paul, 2013a; Rivers et al., 2010). Different continuum models have been used in the past to fit the spectra of 4U 1907+09, and for completeness, we have given results from the spectral fit with all the five models. With three of the spectral models that gave a relatively poorer fit to the LAXPC spectrum, the cyclotron line energy is about 0.5 keV larger than the value obtained with the other two models. We also note that an additional broad 10 keV component that was included in the *Suzaku* spectrum in Rivers et al. (2010) has been shown to be not necessary in reanalysis of the *Suzaku* spectrum by Maitra and Paul (2013a), *INTEGRAL* spectrum by Hemphill et al. (2013) and the LAXPC spectrum in the current work.

Some accretion-powered pulsars show a dependence of the cyclotron energy on luminosity. In the super-critical luminosity regime, a negative correlation between CRSF energy and luminosity is expected, and the opposite is expected in the sub-critical regime (Becker et al., 2012). Barring singular aspects of some sources, both the expected correlations have been seen in accreting pulsars: a negative correlation in V 0332+53 (Doroshenko et al., 2017) and a positive correlation in Her X-1 (Staubert et al., 2007) and GX 304–1 (Klochkov et al., 2012) being prime examples. At much lower luminosity, below L_{coul}, the cyclotron line energy is expected to be independent of X-ray luminosity and the same has been observed in A 0535+26 over a luminosity range of two decades and a positive correlation at the highest luminosity range for this source (Caballero et al., 2007; Sartore et al., 2015). Assuming canonical neutron star parameters M = 1.4 $M_{\odot}$ and R = 10 km, 4U 1907+09 is well within L_{coul} (Hemphill et al., 2013). A weak positive correlation between the cyclotron line energy and 5-100 keV X-ray luminosity was reported for 4U 1907+09 making it the lowest luminosity cyclotron line source to exhibit this relationship (Hemphill et al., 2013) and indicating that perhaps the sub-critical regime is more relevant for this source. The highest 5-100 keV X-ray luminosity at which CRSF has been reported in 4U 1907+09 is about 3×10^{36} erg s^{-1} with the *Suzaku* observation in 2007. For comparison with the observations mentioned in Hemphill et al. (2013), we have extrapolated the flux to the 5-100 keV band and calculated the luminosity for a distance of 5 kpc (Cox et al., 2005). The averaged luminosity was $\sim 2 \times 10^{36}$ erg s^{-1}, and the luminosity during the low and high intensity parts as reported in Table 2 was 1.6 $\times 10^{36}$ erg s^{-1} and 4.2 $\times 10^{36}$ erg s^{-1} respectively, the cyclotron line in all of them being consistent with 18.5 ± 0.2 keV. Thus the LAXPC observations marginally extend the luminosity range over which the CRSF has been detected in 4U 1907+09 without providing additional support for a luminosity dependence of the line energy. The measurements of CRSF energy at two luminosities during LAXPC observations, along with other observations in the past, is shown in Figure 3.16. The current observation itself gives a luminosity range of 2.6, over which the CRSF is found to be non-varying beyond 3%. The *AstroSat* observations rules out the positive correlations of CRSF energy in a wider luminosity range of (0.8-4.2)$\times 10^{36}$ ergs^{-1} which was reported in range (0.8-3.0)$\times 10^{36}$ ergs^{-1} (Hemphill et al., 2013). The CRSF characteristics of 4U 1907+09 appear more like A0535+262, with no strong correlation between the CRSF energy and luminosity.

3.7.1.3 Pulse Phase Dependence Of The CRSF

The LAXPC results are consistent with the earlier reported pulse phase-resolved spectroscopy of 4U 1907+09 with *Suzaku* with six independent phase bins by Rivers et al. (2010) and eight independent phase bins by Maitra and Paul (2013a) respectively. Mainly, the line depth was found to be highest just before the secondary peak, and the line energy was found to be highest just after it. *Suzaku* observations were also useful to demonstrate that the pulse phase behavior of CRSF parameters has a similar pattern with a change in luminosity by a factor of 2.5 between 2006 and 2007. The LAXPC pulse phase-resolved spectroscopy carried out with 10 independent phase bins shows the line to be strongest around the secondary peak. Given the poor phase resolution in all the phase-resolved spectroscopy with limited statistics, these results are consistent with the *Suzaku* results. The line being strongest near the secondary peak is somewhat surprising for 4U 1907+09 which has a lower luminosity, and hence is expected to have a pencil beam emission and low depth of CRSF at the pulse peak. This indicates the beaming pattern in the two magnetic poles to be different, a complex beaming pattern, or perhaps a deviation from a dipole geometry of the neutron star magnetic field. We also note that the variation in cyclotron line energy in 4U 1907+09 is about 13%, which is smaller compared to some other sources like Vela X-1, 1A 1118–61, and XTE J1946+274 (Maitra, 2017).

3.7.2 4U 1538–522

3.7.2.1 Long Term Increase In Cyclotron Line Energy

Hemphill et al. (2016) reported a long term increase in the CRSF centroid energy by ~ 1.5 keV between the 1996–2004 *RXTE* and 2012 *Suzaku* measurements. The authors obtained a linear increasing trend of 0.058 ± 0.014 keV yr^{-1}. This would imply an increase of 0.29 keV between the *Suzaku* and *AstroSat* measurements, which would be impossible to detect given the error bars of the measurements. Our reported centroid energies of $E_{cyc} = 21.9 \pm 0.2$ keV with the NEWHCUT continuum model and $E_{cyc} = 22.76 \pm 0.26$ keV with the FDCUT continuum model are however consistent with that obtained from the *Suzaku* data while all the earlier *RXTE* measurements were below 21 keV. Our results are comparable to results obtained by Hemphill et al. (2016). The results from our work further strengthen the claim of a long term increase in E_{cyc}, rather than the *Suzaku*, measurement representing a short-term or a local increase in E_{cyc}. This result has also been confirmed by a recent *NuSTAR* observation of 4U 1538–522 (Hemphill et al., 2019). The long term behavior of CRSF in this source

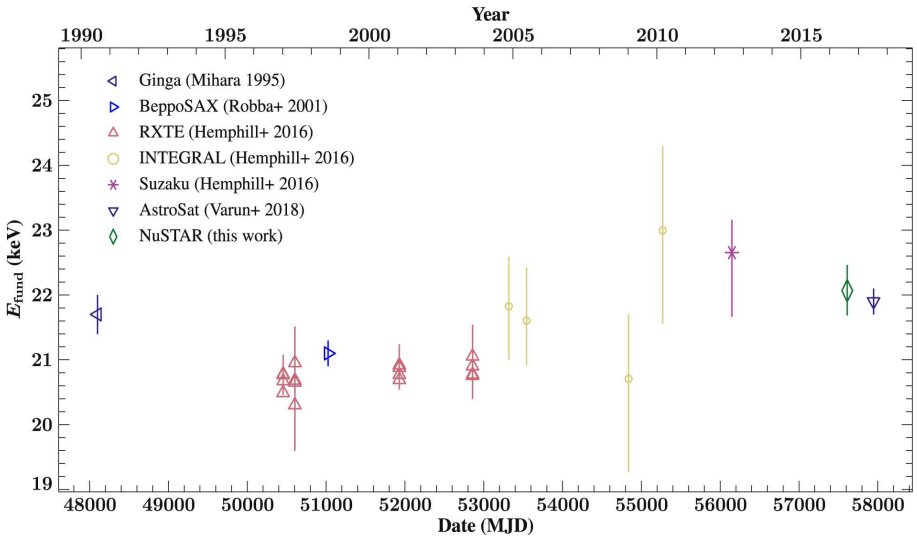

Fig. 3.17 The long term behavior of CRSF energy in 4U 1538–522, measured with various telescopes along with the *AstroSat* observation presented in this chapter. Figure credit: Hemphill et al. (2019).

using data from *AstroSat* observation along with previous measurements is shown in Figure 3.17. The long term increase indicates a local change or reconfiguration in the line forming region, thereby resulting in an increased effective magnetic field strength (Mukherjee and Bhattacharya, 2012). However future observations separated by sufficiently large time gaps will be able to ascertain whether the trend is linearly increasing or the increase was due to a sudden change in the line-forming region which caused this change in E_{cyc}.

3.7.2.2 Variation of Cyclotron Line Energy With Pulse Phase

Our results of the phase dependence of CRSF energy are in agreement with earlier works. Clark et al. (1990) studied CRSF energy variation with pulse phase using *Ginga* observation. They used power-law as a continuum component along with a gabs component for CRSF. They found a 14% variation in CRSF energy with pulse phase. Hemphill et al. (2014) used *Suzaku* observations and found 10% variation of same using HIGHECUT, FDCUT, and NPEX models. The variation using *AstroSat*-LAXPC observation is $\sim 13\%$.

3.7.2.3 The Emission Pattern of High Energy Radiation In This Pulsar

The measured flux of 4U 1538–522 in the energy range of 4.0–40.0 keV indicates a luminosity of 5.1×10^{36} erg s^{-1} at a distance of 6.4 kpc. At this luminosity, the source is expected to be accreting at the super-critical regime, with the expected value of $L_{\rm crit}$ at $\sim 2 - 4 \times 10^{36}$ erg s^{-1} (see Hemphill et al., 2016, assuming the same distance). At this regime, the source is expected to transform from a plasma-dominated regime with a dominant pencil-like emission beaming pattern to a radiation dominated regime with a dominant fan-like emission beaming pattern (Basko and Sunyaev, 1976; Becker et al., 2012; Mushtukov et al., 2015a). The complex pulse profile morphology and its energy dependence in 4U 1538–522 is however difficult to be identified with a pure pencil-like or fan-like beaming pattern. The CRSF parameters exhibit strong pulse phase dependence, but effects like lightbending, relativistic beaming, reflection, and the mixing of two columns make the interpretation of the CRSF parameters very difficult. While the results indicate an overall complex beaming geometry, a detailed modeling of the energy dependence of the pulse profiles together with the pulse phase dependence of the CRSF parameters is required to map the complex variations, a.k.a the accretion geometry in this source. We leave this for future works.

3.8 Conclusions

3.8.1 4U 1907+09

In this chapter, we have reported the results from an observation of the HMXB pulsar 4U 1907+09 with the *AstroSat*-LAXPC. Two peaks of the pulse profile of 4U 1907+09 exhibited different energy dependence: the pulsed fraction of the main peak increased till about 40 keV and decreased after that while the secondary peak disappeared at energy above about 20 keV. The pulsar was found to continue on the spin-down trend. A CRSF was detected at 18.5 ± 0.2 keV in the X-ray spectrum. A flare was detected at the beginning of the observation with flux 2.6 times compared to the rest of the observation. The cyclotron line energy during the flare was found to be consistent with the rest of the observation. Pulse phase-resolved spectroscopy was carried out with 10 independent phase bins, and variations of the CRSF parameters with pulse phase were found to be consistent with previous results from two *Suzaku* observations of 4U 1907+09.

3.8.2 4U 1538–522

In this chapter, we have presented our results on cyclotron line study of the High mass X-ray Binary pulsar 4U 1538–522 with the *AstroSat*-LAXPC. During the observation of source which spanned about one day with a net exposure of 50 ks, the source X-ray flux remained constant. Pulse profile is double-peaked in low energy range and has a single peak in high energy range, the transition taking place around the cyclotron line energy of the source. CRSF is detected at $\sim$ 22 keV with a very high significance in phase-averaged spectrum. It is one of the highest signal to noise ratio detection of CRSF for this source. We have performed a detailed pulse phase resolved spectral analysis with 10 independent phase bins. We have reported the results of pulse phase-resolved spectroscopy of the continuum and CRSF parameters. The cyclotron line parameters showed pulse phase dependence over the entire phase with a CRSF energy variation of $\sim$ 13% which is in agreement with previous studies. We also confirm the increase in the centroid energy of the CRSF observed between the 1996–2004 (*RXTE*) and the 2012 (*Suzaku*) observations, reinforcing that the increase was a long-term change.

Chapter 4

AstroSat-LAXPC Observations Of Some Isolated Neutron Stars

4.1 Introduction

After *AstroSat* was launched on the 28th of September 2015, a series of standard astronomical sources were observed for instrument calibrations and better understanding of the scientific instruments (Agrawal, 2017; Bhattacharya, 2017). The Crab nebula is naturally the first choice for high energy instruments like LAXPC for this purpose. It was observed on the 19th of October 2015 and its signature pulse profile was obtained from this first light of LAXPC. Later more observations of the Crab nebula were performed for detailed calibration of this instrument (Antia et al., 2017). LAXPC is an excellent instrument for timing and moderately good for spectroscopy in 3.0-80.0 keV range. All types of Isolated neutron stars (INS) emit in X-rays. X-ray observations of INS have given some of the crucial observational insights which were missed by radio observations. Even with a smaller sample of a few tens of sources in X-rays, they provide a different view on a variety of phenomena in standard in rotation powered pulsars. Some of the INSs like rotation powered pulsars and magnetars are active in LAXPC energy band. Some standard INSs were also observed in the performance verification phase of *AstroSat*. We have carried out analysis of data from observations of four INSs which cover a wide range of source properties: X-ray flux, pulse period, pulse profile, and X-ray spectral shape. Three of the sources analyzed in this chapter are part of Supernova Remnants (SNR) (See 4.1). The fourth source 1E 1048.1-593 does not have an association with SNR. Crab nebula is chosen as a bright source due to its large flux in 3.0-80.0 keV band. We have used data from observation of Crab Nebula over one orbit of satellite to see the pulse profile behavior with energy. Then, we have

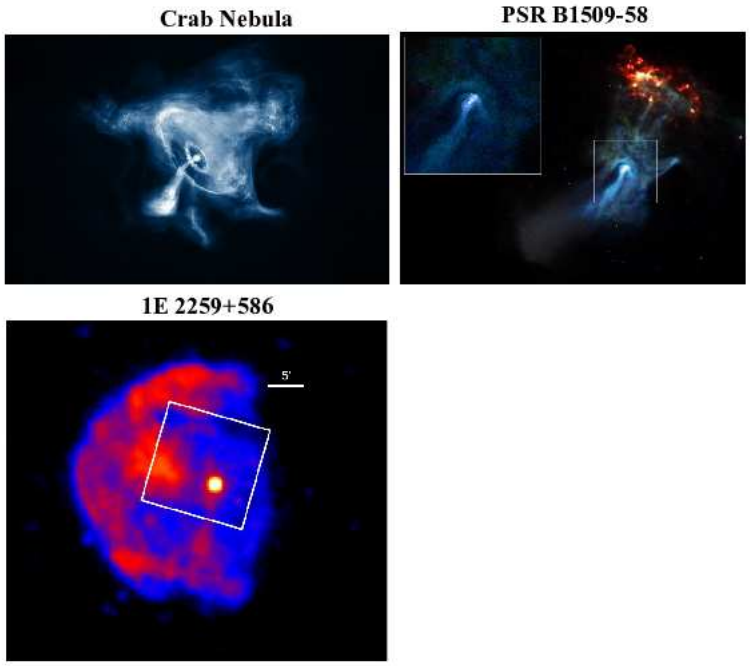

Fig. 4.1 X-ray Images of the sources analyzed here. Images of Crab nebula and PSR B1509–58 are taken from *Chandra* repository and image of 1E 2259+586 is from a *ROSAT* observation. Image Credit: CXC and (Vogel et al., 2014)

carried out analysis of a moderately bright rotation powered pulsar PSR B1509–58. For this source, we have done timing analysis in a different energy bands and spectral analysis with different combination of layers and event types. We have also analyzed data from observations of two magnetars 1E 2259+586 and 1E 1048.1-593. These two sources are very faint and only detected in low energy bands. The work in this chapter has given us a good idea on how to handle LAXPC data of different types of sources. Some of the insights gained from the analysis of these sources have been helpful to us in other works also.

4.2 *AstroSat* Observations Of Rotation Powered Pulsar.

Rotation Powered Pulsar (RPP) is historically the first class of pulsars to be discovered. The first pulsar to be discovered, PSR B1919+21, was an RPP. Also, one of the most

important astronomical source, "Crab", is also an RPP. These are fast rotating neutron stars. Most of them spin down steadily, converting their rotational energy into electromagnetic radiation and particle outflows. They typically have spin periods of $\sim$ 0.1–10 s and period derivatives of $\sim 10^{-12}$–10^{-17} s s^{-1}, implying magnetic fields of B $\sim 10^{11}$ –10^{13} G. Currently, there are $\sim$ 1700 RPPs known in radio[1], 12 in optical (+NIR+UV) (Mignani, 2011), $\sim$ 100 in X-rays (Kargaltsev and Pavlov, 2014), and $\sim$ 150 in γ-rays (Kuiper and Hermsen, 2015). Most of the RPPs are distributed towards the galactic plane.

4.2.1 The Crab Nebula

The Crab nebula is a remnant of a supernova explosion in 1054 AD. It was registered and monitored by contemporary Chinese astronomers. Since then the remainder of the explosion, the Crab nebula and its pulsar, has been studied over the centuries. Edwin Hubble correctly measured the expansion velocity and deduced that the nebula was the remainder of the 1054 AC supernova explosion. Crab nebula is the brightest sources in the sky at photon energies $\geq$ 30 keV. It can be studied in great detail due to its high luminosity L $\approx 1.3 \times 10^{38}$ erg s^{-1} (Hester, 2008) and its closeness $\sim$ 2 kpc (Trimble, 1973). It is, therefore, our prime laboratory to study non-thermal processes in the Universe. Many discoveries have been made in the Crab and then been seen in other non-thermal sources such as polarized synchrotron radiation or pulse optical emission (Cocke et al., 1969).

In the center of the nebula, there is a high magnetic field neutron star with a spin period of $\sim$ 33 ms, which was discovered in 1968 (Staelin and Reifenstein, 1968). The pulsar is slowing down at a rate of $\dot{P} = 4.2 \times 10^{-13}$ ss^{-1} (Manchester et al., 2005). The loss of rotational kinetic energy from neutron star powers the whole nebula. The radiation is thought to be collimated in beams of light, which sweeps the line of sight from the earth, creating the observed pulsations. The pulsed emission is visible across the entire electromagnetic spectrum. In all the energy bands, the pulse profile is double-peaked and most of the emission from the neutron star is concentrated in two peaks (Abdo and et al., 2010). The main peak P1 and inter-pulse P2 are separated by phase 0.4 over all the energies (Pravdo et al., 1997). The pulse shape is found to quite stable with time in soft X-ray (2.0-20.0 keV) and hard X-ray (30.0-100.0 keV) (Jain and Paul, 2011). However, the pulse shape varies as a function of energy. The relative intensity of the two peaks first increases and then decreases with increasing

[1]http://www.atnf.csiro.au/research/pulsar/psrcat

energy. The first peak is more pronounced in radio, optical bands and up to hard X-rays (Oosterbroek et al., 2006). The second peak becomes more prominent at soft γ-rays. With a further increase in energy, the first peak against becomes dominant (Kuiper et al., 2001). In this chapter, we present the timing analysis of Crab from the data observed with LAXPC instrument onboard *AstroSat*.

4.2.2 PSR B1509–58

PSR B1509–58 is a pulsar situated in the supernova remnant MSH 15-52 near its geometric center. The 150 ms spin period was discovered by the *Einstein* satellite (Seward and Harnden, 1982) which was confirmed quickly with the help of radio observations (Manchester et al., 1982). This pulsar is one of the youngest and most energetic pulsars known in the galaxy with a characteristic age of 1700 yrs and period derivative, $\dot{P} = 1.49 \times 10^{-12}$ ss^{-1} (Kaspi et al., 1994; Weisskopf et al., 1983). The inferred spin down power is $\dot{E} = 1.8 \times 10^{37}$ erg s^{-1}. Assuming a dipolar form of the magnetic field the inferred surface magnetic field is 1.5×10^{13} G. The measurement of pulsar braking index shows that this assumption is nearly correct (Livingstone et al., 2005). The distance to the source is found to be 5.2 ± 1.4 kpc using HI absorption measurement (Gaensler et al., 1999). The average pulse profile in X-ray has a single broad peak followed by a broad minimum. The shape of average pulse profile is found to be steady with time (Pradhan et al., 2015). The broad X-ray pulse profile can be described by two Gaussian components (Cusumano et al., 2001). On the other hand, the pulse profile in radio band shows a narrow peak. The X-ray pulse lags radio pulse by about one quarter of a cycle (Kawai et al., 1991).

The X-ray spectrum of this source has been studied in detail due to large flux which is not possible for most of the other rotation-powered pulsars. The spectrum of the nebula is described well by an absorbed powerlaw with photon index $\alpha \sim 1.86$ and column density $N_H \sim 6.6{\times}10^{21}$ cm^{-2} in the energy range 1.6-11 keV (Trussoni et al., 1990). Using the pulsed spectrum in 0.1-2.4 keV energy range and restricting to powerlaw photon index to the values 0.3-1.4 the column density was determined to be $\sim 9.5{\times}10^{21}$ cm^{-2} (Greiveldinger et al., 1995). The spectrum of pulsed component is fitted by power law of photon index 1.36 ± 0.01. The off-pulse emission shows a softer spectrum with $\Gamma = 2.215 \pm 0.005$ (Marsden et al., 1997). The power-law photon index, obtained from by using the off-pulse emission as background to the pulsed emission, varies with phase from 1.33 to 1.47 as obtained by using 15 years of *RXTE* data (Ge et al., 2012). The broadband spectrum between 0.1-300 keV is better fitted by a curve log-parabolic model than by single PL (Cusumano et al., 2001). The broadband

Table 4.1 Summary of Observations of different type of sources used in the study

Source Name	Obs ID	Obs Date	Exposure (ks)	Source Class	P_{spin} (sec)
Crab	T01_052T01_9000000312	04-02-2016	16.0	RPP	0.033
PSR B1509–58	T01_029T01_9000000352	01-03-2016	24.9	RPP	0.150
1E 1048.1-593	G06_023T01_9000000762	28-10-2016	63.4	Magnetar	6.98
1E 2259+586	G06_026T01_9000000962	13-01-2017	68.4	Magnetar	6.46

spectrum of this source in 3.0-79.0 keV also fitted well with the log-parabolic model although best-fit parameters are slightly different than obtained by *BeppoSAX* data.

4.2.3 Observations

The Crab was observed on 4th of February 2016 for 5 *AstroSat* orbits using LAXPC instrument. Total on source time during the observation was $\sim$ 16 ks. We have used the first $\sim$ 3.5 ks on source data from this observation. PSR B1509–58 was observed on 1st of March 2016 for 8 *AstroSat* orbits using LAXPC instrument. We have obtained $\sim$ 16 ks on source data from this observation and the same was used for data analysis. Both these observations were carried out during the performance verification of the observatory. Details of both the observation can be found the Table 4.1. Here we present the detailed timing results for the Crab Nebula. For the PSR B1509–58 we present timing and spectroscopic results of data from its LAXPC observation. The data from the event analysis mode were used. Raw data files were reduced with Level1 to Level2 data processing guide[2] version 1. Level2 products were used to create light curves and spectral files. Further timing and spectral analysis were done using tools in HEASOFT software suite, version 6.19. Time intervals when the source is occulted by the earth and satellite is passing through South Atlantic Anomaly (SAA) region have been removed for the creation of light curve and spectral file.

4.2.4 Timing Analysis

For Crab, the light curve from the first $\sim$ 3.5 ks on source data was created with a bin time of 100 μs. A light curve extracted when the source is occulted by the earth is used as the background. The average count rate obtained from such a light curve was subtracted from the source light curve. The background subtracted light curves from three LAXPC units in full energy band are shown in figure 4.2 with a bin size

[2]http://www.rri.res.in/~rripoc/POC.html

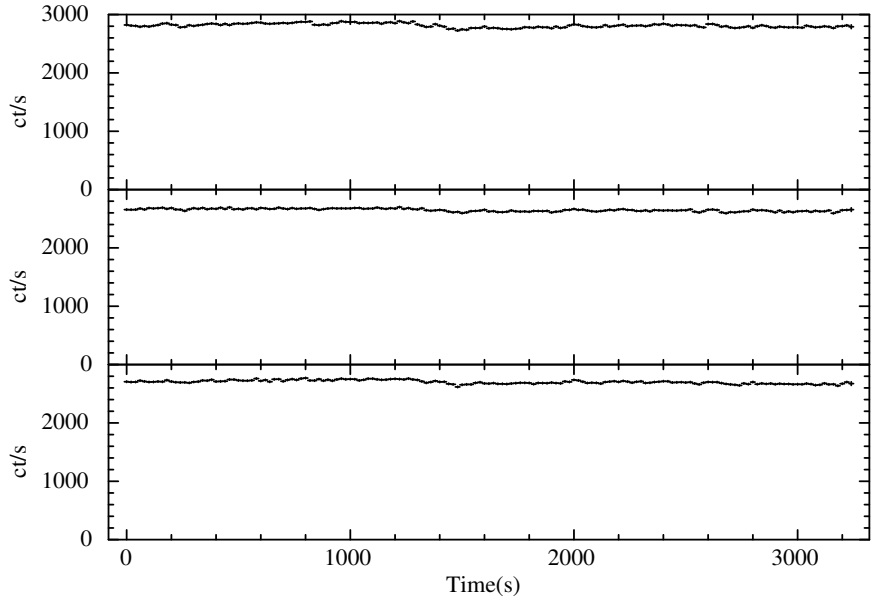

Fig. 4.2 Light curves of the Crab Nebula from the *AstroSat* observation with LAXPC. Three panel from top to bottom show data form 3 detectors LXP10, LXP20, and LXP30 respectively, with a time bin size of 20 s.

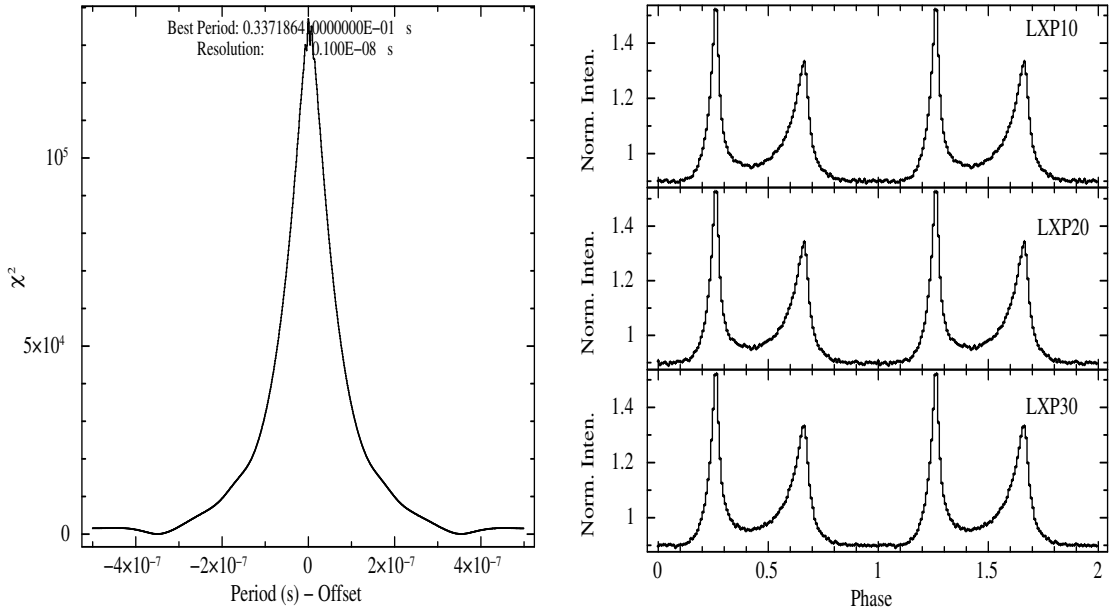

Fig. 4.3 Left: χ^2 in light curve for different trial pulse period values is shown for the Crab Nebula observation. Right. Pulse profiles created using the best period determined during this observation using data from 3 detectors LXP10, LXP20, and LXP30. Full spin period is divided in 128 phasebins.

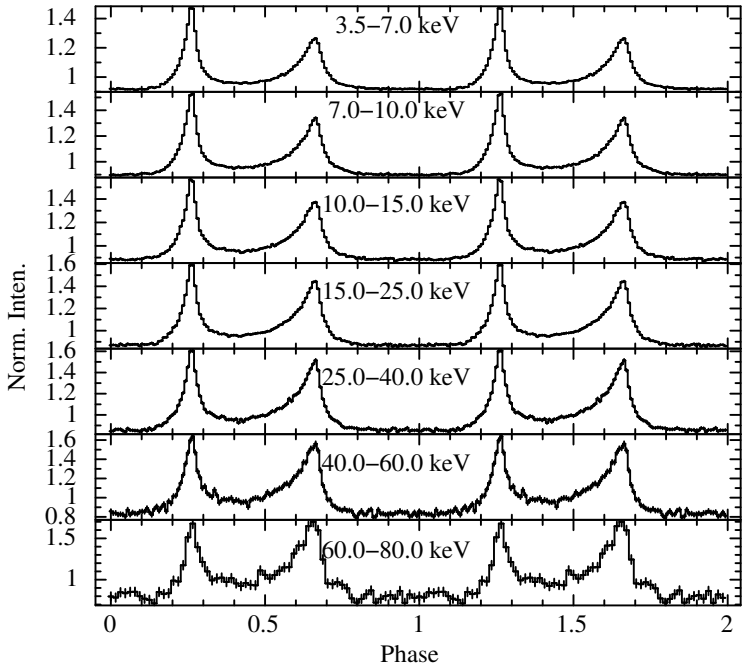

Fig. 4.4 The energy resolved pulse profiles of the Crab Nebula from the combined data of 3 detectors. Pulse profile in top 6 panels are created with 128 phase bins and in last panel with 64 phase bins.

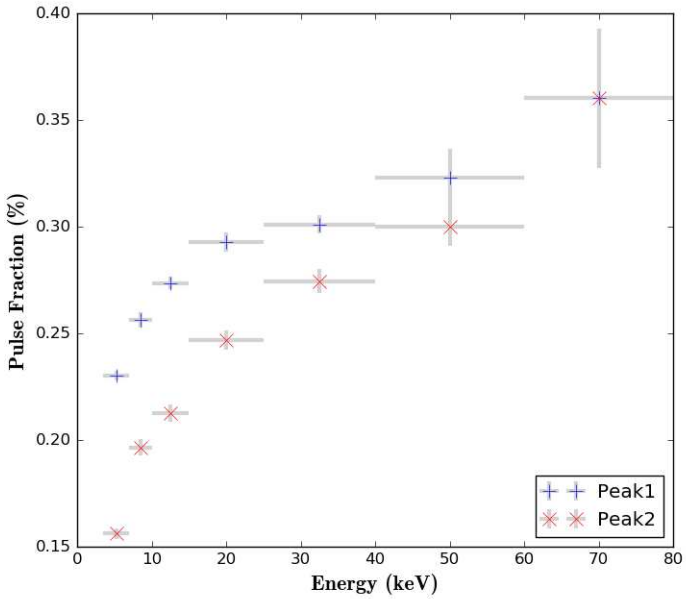

Fig. 4.5 The pulse fraction in two pulse peaks of Crab nebula pulse profile.

20 s. As this is a very bright source, we get very high count rates in LAXPC. Three detectors LXP10, LXP20 and LXP30 have an average count rate of 2812, 2649 and 2702 per sec respectively. The count rate is almost steady throughout this observation. A small dromp in count rate at $\sim$ 1400 seconds is related to change in satellite pointing. We searched for periodicity on the barycenter corrected light curve using the FTOOL `efsearch` and obtained a period of 0.033718641 $\pm$ 0.000000001 s. The light curve folded with this spin period obtained from this observation showed the signature pulse profile of this source in three detectors (See Figure 4.3). Pulse profile obtained from three detectors are identical with two narrow peaks separated by a bridge. The second peak is smaller in these pulse profiles created from full 3.0-80.0 keV data. There is also a broad minimum after the second peak. The first peak has a sharp rise and fall, whereas the second peak rises slowly but falls comparatively faster. The pulse profile of the Crab pulsar is known to vary with energy. So, we created the energy resolved pulse profile in 7 energy bands : 3.5-7.0 keV, 7.0-10 keV, 10.0-15.0 keV, 15.0-25.0 keV, 25.0-40.0 keV, 40.0-60.0 keV and 60.0-80.0 keV. Figure 4.4 shows the energy resolved pulse profiles with combined data from 3 detectors. Pulse profiles from the first six energy bands are created with 128 bins and in the last energy band with 64 bins. Pulsations are detected in all seven energy bands. The pulse shape is almost similar in all the energy bands except that the pulse amplitude seems to be increasing with energy. Both pulse peaks become almost comparable in the 60.0-80.0 keV band. The strength of pulse peaks is determined in terms of pulse fraction (PF = $\frac{I_{max}-I_{min}}{I_{max}+I_{min}}$). The pulse fraction of both peaks in all seven energy bands is shown in Figure 4.5. The Pulse Fraction in first peak increases from 23 % in 3.5-7.0 keV to 36 % in 60.0-80.0. The pulse fraction in the second peak is smaller than the first peak at lower energies shows a sharper increase with energy. Pulse fraction in this peak increases from 16 % in 3.5-7.0 keV to 36 % in 60.0-80.0 keV. The pulse fraction in both peaks is equal in 60.0-80.0 keV energy band.

For PSR B1509–58, a light curve from entire observation was extracted with the bins size of 1 ms. Barycenter correction was done of the light curve using tool `as1bary`[3] along with the online tool *AstroSat* orbit file generator[4]. The top panel in Figure 4.6 shows the light curves from the complete observation binned at 100s for LXP10. It contains sections of high and low count rate. Low count rate sections correspond to the time when the satellite is pointed at source but is occulted by the earth. We separated these two regions using time windows based on elevation criterion. The

[3]http://astrosat-ssc.iucaa.in/?q=data_and_analysis
[4]http://astrosat-ssc.iucaa.in:8080/orbitgen/

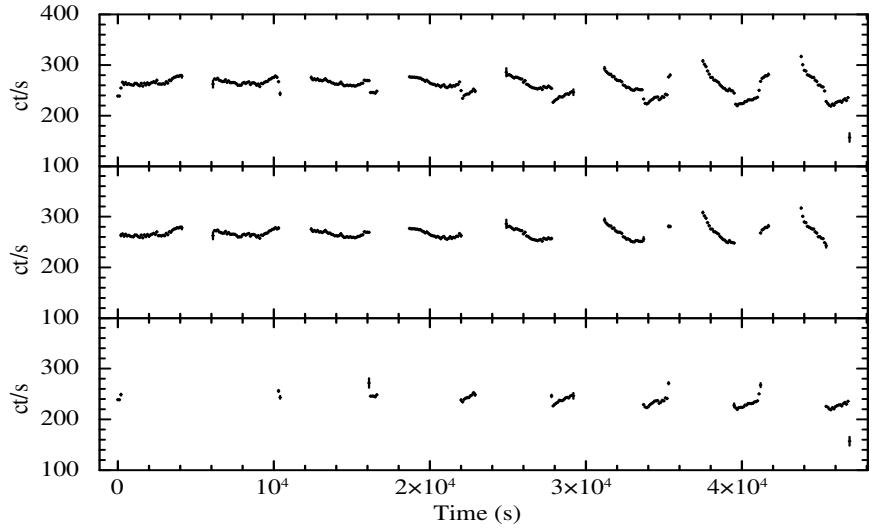

Fig. 4.6 Light curves of PSR B1509–58 from LXP10 binned with 100 s bin time. Full light curve (Top panel) has regions of high and low count rates due to strong background variations. The source and background light curves are shown separately in middle and bottom panels.

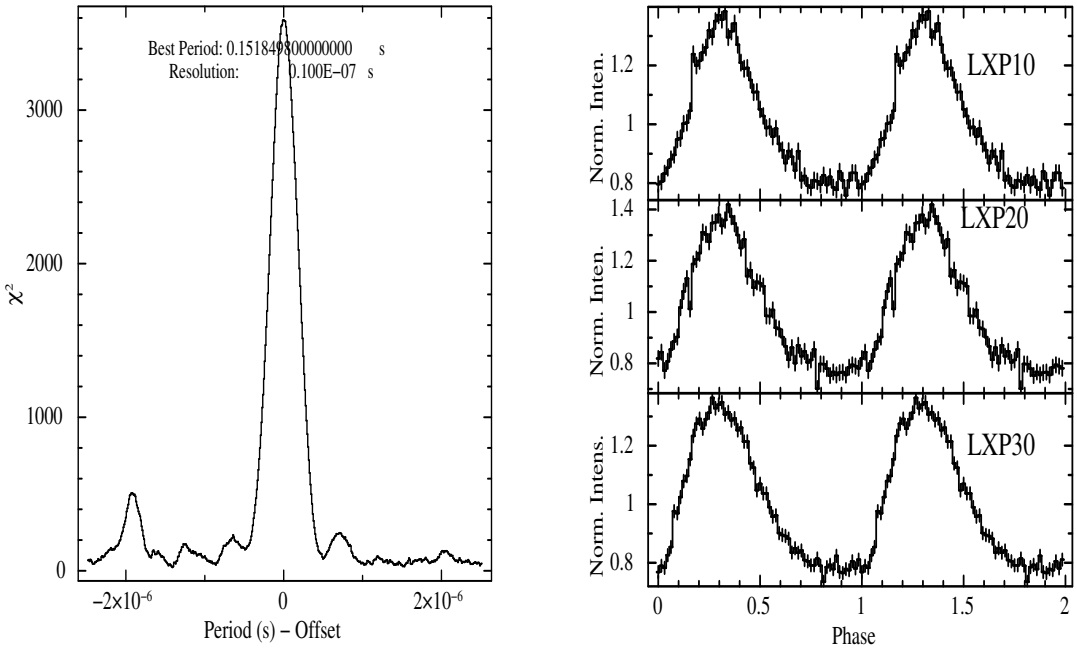

Fig. 4.7 Left: Period search results of PSR B1509–58 from LXP10 detector. The χ^2 obtained using different trial period is shown here. Right: Pulse profiles from 3 detectors LXP10 (top), LXP20 (middle), and LXP30 (bottom) in 3.0-80.0 keV.

Table 4.2 Channel ranges corresponding to 7 energy bands in different LAXPC detectors for all the sources in this chapter.

Energy Range	LXP10	LXP20	LXP30
(keV)			
3.5-7.0	25-55	27-51	24-53
7.0-10.0	56-81	52-72	54-80
10.0-15.0	82-124	73-106	81-122
15.0-25.0	125-208	107-173	123-205
25.0-40.0	209-327	174-240	206-323
40.0-60.0	328-475	241-387	324-467
60.0-80.0	475-611	388-497	468-597

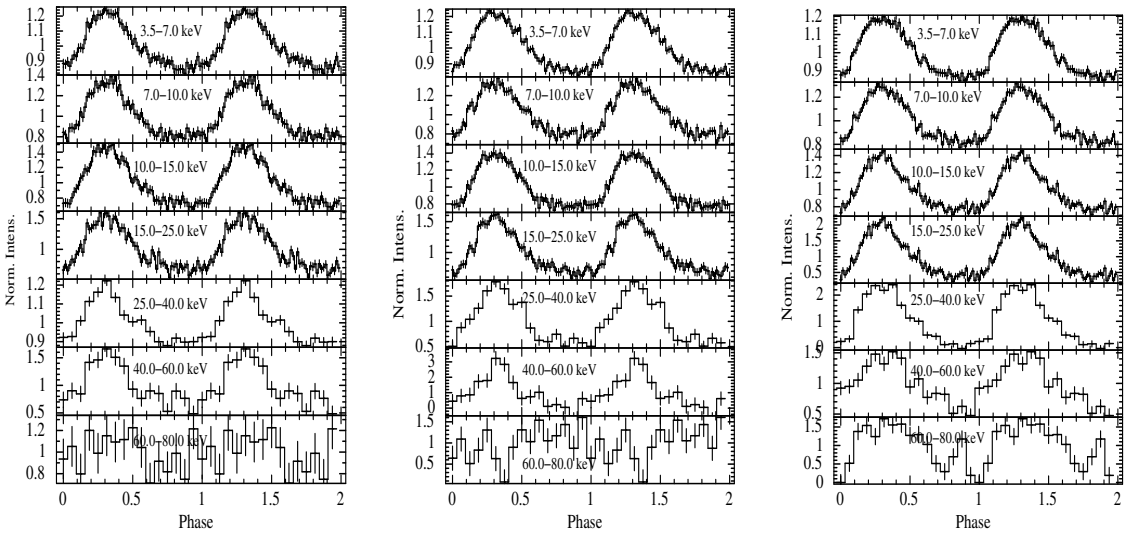

Fig. 4.8 Energy resolved pulse profiles of PSR B1509–58 from LXP10 (left), LXP20 (middle), and LXP30 (right) detectors in 7 energy bands. Pulse profiles in top 4 bands are created with 64 phase bins and in last 3 bands with 16 phase bins.

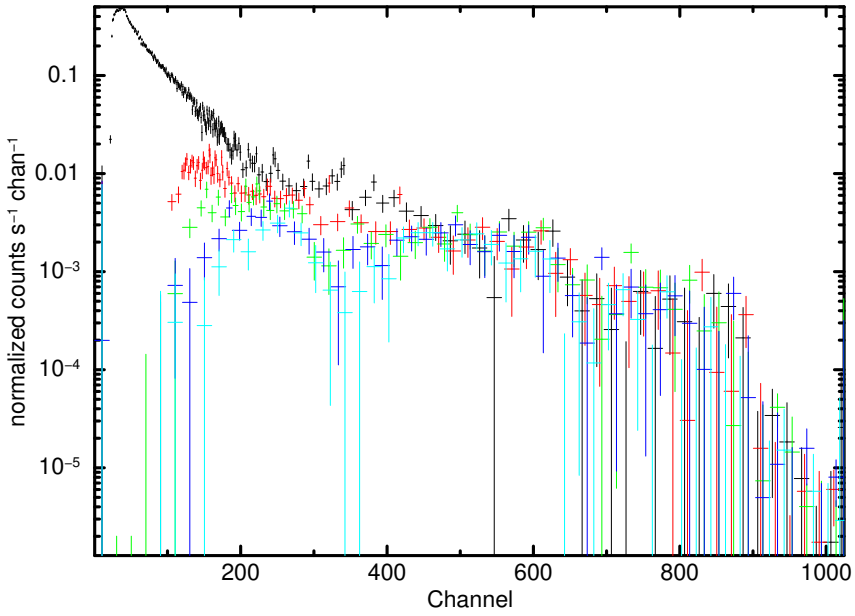

Fig. 4.9 Spectra of PSR B1509–58 by taking event from five different layers (Top(black), second (red), third (green), fourth (dark blue), fifth (light blue)).

clean source and earth occulted sections are shown in the middle and bottom panels of Figure 4.6. We searched for pulsations in the clean source light curve using FTOOL `efsearch` and obtained a period of 0.15184980 ± 0.00000035 s (See Figure 4.7). The pulse profile created using this spin period from the 3 LAXPC detectors in the energy band 3.0-80.0 keV are shown in Figure 4.7. The pulse profile from all three detectors show an identical broad single peak followed by a broad minimum. We also looked for pulsations in different energy bands as those defined for the Crab pulsars. The performance of three LAXPC detectors differs from each other depending upon their operating conditions. Different gains of three detectors leads to a different channel to energy conversion. For the selected energy bands the channel ranges are given the Table 4.2. Channel ranges for LXP10 and LXP30 are very similar in all the energy bands but they are very different for LXP20, especially after 15.0 keV. Pulse profile created from the 3 detectors using these channel ranges is shown in Figure 4.8. Pulsations are detected in all three up to 60.0 keV. There is a slight hint of detection of pulsation in LXP30 in 60.0-80.0 keV band. This might be due to gain variation in this detector during this observation. Due to which channel to energy conversion for this detector might not be accurate.

LAXPC detector has a large instrumental background due to is large size. For a bright source like Crab nebula this few percent of total count rate observed and does not affect the quality of data. On the other hand, the high background can affect

Table 4.3 Channel ranges for which source is detected in different layers.

First Layer	17-700
Second Layer	17-800
Third Layer	120-850
Fourth Layer	150-800
Fifth Layer	170-620

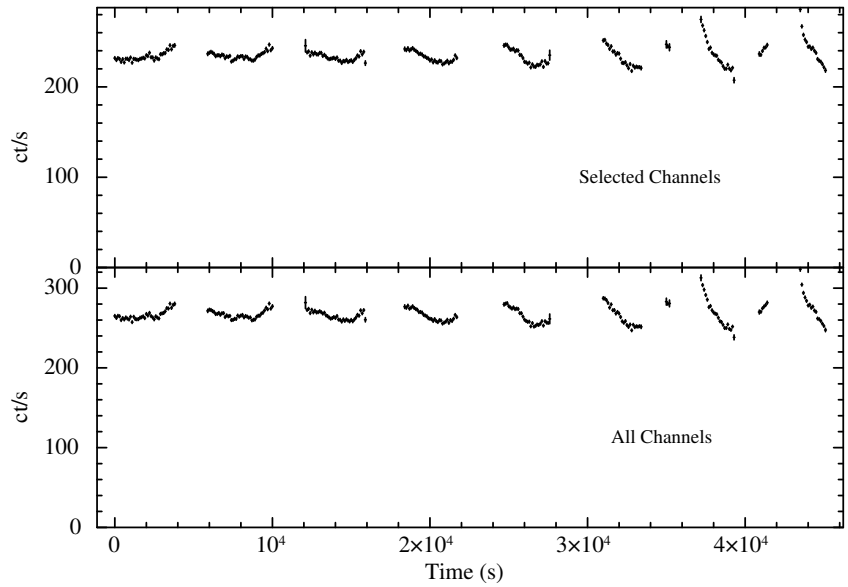

Fig. 4.10 Light curves of PSR B1509–58. Light curve in top panel is created by selecting data from channels with good data statistics and light curve in bottom panel is created using data from all channels of all layers.

the quality of data significantly for faint sources. For example, in the case of PSR B1509–58 the count rate in source sections is $\sim$ 260 of which $\sim$ 230 is attributed to the background. For such sources, one can use the layerwise construction of LAXPC to improve the data quality. For a faint source, events from all channel of all layers might not be useful. In such a case, user can create a layerwise spectrum and check which channels ranges have good statistics. A light curve extracted with such restricted channel range of layer will have a lower background. This will be very helpful for detecting pulsation from faint sources using LAXPC data. A layerwise spectrum from different layers is shown for PSR B1509–58 in Figure 4.9. Most of the photons are absorbed in the top layer. Subsequent layers receive gradually fewer photons. Channel ranges for which data has good quality is given in Table 4.3. A light curve created by selecting only these channel ranges from different layers of LXP10 is shown in Figure

Table 4.4 Spectral parameters of PSR B1509–58 using LXP10

Parameter	All Events	Single Events	Double Events	Single Events
	from all layers	from all layer	from all layers	from top layer
Photon index	1.9 ± 0.8	1.4 ± 0.2	1.9	1.2 ± 0.1
Norm[a]	6.5 ± 0.5	0.8 ± 0.3	0.4 ± 0.1	0.4 ± 0.1
$N_H^{b,c}$	3.3 ± 0.4	12.0 ± 3.8	—	4.0 ± 2.0

[a] $\times 10^{-2}$
[b] $\times 10^{22}$
[c] In Units of atoms cm^{-2}

4.10. For comparison, the original light curve from all channels of all layers is also shown. The count rate in the top light curve is smaller in comparison to the original light curve due to the reduction in background.

4.2.5 Spectral Analysis

The spectrum was created from all channels which cover energy range 3.0-80.0 keV energy band of LAXPC detectors. The source spectrum was generated using events which falls in phase range 0.0-0.7, which is the peak of pulse profile. The off pulse spectrum (phase range 0.7-1.0) is used as a background to the pulse spectrum. The response matrix was selected by finding the relative gains of detectors using a spectrum of K-florescence photons from double events. K-florescence spectra of 3 detectors from the *AstroSat* observation of PSR B1509–58 are shown in Figure 4.11. In case of a double event, the K-florescence can be detected either as first or the second event. Thus, we have two spectra for each detector. Each spectrum is fitted with a Gaussian to determine channel for energy corresponding to K-florescence photon (34 keV). The ratio of the average of two channels from two spectra with channel value gives the relative gain of the detector during the observation. This nominal value was determined by ground calibration of the instruments. The relative gain for LXP10 and LXP20 was found to be 1.0 during this observation. For LXP30, all the double events were not registered in the preset channel window fixed for these double events. The window is decided by gain variability allowed for normal operation of the detector. Thus, the gain of LXP30 cannot be calculated for this observation. For LXP20, the response matrices are not as well understood as for LXP10. Therefore, for the spectral analysis, only LXP10 was used.

We fitted the pulsed spectrum with the POWERLAW model of `XSPEC` (Dorman and Arnaud, 2001) in the energy range 4.0-25.0 keV. Absorption component PHABS

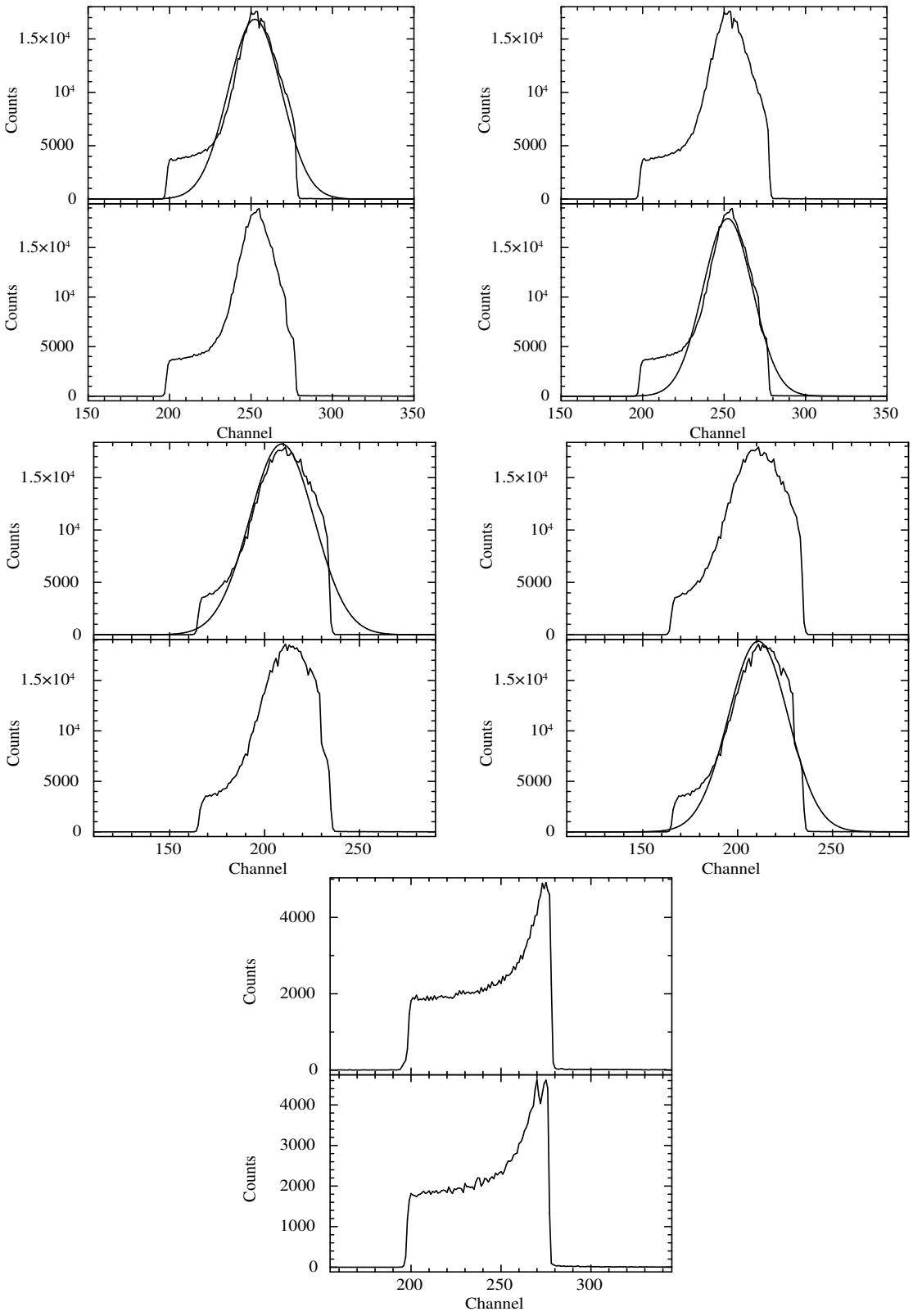

Fig. 4.11 K-events spectra from 3 LAXPC detectors in PSR B1509–58 observation. LXP10 (top left and right) and LXP20 (middle left and right) spectra are fitted with a Gaussian to determine mean channel value. LXP30 (bottom) spectrum is not suitable for fit.

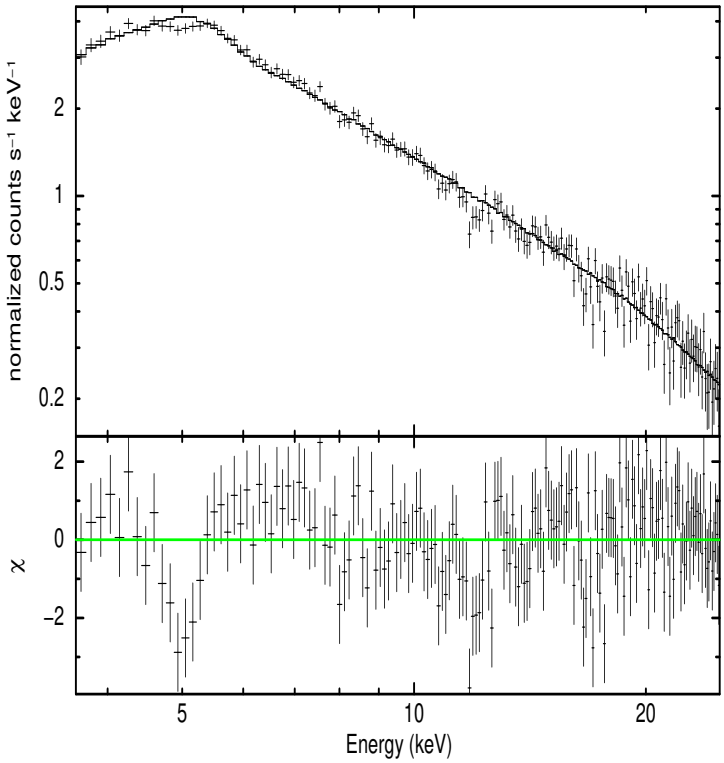

Fig. 4.12 Pulsed spectrum of PSR B1509–58 from all events in all layers data of LXP10 detector.

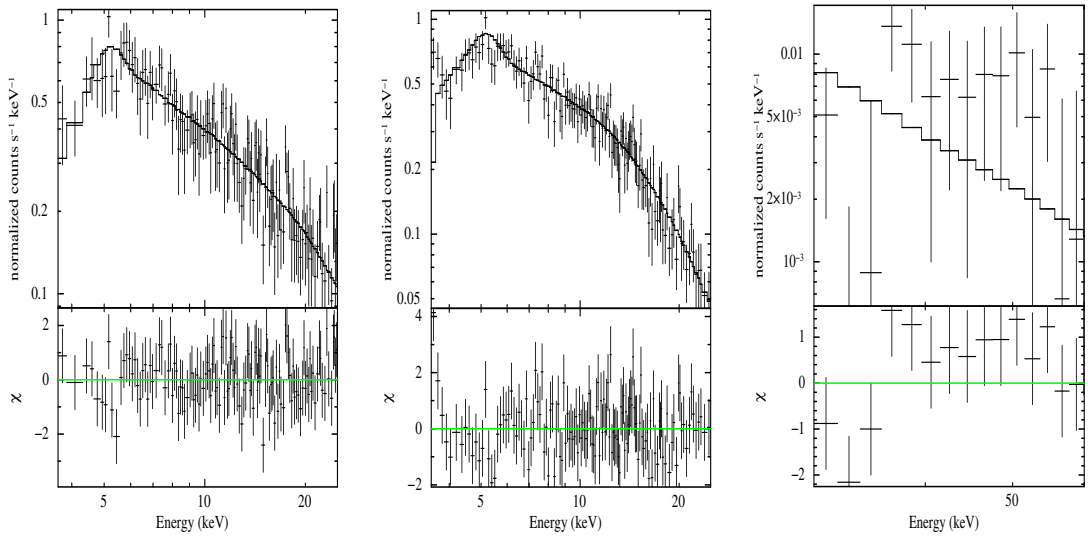

Fig. 4.13 Different types of spectra of PSR B1509–58 created by selecting different types of events from different layers: single events from all layers (left), events from top layers (middle) and double events from all layers.

was multiplied to account for the absorption by the interstellar medium. The combined absorbed POWERLAW model fits well to this data with χ^2 close to one. However there is an absorption feature ~ 5 keV, which is not explained. Data and fitted model are shown in Figure 4.12. LAXPC detector is divided into five layers. Data extraction software allows for selecting events in different layers separately. It is also possible to extract the spectrum of single events or double events. Three more types of pulsed spectrum were extracted for this observation: 1. Single events from all layers 2. Events from top two layers and 3. Double events from the all layers. The spectrum of events in off pulse (phase range 0.7-1.0) is used as background to the spectrum of events in pulse peak (phase range 0.0-0.7). We fitted all these spectra with the same model as in case of spectrum from all events from all layers. Data and fitted model are shown in Figure 4.13 and parameter values are given in Table 4.4. Data quality of spectrum from double events is not good but It is shown here for illustration of different types spectrum possible with LAXPC. The photon index, Γ values are consistent from all types of spectra. The errors are larger in the value obtained from full data. Γ is better constrained in spectra of only single events from all layers. It is even better in spectra from the top layers. It is not possible to constrain the value of Γ in double event spectrum and was fixed at the value obtained with the spectrum of complete data. Normalization in the different spectra is different types of spectra. The value of column density matches within error in the spectrum of all events from all layers with single events from only top layers. The value obtained from the spectrum of single events from all layers is comparatively larger.

4.3 *AstroSat* Observation Of Magnetars

Magnetar is a type of neutron star whose main source of energy is the decay of the magnetic field, instead of rotation or accretion. Historically, magnetars were thought to be two different classes of astrophysical sources: soft Γ-ray repeaters (SGRs) and anomalous X-ray pulsars (AXPs). SGRs were initially mistaken to be a subclass of Γ-ray bursts due to their non-association with any known sources and peculiar softer spectrum. AXPs were initially identified as persistent pulsars in soft X-ray range ($<$ 10 keV) but their other properties such as narrow period distribution, long term spin-down trends, soft X-ray spectrum, did not agree with either X-ray binary pulsars or rotation powered pulsars (Mereghetti and Stella, 1995). There are strong indications that these two are a single class of objects. The surface magnetic fields of magnetars is typically 10^{13}-10^{15} G and their interior magnetic fields might be even stronger.

Magnetars are the most variable sources among different classes of isolated neutron stars. Their emission is characterized by powerful short bursts and giant flares. Some magnetars are persistent sources with typical luminosity $\sim 10^{35}$ erg s^{-1} and some are transient with their luminosity ranging from $\sim 10^{32}$-10^{36} erg s^{-1}. Their pulse periods are in the range 2-12 s which are secularly increasing with $\dot{P} \sim 10^{-13}$-10^{-10} s s^{-1}. At present, there are 24 magnetars known in our galaxy and one each in two Magellanic Clouds (Olausen and Kaspi, 2014a,b). The model which suggests that these object are powered by magnetic fields decay was given in 1992 (Duncan and Thompson, 1992). This model provides the best explanation of the observational properties of magnetars. An alternative model is that the isolated neutron star is being powered from the fall-back disk formed after the supernova explosion (Alpar et al., 2001; Trümper et al., 2010). This model requires some additional process, besides accretion, to explain the powerful bursts and flares observed from these sources.

1E 2259+586 is one of the most studied magnetars to date, which played a key role in the unification of anomalous X-ray pulsar (AXP) with high magnetic fields. It is located near the center of supernova remnant CTR 109, which is known for its half-shell morphology. The 1E 2259+586/CTB 109 was identified as a diffuse X-ray source by *Einstein* satellite in 1980 (Gregory and Fahlman, 1980). X-ray pulsations with P = 6.98 s were discovered in 1983 (Fahlman and Gregory, 1983). The estimated dipolar magnetic field of 1E 2259+586 is B = 5.9 $\times$ 10^{13} G (Dib and Kaspi, 2014), which is toward the lower end of the typical range of magnetic fields of magnetars. The estimated distance and age are 3.2 $\pm$ 0.2 kpc and 10^4 yr (Kothes and Foster, 2012). The emission from the source is mostly constant except sudden giant bursts, which are thought to be associated with its magnetic reconfiguration. One such burst was observed in 2002 by *RXTE*. During this burst, almost all the aspect of the emission changed drastically: the pulsed and persistent flux, shape and pulse fraction of pulse profile and spectral properties (Kaspi et al., 2003; Woods et al., 2004). During the burst in 2002, a glitch was also observed. Furthermore, 80 X-ray bursts were detected during the 14.4 ks *RXTE* observation with durations ranging from 2 ms to 3 s. A second glitch was observed in 2007 (Dib et al., 2008). In contrast to glitches, a radiatively quiet anti-glitch was observed in 2012 (Archibald et al., 2013). Pulse profile of 1E 2259+586 has double-peaked morphology with one shallow and one deep minimum. The double-peaked morphology changes with increasing energy (Kuiper et al., 2006). The dominant peak at energies $\leq$ 4 keV becomes smaller with energy. In 4.0-8.3 keV both peaks are comparable. The second peak becomes dominant above 8 keV.

NuSTAR observation in 2016 has shown that pulsation are detected in 24.0-79.0 keV (Vogel et al., 2014). Also, one of the peak was found to be shifting phase with energy.

1E 1048.1-593 was discovered serendipitously as pulsar by *Einstein* observations of the Carina nebula in 1979. It has a spin period of 6.46 s and a spin-down rate of $\sim 1.5 \times 10^{-11}$ s s^{-11} (Seward et al., 1986). The pulsations are detected up to 8 keV with a single broad pulse profile (Paul et al., 2000). A recent *NuSTAR* observation found pulsation up to 20 keV with a transient secondary peak between 7-20 keV (Yang et al., 2016). Its inferred magnetic field strength is $B = 4 \times 10^{14}$ G. It is a relatively active source which shows X-ray bursts and unstable timing behavior. It was the first AXP to show SGR-like bursts and hence indicated that two classes are possibly a single class. This source showed four long periods of activity with outbursts and bursts in 2001, 2002 and 2007, and 2011 (Archibald et al., 2015; Dib and Kaspi, 2014). The first flux outburst was accompanied by SGR-like burst. Large variation of spin-down rate was seen during the last three flux outbursts. The spectrum of 1E 1048.1-593 is well described by with blackbody plus powerlaw having kT $\sim$ 0.6 keV and $\Gamma \sim 2.9$ (Paul et al., 2000; Tam et al., 2008). During the bursts, a possible emission feature has been reported at $\sim$ 13 keV in the spectrum. Its distance is estimated to be 9 kpc (Durant and van Kerkwijk, 2006). The source lies at a low Galactic latitude, resulting in a significant absorption in soft X-rays ($N_H \sim 10^{22}$ cm^{-2}).

4.3.1 Observations

Magnetar 1E 2259+586 was observed on the 10th of October 2016 for 13 *AstroSat* orbits using the LAXPC instrument. We have $\sim$ 64 ks on source data from this observation. The other magnetar 1E 1048.1-593 was observed on 13th of January 2017 for 14 *AstroSat* orbits using the LAXPC instrument. Both these observations were carried out during the guaranteed time cycle of *AstroSat*. More details of the observations are given in Table 4.1. We here present the timing results of these observations. The data from the event analysis mode were used. Raw data files were reduced with Level1 to Level2 data processing guide[5] version 1. Level2 products were used to create light curves and spectral files. Further timing and spectral analysis were done using tools in HEASOFT software suite, version 6.19. Time intervals when the source is occulted by the earth and satellite is passing through South Atlantic Anomaly (SAA) region have been removed for the creation of light curve and spectral file.

[5]http://www.rri.res.in/~rripoc/POC.html

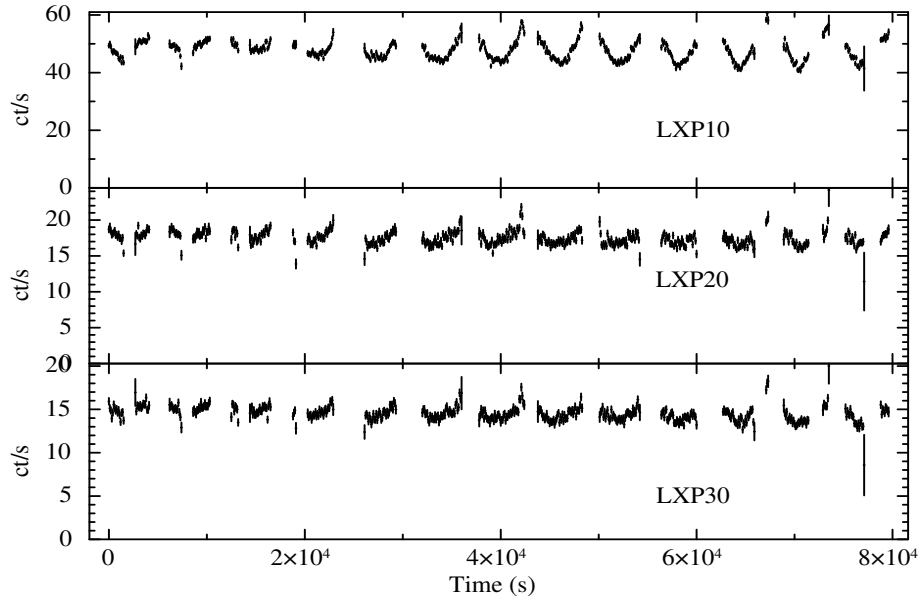

Fig. 4.14 Light curves from LXP10 (top panel), LXP20 (middle panel), and LXP30 (bottom panel) detectors for observation of magnetar 1E 2259+586. Data from only top layers in channel range corresponding to 3.0-12.0 keV was used.

4.3.2 Timing Analysis

These magnetars are very faint sources in high energy and most of the source photons are absorbed in top layers of LAXPC instrument. The spin periods of the pulsar in both sources is $\sim$ 7 s. Therefore we extracted light curves from channel 20-100 of top layers with bin time of 1s. This channel range corresponds to energy range 3.0-12.0 keV. Data from the other layers were mostly background dominated. Figure 4.14 shows the light curves 1E 2259+586 from 3 LAXPC detectors binned at 100s for LXP10, LXP20, and LXP30 with average count rates 47, 18 and 15 ct/s respectively. We searched for pulsations using FTOOL `efsearch`. Figure 4.15 shows the χ^2 plot of a series of trial period using the LXP10 light curve. We found the best period of 6.9797 ± 0.0002 s from all three detectors. Pulse profiles created using this spin period from 3 LAXPC detectors is shown in Figure 4.15. Pulse profile shows two broad peaks of comparable amplitude. There is a shallow minimum between the peaks and a deep minimum after the second peak. We searched for pulsations in energy-resolved light curves in two energy bands: 3.5-7.0 keV and 7.0-10.0 keV. Pulse profiles in the two energy bands are shown in Figure 4.16. Pulsations are detected only in the 3.5-7.0 keV energy band.

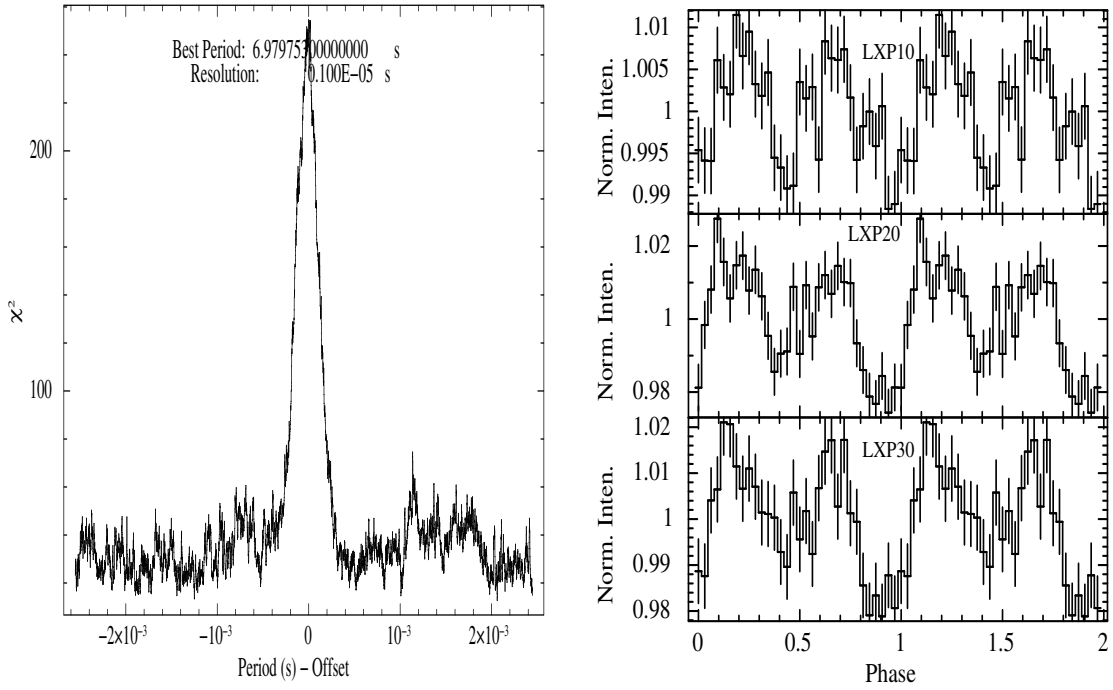

Fig. 4.15 Left: χ^2 for a series of trial periods for 1E 2259+586, obtained from the combined light curve of data from 3 LAXPC detectors. Right: Pulse profile from LXP10 (top), LXP20 (middle), and LXP30 (bottom).

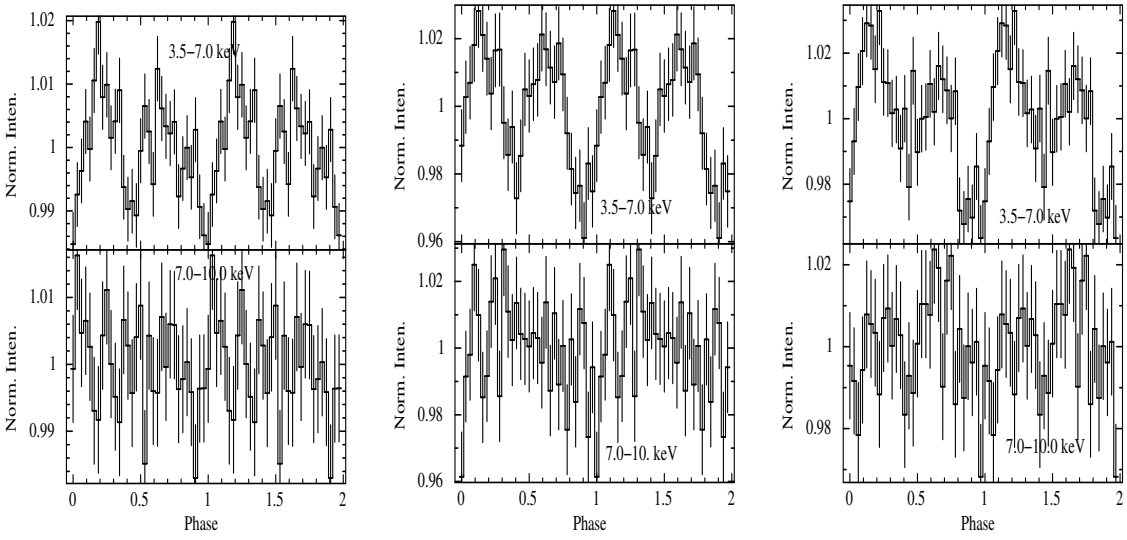

Fig. 4.16 Energy resolved pulse profiles of 1E 2259+586 from LXP10 (left), LXP20 (middle) and LXP30 (right). In each panel, two energy bands are 3.5-7.0 and 7.0-10.0 keV (upper and lower).

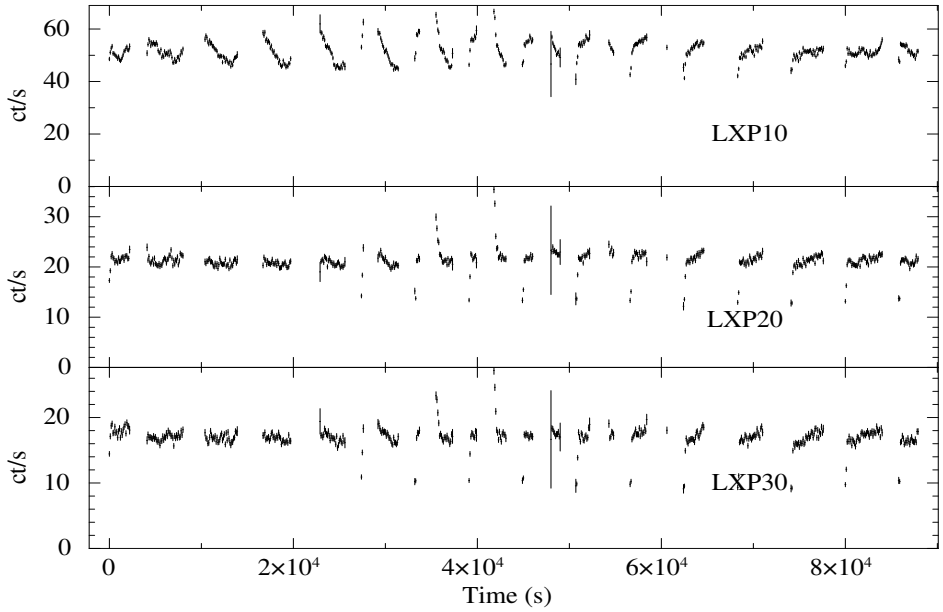

Fig. 4.17 Light curves from LXP10 (top panel), LXP20 (middle panel), and LXP30 (bottom panel) detectors for observation of magnetar 1E 1048.1-593. Data from only top layers in channel range corresponding to 3.0-12.0 keV was used.

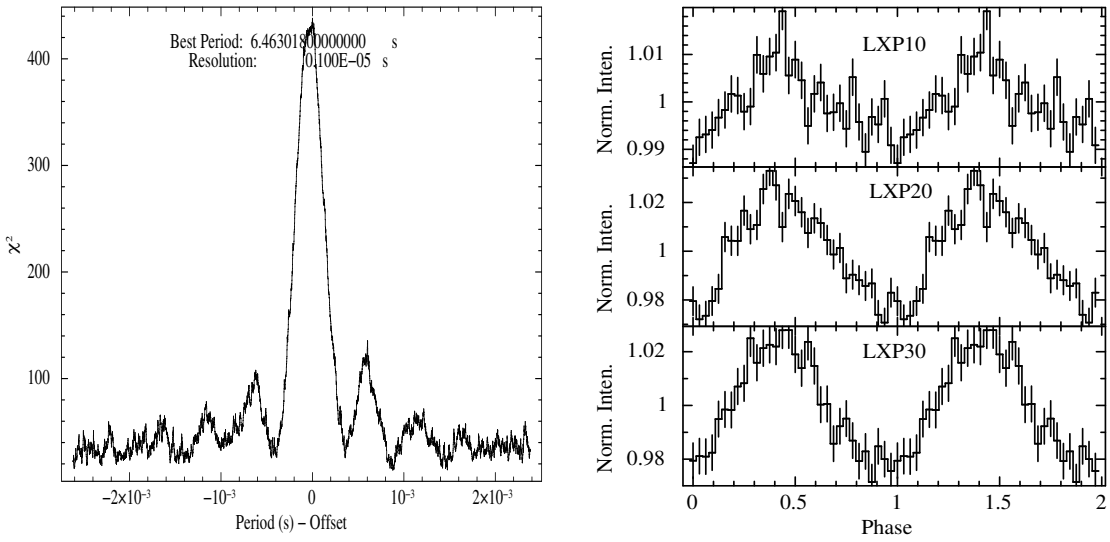

Fig. 4.18 Left: χ^2 for a series of trial periods for 1E 1048.1-593, obtained from the combined light curve of data from 3 LAXPC detectors. Right: Pulse profile from LXP10 (top), LXP20 (middle), and LXP30 (bottom).

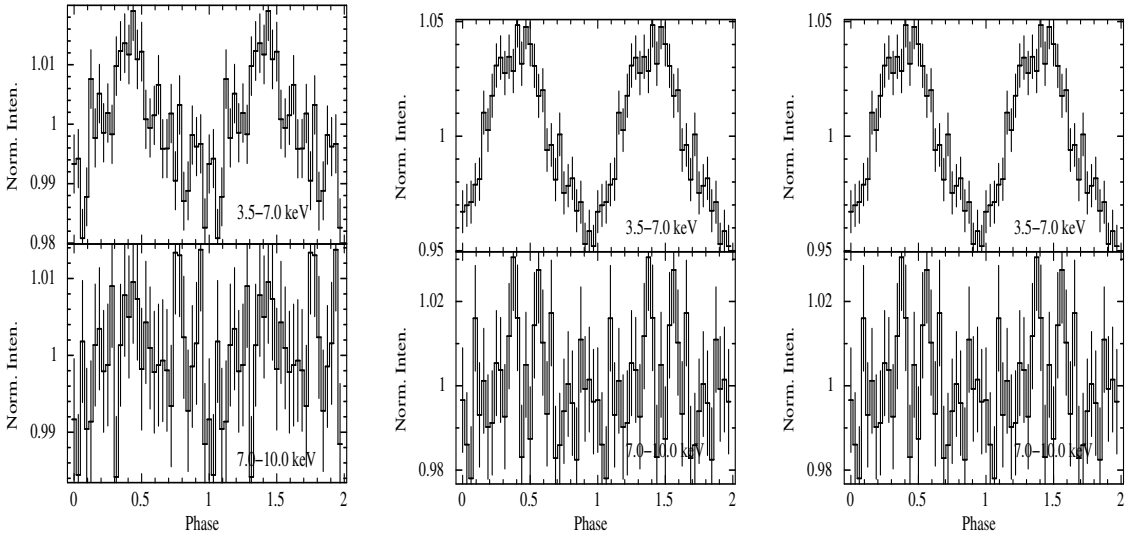

Fig. 4.19 Energy resolved pulse profiles from LXP10 (left), LXP20 (middle) and LXP30 (right) of 1E 1048.1-593. In each panel, two energy bands are 3.5-7.0 and 7.0-10.0 keV (upper and lower).

Light curve from 1E 1048.1-593 from 3 LAXPC detectors with a 100 s time bin for LXP10, LXP20, LXP30 are shown in Figure 4.17. Average count rates from the light curve are 51, 22 and 17 ct/s. We searched for pulsations using FTOOL `efsearch`. Figure 4.18 shows the best period of 6.46301 ± 0.00006 s in the plot of χ^2 for different period values. We folded the light curve from three detectors with the best period using FTOOL `efold`. Pulse profiles from LXP10, LXP20, and LXP30 are shown in Figure 4.18. Pulse profiles consist of a brood single peak followed by a narrow minimum. We created energy-resolved light curve in two energy bands: 3.5-7.0 keV and 7.0 10.0 keV. Pulsations are only detected in the lower energy band 3.5-7.0 keV (see Figure 4.19).

4.4 Summary

In this chapter, we have presented the timing and spectroscopy results of four isolated neutron stars from *AstroSat*-LAXPC observations done during performance verification and guaranteed time cycles of observation. LAXPC has excellent timing capability and moderate spectral resolution. The main aim of the study of these sources was to prove the capability of this instrument for such sources. These are early results on timing and spectroscopy of isolated neutron stars. Techniques developed for studying these sources can be useful for more detailed observations of faint sources.

The Crab pulsar (PSR B0531+21) is one of the best studied astronomical sources across the electromagnetic band. For the Crab pulsar we created pulse profile using data from full band and energy-resolved pulse profiles in 7 energy bands. The *AstroSat* observation shows the clear detection of pulsation up to 80 keV. We found that the all the pulse profiles in different energy bands show two peaks with non zero flux region in between which is named as the bridge. The pulse fraction of both peaks show energy dependent variation. The trend of pulse fraction in both peaks is the same but the change in second peak is sharper. The energy dependent behavior of two pulse peak has been studied across the electromagnetic magnetic band. In the radio and optical bands the first peak is more prominent (Oosterbroek et al., 2008). The pulse fraction in the second peak increases in the soft X-ray band (Mukerjee et al., 1999) and becomes more than the primary peak in the soft γ-ray band (Mineo et al., 2006). In the γ-ray band the first peak again becomes dominant (Kuiper et al., 2001). The *AstroSat* observation further extends this trend up to 80 keV.

We have reported on the energy-resolved pulse profiles and pulsed spectrum of PSR B1509–58. The *AstroSat* observation shows that the pulsations are detected up to 60 keV. Pulse profile consists of a single peak in all the energy bands. Pulse profile in this source has a single peak below $\sim$ 50 keV and an additional feature at higher energy (Marsden et al., 1997). We do not see any new feature in 40.0-60.0 keV energy band. We have not reported on pulse fraction in different energy bands due to large uncertainty in the background during these observations. The pulsed spectrum of PSR B1509–58 is well described by the POWERLAW model multiplied by absorption component.

For both the magnetars, pulsations were not detected using the data of all layers. However, the pulsations were detected from the light curve extracted from top layers in 3.0-12.0 keV band. In the energy resolved analysis pulsation are detected only up to 7.0 keV. For both the magnetars, the X-ray pulse profiles obtained with LAXPC light curves are similar to the known pulse profiles of these two sources in the same energy bands.

Chapter 5

A Hydrogen Like Iron Line in HMXB Pulsar IGR J16320-4751 and Pulse Phase Dependence of Its Neutral Iron Emission Line [1].

5.1 Introduction

Pulse profiles of neutron stars tell us about the emission processes and beaming mechanism. Pulses from neutron star in X-ray binary system are advanced or delayed according to the position of neutron star in its orbit. Using this fact we can determine orbits of neutron stars in binaries. The measurement of binary orbits have contributed much to our understanding of binary stellar evolution, mass transfer mechanism, masses and radii of mass losing supergiants, shape of orbit, and other related astrophysical phenomenon. Most of the transient X-ray pulsars are also Be X-ray binaries which have much wide orbits, and hence it is more difficult to derive their orbital parameters. There are about 300 (Liu et al., 2006, 2007) known X-ray binaries of which complete set of parameters is known for only few systems. For X-ray binaries of known orbital period hosting an X-ray pulsar, the orbital parameters can be determined accurately with the pulse arrival delays method. Applicability of this method requires pulse profile to be stable. Most HMXB pulsars show stable pulse profile from observations with significant number of pulses. However pulse profile can change due to sudden change in luminosity. Long term time variability is also seen in HMXB sources. Some pulsars

[1] This work has been done in collaboration with Nirmal Iyer and Biswajit Paul

also show significant variations between subsequent pulses (Kretschmar et al., 2014; Staubert et al., 1980).

Iron emission lines have been found in spectra of large number of HMXB's and proven to be a useful tool to study stellar wind properties in these systems. Fe Kα and Fe Kβ lines from neutral or relatively low-ionized iron and He-like, H-like lines of Fe have been found in many HMXBs (Aftab and Paul, 2017; Pradhan et al., 2018; Torrejón et al., 2010). For HMXBs the most common site of fluorescence is the stellar wind from the massive companion. An X-ray-irradiated stellar wind is expected to form an onion-like structure of different ionization degrees (McCray et al., 1984). For optically thin gas case (Kallman and McCray, 1982), the zone dominated by He-like and H-like ions iron are formed in the inner region with ionization parameter being around $\log \zeta = 3.0$ and 3.5 respectively.

IGR J16320-4751 was detected with INTEGRAL in 2003 (Tomsick et al., 2003) and identified with the ASCA source AXJ1631.9-4751 detected in 1994 (Sugizaki et al., 2001). It is an HMXB consisting of a neutron star and an O8I companion star (Chaty et al., 2008). It shows periodic intensity modulation at 8.96 days, which is considered to be its orbital period (Corbet et al., 2005), and pulsation at a period of ∼1300 s (Lutovinov et al., 2005). It is located at a distance of ∼3.5 kpc and has an average X-ray luminosity of 3×10^{35} ergs s^{-1} (Lutovinov et al., 2013) in 17-60 keV energy band. Other than orbital modulation, light curves of IGR J16320-4751 show variability at various time scales, from seconds-minutes (Rodriguez et al., 2003) to days-months (Foschini et al., 2004). The pulse fraction is found to be constant with energy in the *XMM-Newton* and *INTEGRAL* energy bands (Rodriguez et al., 2006). The X-ray spectrum of this source is similar to other highly absorbed HMXBs, consisting of a power-law, a prominent iron emission lines along with large absorption column ($N_H \simeq 2 - 5 \times 10^{23} cm^{-2}$). In-spite of large column density, the X-ray spectrum also shows a soft excess below ∼3 keV, which can be best explained with a black body of temperature ∼0.07 keV (Rodriguez et al., 2006). The absorption (N_H) and line emission (EW of Fe K_α) are correlated with each other, as expected from a system with the absorbing material also yielding fluorescence lines (Giménez-García et al., 2015).

We have investigated timing and spectral properties of IGR J16320-4751, using many observations made with *XMM-Newton* and Rossi X-ray Timing Explorer (RXTE). Specifically, we investigated the pulse profile variations with both observations and line

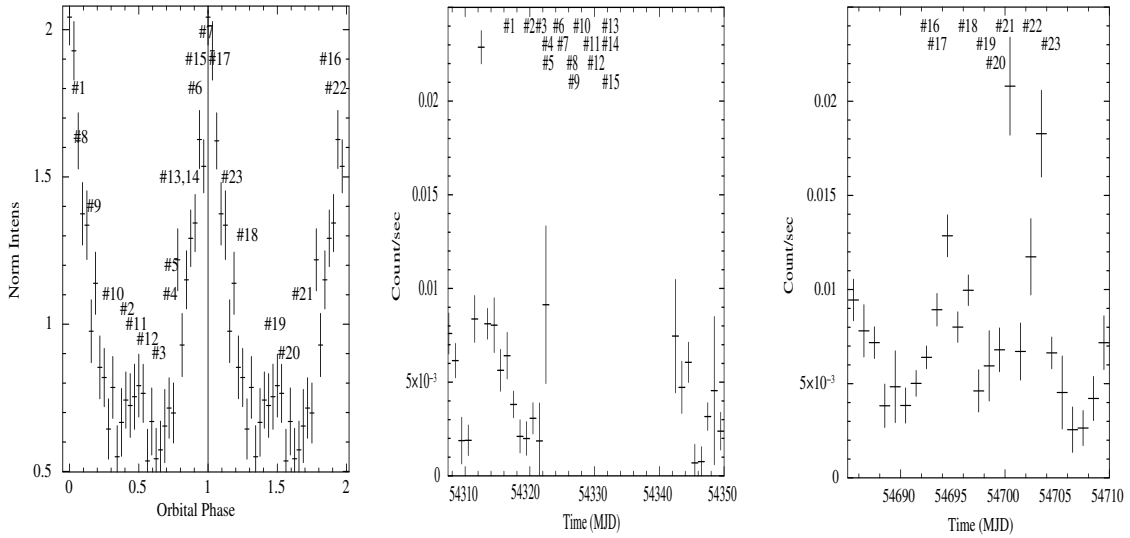

Fig. 5.1 Swift-BAT long term light curve of IGR J16320-4751 folded at orbital period of 8.99 days and epoch as 53417.34 (MJD). Orbital phase of all *RXTE* and *XMM-Newton* observations are indicated on orbital profile in first and second cycle respectively. Marking of observations from *RXTE* and *XMM-Newton* is for visual illustration. Actual observations from *RXTE* and *XMM-Newton* are done almost one year apart. Panels in middle and right shows actual BAT light curve for duration when *RXTE* and *XMM-Newton* observation were done. Start time for Swift-BAT light curves in middle and right panel is at orbital phase zero.

emission features using *XMM-Newton* data. We give details of the instruments and observations used in §5.2. Timing, spectral data reduction and analysis steps are given in §5.3. Finally, we present our results followed by a discussion of these findings in §5.4.

5.2 Observations

We used archival data from *XMM-Newton* and *RXTE* observations of IGR J16320-4751 for our work. IGR J16320-4751 was observed 8 times with XMM-Newton during 14-26 August 2008. Details of these observation details are given in Table 5.1. Observations were of different durations, from 2.2-12.3 ks. These observations have been carried out at different orbital phases, thus giving a fair coverage of one binary orbit. We have used all of these XMM-Newton archival observation for our analysis.

IGR J16320-4751 was observed 15 times with RXTE-PCA during 5-13 August 2007. More information is given in Table 5.1. This set of observations are also made

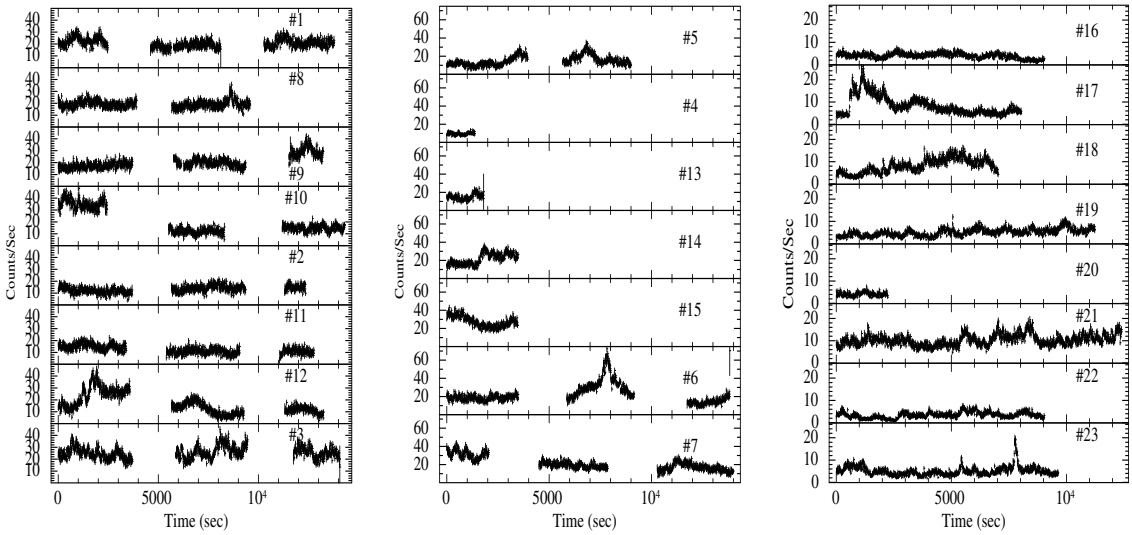

Fig. 5.2 This figure shows light curves from all *RXTE* and *XMM-Newton* data plotted with a time bin of 10.0 s. Time axis has been rescaled to start from zero for all observations. Left and Middle panel shows figure from *RXTE*observations. Right panel shows light curves from *XMM-Newton* observations.

at different orbital phase values covering almost entire orbit. We have analyzed these archival observations of IGR J16320-4751 taken from RXTE-PCA. On an average three PCUs were ON for the observations.

We have used Swift-BAT long term light curve for IGR J16320-4751 for a total ∼12 years (14-02-2005 to 13-12-2016). We searched for periodicity in this light curve and determined a period of 8.99 ± 0.02 days which is agreement with orbital period (8.96 ± 0.1) days of this source earlier reported (Corbet et al., 2005). Orbital profile created with Swift-Bat is shown in Figure 5.1. It is interesting to note that although the source is not an eclipsing HMXB system, it shows very strong orbital intensity modulation. Combining data from *XMM-Newton* and *RXTE* gives us full orbital coverage of this source twice.

5.3 Analysis and Results

5.3.1 Timing

5.3.1.1 *XMM-Newton*Timing

In order to analyze timing features of the *XMM-Newton* EPIC PN data, we took standard event files to extract light curves from a circular region of radius $1'$ centered

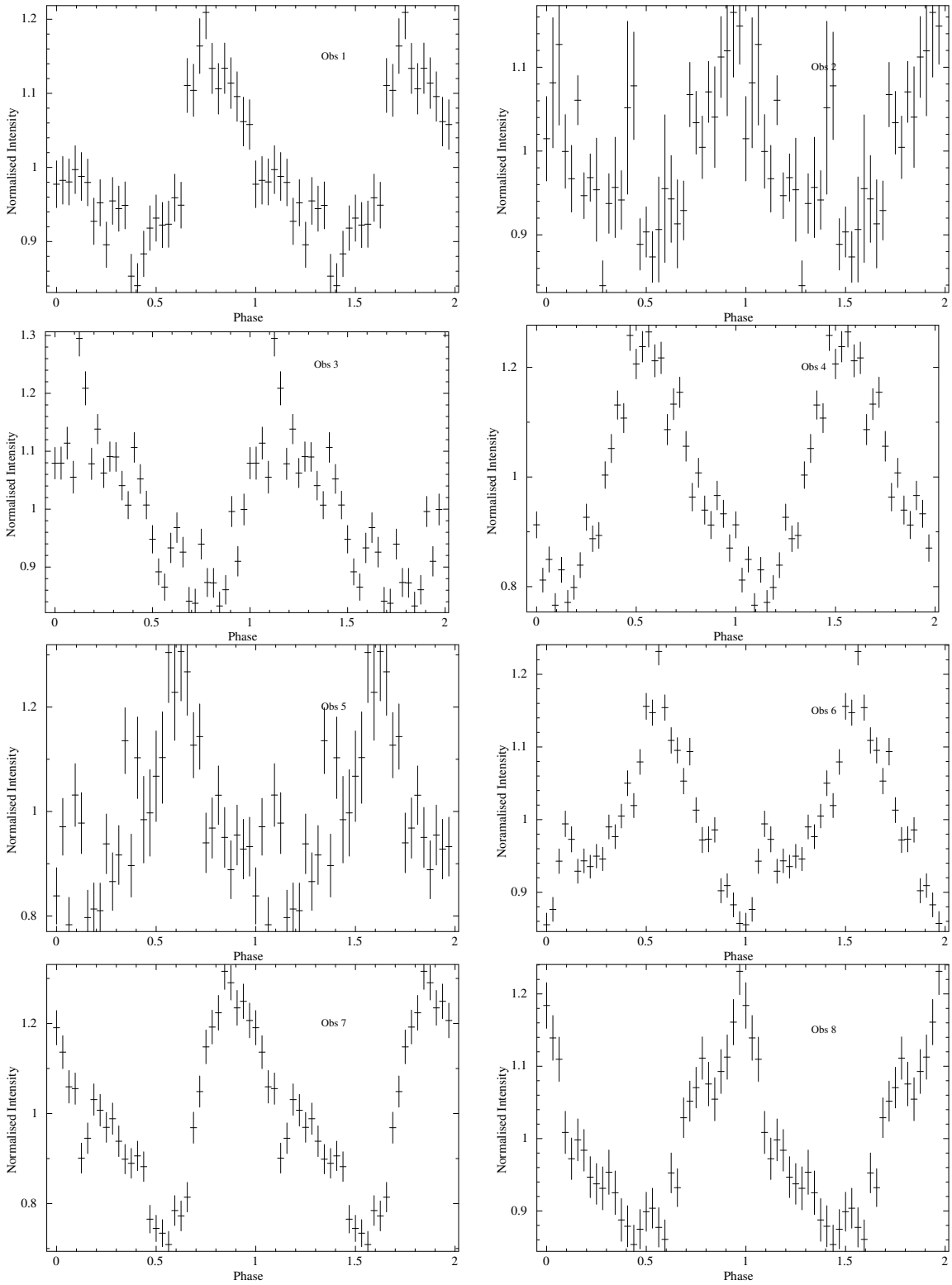

Fig. 5.3 Pulse profile obtained from 8 observations of *XMM-Newton*. All the observations shows a single and narrow peak in pulse profile. Same epoch has been used for creating these pulse profiles and a gradual phase shift can be seen between different observations.

on the position of the source. The analysis of *XMM-Newton* data was done using XMM Science Analysis System (`SAS` version 15.0). Light curves were barycenter corrected using `SAS` tool `barycen`. Figure 5.2 shows all XMM-Newton light curves with 10 s binning. From a visual inspection of these light curves we notice the presence of pulsations at ∼1000 sec in all observations. During two of the observations, obs 2 and 8 in Table 5.1, the source showed flares. We observed that flares affect the shape of the pulse profile and the results of our pulse profile analysis. So we removed these sections from light curves before creating pulse profiles.

We searched for periodicity in each *XMM-Newton* observation using the tool `efsearch`. This gave us a most probable period value of 1305.9 seconds, which was obtained by using data combined from three observations made on two consecutive days, viz. obsids 4, 5 and 6. Pulse profiles were created from each observation in energy band 0.2-10 keV using this most probable period and a reference epoch at 54692.0 (MJD), with the tool `efold`. All pulse profiles (created with 32 phasebins) are shown in Figure 5.3. We note that the pulse profiles show a narrow single peaked feature. One of the pulse profiles (observation 6 in Table 5.1) also shows a small inter pulse.

5.3.1.2 RXTE Timing

For RXTE-PCA data we took the standard products available for light curve, rebinned them with 10 sec and applied barycenter correction to it using tool faxbary. All 15 RXTE-PCA light curves are shown in Figure 5.2. We searched for pulsations in these data and created pulse profiles with the most probable period of 1311.8 seconds (obtained from observation 9) using epoch at 53417 (MJD). Pulse profile created with *RXTE* data in energy band 2.0-30.0 keV show large variation in pulse shape as shown in Figure 5.4. Also these pulse profiles are very different qualitatively than those obtained with *XMM-Newton* data. Pulse profiles in *RXTE* data show much broader pulse peaks compared to *XMM-Newton* pulse profiles. Some of *RXTE* data pulse profiles even have two peaks. For finding pulse arrival lags/delays by correlation method it is important that all the pulse profiles are similar. As *RXTE* data pulse profiles are different among themselves as well as they differ from *XMM-Newton* data pulse profiles, this data is not useful to find orbital solution.

RXTE PCA is a non-imaging instrument with a 1° circular field of view (FOV) and the light curve might be contaminated due to presence of some other X-ray sources in this crowded field. In order to investigate this issue we have examined the INTEGRAL image with radius 1° around IGR J16320-4751. We found that there is one more source (named IGR J16318-4848) in this image which is 4.14′ away. We have compared

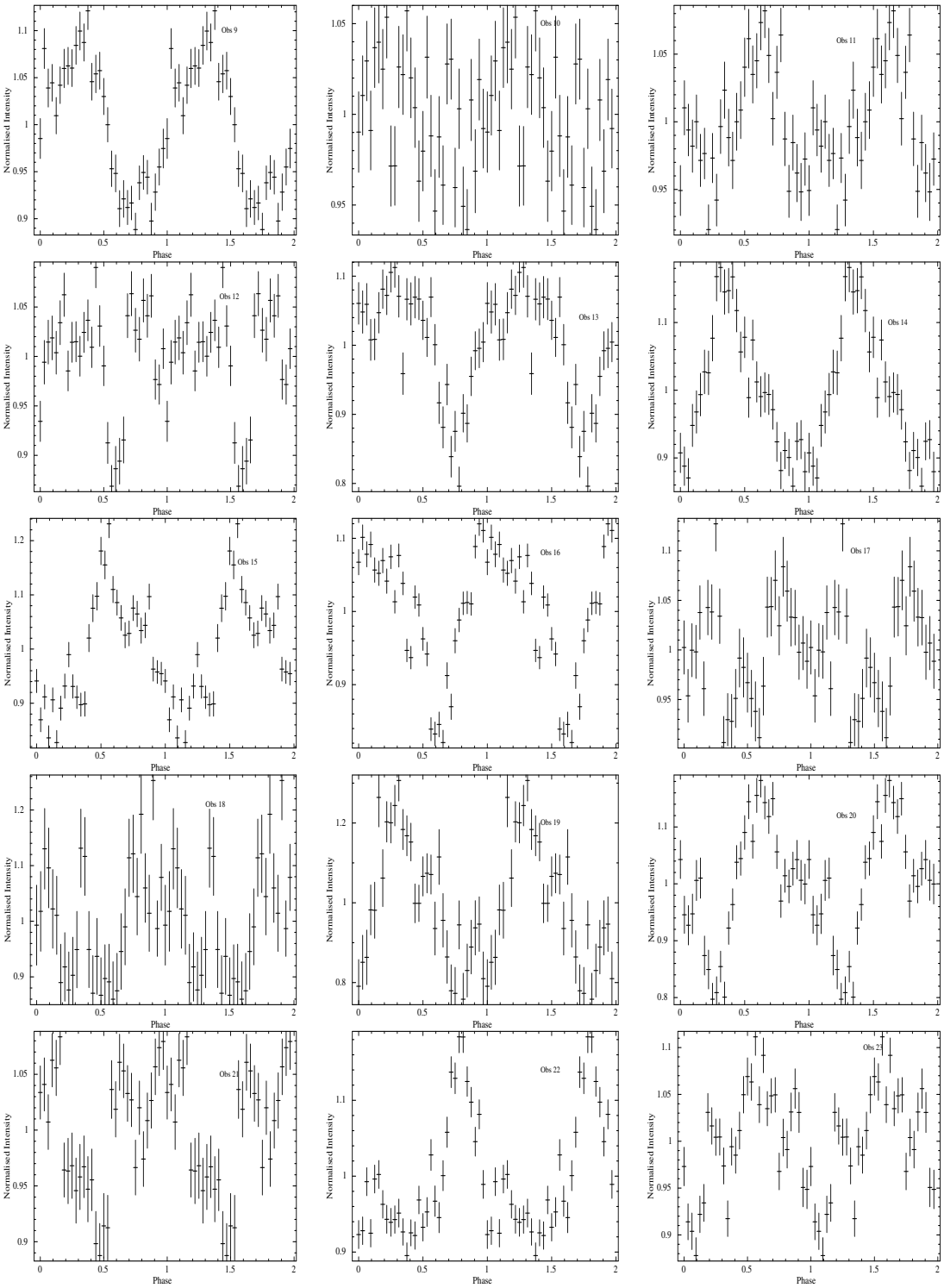

Fig. 5.4 Pulse profiles from 15 RXTE-PCA observation. There is large variation in pulse shape from these observations.

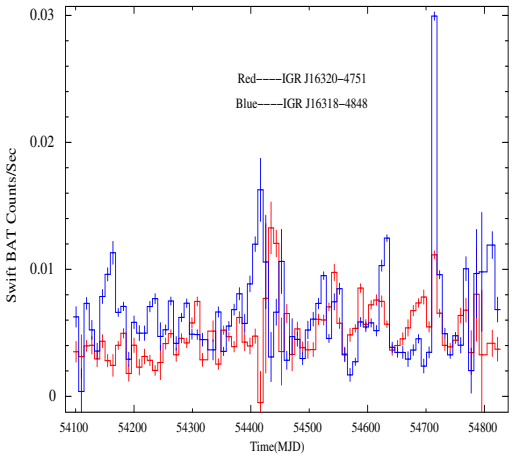

Fig. 5.5 Swift BAT light curves of two adjacent sources in 15-50 keV energy band from Jan 2007 to Dec 2008. Red and Blue colors represent IGR J16320-4751 and IGR J16318-4848 respectively.

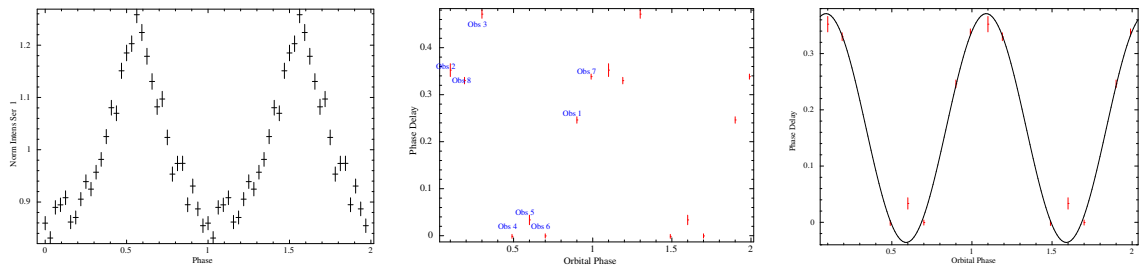

Fig. 5.6 a) Template pulse profile obtained from combining data from observations 4, 5 and 6. b) A plot of phase difference of pulse peak from each observation with respect to pulse peak of best profile. c) Phase difference curve (ignoring point of very large value from observation 3) fitted with sin function.

Swift BAT light curve of this neighboring source with our source for January 2007 to December 2008 in 15.0-50.0 keV energy band. In this energy band both sources have comparable count rates for most of times as shown in figure 5.5. This means that neighboring source in *RXTE* PCA FOV is contaminating data from our source. Contamination by the IGR J16318-4848 effects the unpulsed level of the pulse profile of our source.

5.3.1.3 Variation In Pulse Profile and Pulse Arrival Delays

In order to measure the lags/leads between the pulse profiles from the *XMM-Newton* observations, we created a template pulse profile from the combined obs. 4, 5 and 6. This is shown in Figure 5.6, with the interpulse seen more clearly. We used the

tool `crosscor` to correlate all pulse profiles with the template profile. A plot of phase difference for different observations is given in Figure 5.6.

The phase-lag profile plotted as a function of orbital phase does show a sinusoidal modulation (with the exception of point from obs 3) as seen in Figure 5.6. If we ignore the point of very large phase delay value from obs 3 and fit remaining modulation curve with a sin function, we get a large projected orbital semi-major axis $a_x sin(i) = 251.5$ lt-sec. This implies a large mass function of companion mass of $\simeq 280 M_\odot$. The fact that the BAT light curve does not have any signature of an X-ray eclipse places a upper limit on the inclination angle. This gives very improbably high value for the mass of companion star. Since most HMXBs have companions in the mass range 10 to 70 $M_\odot$ (Martins et al., 2005), we suspect that fit to apparent pulse arrival time delay shown in Figure 5.6 is incorrect. We suspect this is due to intrinsic variations in the average pulse profiles.

For pulse timing analysis pulse profile of neutron star should be stable. If pulse profile is variable it will introduce error in arrival time of the pulses, since it would be difficult to have a unique time marker in pulse profile. 8 pulse profiles from *XMM-Newton* data that are shown in Figure 5.3 are similar qualitatively but there are small discrepancy between them. Profile 3 and 6 have sharp pulse peak whereas profiles 1 and 4 have broader pulse peaks. Profile 6 and 8 show a small secondary pulse peaks whereas profile 7 has a small dip. Data in observation 5 is about 3 ks, so there are about only two and half pulses in it which leads to a poor pulse profile for this observation. Pulse fraction in these profiles varies between 0.16-0.3. Hence pulse shape and pulse fraction of *XMM-Newton* pulse profiles are variable. All these differences can affect pulse arrival delays computed from cross correlating the pulse profiles. We discuss possible reasons for this variation in §5.4.

5.3.2 Spectroscopy

5.3.2.1 XMM-Newton Spectral Analysis

We analyzed *XMM-Newton* EPIC PN data for studying the spectral behavior of the source. To do this, source spectra were extracted from a circular region of radius $1'$ centered on the position of the target. Background events were extracted from a similar source-free circular region. The spectra so obtained, were grouped to have a minimum of 25 counts in each bin with `SPECGROUP`. The resulting spectra were fitted in `XSPEC V12.8.3`. Initially, we tried fitting the spectrum using a model consisting of an absorbed power-law and a Gaussian line for Fe Kα emission line. With this model

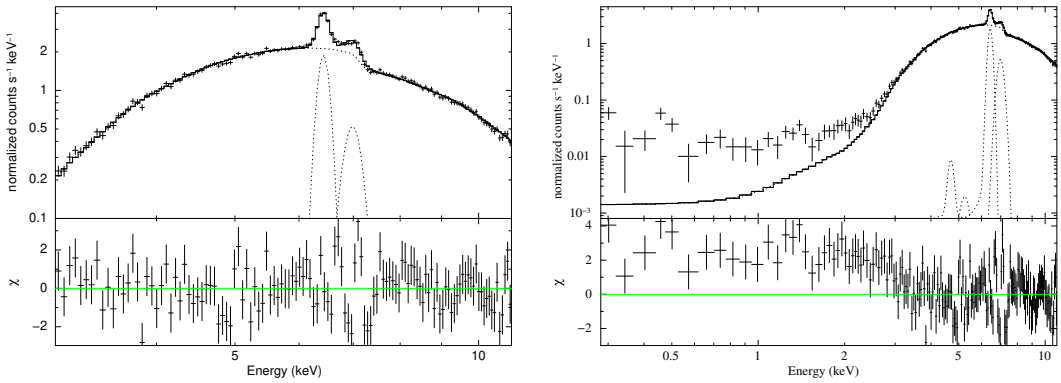

Fig. 5.7 Spectrum of IGR J16320-4751 with a model fit from observation 6. Left : Spectrum in range 3-11 keV. Model used for fitting is single absorbed powerlaw and two iron lines. Right : Spectrum in range 0.3-11 keV. Bottom panels shows residuals of fitted model.

fit, some residuals are seen around 7 keV and at energies lower than 3 keV. We obtain a relatively better fit and improved χ^2 (in range 0.96-1.43) if we add another Gaussian component (to account for the 7 keV residuals). For observations 4 and 5 width of second line could not be constrained, hence for these observations we fixed its value to be 153 eV (Average of width from rest of observations). Table 5.2 gives best fitted parameters in 3.0-11.0 keV. Figure 5.7 shows spectral data and model fit observation 6. We tried bremsstrahlung and blackbody models below 3 keV to account for the soft excess. For finding parameter values of these components we fixed other parameters of model. The RXTE PCA field is crowded and due to potentially higher background of unresolved sources in FOV (field of view), we did not carry out spectral analysis using PCA.

5.3.2.2 Additional components in the X-ray spectrum

We tried to check the nature of the additional Gaussian component that has a line energy of about 7 keV. The Iron K_α flourescence energy is about 6.40 keV. The additional component at 6.95 keV may correspond either to neutral Fe K_β (7.05 keV) or to hydrogen like iron fluorescence (6.95 keV). To distinguish between these we investigated the ratio of the energy of the two iron lines. Line energy values may slightly differ from exact known values due to instrument calibration uncertainties. However ratio of line center value of two lines is largely independent of these uncertainties. This ratio value for all XMM-Newton observation is shown in Figure 5.8. For all observations this value is close to 1.085 except observation 5 at which it is consistent with 1.101. In this observation we have only a 3 ks data, thereby having limited statistics. Thus

Table 5.1 Table Of Observations

Obs.No.	Obs. Id	Date-Start	Tstart	Date-End	Tend	Duration[s]	Orbit Phase	Satellite	Data Mode
1	93034-02-01-00	05-08-2007	00:33:16	05-08-2007	04:23:00	13785	0.08	RXTE	Standard2f
2	93034-02-05-00	08-08-2007	00:30:44	08-08-2007	03:56:41	12358	0.43	RXTE	Standard2f
3	93034-02-08-00	10-08-2007	05:55:55	10-08-2007	09:50:26	14072	0.66	RXTE	Standard2f
4	93034-02-09-01	10-08-2007	23:50:28	11-08-2007	00:13:20	1372	0.74	RXTE	Standard2f
5	93034-02-09-00	11-08-2007	00:47:28	11-08-2007	03:17:23	8996	0.75	RXTE	Standard2f
6	93034-02-11-00	12-08-2007	11:31:50	12-08-2007	15:22:10	13822	0.92	RXTE	Standard2f
7	93034-02-12-00	13-08-2007	06:35:02	13-08-2007	10:28:19	13998	0.00	RXTE	Standard2f
8	93034-02-02-00	14-08-2007	18:26:35	14-08-2007	21:06:19	9584	0.16	RXTE	Standard2f
9	93034-02-03-00	15-08-2007	11:47:16	15-08-2007	15:27:49	13234	0.19	RXTE	Standard2f
10	93034-02-04-00	16-08-2007	05:05:19	16-08-2007	09:03:58	14320	0.33	RXTE	Standard2f
11	93034-02-06-00	17-08-2007	18:51:32	17-08-2007	22:24:29	12778	0.50	RXTE	Standard2f
12	93034-02-07-00	18-08-2007	10:30:20	18-08-2007	14:11:23	13264	0.58	RXTE	Standard2f
13	93034-02-10-00	20-08-2007	16:24:15	20-08-2007	16:54:16	1802	0.82	RXTE	Standard2f
14	93034-02-10-01	20-08-2007	17:30:28	20-08-2007	18:28:36	3488	0.82	RXTE	Standard2f
15	93034-02-10-02	20-08-2007	19:04:57	20-08-2007	20:02:48	3472	0.83	RXTE	Standard2f
16	0556140101	14-08-2008	22:44:10	15-08-2008	01:14:43	9033	0.90	XMM	Full Window
17	0556140201	16-08-2008	17:41:23	16-08-2008	19:55:16	8033	0.10	XMM	Full Window
18	0556140301	18-08-2008	13:36:12	18-08-2008	15:33:26	7033	0.30	XMM	Full Window
19	0556140401	20-08-2008	07:36:07	20-08-2008	10:43:20	11233	0.50	XMM	Full Window
20	0556140501	21-08-2008	07:04:12	21-08-2008	07:41:30	2238	0.60	XMM	Full Window
21	0556140601	22-08-2008	03:55:58	22-08-2008	07:22:36	12397	0.70	XMM	Full Window
22	0556140701	24-08-2008	18:30:00	24-08-2008	21:00:33	9033	0.99	XMM	Full Window
23	0556140801	26-08-2008	13:34:33	26-08-2008	16:15:06	9632	0.19	XMM	Full Window

Table 5.2 Results of the spectral fitting of IGR 16320-4751 with model.

Parameter	Obs 1	Obs 2	Obs 3	Obs 4	Obs 5	Obs 6	obs 7	Obs 8
Parameter values Of absorbed Power Law and Two Iron Lines								
N_H^1	$30.7^{+1.27}_{-1.27}$	$21.74^{+0.77}_{-0.77}$	$21.31^{+0.81}_{-0.80}$	$25.41^{+0.84}_{-0.80}$	$24.93^{+2.33}_{-2.24}$	$22.61^{+0.56}_{-0.55}$	$45.97^{+2.60}_{-2.56}$	$23.0^{+0.88}_{-0.86}$
Γ	$0.83^{+0.076}_{-0.074}$	$0.54^{+0.053}_{-0.053}$	$0.56^{+0.056}_{-0.056}$	$0.82^{+0.056}_{-0.056}$	$0.83^{+0.148}_{-0.147}$	$0.49^{+0.037}_{-0.037}$	$0.36^{0.112}_{0.113}$	$0.75^{+0.06}_{-0.06}$
Norm^2	$9.36^{+1.76}_{-1.43}$	$9.12^{+1.13}_{-1.01}$	$8.9^{+1.19}_{-1.04}$	$10.4^{+1.4}_{-1.2}$	$8.28^{+3.26}_{-2.32}$	$10.3^{+0.89}_{-0.82}$	$41.1^{+12.8}_{-9.8}$	$8.39^{+1.20}_{-1.04}$
$EC_{K_\alpha}(keV)$	$6.43^{+0.01}_{-0.01}$	$6.43^{+0.01}_{-0.01}$	$6.43^{+0.01}_{-0.01}$	$6.43^{+0.01}_{-0.01}$	$6.42^{+0.02}_{-0.02}$	$6.43^{+0.01}_{-0.01}$	$6.42^{+0.01}_{-0.01}$	$6.42^{-0.01}_{-0.01}$
EQW (eV)	251^{+25}_{-21}	209^{+18}_{-19}	177^{+21}_{-20}	186^{+16}_{-16}	182^{+53}_{-38}	231^{+12}_{-13}	462^{+56}_{-32}	215^{+21}_{-18}
$EC_{L2}(keV)$	$7.04^{+0.05}_{-0.05}$	$6.95^{+0.06}_{-0.08}$	$6.97^{+0.08}_{-0.07}$	$7.02^{+0.05}_{-0.05}$	$7.07^{+0.12}_{-0.12}$	$6.99^{+0.03}_{-0.03}$	$6.95^{+0.04}_{-0.06}$	$6.98^{+0.05}_{-0.05}$
EQW (eV)	55^{+21}_{-23}	78^{+23}_{-21}	80^{+25}_{-17}	64^{+15}_{-15}	84^{+43}_{-39}	122^{+15}_{-15}	205^{+43}_{-24}	98^{+25}_{-21}
χ^2_{red}	1.07	1.05	1.13	1.08	0.96	1.39	1.43	1.12

1 10^{22} atoms cm^{-2}

2 10^{-3} Photons $keV^{-1}cm^{-2}s^{-1}$ at 1 keV

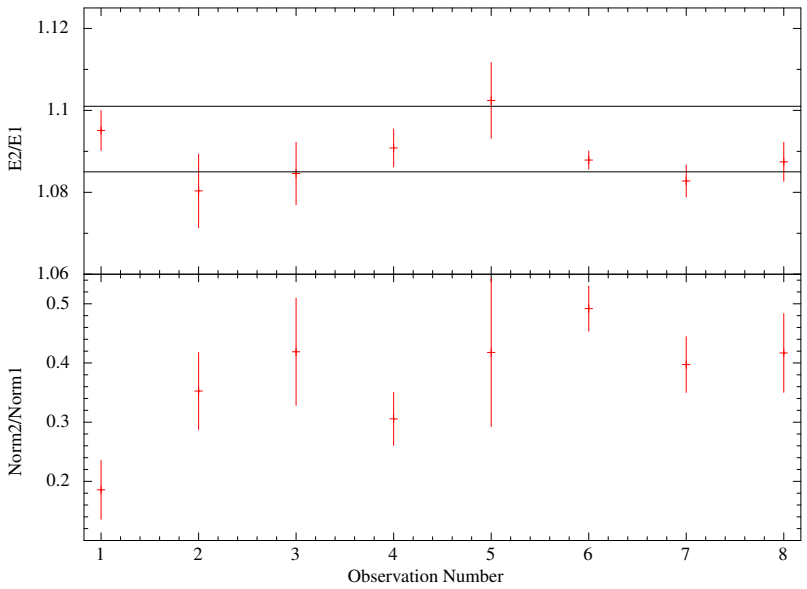

Fig. 5.8 Top panel shows ratio of the line center values two emission lines seen in spectra of IGR J16320-4751. Two horizontal lines in black show ratio of line energies of Fe Kβ to Fe Kα (at 1.101) and Hydrogen line Fe to Fe Kα (at 1.085). All observations (except one) indicates that second line in spectra is a hydrogen like iron line. Bottom panel shows ratio of fluxes of two lines for all *XMM-Newton* observations.

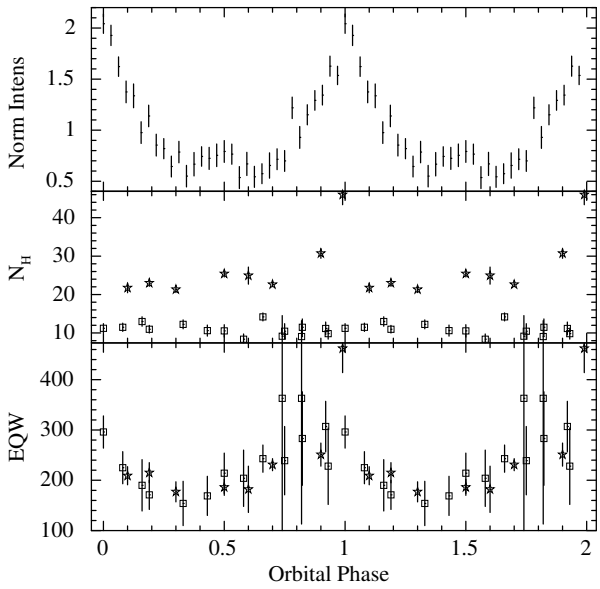

Fig. 5.9 Variation of spectral parameters with orbital phase. Intensity, N_H and Equivalent width of iron line with orbital phase. Top panel is orbital profile of BAT data. In Middle and Bottom panel star and rectangular marker represent *XMM-Newton* and *RXTE* data points.

second line in speatra is hydrogen like iron line. Ratio of two line fluxes is ∼0.2 for first observation and for other observations it is in range of 0.3-0.5.

Spectra of IGR J16320-4751 is well fitted with an absorbed powerlaw and two Gaussian lines in 3.0-11.0 keV energy range but at lower energies a soft excess is seen some of the *XMM-Newton* observations (see for example Figure 5.7). For understanding this soft excess we tried two components in the model : 1. Unabsorbed bremsstrahlung and 2. Absorbed Blackbody. None of these models seems to account for soft excess completely. Bremsstrahlung model gives very high temperature for material that can not be found in a binary environment and for Blackbody model parameters are not well constrained. However in order to just estimate the flux of soft excess component we used an unabsorbed Blackbody component in model. We have found that flux of Blackbody component for observation 1, 2 and 6 is 2.4×10^{-14}, 3.7×10^{-14} and 3.4×10^{-13} erg s^{-1} cm^{-2} respectively. For other observations flux value is consistent with zero. Phase value for these observations are 0.90, 0.10 and 0.70 respectively as shown in Figure 5.9. A strong variation of N_H is seen at phase 1.0. This large variation of N_H is close to superior conjunction of this system (Heras et al., 2009). This means soft excess in this source is present in phases near to superior conjunction.

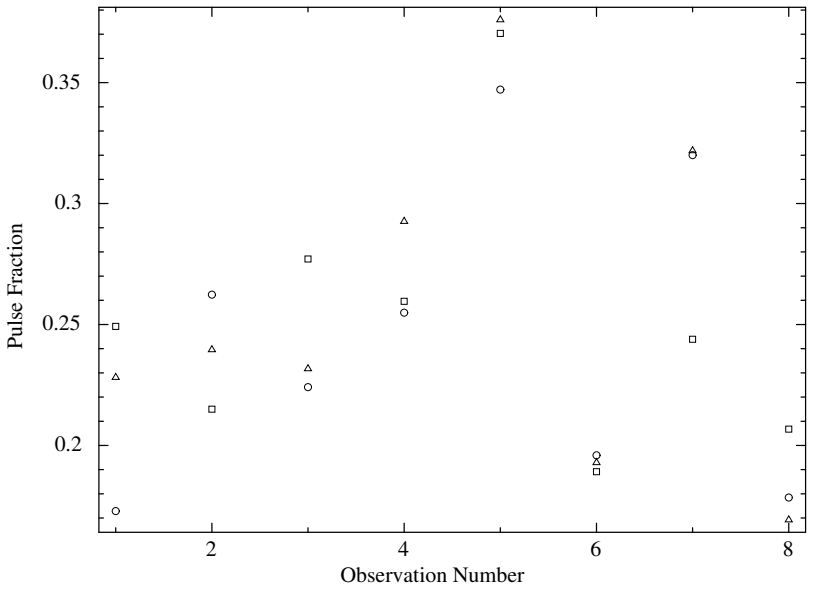

Fig. 5.10 Pulse fraction from energy resolved pulse profiles in 3 band :1) 3.0-6.2 keV 2) 6.2-7.5 keV 3) 7.5-10.0 keV. Circle, rectangle and triangle marker represent data from band 1, 2 and 3 respectively.

5.3.2.3 Energy Resolved Pulse Profiles

The X-ray spectrum of IGR J16320-4751 shows very strong absorption with a column density in excess of 10^{23} atoms cm^{-2}. Consistent with the large column density, source also shows a very strong iron emission line at 6.4 keV with equivalent width in the range of 177-462 eV. If the iron emission line is produced in a large region surrounding the neutron star, the line photons may have smaller pulse fraction due to light travel time variations across the reprocessing region. Pulse fraction of line emission will also be smaller if matter is distributed isotropically all around the neutron star. On the other hand, if the line producing region is very near to the source and distributed in non-isotropic manner around the neutron star, the line component can have a strong pulsation, albeit with a different pulse profile compared to the pulse profile of the continuum spectral component. The individual XMM observations are not long enough, and therefore have limited statistical quality to carry out pulse phase resolved spectroscopy in several phase bins.

To investigate any variation in the iron line flux with pulse phase, we created pulse profiles from all *XMM-Newton* observations in iron line energy band (6.2-7.5 keV). We also created pulse profiles in 3.0-6.2 keV (Low energy) and 7.5-10.0 keV (High energy). Pulse fraction of main peak in energy resolved pulse profiles from all observations is shown in Figure 5.10. For all observations pulse fraction in iron band is found to

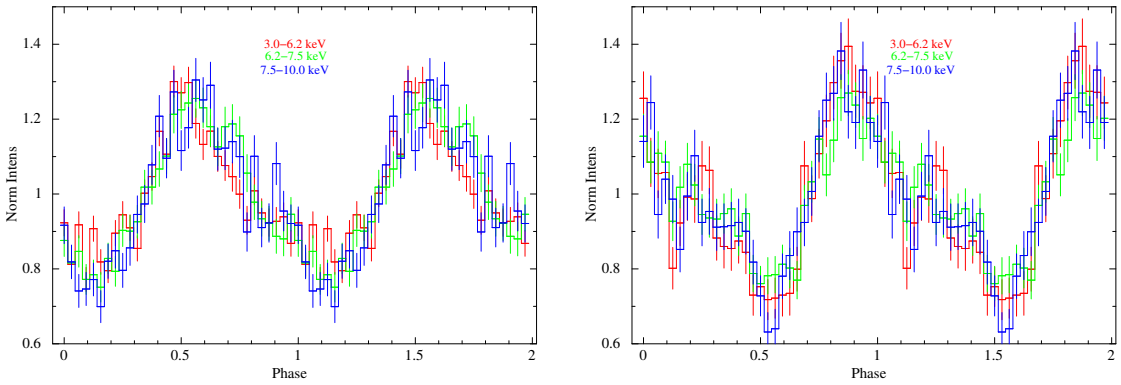

Fig. 5.11 Energy resolved pulse profile in three energy band from observation 4 and 7. Red, Blue and Green color shows Low, Mid and High energy bands as explained in text above.

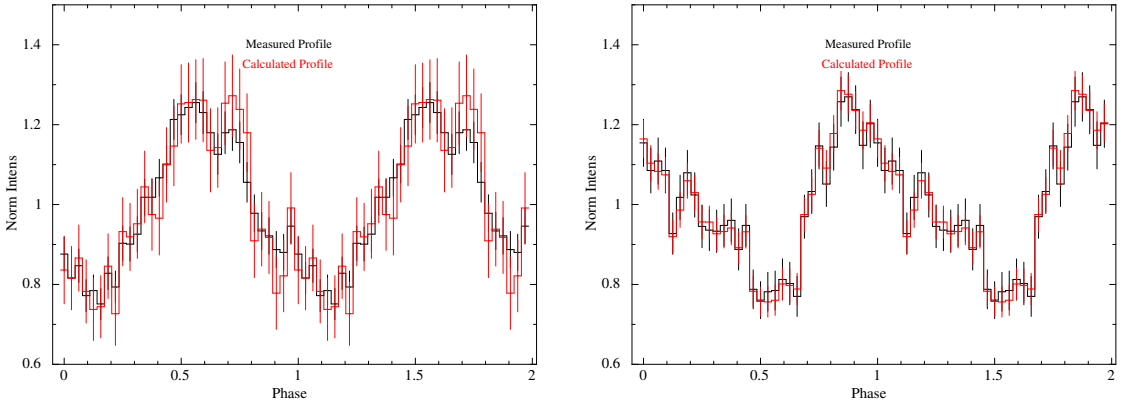

Fig. 5.12 Pulse profiles in iron line energy band for observation 4 and 7. Black is the observed pulse profile in the 6.2-7.5 keV energy band and red is the calculated profile as explained in the text above.

be comparable to lower and higher energy band. Energy resolved pulse profiles from selected individual observations (4 and 7 in Table 5.1) are shown in Figure 5.11. These pulse profiles are used to compare emission behavior in mid energy band from rest of energy band. We found that pulse fraction and pulse profile behavior in mid energy and rest of energy range is quite similar. This behavior suggest that distribution of reprocessing matter around the neutron star is not symmetrical.

To confirm this, we calculated iron line pulse profile from mid energy pulse profile. The mid energy range profile has contribution from the line photons and the continuum photons in that energy band. Since the continuum pulse profile in the band below and above the line energy are nearly identical, we assumed the continuum pulse profile of the mid-energy band to be the average of the two other profiles. We subtracted the same from the mid-energy pulse profile to obtain the pulse profile of the line emission

in the following manner. The normalized pulse profile in the three energy bands, as shown in Figure 5.11 have been used for the same.

$I_{Avg}(n)$ is calculated from the normalized pulse of the low and high energy pulse profile as :

$$I_{Avg}(n) = \frac{I_{Low}(n) + I_{High}(n)}{2} \tag{5.1}$$

Here we have assumed that pulsation behavior of continuum in whole *XMM-Newton* band is same. Intensity in n^{th} bin of line energy pulse profile :

$$I_{Line}(n) = 1 + \frac{BW}{EQW}\left(\Big(I_{Mid}(n) - 1\Big) - \Big(1 - \frac{EQW}{BW}\Big)\Big(I_{Avg}(n) - 1\Big)\right) \tag{5.2}$$

In this equation EQW is Equivalent Width of iron K_α line, BW is total band width if mid energy range. These iron line pulse profile are plotted against measured mid energy profiles as seen in Figure 5.12 for observation 4 and 7 that have highest statistical quality among all the XMM observations. Here also we see almost similar emission in both mid energy and line profile. However we expect much lower pulse fraction in pure iron line pulse profile because of X-ray reprocessing from a wind surrounding the neutron star.

5.3.2.4 RXTE Spectral Analysis

We analyzed *RXTE* PCA data to check whether the behavior of spectral parameters can be confirmed with these observations. For broad band *RXTE* spectral analysis we took standard spectra files available for all observations. We fitted the data in 3.0-15.0 keV band with a model consisting of powerlaw for the continuum, a gaussian component for emission line at 6.4 keV, and photoelectric absorption in line-of-sight (Xspec model wabs). Since this source falls in galactic plane, we also used model components to account for Galactice ridge emission and cosmic X-ray background with appropriate normalizations (Valinia and Marshall, 1998). Orbital phase variation of N_H and equivalent width of gaussian line is shown in 5.9. N_H value from *RXTE* data lies between 8.0-13.0 ($\times 10^{22}$ atoms cm^{-2}) and does not vary much with orbital phase. N_H values from *RXTE* data is significantly lower than *XMM-Newton* values. Equivalent width of iron line from *RXTE* data show a correlation with orbital intensity and agrees mostly with trend obtained from *XMM-Newton* data except at the peak of orbital intensity.

5.4 Discussion

Pulse profiles of IGR J16320-4751 are found to be variable on day to day basis. Variability is in pulse shape as well as in pulse fraction. Even larger variability is detected in pulse profiles obtained with *RXTE*-PCA data. Highly variable average pulse profile of the source could be due to variations in the accretion from the medium surrounding the compact object. A high density accretion stream can also cause changes in the shape of the pulse profile and thereby make it difficult to estimate pulse arrival time delays using correlation of the pulse profile. A mass function of $\sim$280 $M_{\odot}$ determined by *XMM-Newton* observations seems unlikely and is perhaps due to intrinsic variabilities of the pulse profiles. A systematic study of these phase delays and orbital intensity in more such orbits will be needed to confirm this. If this is indeed true, using hard X-ray pulse profiles and phase lags with NuSTAR/AstroSat can possibly give the orbital solution.

It is interesting to note the presence of a $Ly\alpha$ line from hydrogen-like iron in addition to ubiquitous Fe Kα line and the absence of helium-like iron line in the X-ray spectrum. The 6.4 keV line has been reported in this source earlier (Rodriguez et al., 2006) and is interpreted as fluorescence of iron in a wind or circumstellar medium. GX 1+4 (Paul et al., 2005) and Her X-1 (Jimenez-Garate et al., 2005) are two other sources which shows these two lines while helium-like iron is absent from their spectra. There are some sources like Vela X-1, CenX-3 which show helium-like iron also. These three lines can be produced in an onion-like structure in accretion matter with changing ionization degree and different ionization levels of metals. On the other hand, for sources like IGR J16320-4751 it has been suggested that 6.4 and 6.95 keV lines originate from two completely different regions. One possibility is that 6.4 keV fluorescence line originates very far from neutron star and hydrogen-like iron line originates from a hot gas inside or near the Alfvén shell, where ionization parameter is quite high.

From a comparative analysis fo the pulse profiles in different energy bands, we have detected a pulsating nature of the fluorescent flux in the neutral iron line band. This suggest that reprocessing material is neither symmetrically distributed around the neutron star nor large enough in size to smear out the pulsations of the iron fluorescence emission. This is seen in source like 1A 1118-61 (Maitra et al., 2012) where pulse profiles in energy band 6-7 Kev shows a somewhat different pulse profile compared to lower and higher energy bands.

Soft excess emission is a spectral feature of excess intensities over the extrapolation of a power law fitted to higher energies. Soft excess is seen in many HMXBs like LMC X-1 (Woo et al., 1996), SMC X-1 (Wojdowski et al., 1998), RXJ0059.2-7138 (Hughes,

1994), XTE J011.2-7317 (Yokogawa et al., 2000). Origin of soft excess in XBPs can by explained by 4 types possible mechanism (Hickox et al., 2004) : (1) emission from accretion column (2) thermal emission by collisionally energized diffuse gas around the neutron star (3) reprocessing of hard X-rays by diffuse material around neutron star and (4) reprocessing by optically thick, dense material around the neutron satr. In some HMXB sources with low column density (Her X-1, SMC X-1, LMX X-4 etc.) with low column density and high L_X soft excess is found to be reprocessing by optically thick structures in accretion disk. In IGR J16320-4751 soft excess is detected even when power-law component of emission is highly absorbed with column density of of $\sim 10^{23}$ atoms cm^{-2}. Soft excess component in this source is therefore likely to have different origin, like in GX 302-1 (Islam and Paul, 2014). It could be, for example, the emission by a collisionally energized cloud or reprocessing of hard X-rays either by a diffuse cloud. For IGR J16320-4751 this soft excess has been fitted by Blackbody component and suggested to be an emission by a collisionally energized cloud in which compact object is embedded (Rodriguez et al., 2006). In our analysis of soft excess the parameters are not well constrained by Blackbody component. However soft excess is definitively present when system is near superior conjunction. Soft excess near to superior conjunction has been seen in three other sources 4U 1700-37 (Haberl et al., 1989) Centaurus X-3 (Burderi et al., 2000) and IGR J19140+0951 (Prat et al., 1977).

5.5 Conclusion

The main results that we have from our analysis presented above are

- Pulse profiles of IGR J16320-4751 are highly variable. Qualitative variations of pulse profiles from *XMM-Newton* data and contamination of pulse profiles from *RXTE* data due to a neighbouring sources hinders us from finding orbital solution of this system.
- Spectra of IGR J16320-4751 from *XMM-Newton* observations shows hydrogen like iron line along with previously reported Fe Kα line.
- Pulse profiles in iron line band shows pulsations and are qualitatively similar to low and high energy band.
- X-ray spectrum in three *XMM-Newton* observations shows soft excess component. Orbital phase of these observations are around superior conjunction of system.

Chapter 6

Experimental X-ray polarimetric activities

6.1 Experiments on Photo-Electron Polarimeter

6.1.1 Photo-electron Polarimeters

Polarimetry is widely considered to be a powerful observational technique in X-ray astronomy, useful to enhance our understanding of emission mechanisms, geometry and magnetic field arrangement of many compact objects. Conventional X-ray polarimeters are based on Bragg reflection and Thomson/Compton scattering. The photoelectric effect is much more sensitive to photon polarization than these methods in the few keV energy range. In this energy range, this process has a very large interaction cross-section. Thompson/Compton scattering has a very small cross-section in this energy band. Bragg reflection based polarimeters work in only a narrow energy range. The photo-electron polarimeter can work over a dynamic range of 5 or so (2-10 keV) compared to a few eV at 2.6 keV for a Bragg polarimeter made using graphite crystal. For this reason, this process has been considered as a base principle of good X-ray polarimeters in 2-10 keV energy range. Many groups are developing X-ray polarimeter based on the study of photo-electron track in a gas-based medium. Historically, the first scientist who studied X-ray polarization through the photo-electron track was P.W. Sanford, in 1970 (Sanford et al., 1970). In recent years, this type of polarimeters has brought major advancement in polarization measurement sensitivity with the development of GEM-based micro-pattern polarimeter (Bellazzini et al., 2002; Costa et al., 2001) and Micro-pattern time projection chamber polarimeter (Black et al.,

2007). These polarimeters which image the photo-electron track in a gaseous medium, are useful along with X-ray focusing optics.

Here we discuss the development of a photo-electron polarimeter that will enable polarization measurements without using focusing optics. We use a proportional counter with closely spaced wires, interleaved as two sets of anodes. An incident photon with its polarization parallel to the direction of wires deposits most charges in any of the anodes, whereas a photon with its polarization perpendicular to the direction of wires deposits charges equally in two anodes. This technique can be scaled up to make a large area polarimeter by using multiple detector units. Here we describe the experiments to establish the proof of concept of this technique.

6.1.2 Photo-Electron Interaction

In the photoelectric absorption process, a photon undergoes an interaction with an absorber atom in which the photon completely disappears. In its place, an energetic photo-electron is ejected by the atom from one of its bound shells. The interaction is with the atom as a whole and cannot take place with free electrons. For any photon with energy higher than the binding energy of the K-shell electrons, the most probable origin of the photo-electron is the most tightly bound or K shell of the atom. The photo-electron appears with an energy given by

$$E_{e^-} = h\nu - E_b \tag{6.1}$$

The direction of emitted photo-electron is dependent on the linear polarization of the incident photons. The analytical expression of the differential cross-section distribution of the photo-electron, in the non-relativistic approximation, is

$$\frac{\partial\sigma}{\partial\Omega} = r_0^2 \frac{Z^5}{137^4} \left(\frac{mc^2}{h\nu}\right)^{\frac{7}{2}} \frac{4\sqrt{2}\sin^2(\theta)\cos^2(\phi)}{(1-\beta\cos(\theta))^4} \tag{6.2}$$

where $\theta \equiv$ The polar angle between the direction of incoming photon and the ejected electron (from K-shell).
$\phi \equiv$ The azimuthal angle of the latter with respect to the X-ray polarization vector.
$Z \equiv$ The atomic number of the absorption material.
$r_0 \equiv$ The classical radius of the electron.
$\beta \equiv$ Speed of electron divided by c.

The $\sin^2(\theta)$ term in the numerator represents the dependence of differential cross-section of the photo-electron on polar angle. For photons with energy of few keV, photo-electron are essentially emitted in the plane perpendicular to the direction of incident photon (at 90° polar angle). In this plane, the direction of the photo-electron follows a $\cos^2(\phi)$ angular dependence. The distribution has maximum probability in the direction of electric field vector of photon. The term in the denominator accounts for the tilt of the distribution with the increasing energy of the photo-electron.

6.1.3 Principle of Polarization Measurement in PE Detector

When a photon interacts with gas molecule via photo-electric interaction, a photo-electron is ejected in the direction of polarization of incoming radiation. The primary photo-electron further ionizes the other gas molecules and losses its energy in the process. In the first few interactions, when the photo-electron is very energetic, it deviates very less from this original direction. Hence electron-ion pairs are created in the initial direction of photo-electron. This ensemble of charges is called a charge cloud or charge track. Thus the information about the polarization of the incoming radiation is captured in this photo-electron track.

We use two sets of interleaved anodes for detecting the direction of the photo-electron tracks. When the charge track is along the anodes, most of the charges are deposited at one of the anodes and very less in the second anode. On the other hand, when the charge track is created perpendicular to the direction of anodes, the charge is deposited in both the anodes. For the track direction in between, charges are split between two anodes in a ratio which is indicative of track direction, which in turn is dependent on the polarization of the initial photon. Hence, the ratio of the charge collected in the two anodes gives us a measure of the polarization angle of incoming photons.

6.1.4 PE Detector

The PE detector wireframe is realized using a printed circuit board (PCB) with a cutout at the center, as shown in Figure 6.1. The use of PCB as wireframe facilitates easy change of wire separation for experimentation. In the current tests, the separation between adjacent anodes on the PCB is 2.4 mm. Anode wires are made of 25 micron thick Stainless Steel (SS), coated with Gold. The cathode is made of 50 micron

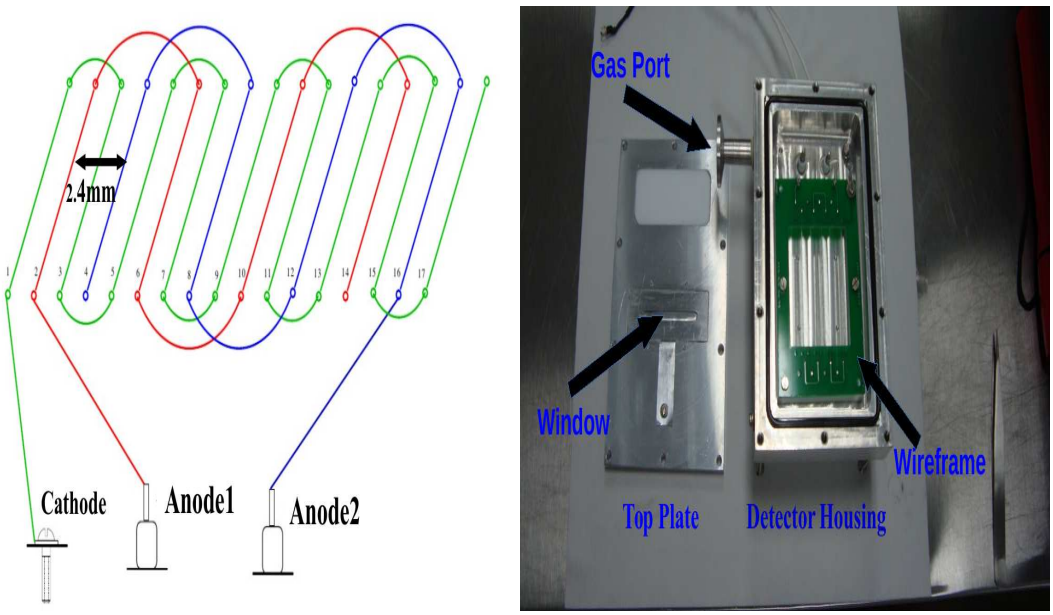

Fig. 6.1 Left panel shows a schematic of wiring configuration in PE detector. Right panel shows the PCB of wires inside the detector housing along with the top plate. Image Credit: Rishin P. V.

thick alloy of Beryllium and Copper. PCB is mounted inside the detector housing on a Teflon spacer. This spacer keeps anodes and cathode at a reasonable distance from the top plate and bottom of the detector housing. The interior of the detector should not have any sharp or irregular connections. Otherwise, this can lead to unnecessary sparks due to the discharge of high voltage used for detector biasing. Due to this reason, the detector wires are soldered to PCB wireframe using ball soldering technique. The detector housing is made of aluminum material. The detector has a gas port, located at the side of the detector housing. It serves the purpose of filling the detector to the required pressure level. It also helps in evacuating the detector chamber to the required level of vacuum before filling the detector with gas. The detector is closed with a top plate, and it is sealed with detector housing with the help of an O-ring, which makes it leak proof and helps in maintaining its gas pressure. The incoming radiation enters through a small window in the top plate, which is made of 50 micron thick aluminum. The detector is filled with P10 gas (90% argon and 10% methane) at different gas pressures. Argon has large cross-section for the absorption of X-rays by photo-electric process and provides higher mobility of electrons in the gas. Methane is added as a quench gas. Figure 6.1 shows a top view of detector housing and top plate before the assembly.

The Photo-Electron (PE) detector is a variant of the proportional counter. The detector unit is made of closely spaced wires divided into two anodes and one cathode. A high voltage of positive polarity is applied to anodes, and negative polarity is applied to the cathode. The interaction of an incoming photon with a gas molecule emits photo-electron which further creates a charge track via collision with other molecules. The electrons and the ions in charge track drift towards the electrodes of opposite polarity. Ions have low mobility due to their high mass. Free electrons are easily accelerated by the applied voltage and gain significant kinetic energy. If this energy is greater than the ionization energy of the neutral gas molecule, it is possible fora dditional ion pair to be created in the collision. The electron emitted by secondary ionization will also be accelerated by the high voltage, and during their subsequent drift, they further create more ionization. The process, therefore, creates a form of an avalanche in which more free electrons are created. The electrons created inprocess are collected at anodes as a charge pulse.

The output charge pulse of the detector is given to a Charge Sensitive Pre-Amplifier (CSPA), which amplifies and converts it into proportional a voltage pulse. The amplification factor is 4.8×10^{12} V/coulomb or 0.76 μV/electron. The output of CSPA is passed to a peak detector as well as to a comparator. The peak detector holds the peak value of the voltage pulse while the comparator compares whether the incoming pulse height is more than the predefined voltage or not. For a pulse whose peak value is more than this pre-defined threshold voltage, it generates a square wave of same time duration as the incoming pulse. The output of the comparator is passed to a Field-Programmable Gate Array (FPGA). If the duration of square wave pulse from the comparator is more than a preset time, the FPGA considers it as a valid pulse and sends a signal to analog to digital converter (ADC) to digitize the pulse held in peak detector. The digitized value is acquired in a PC using a PCI based data acquisition card and stored in a file for further offline processing. Once the pulse is digitized, the peak detector is again reset for the next pulse.

6.1.5 Charge Division Experiment

The idea of charged division is central to the working of PE detector. We first tested this idea using radioactive sources which give unpolarized X-rays. For this test, the detector was filled with P10 gas at three different gas pressure 300, 400, and 600 Torr. We carefully aligned the X-ray sources with the window opening of the detecor. The

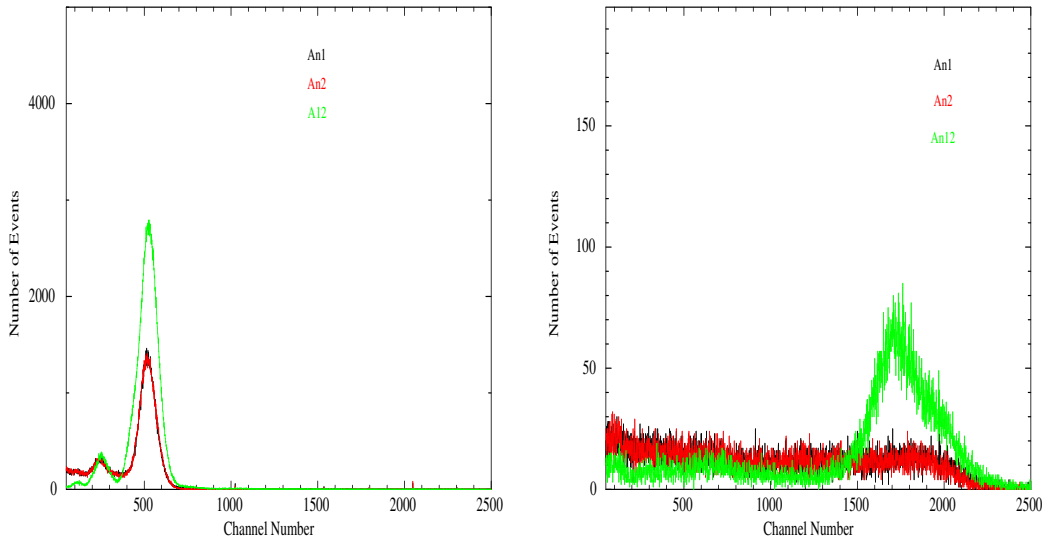

Fig. 6.2 The pulse height histograms for exposure to 6 (left) and 23 (right) keV X-rays. The histograms of pulse heights in anode1 and anode2 are shown in black and red. The pulse height of sum of charges in two anodes is green.

radioactive source Fe-55 and Cd-109 emit X-ray photons of $\sim$ 6 and $\sim$ 23 keV, respectively. The exposure time of 5 min was used for each source. Figure 6.2 shows the pulse height histograms for both the sources at 600 Torr gas pressure. The black and red curves represent the charge collected in anode1 and anode2, denoted by An1 and An2. The green curve represents the sum of charges collected in both the anodes. This is denoted by An12. For Fe-55, the results are shown in the left panel. The number of events up to 400 channel are very low in An1 and An2. After channel 400, the number of events increases sharply, peaks at $\sim$ 500 and falls to zero at $\sim$ 650. The peak centered at channel 500 corresponds to the 6 keV photons. A large number of 6 keV photons are present in An1 and An2. This is also seen for An12. The presence of a large number events of 6 keV in An1 and An2, indicates that the charge tracks are so small that most charges get deposited on an anode which is closer to it, irrespective of its orientation with respect to anode wires. For Cd-109, the results are shown in the right panel of Figure 6.2. For An1 and An2, the number of events up to 2000 channel are constant, and after that, it rapidly decreases to zero. For An12, the number of events are low up to 1500 channels, then it rises and peaks at $\sim$ 1700 channel. After 1700, it goes down again and becomes zero at 2200. The small number of 23 keV events in An1 and An2, indicates that the charge tracks are big for this energy. Whenever they are aligned with respect to wires at some angle, the charge is divided in both the anodes. The efficiency of charge division is seen to improve gradually at lower gas pressures of 400 and 300 Torr. For the same energy of incident photons, the length

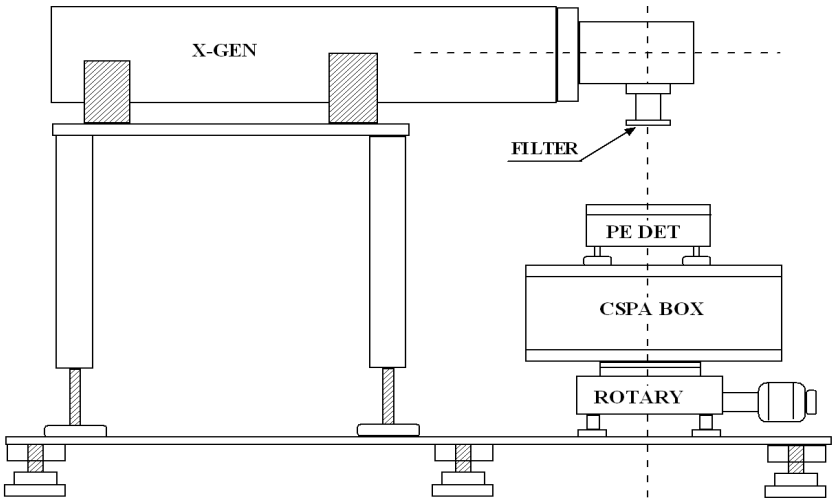

Fig. 6.3 The test setup of polarization experiments. Image Credit: Rishin P. V.

charge track increases at lower gas pressures, which results in more efficient charge division.

6.1.6 Experiments with Polarized X-rays

6.1.6.1 Experimental Setup

The setup consists of an electron X-ray generator, from whose continuum, polarized X-rays are extracted. In the X-ray generator, the electrons accelerated by the high voltage supply hit the metal target where both Bremsstrahlung X-rays and characteristic X-rays are produced. The generator was operated at 23.5 kV and 0.095 mA. We have used a filter which cutoff 95% lower energy photons. The X-rays of the highest energy are polarized. The detector and the electronics are mounted on a rotary stage which is driven by microstepping stepper motor controller. The experimental setup is shown in Figure 6.3. The detector was filled with P10 gas at 600 Torr pressure. The operating high voltage was set at 1565 V. At first, the detector and generator orientation were fixed such that the polarization of incoming photons is parallel to the direction of anodes. Then the detector was rotated in the step of 15° so that

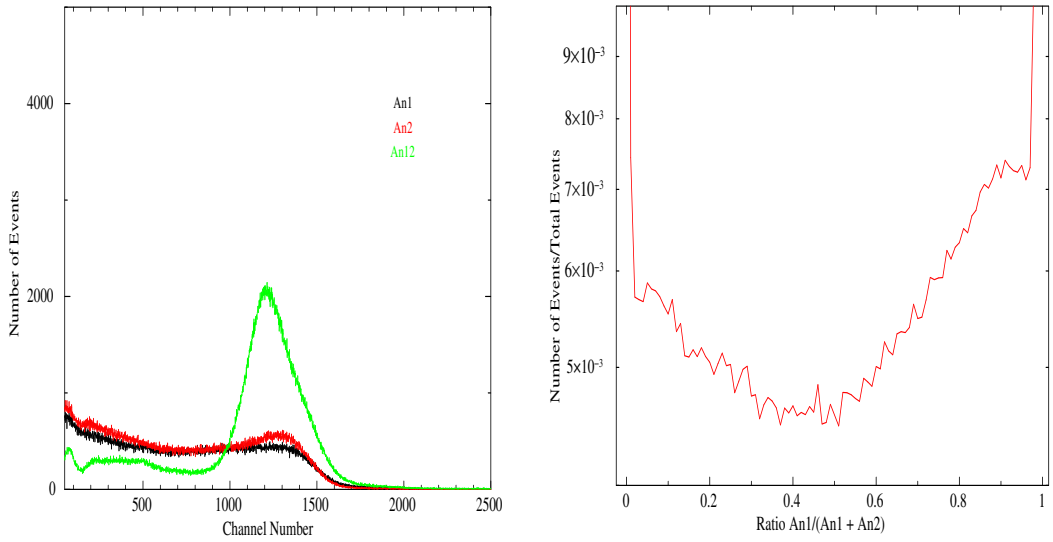

Fig. 6.4 Pulse height histograms for X-rays with 90° polarization. Right: Ratio histogram of the same.

polarization of incoming photons is 15°, 30°, 45°, 60°, 75°, and 90° with respect to anodes. At each position, $\sim$ 1 million photons were collected in the detector.

6.1.6.2 Results

The left panel of Figure 6.4 shows pulse height histogram in anode1 and anode2 for incoming photons with linear polarization at 90° to the anodes. If there is no charge division, the pulse height in one of the anode is large and added as an event at higher channel value between 1000 and 1500. Pulse height in another anode is very small in this case and gets added in a small channel. Anode1 and anode2 are denoted by An1 and An2. An12 denotes the histogram sum of pulse heights in both the anodes.

For further analysis, we chose only those events which fall under the peak of An12. These events correspond to 23 keV incoming photons. Below the peak, the events are a combination of X-rays $<$ 23 keV from generator and background cosmic rays. From all the events which fall under the peak of An12, we created the histogram of pulse heights in anode1 to the sum of pulse height in both anodes as shown in the right panels of Figure 6.4 for 90° polarization. The y-axis represents the number of events for a particular ratio value, normalized by the total number of events. In ratio histogram, small values (close to 0) denote those events for which the pulse height in anode1 was small. The value close to 1 is for those events when the pulse height in anode1 was large. Both these regions represent the events whose the charge is not divided between

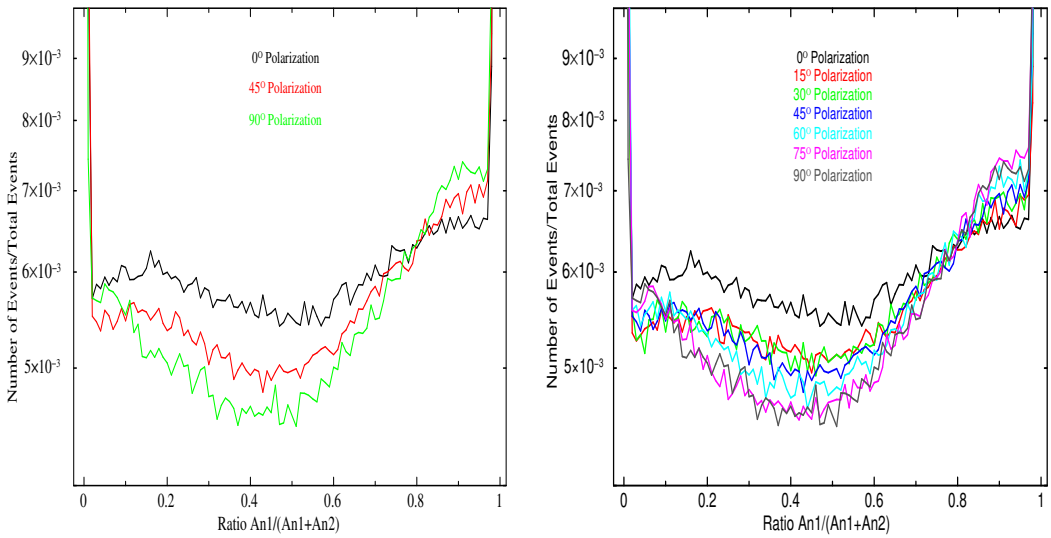

Fig. 6.5 Ratio histogram for different polarization angles.

anodes. The values in between are cases when charge divided into two anodes. This region is more important to us in our analysis as the charge division of charge track contains the information about polarization. We expect the ratio histogram pattern to be different for these values when shined with the polarized source at different angles.

The ratio histograms for polarized X-ray photons with different polarization with respect to anodes are shown in Figure 6.5. The pattern shape remains same for all the cases but are quantitatively different for the ratio 0.2-0.8. These ratio values corresponds to events with charge division between the two anodes. Left panel shows the ratio histograms for three different angles 0°, 45°, and 90°. The depth of histogram increases as the angle increases. The ratio histogram are shown for all 7 angles in right panel. The same behavior is seen this also with increase of depth with increasing angles.

The charge ratio histograms generated by varying orientation of the X-ray detector in the experimental setup shows its potential for X-ray polarization measurement. However, further investigations are required to quantify the shapes of the histograms with respect to the polarization angles, and degree of polarization. The dependence of the histogram shape variation on i) the energy of the X-ray photons, ii) gas pressure, iii) gas mixture, and iv) separation of the anode wires need to be investigated in detail to establish and optimize usage of this technique in astronomical X-ray polarization

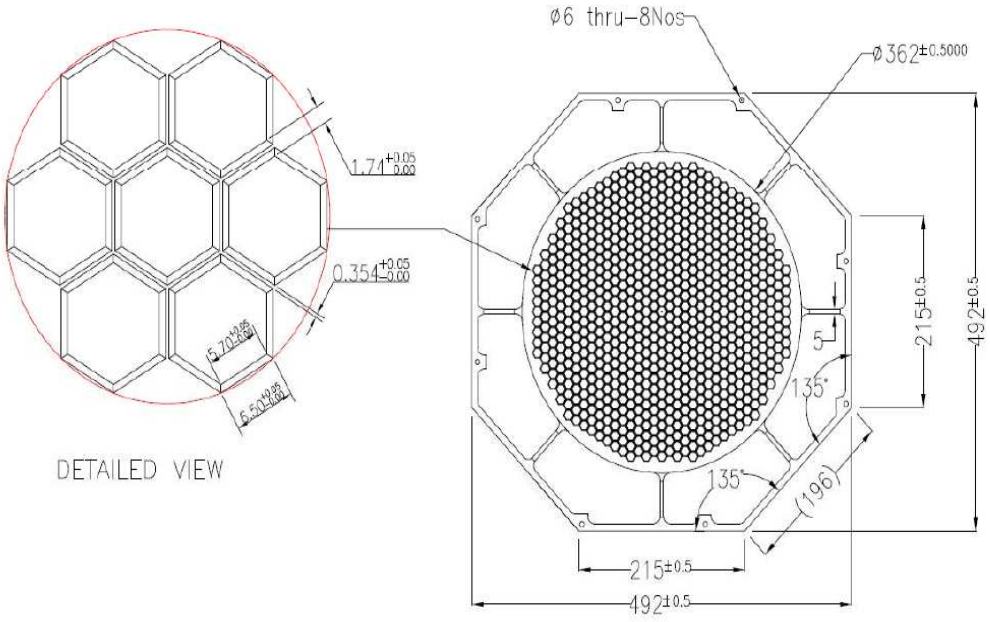

Fig. 6.6 A geometrical sketch of POLIX collimator. Unit of all length is in mm. A zoomed view of few cells is shown in the Left. Image Credit: Rishin P. V.

measurement.

6.2 Collimator Calibration Experiments for *POLIX*

POLIX is an X-ray polarimeter instrument based on Thomson scattering in the energy band of 8-30 keV. The aim of this instrument is to measure the polarization of X-ray sources, like the accretion-powered pulsars and black holes, etc. whose spectrum is dominant in this energy band. A complete understanding of its scientific instruments is paramount to the usage of *POLIX* in polarization measurement. For this, it needs to be well calibrated on the ground before its launch and in space after launch. The calibration for the *POLIX* is different from most other timing, spectroscopic, or imaging instruments due to its different objective, type of instrument, and operational requirements. Some of the important considerations for X-ray polarization measurements with *POLIX* are the following: identifying the cell-ID for a photon, precise timing of incoming photons, and dependence of detector gain and spectral resolution on various operational parameters. The calibration experiments on these aspects are underway

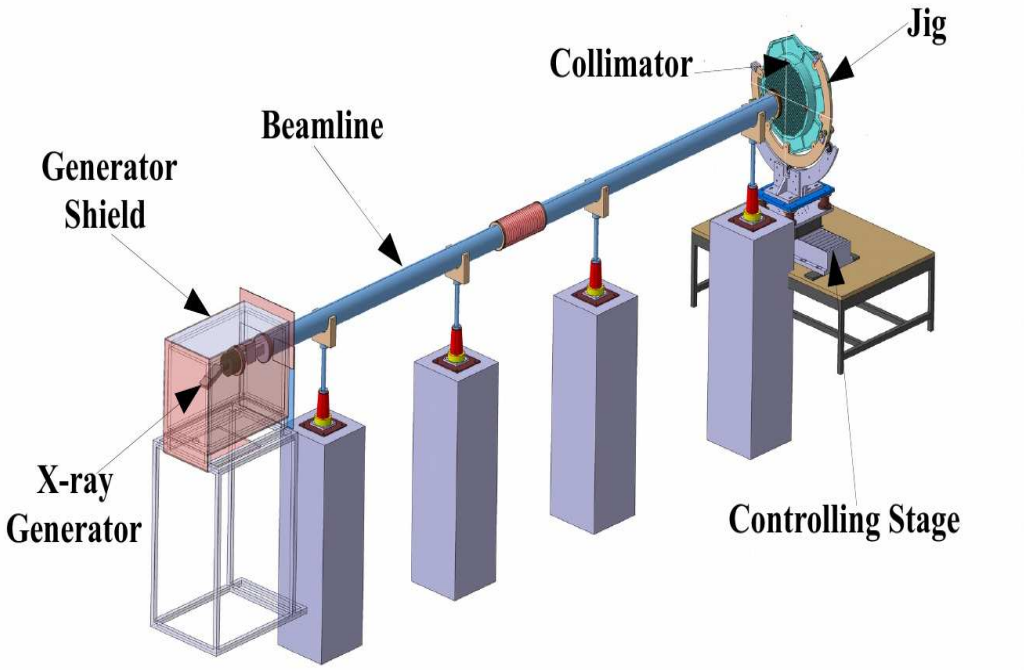

Fig. 6.7 Experimental setup for the collimator response calibration. Figure not the scale. Image Credit: Abhilash P Kulkarni.

separately. Some other considerations come into the picture due to design modification in components of *POLIX*. The *POLIX* collimator is designed with some improvements on classical collimators used in other instruments. It is made of 757 hexagonal cells, which are slightly tapered. Each hexagonal cell is made of two hexagonal openings, with the bigger hexagon being near the detector and the smaller hexagon being open to the sky. Each side of the smaller hexagon is 5.7 mm. Each side of the bigger hexagon is 6.5 mm. Depth of each cell is 200 mm. Figure 6.6 shows a geometrical sketch from the face on view. This leads to small decrease in its throughput and a significant flat-top angular response which mitigate the effect of small pointing error. These modifications also lead to a different angular response and different azimuthal distribution in the presence of an off-axis unpolarized X-ray source. Here, I describe the collimator calibration experiments which I have conducted on these aspects.

6.2.1 Collimator Angular Response

A collimator is used to restrict the FOV of an instrument to a few or possible one sources and avoid the contamination from other neighboring sources. About 50 bright

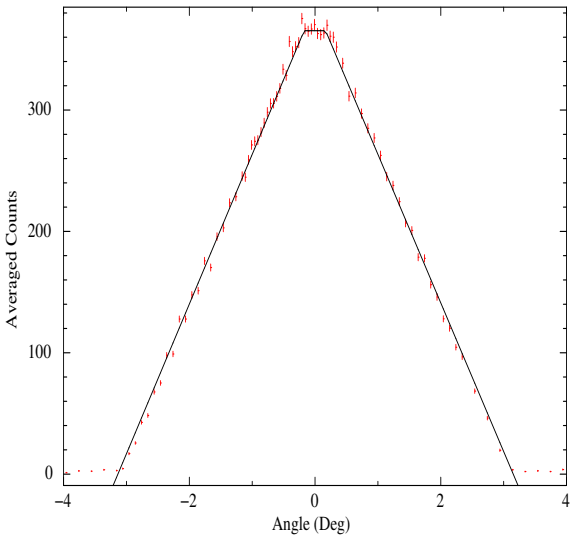

Fig. 6.8 Data and the fitted model of angular response of collimator.

X-ray sources are within the sensitivity range of *POLIX*, and many of these sources are in the plane of the Milky Way with angular separation between a fraction of a degree to several degrees. While a very small field of view is preferred for avoiding any other X-ray sources in the FOV, there are several limiting factors for FOV: increasing collimator mass, increasing dead area, and more stringent pointing requirement with smaller FOV. Considering all these aspects, a $3^\circ \times 3^\circ$ FOV at full width half maximum has been selected for *POLIX*. Polarization of incoming X-ray photons leads to the asymmetry in the distribution of scattered X-rays. However, a small pointing error may also lead to an asymmetrical azimuthal distribution of X-ray photons. The collimator is slightly tapered resulting into a flat-top angular response to mitigate the effect of small pointing error. The collimator response has an estimated angular extent of 6.68° with a flat-top of 0.44°.

The angular response is measured by scanning the collimator across its diameter at the different orientations to the direction of the incoming X-ray beam. A full scan of the collimator is needed to check the uniformity of collimator construction. A collimator calibration jig has been made for this purpose. The jig has a provision of height adjustment and angular orientation adjustment. The testing uses a micro-position controller motor with a translational stage and a rotational stage. X-ray sources in the lab have divergent beams. Such a beam will smoothen sharp feature in the collimator angular response. This is very important near the flat top part of the angular response. Hence, a small, non-divergent beam is required to measure the angular re-

sponse. To get a narrow beam at the detector, an X-ray beamline of 12 meter length is used, which is kept at $\sim 10^{-5}$ bar pressure of air. At the detector, a 1 mm slit is used to give a very narrow beam of $\sim 0.01°$. The experimental setup (see Figure 6.7) consists of an X-ray generator at one end of the beamline, the collimator on its jig placed on the controlling stage before the detector with a slit at the other end. A semiconductor detector, along with its processing unit, is used in this experiment. The photon counting mode of the detector is used for data acquisition. The starting orientation of the collimator is $-4°$ away from the direction of the incoming beam. At each angular position, the collimator is translated across its full length and then rotated by 0.2°. Near the direction of the beam, the collimator is rotated in steps of 0.1°, after every scan. As the collimator rotates away from the beam direction on the other side, the step size of rotation is again 0.2°, after every scan. The final scan is taken at $+4°$ away from the direction of the incoming beam.

The data is checked very carefully for any cell to cell variation in each scan. Data from each scan is added and averaged by the total time taken to complete each scan. Figure 6.8 shows averaged counts at each angular position. Data is fitted with box function with two slopes. The total angular coverage of collimator is found to be $\pm 3.25°$ with a flat-top of $\pm 0.18°$.

6.2.2 Collimator Calibration for the Presence of Unpolarized X-ray Source

If the X-ray source is on-axis, an equal number of X-ray photons fall on the scatterer at any azimuthal angle. However, due to a hexagonal construction of collimator cells, an off-axis X-ray source should produce a six-fold X-ray intensity pattern along the azimuthal direction. The shape and the amplitude of this modulation depend on the offset angle. It is due to the change in the projected area of the smaller hexagon onto the bigger hexagon as seen in Figure 6.9. The projected area is proportional to the number of photons which will go through the collimator and strike the scatterer. A polarized source will also produce a modulation pattern in the detector due to the asymmetric distribution of the scattered photons. The nature of modulation patterns will be different in two cases. The modulation pattern will be a superposition of these two patterns when there are two sources present in the FOV of POLIX . Hence, it is important to measure the modulation patterns due to an off-axis source at various offset angles for meaningful interpretation of polarization data. A sample modulation

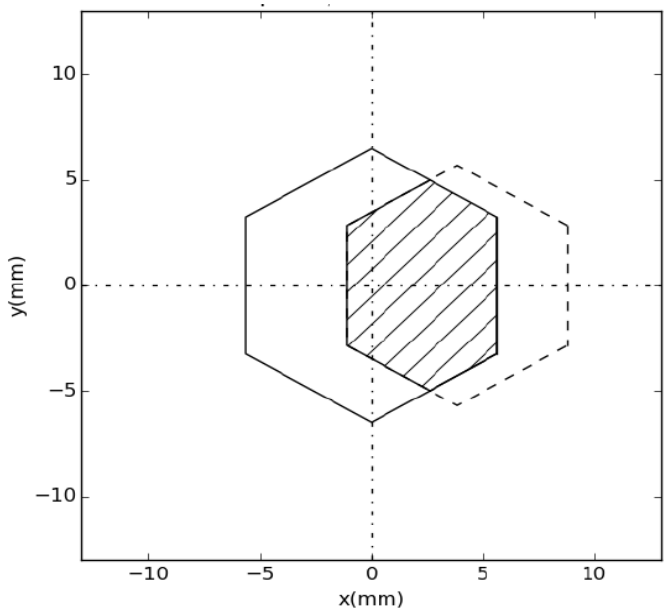

Fig. 6.9 Projection of front hexagon onto the back hexagon. The hatched area is area of overlap at this angular position. Image Credit: Nirmal Iyer.

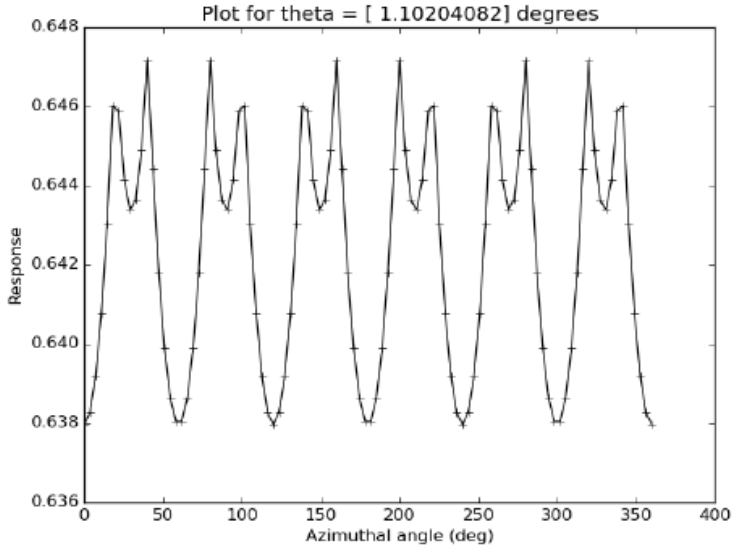

Fig. 6.10 Simulated pattern of collimator response for a source at an offset angle with respect to the viewing axis of the collimator. Image Credit: Nirmal Iyer.

Fig. 6.11 Small collimator used for the calibration of modulation pattern produced by an off-axis source due to the spin of satellite. Image Credit: Rishin P.V.

pattern is shown in Figure 6.10 for an unpolarized X-ray source at 1.1° offset angle.

A small proportional counter detector was made for this experiment. It is made of a single anode wire mounted on a Teflon spacer. The wire is made of 25 microns thick stainless steel (SS), coated with Gold. The detector housing works as a cathode. The detector has a gas port located at the side of the detector housing. The detector is closed with a top plate, and it is sealed with detector housing with the help of an O-ring. The incoming radiation enters through a 3cm × 3cm window, which is made of 50-micron thick mylar. The detector is filled with P10 gas (90% argon and 10% methane). In this experiment, we have used a small test collimator (See Figure 6.11) with identical hexagonal cells. The design and cell dimension of the small collimator is identical to final POLIX collimator except that it has a smaller number of cells.

The experimental setup (see Figure 6.12) consists of an X-ray generator at one end of the beamline. The collimator and detector, mounted together in front of the other end of the beamline. The collimator is mounted on a rotation stage. All the

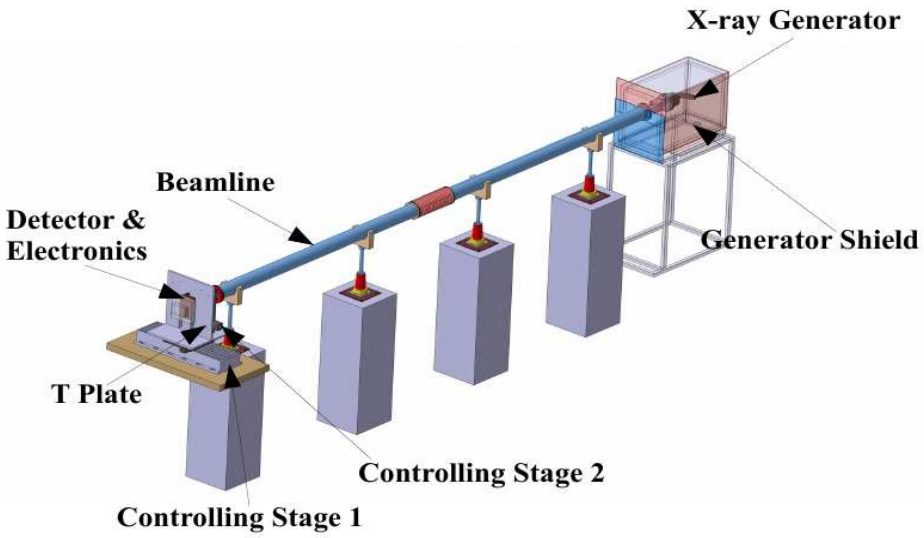

Fig. 6.12 Experimental Setup for modulation intensity variation of an offaxis source. Figure not to the scale. Image Credit: Abhilash P Kulkarni.

cells of the collimator are blocked, except one, using a 2 mm thick stainless steel cap. The detector is at the back of collimator mounted vertically on a T-plate. Both the detector and collimator are mounted on another rotary stage. The beam spot size is 0.15° at the position of the detector. The collimator axis is first aligned to the X-ray beam by scanning it in the horizontal direction. However there can be a small residual misalignment in the vertical direction. In addition, there can be a small misalignment between the collimator axis and the spin axis of the rotational stage on which the collimator is mounted. Intensity profile of X-rays in the proportional counter detector was obtained by rotating the collimator, first around the best aligned position and then by varying the collimator spin axis with respect to the beam line. The rotation speed of collimator was fixed at 0.4° sec^{-1}. 10 full rotation are completed at each offset angle. The full data is carefully examined for any variations between different cycles at particular offset. The data from 10 the rotation cycle is added and normalized to get the intensity modulation pattern. Modulation patterns at five angular positions are shown in Figure 6.13.

All the profiles show a single modulation over 360 degree rotation with an amplitude of about 4%. This is related to the unknown small angle between the collimator axis and the spin axis. With increasing offset angles between the spin-axis and the X-ray beam, a six fold modulation appears, which is quite prominent for 1.6 degree

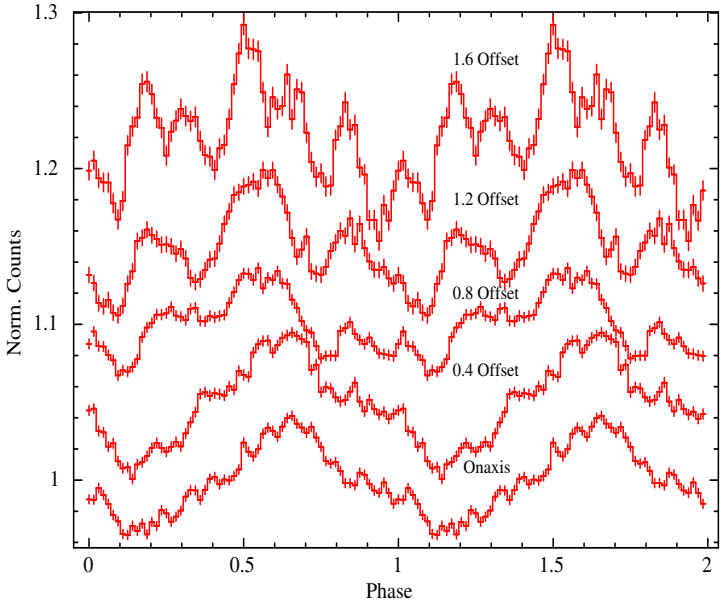

Fig. 6.13 Intensity Modulation Pattern due to the presence of secondary source at an offset. Modulation patterns are shift up by 0.05 for 0.4°, 0.8°, and 1.2° offset. Modulation pattern for 1.6° offset is shifted up by 0.08.

offset. The amplitude of the 6 fold modulation can be used to determine any offset between an X-ray source and spin-axis of the satellite. Any possible offset between spin axis of the satellite and the collimator axis can be determined from the single modulation over 360°.

Chapter 7

Summary and Future Works

7.1 Summary

In this thesis, we have reported the results from *AstroSat*-LAXPC observations of two HMXB pulsars and four INSs. The behavior of CRSF is investigated in two HMXB 4U 1907+09 and 4U 1538–522. The timing capability of LAXPC is demonstrated to study the isolated neutron stars of different properties: X-ray flux, pulse period, and pulse profile. In the experimental section of this thesis, we have reported the results of calibration experiments of *POLIX* to verify its angular response and study the effect of presence of a secondary source in the field. Also, we have reported the experimental results of a new polarization technique based on photo-electron interaction. The results are summarized below

- In chapter 3, we reported results from detailed timing and spectral study of two HMXB sources 4U 1538–522 and 4U 1907+09. We studied the energy dependence of pulse profiles of these two sources. The broad band coverage of LAXPC allows to study the pulse profile behavior in 3.0-80.0 keV with a single instrument. Both the sources show a strong energy dependence of the pulse profile with energy. The two peaks in the pulse profile of 4U 1907+09, vary differently with energy. The pulse fraction of primary peak increases from up to 40 keV and the it drop in 40.0-60.0 keV band. The secondary peak becomes weaker in the hard X-ray band and sharp change is seen near the CRSF energy. The secondary peak in the pulse profiles of 4U 1538–522, decreases in strength until it disappear for energy > 19 keV. The primary peak becomes narrow with energy with increase in pulse fraction from 48 % in 3.5-7.0 keV to 98 % in 40.0-60.0 keV band. Pulse fraction in the lower energy side of CRSF energy is higher compared to the en-

ergy band on the higher side. We carried out a pulse phase resolved spectroscopy of spectral parameters for both the sources with 10 independent phasebins. The *AstroSat* observations shows strong pulse phase variations of CRSF parameters for both the sources. The variation of CRSF parameters is studied in great detail for the first time, especially the CRSF depth. The variation of CRSF energy is found to be 10-15%. For 4U 1907+09, a positive correlations is reported between the CRSF energy and luminosity in range (0.8-3.0)$\times 10^{36}$ ergs^{-1} (Hemphill et al., 2013). The *AstroSat* observation rules out the possibility of such correlations in a wider luminosity range of (0.8-4.2)$\times 10^{36}$ ergs^{-1}. For 4U 1538–522, the *AstroSat* observations support the long term evolution of CRSF energy as suggested by an earlier *Suzaku* observation (Hemphill et al., 2016).

- In chapter 4, we carried out an energy resolved timing of two rotation powered pulsars (Crab nebula and PSR B1509–58) and two magnetars (1E 2259+586 and 1E 1048.1-593). For the Crab pulsar, the pulsations are detected up to 80.0 keV. The pulse fraction in both the peaks increase with energy. The pulse fraction in primary peak is higher in the lower energy bands but the change in pulse fraction of secondary peak is shaper than the primary peak. In the 60.0-80.0 keV band both peaks have same pulse fraction. For PSR B1509–58, a single peaked pulse profiles is detected upto 60.0 keV. For both the magnetars, the energy resolved timing analysis shows that the pulsations are detected only in 3.5-7.0 keV energy band.

- In chapter 5, we analyzed data from *XMM-Newton* and *RXTE* of HMXB pulsar IGR J16320-4751. There are many observations at different orbital phases of the binary, covering one full orbit for each instrument. We presented our attempt to derive the orbital parameters. We have presented the difficulties and limitations of the available data. We performed a spectral analysis of the *XMM-Newton* data. We found that the system has hydrogen like iron line at certain orbital phases, in addition to the neutral iron line which has been reported earlier. IGR J16320-4751 shows pulsations in the iron line band which indicates the presence of non-symmetric matter distribution in the system. X-ray spectrum in three *XMM-Newton* observations near the superior conjunction of the system shows a soft excess component which is suggested to be an emission by a collisionally

energized cloud in which the neutron star is embedded.

- In chapter 6, we have shown the results of X-ray experiments. For the photoelectron polarization detector, we have successfully demonstrated the concept of charge division using two radioactive sources Fe-55 and Cd-109 which emits the X-ray photons of 6 and 23 keV respectively. The charge division is very efficient for 23 keV photons. We performed a polarization experiment with 23 keV photons by changing the orientation of anodes in the detector with respect to the polarization direction of the incoming photons. The charge ratio histograms for the polarized X-rays with different polarization show a gradual change for increasing angles. This shows the potential of PE detector for X-ray polarization measurement.

  The experimentally measured angular response of *POLIX* collimator has a total opening of $\pm 3.25^\circ$ with a flat-top of $\pm 0.18^\circ$. We have experimentally found out the intensity modulation patterns due to the presence of a secondary source in the field of view of *POLIX*. The patterns have two component: 1) A single modulation over 360° rotation related to the unknown small angle between the collimator axis and the spin axis. 2) A six fold modulation due to secondary source which is most prominent at 1.6°.

7.2 Future Works

– The study of CRSF in HMXBs is a rich field and has the potential to give insight about their accretion geometry and magnetic field geometry. The pulse phase resolved spectroscopy of CRSF in 4U 1907+09 and 4U 1538–522 demonstrates the capability of LAXPC to study these features. These are early works on CRSF in accretion-powered pulsars with *AstroSat* and opens up the possibility of such studies for many other sources. The *AstroSat* observation of 4U 1907+09 was carried out at 0.5 orbital phase away the peak of orbital intensity profile. We plan to propose one more observation 4U 1907+09 with *AstroSat* at the peak in the orbital profile which, together with the already existing measurements, will allow investigation

of the cyclotron line charactirstic over a wider range of X-ray luminosity.

For both the sources, we have data from SXT and CZTI instruments of *AstroSat*. We plan to analyze this data to get more information about these sources, especially the absorption column density and the iron emission line.

– The experiments with photo-electron polarimeter demonstrates its capability for X-ray polarization measurements. We plan to perform more experiments to characterize the working parameters of this detector. The performance of this detector depends on the energy of the incoming photons, type of gas, gas pressure, and separation between two anodes. We plan to investigate all these aspects in more details to find out the suitability of this technique for more sensitive astronomical observations. In addition, we want to simulate the detector environment using *GEANT* software to aid the experiments in gaining these insights.

References

A. A. Abdo and et al. Fermi Large Area Telescope Observations of the Crab Pulsar And Nebula. *ApJ*, 708:1254–1267, January 2010. doi: 10.1088/0004-637X/708/2/1254.

N. Aftab and B. Paul. X-ray reprocessing: Through eclipse spectra of high and low mass X-ray binaries. In J.-U. Ness and S. Migliari, editors, *The X-ray Universe 2017*, page 28, October 2017.

P. C. Agrawal. A broad spectral band Indian Astronomy satellite Astrosat. *Advances in Space Research*, 38:2989–2994, January 2006. doi: 10.1016/j.asr.2006.03.038.

P. C. Agrawal. AstroSat: From Inception to Realization and Launch. *Journal of Astrophysics and Astronomy*, 38:27, June 2017. doi: 10.1007/s12036-017-9449-6.

P. C. Agrawal, J. S. Yadav, H. M. Antia, Dhiraj Dedhia, P. Shah, Jai Verdhan Chauhan, R. K. Manchand a, V. R. Chitnis, V. M. Gujar, and Tilak Katoch. Large Area X-Ray Proportional Counter (LAXPC) Instrument on AstroSat and Some Preliminary Results from its Performance in the Orbit. *Journal of Astrophysics and Astronomy*, 38(2):30, Jun 2017. doi: 10.1007/s12036-017-9451-z.

S. G. Alexander and P. Meszaros. Cyclotron Harmonics in Accreting Pulsars and Gamma-Ray Bursters: Effect of Two-Photon Processes. *ApJ*, 372:565, May 1991. doi: 10.1086/170001.

E. Aliu, et al., and MAGIC Collaboration. Observation of Pulsed γ-Rays Above 25 GeV from the Crab Pulsar with MAGIC. *Science*, 322(5905):1221, Nov 2008. doi: 10.1126/science.1164718.

M. Ali Alpar, Askin Ankay, and Efe Yazgan. Pulsar Spin-down by a Fallback Disk and the P-P Diagram. *ApJ*, 557(1):L61–L65, Aug 2001. doi: 10.1086/323140.

E. Anders and N. Grevesse. Abundances of the elements: Meteoritic and solar. *Geochimica Cosmochimica Acta*, 53(1):197–214, Jan 1989. doi: 10.1016/0016-7037(89)90286-X.

H. M. Antia, J. S. Yadav, P. C. Agrawal, J. Verdhan Chauhan, R. K. Manchanda, V. Chitnis, B. Paul, D. Dedhia, P. Shah, V. M. Gujar, T. Katoch, V. N. Kurhade, P. Madhwani, T. K. Manojkumar, V. A. Nikam, A. S. Pandya, J. V. Parmar, D. M. Pawar, M. Pahari, R. Misra, K. H. Navalgund, R. Pandiyan, K. S. Sharma, and K. Subbarao. Calibration of the Large Area X-Ray Proportional Counter (LAXPC) Instrument on board AstroSat. *ApJS*, 231:10, July 2017. doi: 10.3847/1538-4365/aa7a0e.

R. A. Araya and A. K. Harding. Cyclotron Line Features from Near-critical Magnetic Fields: The Effect of Optical Depth and Plasma Geometry. *ApJ*, 517:334–354, May 1999. doi: 10.1086/307157.

R. F. Archibald, V. M. Kaspi, C. Y. Ng, K. N. Gourgouliatos, D. Tsang, P. Scholz, A. P. Beardmore, N. Gehrels, and J. A. Kennea. An anti-glitch in a magnetar. *Nature*, 497(7451):591–593, May 2013. doi: 10.1038/nature12159.

R. F. Archibald, V. M. Kaspi, C. Y. Ng, P. Scholz, A. P. Beardmore, N. Gehrels, and J. A. Kennea. Repeated, Delayed Torque Variations Following X-Ray Flux Enhancements in the Magnetar 1E 1048.1-5937. *ApJ*, 800(1):33, Feb 2015. doi: 10.1088/0004-637X/800/1/33.

K. A. Arnaud. XSPEC: The First Ten Years. In George H. Jacoby and Jeannette Barnes, editors, *Astronomical Data Analysis Software and Systems V*, volume 101 of *Astronomical Society of the Pacific Conference Series*, page 17, Jan 1996.

R. Basak, S. Iyyani, V. Chand, T. Chattopadhyay, D. Bhattacharya, A. R. Rao, and S. V. Vadawale. Surprise in simplicity: an unusual spectral evolution of a single pulse GRB 151006A. *MNRAS*, 472(1):891–903, Nov 2017. doi: 10.1093/mnras/stx1970.

M. M. Basko and R. A. Sunyaev. Radiative transfer in a strong magnetic field and accreting X-ray pulsars. *A&A*, 42:311–321, September 1975.

M. M. Basko and R. A. Sunyaev. The limiting luminosity of accreting neutron stars with magnetic fields. *MNRAS*, 175:395–417, May 1976.

A. Baykal, S. Ç. İnam, and E. Beklen. Evidence of a change in the long-term spin-down rate of the X-ray pulsar 4U 1907+09. *MNRAS*, 369(4):1760–1764, Jul 2006. doi: 10.1111/j.1365-2966.2006.10412.x.

Altan Baykal, C. Inam, M. Ali Alpar, Jean in't Zand, and Tod Strohmayer. The steady spin-down rate of 4U 1907+09. *MNRAS*, 327(4):1269–1272, Nov 2001. doi: 10.1046/j.1365-8711.2001.04804.x.

P. A. Becker. Dynamical Structure of Radiation-dominated Pulsar Accretion Shocks. *ApJ*, 498:790–801, May 1998. doi: 10.1086/305568.

P. A. Becker, D. Klochkov, G. Schönherr, O. Nishimura, C. Ferrigno, I. Caballero, P. Kretschmar, M. T. Wolff, J. Wilms, and R. Staubert. Spectral formation in accreting X-ray pulsars: bimodal variation of the cyclotron energy with luminosity. *A&A*, 544:A123, August 2012. doi: 10.1051/0004-6361/201219065.

R. H. Becker, J. H. Swank, E. A. Boldt, S. S. Holt, P. J. Serlemitsos, S. H. Pravdo, and J. R. Saba. A1540-53, an eclipsing X-ray binary pulsator. *ApJ*, 216:L11–L14, August 1977. doi: 10.1086/182498.

R. Bellazzini, F. Angelini, L. Baldini, A. Brez, E. Costa, L. Latronico, N. Lumb, M. M. Massai, N. Omodei, and P. Soffitta. X-ray polarimetry with a micro pattern gas detector with pixel readout. *IEEE Transactions on Nuclear Science*, 49(3):1216–1220, Jun 2002. doi: 10.1109/TNS.2002.1039640.

V. Bhalerao, D. Bhattacharya, A. Vibhute, P. Pawar, A. R. Rao, M. K. Hingar, R. Khanna, A. P. K. Kutty, J. P. Malkar, M. H. Patil, Y. K. Arora, S. Sinha, P. Priya, E. Samuel, S. Sreekumar, P. Vinod, N. P. S. Mithun, S. V. Vadawale, N. Vagshette, K. H. Navalgund, K. S. Sarma, R. Pandiyan, S. Seetha, and K. Subbarao. The Cadmium Zinc Telluride Imager on AstroSat. *Journal of Astrophysics and Astronomy*, 38:31, June 2017. doi: 10.1007/s12036-017-9447-8.

D. Bhattacharya. Observing Compact Stars with AstroSat. *Journal of Astrophysics and Astronomy*, 38:51, September 2017. doi: 10.1007/s12036-017-9461-x.

Dipankar Bhattacharya, Ralph A. M. J. Wijers, Jan W. Hartman, and Frank Verbunt. On the decay of the magnetic fields of single radio pulsars. *A&A*, 254:198–212, Feb 1992.

J. K. Black, R. G. Baker, P. Deines-Jones, J. E. Hill, and K. Jahoda. X-ray polarimetry with a micropattern TPC. *Nuclear Instruments and Methods in Physics Research A*, 581(3):755–760, Nov 2007. doi: 10.1016/j.nima.2007.08.144.

P. A. Boldin, S. S. Tsygankov, and A. A. Lutovinov. On timing and spectral characteristics of the X-ray pulsar 4U 0115+63: Evolution of the pulsation period and the cyclotron line energy. *Astronomy Letters*, 39(6):375–388, Jun 2013. doi: 10.1134/S1063773713060029.

A. A. Breeveld, T. S. Poole, C. H. James, A. J. Blustin, S. R. Rosen, W. Landsman, P. Boyd, C. Gronwall, S. Holland, S. D. Hunsberger, M. Ivanushkina, K. O. Mason, K. McGowan, M. de Pasquale, P. W. A. Roming, and M. Still. On-orbit calibration of the Ultraviolet/Optical Telescope (UVOT) on swift: part 2. In O. H. W. Siegmund, editor, *UV, X-Ray, and Gamma-Ray Space Instrumentation for Astronomy XIV*, volume 5898 of *Proc. SPIE*, pages 391–402, August 2005. doi: 10.1117/12.616817.

John C. Brown. The Deduction of Energy Spectra of Non-Thermal Electrons in Flares from the Observed Dynamic Spectra of Hard X-Ray Bursts. *Sol. Phys.*, 18(3):489–502, Jul 1971. doi: 10.1007/BF00149070.

L. Burderi, T. Di Salvo, N. R. Robba, A. La Barbera, and M. Guainazzi. The 0.1-100 KEV Spectrum of Centaurus X-3: Pulse Phase Spectroscopy of the Cyclotron Line and Magnetic Field Structure. *ApJ*, 530:429–440, February 2000. doi: 10.1086/308336.

D. N. Burrows, J. E. Hill, J. A. Nousek, A. A. Wells, G. Chincarini, A. F. Abbey, A. P. Beardmore, J. Bosworth, H. W. Bräuninger, W. Burkert, S. Campana, M. Capalbi, W. Chang, O. Citterio, M. J. Freyberg, P. Giommi, G. D. Hartner, R. Killough, B. Kittle, R. Klar, C. Mangels, M. McMeekin, B. J. Miles, A. Moretti, K. Mori, D. C. Morris, K. Mukerjee, J. P. Osborne, A. D. T. Short, G. Tagliaferri, F. Tamburelli, D. J. Watson, R. Willingale, and M. E. Zugger. The Swift X-Ray Telescope. In K. A. Flanagan and O. H. W. Siegmund, editors, *X-Ray and Gamma-Ray Instrumentation for Astronomy XIII*, volume 5165 of *Proc. SPIE*, pages 201–216, February 2004. doi: 10.1117/12.504868.

Ş. Şahiner, S. Ç. Inam, and A. Baykal. A comprehensive study of RXTE and INTEGRAL observations of the X-ray pulsar 4U 1907+09. *ApJ*, 216:L11–L14, August 1977. doi: 10.1086/182498.

I. Caballero, P. Kretschmar, A. Santangelo, R. Staubert, D. Klochkov, A. Camero, C. Ferrigno, M. H. Finger, I. Kreykenbohm, V. A. McBride, K. Pottschmidt, R. E. Rothschild, G. Schönherr, A. Segreto, S. Suchy, J. Wilms, and C. A. Wilson. A 0535+26 in the August/September 2005 outburst observed by RXTE and INTEGRAL. *A&A*, 465:L21–L24, April 2007. doi: 10.1051/0004-6361:20067032.

A. Celotti and G. Matt. Polarization Properties of Synchrotron Self-Compton Emission. *MNRAS*, 268:451, May 1994. doi: 10.1093/mnras/268.2.451.

Vikas Chand, Tanmoy Chattopadhyay, Gor Oganesyan, A. R. Rao, Santosh V. Vadawale, Dipankar Bhattacharya, V. B. Bhalerao, and Kuntal Misra. AstroSat-CZTI Detection of Variable Prompt Emission Polarization in GRB 171010A. *ApJ*, 874(1):70, Mar 2019. doi: 10.3847/1538-4357/ab0826.

Tanmoy Chattopadhyay, Santosh V. Vadawale, E. Aarthy, N. P. S. Mithun, Vikas Chand, Rupal Basak, A. R. Rao, Sujay Mate, Vidushi Sharma, Varun Bhalerao, and Dipankar Bhattacharya. Prompt emission polarimetry of Gamma Ray Bursts with ASTROSAT CZT-Imager. *arXiv e-prints*, art. arXiv:1707.06595, Jul 2017.

S. Chaty, F. Rahoui, C. Foellmi, J. A. Tomsick, J. Rodriguez, and R. Walter. Multi-wavelength observations of Galactic hard X-ray sources discovered by INTEGRAL. I. The nature of the companion star. *A&A*, 484:783–800, June 2008. doi: 10.1051/0004-6361:20078768.

M. Chauvin, H. G. Florén, M. Friis, M. Jackson, T. Kamae, J. Kataoka, T. Kawano, M. Kiss, V. Mikhalev, T. Mizuno, N. Ohashi, T. Stana, H. Tajima, H. Takahashi, N. Uchida, and M. Pearce. Accretion geometry of the black-hole binary Cygnus X-1 from X-ray polarimetry. *Nature Astronomy*, 2:652–655, Jun 2018. doi: 10.1038/s41550-018-0489-x.

G. W. Clark. The Orbit of the Binary X-Ray Pulsar 4U 1538-52 from Rossi X-Ray Timing Explorer Observations. *ApJ*, 542:L131–L133, October 2000. doi: 10.1086/312926.

G. W. Clark, J. W. Woo, F. Nagase, K. Makishima, and T. Sakao. Discovery of a cyclotron absorption line in the spectrum of the binary X-ray pulsar 4U 1538 - 52 observed by GINGA. *ApJ*, 353:274–280, April 1990. doi: 10.1086/168614.

W. J. Cocke, M. J. Disney, and D. J. Taylor. Discovery of Optical Signals from Pulsar NP 0532. *Nature*, 221:525–527, February 1969. doi: 10.1038/221525a0.

R. Corbet, L. Barbier, S. Barthelmy, J. Cummings, E. Fenimore, N. Gehrels, D. Hullinger, H. Krimm, C. Markwardt, D. Palmer, A. Parsons, T. Sakamoto, G. Sato, J. Tueller, and Swift-Survey Team. Swift/BAT Discovery of the Orbital Period of IGR J16320-4751. *The Astronomer's Telegram*, 649, November 2005.

Enrico Costa, Paolo Soffitta, Ronaldo Bellazzini, Alessandro Brez, Nicholas Lumb, and Gloria Spandre. An efficient photoelectric X-ray polarimeter for the study of black holes and neutron stars. *Nature*, 411(6838):662–665, Jun 2001.

N. L. J. Cox, L. Kaper, and M. R. Mokiem. VLT/UVES spectroscopy of the O supergiant companion to <ASTROBJ>4U 1907+09</ASTROBJ>(7). *A&A*, 436: 661–669, June 2005. doi: 10.1051/0004-6361:20040511.

G. Cusumano, T. di Salvo, L. Burderi, M. Orlandini, S. Piraino, N. Robba, and A. Santangelo. Detection of a cyclotron line and its second harmonic in 4U1907+09. *A&A*, 338:L79–L82, October 1998.

G. Cusumano, T. Mineo, E. Massaro, L. Nicastro, E. Trussoni, S. Massaglia, W. Hermsen, and L. Kuiper. The curved X-ray spectrum of PSR B1509-58 observed with BeppoSAX. *A&A*, 375:397–404, Aug 2001. doi: 10.1051/0004-6361:20010884.

Rim Dib and Victoria M. Kaspi. 16 yr of RXTE Monitoring of Five Anomalous X-Ray Pulsars. *ApJ*, 784(1):37, Mar 2014. doi: 10.1088/0004-637X/784/1/37.

Rim Dib, Victoria M. Kaspi, and Fotis P. Gavriil. 10 Years of RXTE Monitoring of Five Anomalous X-Ray Pulsars. In C. Bassa, Z. Wang, A. Cumming, and V. M. Kaspi, editors, *40 Years of Pulsars: Millisecond Pulsars, Magnetars and More*, volume 983 of *American Institute of Physics Conference Series*, pages 262–264, Feb 2008. doi: 10.1063/1.2900157.

B. Dorman and K. A. Arnaud. Redesign and Reimplementation of XSPEC. In Jr. Harnden, F. R., Frances A. Primini, and Harry E. Payne, editors, *Astronomical Data Analysis Software and Systems X*, volume 238 of *Astronomical Society of the Pacific Conference Series*, page 415, Jan 2001.

V. Doroshenko, S. S. Tsygankov, A. A. Mushtukov, A. A. Lutovinov, A. Santangelo, V. F. Suleimanov, and J. Poutanen. Luminosity dependence of the cyclotron line and evidence for the accretion regime transition in V 0332+53. *MNRAS*, 466:2143–2150, April 2017. doi: 10.1093/mnras/stw3236.

M. Dovčiak, F. Muleri, R. W. Goosmann, V. Karas, and G. Matt. Light-bending Scenario for Accreting Black Holes in X-ray Polarimetry. *ApJ*, 731(1):75, Apr 2011. doi: 10.1088/0004-637X/731/1/75.

M. Dovčiak, F. Muleri, R. W. Goosmann, V. Karas, and G. Matt. Polarization in lamp-post model of black-hole accretion discs. In *Journal of Physics Conference Series*, volume 372, page 012056, Jul 2012. doi: 10.1088/1742-6596/372/1/012056.

Robert C. Duncan and Christopher Thompson. Formation of Very Strongly Magnetized Neutron Stars: Implications for Gamma-Ray Bursts. *ApJ*, 392:L9, Jun 1992. doi: 10.1086/186413.

Martin Durant and Marten H. van Kerkwijk. Distances to Anomalous X-Ray Pulsars Using Red Clump Stars. *ApJ*, 650(2):1070–1081, Oct 2006. doi: 10.1086/506380.

Wilhelm J. Egle, Wolfgang Hafner, Axel Matthes, Georg Willma, Alexander Ilg, and Heinz Schiehle. Fabrication of segmented Wolter type-1 mandrels for the Constellation-X mirror development program. In Oberto Citterio and Stephen L. O'Dell, editors, *Optics for EUV, X-Ray, and Gamma-Ray Astronomy*, volume 5168 of *Society of Photo-Optical Instrumentation Engineers (SPIE) Conference Series*, pages 157–167, Feb 2004a. doi: 10.1117/12.507733.

Wilhelm J. Egle, Axel Matthes, Georg Willma, Alexander Ilg, Andy Schmidt, and Andreas Seifert. Figuring, polishing, metrology, and performance: analyses of Wolter type 1 forming mandrels for the Constellation-X mirror development program. In Günther Hasinger and Martin J. L. Turner, editors, *UV and Gamma-Ray Space Telescope Systems*, volume 5488 of *Society of Photo-Optical Instrumentation Engineers (SPIE) Conference Series*, pages 351–360, Oct 2004b. doi: 10.1117/12.563521.

A. G. Emslie and J. C. Brown. The polarization and directivity of solar-flare hard X-ray bremsstrahlung from a thermal source. *ApJ*, 237:1015–1023, May 1980. doi: 10.1086/157947.

Teruaki Enoto, Kazuo Makishima, Yukikatsu Terada, Tatehiro Mihara, Kazuhiro Nakazawa, Tsuyoshi Ueda, Tadayasu Dotani, Motohide Kokubun, Fumiaki Nagase, Sachindra Naik, Motoko Suzuki, Motoki Nakajima, and Hiromitsu Takahashi. Suzaku Observations of Hercules X-1: Measurements of the Two Cyclotron Harmonics. *PASJ*, 60:S57, Jan 2008. doi: 10.1093/pasj/60.sp1.S57.

Y. Evangelista. On-ground characterization of the IXPE polarization angle knowledge. In *Society of Photo-Optical Instrumentation Engineers (SPIE) Conference Series*, volume 10397 of *Society of Photo-Optical Instrumentation Engineers (SPIE) Conference Series*, page 103971H, August 2017. doi: 10.1117/12.2275235.

A. C. Fabian, D. R. Wilkins, J. M. Miller, R. C. Reis, C. S. Reynolds, E. M. Cackett, M. A. Nowak, G. G. Pooley, K. Pottschmidt, J. S. Sand ers, R. R. Ross, and J. Wilms. On the determination of the spin of the black hole in Cyg X-1 from X-ray reflection spectra. *MNRAS*, 424(1):217–223, Jul 2012. doi: 10.1111/j.1365-2966.2012.21185.x.

G. G. Fahlman and P. C. Gregory. The pulsation period and possible orbit of 1E2259+586. In J. Danziger and P. Gorenstein, editors, *Supernova Remnants and their X-ray Emission*, volume 101 of *IAU Symposium*, pages 445–453, Jan 1983.

M. Falanga, E. Bozzo, A. Lutovinov, J. M. Bonnet-Bidaud, Y. Fetisova, and J. Puls. Ephemeris, orbital decay, and masses of ten eclipsing high-mass X-ray binaries. *A&A*, 577:A130, May 2015. doi: 10.1051/0004-6361/201425191.

C. Ferrigno, P. A. Becker, A. Segreto, T. Mineo, and A. Santangelo. Study of the accreting pulsar 4U 0115+63 using a bulk and thermal Comptonization model. *A&A*, 498(3):825–836, May 2009. doi: 10.1051/0004-6361/200809373.

L. Foschini, J. A. Tomsick, J. Rodriguez, R. Walter, A. Goldwurm, S. Corbel, and P. Kaaret. High-energy emission from IGR J16320-4751. In V. Schoenfelder, G. Lichti, and C. Winkler, editors, *5th INTEGRAL Workshop on the INTEGRAL Universe*, volume 552 of *ESA Special Publication*, pages 247–252, October 2004.

S. Fritz, I. Kreykenbohm, J. Wilms, R. Staubert, F. Bayazit, K. Pottschmidt, J. Rodriguez, and A. Santangelo. A torque reversal of 4U 1907+09. *A&A*, 458:885–893, November 2006. doi: 10.1051/0004-6361:20065557.

Felix Fuerst, K. Pottschmidt, J. Wilms, J. Tomsick, M. Bachetti, S. E. Boggs, F. Christensen, W. W. Craig, B. Grefenstette, C. J. Hailey, F. Harrison, K. Madsen, J. M. Miller, D. Stern, D. Walton, and W. Zhang. NuSTAR discovery of a luminosity dependent cyclotron line energy in Vela X-1. In *American Astronomical Society Meeting Abstracts #223*, volume 216 of *American Astronomical Society Meeting Abstracts*, pages L11–L14, August 2014. doi: 10.1086/182498.

F. Fürst, K. Pottschmidt, H. Miyasaka, V. Bhalerao, M. Bachetti, S. E. Boggs, F. E. Christensen, W. W. Craig, V. Grinberg, C. J. Hailey, F. A. Harrison, J. A. Kennea, F. Rahoui, D. Stern, S. P. Tendulkar, J. A. Tomsick, D. J. Walton, J. Wilms, and W. W. Zhang. Distorted Cyclotron Line Profile in Cep X-4 as Observed by NuSTAR. *ApJ*, 806(2):L24, Jun 2015. doi: 10.1088/2041-8205/806/2/L24.

B. M. Gaensler, K. T. S. Brazier, R. N. Manchester, S. Johnston, and A. J. Green. SNR G320.4-01.2 and PSR B1509-58: new radio observations of a complex interacting system. *MNRAS*, 305:724–736, May 1999. doi: 10.1046/j.1365-8711.1999.02500.x.

M. Y. Ge, F. J. Lu, J. L. Qu, S. J. Zheng, Y. Chen, and D. W. Han. X-Ray Phase-resolved Spectroscopy of PSRs B0531+21, B1509-58, and B0540-69 with RXTE. *ApJS*, 199:32, April 2012. doi: 10.1088/0067-0049/199/2/32.

U. Geppert and V. Urpin. Accretion-driven magnetic field decay in neutron stars. *MNRAS*, 271:490, Nov 1994. doi: 10.1093/mnras/271.2.490.

R. Giacconi, E. Kellogg, P. Gorenstein, H. Gursky, and H. Tananbaum. An X-Ray Scan of the Galactic Plane from UHURU. *ApJ*, 165:L27, April 1971. doi: 10.1086/180711.

R. Giacconi, S. Murray, H. Gursky, E. Kellogg, E. Schreier, and H. Tananbaum. The Uhuru catalog of X-ray sources. *ApJ*, 216:L11–L14, August 1977. doi: 10.1086/182498.

A. Giménez-García, J. M. Torrejón, W. Eikmann, S. Martínez-Núñez, L. M. Oskinova, J. J. Rodes-Roca, and G. Bernabéu. An XMM-Newton view of FeKα in High Mass X-rays Binaries. In A. J. Cenarro, F. Figueras, C. Hernández-Monteagudo, J. Trujillo Bueno, and L. Valdivielso, editors, *Highlights of Spanish Astrophysics VIII*, pages 482–487, May 2015.

I. N. Gnedin and R. A. Sunyaev. Polarization of optical and X-radiation from compact thermal sources with magnetic field. *A&A*, 36:379–394, December 1974.

R. A. Gowen, B. A. Cooke, R. E. Griffiths, and M. J. Ricketts. An upper limit to the linear X-ray polarization of Sco X-1. *MNRAS*, 179:303–310, May 1977. doi: 10.1093/mnras/179.3.303.

P. C. Gregory and G. G. Fahlman. An extraordinary new celestial X-ray source. *Nature*, 287(5785):805–806, Oct 1980. doi: 10.1038/287805a0.

C. Greiveldinger, S. Caucino, S. Massaglia, H. Oegelman, and E. Trussoni. PSR 1509-58 and Its Plerionic Environment. *ApJ*, 454:855, Dec 1995. doi: 10.1086/176538.

F. Haberl, N. E. White, and T. R. Kallman. An EXOSAT X-ray observation of one orbital cycle of 4U 1700-37/HD 153919. *ApJ*, 343:409–425, August 1989. doi: 10.1086/167714.

Frank Haberl. The magnificent seven: magnetic fields and surface temperature distributions. *Ap&SS*, 308(1-4):181–190, Apr 2007. doi: 10.1007/s10509-007-9342-x.

W. A. Heindl, W. Coburn, D. E. Gruber, M. R. Pelling, R. E. Rothschild, J. Wilms, K. Pottschmidt, and R. Staubert. Discovery of a Third Harmonic Cyclotron Resonance Scattering Feature in the X-Ray Spectrum of 4U 0115+63. *ApJ*, 521(1): L49–L53, Aug 1999. doi: 10.1086/312172.

W. A. Heindl, R. E. Rothschild, W. Coburn, R. Staubert, J. Wilms, I. Kreykenbohm, and P. Kretschmar. Timing and Spectroscopy of Accreting X-ray Pulsars: the State of Cyclotron Line Studies. In Philip Kaaret, Frederick K. Lamb, and Jean H. Swank, editors, *X-ray Timing 2003: Rossi and Beyond*, volume 714 of *American Institute of Physics Conference Series*, pages 323–330, Jul 2004. doi: 10.1063/1.1781049.

P. B. Hemphill, R. E. Rothschild, I. Caballero, K. Pottschmidt, M. Kühnel, F. Fürst, and J. Wilms. Measurements of Cyclotron Features and Pulse Periods in the High-mass X-Ray Binaries 4U 1538-522 and 4U 1907+09 with the International Gamma-Ray Astrophysics Laboratory. *ApJ*, 777:61, November 2013. doi: 10.1088/0004-637X/777/1/61.

P. B. Hemphill, R. E. Rothschild, A. Markowitz, F. Fürst, K. Pottschmidt, and J. Wilms. A Clumpy Stellar Wind and Luminosity-dependent Cyclotron Line Revealed by the First Suzaku Observation of the High-mass X-Ray Binary 4U 1538-522. *ApJ*, 792:14, September 2014. doi: 10.1088/0004-637X/792/1/14.

P. B. Hemphill, R. E. Rothschild, F. Fürst, V. Grinberg, D. Klochkov, P. Kretschmar, K. Pottschmidt, R. Staubert, and J. Wilms. Evidence for an evolving cyclotron line energy in 4U 1538-522. *MNRAS*, 458:2745–2761, May 2016. doi: 10.1093/mnras/stw470.

P. B. Hemphill, R. E. Rothschild, D. M. Cheatham, F. Fürst, P. Kretschmar, M. Kühnel, K. Pottschmidt, R. Staubert, J. Wilms, and M. T. Wolff. The First NuSTAR Observation of 4U 1538-522: Updated Orbital Ephemeris and a Strengthened Case for an Evolving Cyclotron Line Energy. *ApJ*, 873:62, March 2019. doi: 10.3847/1538-4357/ab03d3.

J. A. Z. Heras, S. Chaty, L. Prat, and J. Rodriguez. Spectral Evolution Along the Orbit of IGR J16320-4751 with XMM-Newton. In J. Rodriguez and P. Ferrando, editors, *American Institute of Physics Conference Series*, volume 1126 of *American Institute of Physics Conference Series*, pages 313–315, May 2009. doi: 10.1063/1.3149440.

J. J. Hester. The Crab Nebula : an astrophysical chimera. *ARA&A*, 46:127–155, Sep 2008. doi: 10.1146/annurev.astro.45.051806.110608.

R. C. Hickox, R. Narayan, and T. R. Kallman. Origin of the Soft Excess in X-Ray Pulsars. *ApJ*, 614:881–896, October 2004. doi: 10.1086/423928.

J. P. Hughes. A new transient pulsar in the Small Magellanic Cloud with an unusual x-ray spectrum. *ApJ*, 427:L25–L28, May 1994. doi: 10.1086/187356.

J. J. M. in 't Zand, A. Baykal, and T. E. Strohmayer. Recent X-Ray Measurements of the Accretion-powered Pulsar 4U 1907+09. *ApJ*, 496:386–394, March 1998. doi: 10.1086/305362.

S. Ç. Inam, Ş. Şahiner, and journal = ApJ keywords = Eclipsing Binary Stars, Pulsars, X Ray Astronomy, X Ray Stars, Early Stars, Giant Stars, Light Curve, Oso-8, Spectral Energy Distribution year = 1977 month = aug volume = 216 pages = L11-L14 doi = 10.1086/182498 adsurl = http://adsabs.harvard.edu/abs/1977ApJ...216L..11B adsnote = Provided by the SAO/NASA Astrophysics Data System Baykal, A. title = "A1540-53, an eclipsing X-ray binary pulsator".

Michael Isenberg, D. Q. Lamb, and John C. L. Wang. Effects of the Geometry of the Line-forming Region on the Properties of Cyclotron Resonant Scattering Lines. *ApJ*, 505(2):688–714, Oct 1998. doi: 10.1086/306171.

N. Islam and B. Paul. Orbital phase resolved spectroscopy of GX 301-2 with MAXI. *MNRAS*, 441:2539–2545, July 2014. doi: 10.1093/mnras/stu756.

K. Jahoda, J. H. Swank, A. B. Giles, M. J. Stark, T. Strohmayer, W. Zhang, and E. H. Morgan. In-orbit performance and calibration of the Rossi X-ray Timing Explorer (RXTE) Proportional Counter Array (PCA). In O. H. Siegmund and M. A. Gummin, editors, *EUV, X-Ray, and Gamma-Ray Instrumentation for Astronomy VII*, volume 2808 of *Proc. SPIE*, pages 59–70, October 1996. doi: 10.1117/12.256034.

Chetana Jain and Biswajit Paul. Pulse profile stability of the Crab pulsar. *Research in Astronomy and Astrophysics*, 11(10):1134–1142, Oct 2011. doi: 10.1088/1674-4527/11/10/002.

Gaurava K. Jaisawal and Sachindra Naik. Broad-band spectroscopy of the eclipsing high-mass X-ray binary 4U 1700-37 with Suzaku. *MNRAS*, 448(1):620–628, Mar 2015. doi: 10.1093/mnras/stv029.

Gaurava K. Jaisawal and Sachindra Naik. Detection of cyclotron resonance scattering feature in high-mass X-ray binary pulsar SMC X-2. *MNRAS*, 461(1):L97–L101, Sep 2016. doi: 10.1093/mnrasl/slw108.

M. A. Jimenez-Garate, J. C. Raymond, D. A. Liedahl, and C. J. Hailey. Identification of an Extended Accretion Disk Corona in the Hercules X-1 Low State: Moderate Optical Depth, Precise Density Determination, and Verification of CNO Abundances. *ApJ*, 625:931–950, June 2005. doi: 10.1086/426702.

T. R. Kallman and R. McCray. X-ray nebular models. *ApJS*, 50:263–317, December 1982. doi: 10.1086/190828.

Oleg Kargaltsev and George Pavlov. X-ray emission properties of rotation-powered pulsars. In *40th COSPAR Scientific Assembly*, volume 40, pages E1.15–10–14, Jan 2014.

V. M. Kaspi, R. N. Manchester, B. Siegman, S. Johnston, and A. G. Lyne. On the Spin-down of PSR B1509-58. *ApJ*, 422:L83, Feb 1994. doi: 10.1086/187218.

V. M. Kaspi, F. P. Gavriil, P. M. Woods, J. B. Jensen, M. S. E. Roberts, and D. Chakrabarty. A Major Soft Gamma Repeater-like Outburst and Rotation Glitch in the No-longer-so-anomalous X-Ray Pulsar 1E 2259+586. *ApJ*, 588(2):L93–L96, May 2003. doi: 10.1086/375683.

N. Kawai, R. Okayasu, W. Brinkmann, R. Manchester, A. G. Lyne, and N. D'Amico. X-ray and radio pulse phase comparison for PSR 1509 - 58. *ApJ*, 383:L65, December 1991. doi: 10.1086/186242.

D. Klochkov, R. Staubert, K. Postnov, N. Shakura, A. Santangelo, S. Tsygankov, A. Lutovinov, I. Kreykenbohm, and J. Wilms. INTEGRAL observations of Hercules X-1. *A&A*, 482:907–915, May 2008. doi: 10.1051/0004-6361:20078953.

D. Klochkov, V. Doroshenko, A. Santangelo, R. Staubert, C. Ferrigno, P. Kretschmar, I. Caballero, J. Wilms, I. Kreykenbohm, and K. Pottschmidt. Outburst of GX 304-1 monitored with INTEGRAL: positive correlation between the cyclotron line energy and flux. *A&A*, 542:L28, Jun 2012. doi: 10.1051/0004-6361/201219385.

Dmitriy Klochkov, P. A. Becker, A. Santangelo, R. Staubert, C. Ferrigno, R. E. Rothschild, P. Kretschmar, and G. Schoenherr. Pulse-to-Pulse Spectroscopy of Bright Accreting Pulsars. In *AAS/High Energy Astrophysics Division #12*, AAS/High Energy Astrophysics Division, page 42.04, Sep 2011.

R. Kothes and T. Foster. A Thorough Investigation of the Distance to the Supernova Remnant CTB109 and Its Pulsar AXP J2301+5852. *ApJ*, 746(1):L4, Feb 2012. doi: 10.1088/2041-8205/746/1/L4.

Henric Krawczynski. Tests of General Relativity in the Strong-gravity Regime Based on X-Ray Spectropolarimetric Observations of Black Holes in X-Ray Binaries. *ApJ*, 754(2):133, Aug 2012. doi: 10.1088/0004-637X/754/2/133.

P. Kretschmar, D. Marcu, M. Kühnel, D. Klochkov, K. Pottschmidt, R. Staubert, C. A. Wilson-Hodge, P. A. Jenke, I. Caballero, and F. Fürst. Pulse-to-pulse variations in accreting X-ray pulsars. In *European Physical Journal Web of Conferences*, volume 64 of *European Physical Journal Web of Conferences*, page 06012, January 2014. doi: 10.1051/epjconf/20136406012.

I. Kreykenbohm, P. Kretschmar, J. Wilms, R. Staubert, E. Kendziorra, D. E. Gruber, W. A. Heindl, and R. E. Rothschild. VELA X-1 as seen by RXTE. *A&A*, 341: 141–150, Jan 1999.

I. Kreykenbohm, W. Coburn, J. Wilms, P. Kretschmar, R. Staubert, W. A. Heindl, and R. E. Rothschild. Confirmation of two cyclotron lines in Vela X-1. *A&A*, 395: 129–140, Nov 2002. doi: 10.1051/0004-6361:20021181.

H. A. Krimm, S. T. Holland, R. H. D. Corbet, A. B. Pearlman, P. Romano, J. A. Kennea, J. S. Bloom, S. D. Barthelmy, W. H. Baumgartner, and J. R. Cummings. The Swift/BAT Hard X-Ray Transient Monitor. *ApJS*, 209(1):14, Nov 2013. doi: 10.1088/0067-0049/209/1/14.

L. Kuiper and W. Hermsen. The soft γ-ray pulsar population: a high-energy overview. *MNRAS*, 449(4):3827–3866, Jun 2015. doi: 10.1093/mnras/stv426.

L. Kuiper, W. Hermsen, G. Cusumano, R. Diehl, V. Schönfelder, A. Strong, K. Bennett, and M. L. McConnell. The Crab pulsar in the 0.75-30 MeV range as seen by CGRO COMPTEL. A coherent high-energy picture from soft X-rays up to high-energy gamma-rays. *A&A*, 378:918–935, Nov 2001. doi: 10.1051/0004-6361:20011256.

L. Kuiper, W. Hermsen, P. R. den Hartog, and W. Collmar. Discovery of Luminous Pulsed Hard X-Ray Emission from Anomalous X-Ray Pulsars 1RXS J1708-4009, 4U 0142+61, and 1E 2259+586 by INTEGRAL and RXTE. *ApJ*, 645(1):556–575, Jul 2006. doi: 10.1086/504317.

V. La Parola, G. Cusumano, A. Segreto, and A. D'Aì. The Swift-BAT monitoring reveals a long-term decay of the cyclotron line energy in Vela X-1. *MNRAS*, 463(1): 185–190, Nov 2016. doi: 10.1093/mnras/stw1915.

D. A. Leahy. Hollow-Cone Accretion Columns and Light-bending Effects. *ApJ*, 596 (2):1131–1136, Oct 2003. doi: 10.1086/378151.

A. M. Levine, W. Cui, R. Remillard, H. Bradt, D. A. Smith, R. Shirey, and E. H. Morgan. RXTE ASM Characterization of Temporal/Spectral Behavior of Galactic X-ray Sources. In *American Astronomical Society Meeting Abstracts*, volume 189, page 35.11, Dec 1996.

Q. Z. Liu, J. van Paradijs, and E. P. J. van den Heuvel. Catalogue of high-mass X-ray binaries in the Galaxy (4th edition). *A&A*, 455:1165–1168, September 2006. doi: 10.1051/0004-6361:20064987.

Q. Z. Liu, J. van Paradijs, and E. P. J. van den Heuvel. A catalogue of low-mass X-ray binaries in the Galaxy, LMC, and SMC (Fourth edition). *A&A*, 469:807–810, July 2007. doi: 10.1051/0004-6361:20077303.

Margaret A. Livingstone, Victoria M. Kaspi, Fotis P. Gavriil, and Richard N. Manchester. 21 Years of Timing PSR B1509-58. *ApJ*, 619(2):1046–1053, Feb 2005. doi: 10.1086/426731.

A. Lutovinov, M. Revnivtsev, M. Gilfanov, P. Shtykovskiy, S. Molkov, and R. Sunyaev. INTEGRAL insight into the inner parts of the Galaxy. High mass X-ray binaries. *A&A*, 444:821–829, December 2005. doi: 10.1051/0004-6361:20042392.

A. A. Lutovinov, M. G. Revnivtsev, S. S. Tsygankov, and R. A. Krivonos. Population of persistent high-mass X-ray binaries in the Milky Way. *MNRAS*, 431:327–341, May 2013. doi: 10.1093/mnras/stt168.

C. Maitra. Cyclotron Lines: From Magnetic Field Strength Estimators to Geometry Tracers in Neutron Stars. *Journal of Astrophysics and Astronomy*, 38:50, September 2017. doi: 10.1007/s12036-017-9476-3.

C. Maitra and B. Paul. Pulse-phase-resolved Spectroscopy of Vela X-1 with Suzaku. *ApJ*, 763:79, February 2013a. doi: 10.1088/0004-637X/763/2/79.

C. Maitra, B. Paul, and S. Naik. Timing and broad-band spectroscopy of 1A 1118-61 with Suzaku. *MNRAS*, 420:2307–2317, March 2012. doi: 10.1111/j.1365-2966.2011.20196.x.

C. Maitra, B. Paul, F. Haberl, and G. Vasilopoulos. Detection of a cyclotron line in SXP 15.3 during its 2017 outburst. *MNRAS*, 480:L136–L140, October 2018. doi: 10.1093/mnrasl/sly141.

Chandreyee Maitra and Biswajit Paul. Pulse-phase-dependent Variations of the Cyclotron Absorption Features of the Accreting Pulsars A0535+26, XTE J1946+274, and 4U 1907+09 with Suzaku. *ApJ*, 771(2):96, Jul 2013b. doi: 10.1088/0004-637X/771/2/96.

Chandreyee Maitra and Biswajit Paul. Latest results of pulse phase resolved spectroscopy of cyclotron lines in accretion powered pulsars. In *European Physical Journal Web of Conferences*, volume 64 of *European Physical Journal Web of Conferences*, page 06008, Jan 2014. doi: 10.1051/epjconf/20136406008.

Chandreyee Maitra, Harsha Raichur, Pragati Pradhan, and Biswajit Paul. Understanding the nature of the intriguing source X Persei: a deep look with a Suzaku observation. *MNRAS*, 470(1):713–722, Sep 2017. doi: 10.1093/mnras/stx1281.

K. Makishima and T. Mihara. Magnetic Fields of Neutron Stars. In Y. Tanaka and K. Koyama, editors, *Frontiers Science Series*, page 23, 1992.

K. Makishima, N. Kawai, K. Koyama, N. Shibazaki, F. Nagase, and M. Nakagawa. Discovery of a 437.5-s X-ray pulsation from 4U 1907+09. *PASJ*, 36:679–689, Jan 1984.

K. Makishima, K. Koyama, S. Hayakawa, and F. Nagase. Spectra and pulse period of the binary X-ray pulsar 4U 1538-52. *ApJ*, 314:619–628, March 1987. doi: 10.1086/165091.

K. Makishima, T. Mihara, M. Ishida, T. Ohashi, T. Sakao, M. Tashiro, T. Tsuru, T. Kii, F. Makino, T. Murakami, F. Nagase, Y. Tanaka, H. Kunieda, Y. Tawara, S. Kitamoto, S. Miyamoto, A. Yoshida, and M. J. L. Turner. Discovery of a Prominent Cyclotron Absorption Feature from the Transient X-Ray Pulsar X0331+53. *ApJ*, 365:L59, Dec 1990. doi: 10.1086/185888.

K. Makishima, T. Mihara, F. Nagase, and Y. Tanaka. Cyclotron Resonance Effects in Two Binary X-Ray Pulsars and the Evolution of Neutron Star Magnetic Fields. *ApJ*, 525:978–994, November 1999. doi: 10.1086/307912.

Kazuo Makishima, Hiromitsu Takahashi, Shin'ya Yamada, Chris Done, Aya Kubota, Tadayasu Dotani, Ken Ebisawa, Takeshi Itoh, Shunji Kitamoto, Hitoshi Negoro, Yoshihiro Ueda, and Kazutaka Yamaoka. Suzaku Results on Cygnus X-1 in the Low/Hard State. *PASJ*, 60:585, Jun 2008. doi: 10.1093/pasj/60.3.585.

C. Malacaria, D. Klochkov, A. Santangelo, and R. Staubert. Luminosity-dependent spectral and timing properties of the accreting pulsar GX 304-1 measured with INTEGRAL. *A&A*, 581:A121, Sep 2015. doi: 10.1051/0004-6361/201526417.

R. N. Manchester, I. R. Tuohy, and N. Damico. Discovery of radio pulsations from the X-ray pulsar in the supernova remnant G320.4-1.2. *ApJ*, 262:L31–L33, November 1982. doi: 10.1086/183906.

R. N. Manchester, G. B. Hobbs, A. Teoh, and M. Hobbs. The Australia Telescope National Facility Pulsar Catalogue. *AJ*, 129(4):1993–2006, Apr 2005. doi: 10.1086/428488.

D. Marsden, P. R. Blanco, D. E. Gruber, W. A. Heindl, M. R. Pelling, L. E. Peterson, R. E. Rothschild, A. H. Rots, K. Jahoda, and D. J. Macomb. The x-ray spectrum of the plerionic system PSR b1509-58/MSH 15-52. *The Astrophysical Journal*, 491(1): L39–L42, dec 1997. doi: 10.1086/311054. URL https://doi.org/10.1086%2F311054.

N. Marshall and M. J. Ricketts. Determination of a binary period for the variable X-ray source A1907+09. *MNRAS*, 193:7P–13P, October 1980. doi: 10.1093/mnras/193.1.7P.

F. Martins, D. Schaerer, and D. J. Hillier. A new calibration of stellar parameters of Galactic O stars. In F. Casoli, T. Contini, J. M. Hameury, and L. Pagani, editors, *SF2A-2005: Semaine de l'Astrophysique Francaise*, page 633, December 2005.

R. McCray, T. R. Kallman, J. I. Castor, and G. L. Olson. Spectral variability in early-type binary X-ray systems. *ApJ*, 282:245–255, July 1984. doi: 10.1086/162197.

S. Mereghetti and L. Stella. The Very Low Mass X-Ray Binary Pulsars: A New Class of Sources? *ApJ*, 442:L17, Mar 1995. doi: 10.1086/187805.

P. Mészáros. Gamma-ray bursts. *Reports on Progress in Physics*, 69(8):2259–2321, Aug 2006. doi: 10.1088/0034-4885/69/8/R01.

P. Meszaros, R. Novick, A. Szentgyorgyi, G. A. Chanan, and M. C. Weisskopf. Astrophysical Implications and Observational Prospects of X-Ray Polarimetry. *ApJ*, 324: 1056, Jan 1988. doi: 10.1086/165962.

Roberto P. Mignani. Optical, ultraviolet, and infrared observations of isolated neutron stars. *Advances in Space Research*, 47(8):1281–1293, Apr 2011. doi: 10.1016/j.asr.2009.12.011.

T. Mineo, C. Ferrigno, L. Foschini, A. Segreto, G. Cusumano, G. Malaguti, G. Di Cocco, and C. Labanti. INTEGRAL observations of the Crab pulsar. *A&A*, 450(2): 617–623, May 2006. doi: 10.1051/0004-6361:20054305.

N. Mowlavi, I. Kreykenbohm, S. E. Shaw, K. Pottschmidt, J. Wilms, J. Rodriguez, N. Produit, S. Soldi, S. Larsson, and P. Dubath. INTEGRAL observation of the high-mass X-ray transient V 0332+53 during the 2005 outburst decline. *A&A*, 451 (1):187–194, May 2006. doi: 10.1051/0004-6361:20054235.

K. Mukerjee, P. C. Agrawal, B. Paul, A. R. Rao, M. N. Vahia, J. S. Yadav, S. Seetha, and K. Kasturirangan. Energy dependence of x-ray pulse profile of the crab pulsar. *Bulletin of the Astronomical Society of India*, 27:181, Jan 1999.

K. Mukerjee, P. C. Agrawal, B. Paul, A. R. Rao, J. S. Yadav, S. Seetha, and K. Kasturirangan. Pulse characteristics of the x-ray pulsar 4u 1907+09. *The Astrophysical Journal*, 548(1):368, 2001. URL http://stacks.iop.org/0004-637X/548/i=1/a=368.

D. Mukherjee and D. Bhattacharya. A phase-dependent view of cyclotron lines from model accretion mounds on neutron stars. *MNRAS*, 420:720–731, February 2012. doi: 10.1111/j.1365-2966.2011.20085.x.

U. Mukherjee, H. Raichur, B. Paul, S. Naik, and N. Bhatt. Orbital Evolution and Orbital Phase Resolved Spectroscopy of the HMXB Pulsar 4U 1538-52 with RXTE-PCA and BeppoSAX. *Journal of Astrophysics and Astronomy*, 27:411–423, December 2006. doi: 10.1007/BF02709367.

S. Müller, C. Ferrigno, M. Kühnel, G. Schönherr, P. A. Becker, M. T. Wolff, D. Hertel, F.-W. Schwarm, V. Grinberg, M. Obst, I. Caballero, K. Pottschmidt, F. Fürst, I. Kreykenbohm, R. E. Rothschild, P. Hemphill, S. M. Núñez, J. M. Torrejón, D. Klochkov, R. Staubert, and J. Wilms. No anticorrelation between cyclotron line energy and X-ray flux in 4U 0115+634. *A&A*, 551:A6, March 2013. doi: 10.1051/0004-6361/201220359.

A. A. Mushtukov, V. F. Suleimanov, S. S. Tsygankov, and J. Poutanen. The critical accretion luminosity for magnetized neutron stars. *MNRAS*, 447:1847–1856, February 2015a. doi: 10.1093/mnras/stu2484.

Alexander A. Mushtukov, Sergey S. Tsygankov, Alexand er V. Serber, Valery F. Suleimanov, and Juri Poutanen. Positive correlation between the cyclotron line energy and luminosity in sub-critical X-ray pulsars: Doppler effect in the accretion channel. *MNRAS*, 454(3):2714–2721, Dec 2015b. doi: 10.1093/mnras/stv2182.

W. Nagel. Radiative transfer in a strongly magnetized plasma. I - Effects of anisotropy. II - Effects of Comptonization. *ApJ*, 251:278–296, Dec 1981a. doi: 10.1086/159463.

W. Nagel. Radiative Transfer in a Strongly Magnetized Plasma - Part Two - Effects of Comptonization. *ApJ*, 251:288, Dec 1981b. doi: 10.1086/159464.

O. Nishimura. Formation Mechanism for Broad and Shallow Profiles of Cyclotron Lines in Accreting X-Ray Pulsars. *ApJ*, 672:1127–1136, January 2008. doi: 10.1086/523782.

Osamu Nishimura. Influence of a Non-Dipole Magnetic Field on the Peak Energies of Cyclotron Absorption Lines. *PASJ*, 57:769–778, Oct 2005. doi: 10.1093/pasj/57.5.769.

Osamu Nishimura. Superposition of Cyclotron Lines in Accreting X-Ray Pulsars. I. Long Spin Period. *ApJ*, 730(2):106, Apr 2011. doi: 10.1088/0004-637X/730/2/106.

Osamu Nishimura. Variations of Cyclotron Line Energy with Luminosity in Accreting X-Ray Pulsars. *ApJ*, 781(1):30, Jan 2014. doi: 10.1088/0004-637X/781/1/30.

R. Novick. Stellar and Solar X-Ray Polarimetry. *Space Sci. Rev.*, 18(3):389–408, Dec 1975. doi: 10.1007/BF00212912.

R. Novick, M. C. Weisskopf, E. H. Silver, H. L. Kestenbaum, K. S. Long, and R. S. Wolff. Polarization of Cosmic X-ray Sources. In *Proceedings of the Eighth Texas Symposium on Relativistic Astrophysics*, page 312, Jan 1977.

S. A. Olausen and V. M. Kaspi. The McGill Magnetar Catalog. *ApJS*, 212(1):6, May 2014a. doi: 10.1088/0067-0049/212/1/6.

S. A. Olausen and V. M. Kaspi. VizieR Online Data Catalog: The McGill magnetar catalog (Olausen+, 2014). *VizieR Online Data Catalog*, art. J/ApJS/212/6, Jun 2014b.

T. Oosterbroek, J. H. J. de Bruijne, D. Martin, P. Verhoeve, M. A. C. Perryman, C. Erd, and R. Schulz. Absolute timing of the Crab Pulsar at optical wavelengths with superconducting tunneling junctions. *A&A*, 456:283–286, September 2006. doi: 10.1051/0004-6361:20065254.

T. Oosterbroek, I. Cognard, A. Golden, P. Verhoeve, D. D. E. Martin, C. Erd, R. Schulz, J. A. Stüwe, A. Stankov, and T. Ho. Simultaneous absolute timing of the Crab pulsar at radio and optical wavelengths. *A&A*, 488(1):271–277, Sep 2008. doi: 10.1051/0004-6361:200809751.

B. Paul. Astrosat: Some Key Science Prospects. *International Journal of Modern Physics D*, 22:1341009, January 2013. doi: 10.1142/S0218271813410095.

B. Paul, M. Kawasaki, T. Dotani, and F. Nagase. Study of the Long-Term Stability of Two Anomalous X-Ray Pulsars, 4U 0142+61 and 1E 1048.1-5937, with ASCA. *ApJ*, 537(1):319–326, Jul 2000. doi: 10.1086/309028.

B. Paul, T. Dotani, F. Nagase, U. Mukherjee, and S. Naik. High-Resolution X-Ray Spectrum of the Accreting Binary X-Ray Pulsar GX 1+4. *ApJ*, 627:915–919, July 2005. doi: 10.1086/430429.

Biswajit Paul, M. R. Gopala Krishna, and Rishin Puthiya Veetil. POLIX: A Thomson X-ray polarimeter for a small satellite mission. In *41st COSPAR Scientific Assembly*, volume 41, pages E1.15–8–16, Jul 2016.

Tsvi Piran. The physics of gamma-ray bursts. *Reviews of Modern Physics*, 76(4): 1143–1210, Oct 2004. doi: 10.1103/RevModPhys.76.1143.

Katja Pottschmidt, Ingo Kreykenbohm, Jörn Wilms, Wayne Coburn, Richard E. Rothschild, Peter Kretschmar, Vanessa McBride, Slawomir Suchy, and Rüdiger Staubert. RXTE Discovery of Multiple Cyclotron Lines during the 2004 December Outburst of V0332+53. *ApJ*, 634(1):L97–L100, Nov 2005. doi: 10.1086/498689.

Juri Poutanen. Relativistic Jets in Blazars: Polarization of Radiation. *ApJS*, 92:607, Jun 1994. doi: 10.1086/192024.

Juri Poutanen, Alexander A. Mushtukov, Valery F. Suleimanov, Sergey S. Tsygankov, Dmitrij I. Nagirner, Victor Doroshenko, and Alexand er A. Lutovinov. A Reflection Model for the Cyclotron Lines in the Spectra of X-Ray Pulsars. *ApJ*, 777(2):115, Nov 2013. doi: 10.1088/0004-637X/777/2/115.

P. Pradhan, E. Bozzo, and B. Paul. Supergiant fast X-ray transients versus classical supergiant high mass X-ray binaries: Does the difference lie in the companion wind? *A&A*, 610:A50, February 2018. doi: 10.1051/0004-6361/201731487.

Pragati Pradhan, Biswajit Paul, Harsha Raichur, and Bikash Chandra Paul. Variations of the harmonic components of the X-ray pulse profile of PSR B1509-58. *Research in Astronomy and Astrophysics*, 15(1):28-36, Jan 2015. doi: 10.1088/1674-4527/15/1/003.

L. Prat, J. Rodriguez, D. C. Hannikainen, and S. E. Shaw. Peering through the stellar wind of IGR J19140+0951 with simultaneous INTEGRAL/RXTE observations. *MNRAS*, 216:L11–L14, August 1977. doi: 10.1086/182498.

Steven H. Pravdo, Lorella Angelini, and Alice K. Harding. X-Ray Spectral Evolution of the Crab Pulse. *ApJ*, 491(2):808–815, Dec 1997. doi: 10.1086/304996.

V. Radhakrishnan. Polarization and its message in astronomy. *QJRAS*, 30:181–194, Jun 1989.

M. C. Ramadevi, S. Seetha, D. Bhattacharya, B. T. Ravishankar, N. Sitaramamurthy, G. Meena, M. R. Sharma, R. Kulkarni, V. C. Babu, Kumar, B. Singh, A. Jain, R. Yadav, S. Vaishali, B. N. Ashoka, A. Agarwal, K. Balaji, G. Nagesh, M. Kumar, D. R. Gaan, P. Kulshresta, P. Agarwal, M. Sebastian, A. Rajarajan, D. Radhika, A. Nandi, V. Girish, V. K. Agarwal, A. Kushwaha, and N. K. Iyer. Scanning sky monitor (SSM) onboard AstroSat. *Experimental Astronomy*, 44:11–23, October 2017. doi: 10.1007/s10686-017-9536-3.

A. R. Rao, Vikas Chand, M. K. Hingar, S. Iyyani, Rakesh Khanna, A. P. K. Kutty, J. P. Malkar, D. Paul, V. B. Bhalerao, D. Bhattacharya, G. C. Dewangan, Pramod Pawar, A. M. Vibhute, T. Chattopadhyay, N. P. S. Mithun, S. V. Vadawale, N. Vagshette, R. Basak, P. Pradeep, Essy Samuel, S. Sreekumar, P. Vinod, K. H. Navalgund, R. Pand iyan, K. S. Sarma, S. Seetha, and K. Subbarao. AstroSat CZT Imager Observations of GRB 151006A: Timing, Spectroscopy, and Polarization Study. *ApJ*, 833(1):86, Dec 2016. doi: 10.3847/1538-4357/833/1/86.

M. L. Rawls, J. A. Orosz, J. E. McClintock, M. A. P. Torres, C. D. Bailyn, and M. M. Buxton. Refined Neutron Star Mass Determinations for Six Eclipsing X-Ray Pulsar Binaries. *ApJ*, 730:25, March 2011. doi: 10.1088/0004-637X/730/1/25.

A. P. Reynolds, S. A. Bell, and R. W. Hilditch. Optical spectroscopy of the massive X-ray binary QV Nor (4U 1538 - 52). *MNRAS*, 256:631–640, June 1992. doi: 10.1093/mnras/256.3.631.

P. V. Rishin and et al. *Development of a Thomson X-ray polarimeter*, page 83. 2010. doi: 10.1017/CBO9780511750809.012.

E. Rivers, A. Markowitz, K. Pottschmidt, S. Roth, L. Barragán, F. Fürst, S. Suchy, I. Kreykenbohm, J. Wilms, and R. Rothschild. A Comprehensive Spectral Analysis of the X-Ray Pulsar 4U 1907+09 from Two Observations with the Suzaku X-ray Observatory. *ApJ*, 709:179–190, January 2010. doi: 10.1088/0004-637X/709/1/179.

N. R. Robba, L. Burderi, T. Di Salvo, R. Iaria, and G. Cusumano. The BeppoSAX 0.1-100 keV Spectrum of the X-Ray Pulsar 4U 1538-52. *ApJ*, 562:950–956, December 2001. doi: 10.1086/323841.

J. J. Rodes-Roca, J. M. Torrejón, I. Kreykenbohm, S. Martínez Núñez, A. Camero-Arranz, and G. Bernabéu. The first cyclotron harmonic of 4U 1538-52. *A&A*, 508: 395–400, December 2009. doi: 10.1051/0004-6361/200912815.

J. Rodriguez, M. Del Santo, F. Lebrun, G. Belanger, M. Capitanio, Cadolle-Bel F., P. David, L. Foschini, P. Goldoni, A. Goldwurm, A. Gros, P. Laurent, A. Paizis, J. Paul, R. Terrier, S. E. Shaw, and P. Ubertini. First results from the IBIS/ISGRI data obtained during the Galactic Plane Scan. II. The Vela region. *A&A*, 411: L373–L376, November 2003. doi: 10.1051/0004-6361:20031154.

J. Rodriguez, A. Bodaghee, P. Kaaret, J. A. Tomsick, E. Kuulkers, G. Malaguti, P.-O. Petrucci, C. Cabanac, M. Chernyakova, S. Corbel, S. Deluit, G. Di Cocco, K. Ebisawa, A. Goldwurm, G. Henri, F. Lebrun, A. Paizis, R. Walter, and L. Foschini. INTEGRAL and XMM-Newton observations of the X-ray pulsar IGR J16320-4751/AX J1631.9-4752. *MNRAS*, 366:274–282, February 2006. doi: 10.1111/j.1365-2966.2005.09855.x.

R. E. Rothschild, P. R. Blanco, D. E. Gruber, W. A. Heindl, D. R. MacDonald, D. C. Marsden, M. R. Pelling, L. R. Wayne, and P. L. Hink. In-Flight Performance of the High-Energy X-Ray Timing Experiment on the Rossi X-Ray Timing Explorer. *ApJ*, 496(1):538–549, Mar 1998. doi: 10.1086/305377.

Richard E. Rothschild, Matthias Kühnel, Katja Pottschmidt, Paul Hemphill, Konstantin Postnov, Mikhail Gornostaev, Nikolai Shakura, Felix Fürst, Jörn Wilms, Rüdiger Staubert, and Dmitry Klochkov. Discovery and modelling of a flattening of the positive cyclotron line/luminosity relation in GX 304-1 with RXTE. *MNRAS*, 466(3):2752–2779, Apr 2017. doi: 10.1093/mnras/stw3222.

B. C. Rubin, M. H. Finger, D. M. Scott, and R. B. Wilson. Observation of a Long-Term Spin-up Trend in 4U 1538-52. *ApJ*, 488:413–418, October 1997. doi: 10.1086/304679.

P. W. Sanford, A. M. Cruise, and J. L. Culhane. Techniques for Improving the Sensitivity of Proportional Counters Used in X-Ray Astronomy. In Livio Gratton, editor, *Non-Solar X- and Gamma-Ray Astronomy*, volume 37 of *IAU Symposium*, page 35, Jan 1970.

A. Santangelo, A. Segreto, S. Del Sordo, O. Mauro, A. N. Parmar, and D. Dal Fiume. The BeppoSAX view of cyclotron lines from accreting pulsars. In *AAS/High Energy Astrophysics Division #5*, volume 5 of *AAS/High Energy Astrophysics Division*, page 29.05, Oct 2000.

N. Sartore, E. Jourdain, and J. P. Roques. The INTEGRAL/SPI view of A0535+26 during the Giant Outburst of 2011 February. *ApJ*, 806(2):193, Jun 2015. doi: 10.1088/0004-637X/806/2/193.

S. Y. Sazonov and R. A. Sunyaev. Scattering in the inner accretion disk and the waveforms and polarization of millisecond flux oscillations in LMXBs. *A&A*, 373: 241–250, Jul 2001. doi: 10.1051/0004-6361:20010624.

F. W. Schwarm, G. Schönherr, S. Falkner, K. Pottschmidt, M. T. Wolff, P. A. Becker, E. Sokolova-Lapa, D. Klochkov, C. Ferrigno, F. Fürst, P. B. Hemphill, D. M. Marcu-Cheatham, T. Dauser, and J. Wilms. Cyclotron resonant scattering feature simulations. I. Thermally averaged cyclotron scattering cross sections, mean free photon-path tables, and electron momentum sampling. *A&A*, 597:A3, Jan 2017. doi: 10.1051/0004-6361/201629352.

D. A. Schwartz, R. E. Griffiths, J. R. Thorstensen, P. A. Charles, and S. Bowyer. Optical identification of 4U 1907+09 using the HEAO-1 Scanning modulation collimator position. *AJ*, 85:549–554, May 1980. doi: 10.1086/112710.

F. D. Seward and F. R. Harnden, Jr. A new, fast X-ray pulsar in the supernova remnant MSH 15-52. *ApJ*, 256:L45–L47, May 1982. doi: 10.1086/183793.

F. D. Seward, P. A. Charles, and A. P. Smale. A 6 Second Periodic X-Ray Source in Carina. *ApJ*, 305:814, Jun 1986. doi: 10.1086/164294.

K. P. Singh and et al. Soft X-ray Focusing Telescope Aboard AstroSat: Design, Characteristics and Performance. *Journal of Astrophysics and Astronomy*, 38:29, June 2017. doi: 10.1007/s12036-017-9448-7.

A. Słowikowska, G. Kanbach, M. Kramer, and A. Stefanescu. Optical polarization of the Crab pulsar: precision measurements and comparison to the radio emission. *MNRAS*, 397(1):103–123, Jul 2009. doi: 10.1111/j.1365-2966.2009.14935.x.

D. H. Staelin and E. C. Reifenstein, III. Pulsating Radio Sources near the Crab Nebula. *Science*, 162:1481–1483, December 1968. doi: 10.1126/science.162.3861.1481.

R. Staubert, E. Kendziorra, W. Pietsch, C. Reppin, J. Truemper, and W. Voges. Hard X-ray pulses from 4U 0900-40. *ApJ*, 239:1010–1016, August 1980. doi: 10.1086/158189.

R. Staubert, N. I. Shakura, K. Postnov, J. Wilms, R. E. Rothschild, W. Coburn, L. Rodina, and D. Klochkov. Discovery of a flux-related change of the cyclotron line energy in Hercules X-1. *A&A*, 465(2):L25–L28, Apr 2007. doi: 10.1051/0004-6361:20077098.

R. Staubert, D. Klochkov, J. Wilms, K. Postnov, N. I. Shakura, R. E. Rothschild, F. Fürst, and F. A. Harrison. Long-term change in the cyclotron line energy in Hercules X-1. *A&A*, 572:A119, Dec 2014. doi: 10.1051/0004-6361/201424203.

R. Staubert, D. Klochkov, V. Vybornov, J. Wilms, and F. A. Harrison. Continued decay in the cyclotron line energy in Hercules X-1. *A&A*, 590:A91, May 2016. doi: 10.1051/0004-6361/201527955.

R. Staubert, D. Klochkov, F. Fürst, J. Wilms, R. E. Rothschild, and F. Harrison. Inversion of the decay of the cyclotron line energy in Hercules X-1. *A&A*, 606:L13, October 2017. doi: 10.1051/0004-6361/201731927.

R. Staubert, J. Trümper, E. Kendziorra, D. Klochkov, K. Postnov, P. Kretschmar, K. Pottschmidt, F. Haberl, R. E. Rothschild, A. Santangelo, J. Wilms, I. Kreykenbohm, and F. Fürst. Cyclotron lines in highly magnetized neutron stars. *A&A*, 622: A61, Feb 2019. doi: 10.1051/0004-6361/201834479.

A. M. Stirling, R. E. Spencer, C. J. de la Force, M. A. Garrett, R. P. Fender, and R. N. Ogley. A relativistic jet from Cygnus X-1 in the low/hard X-ray state. *MNRAS*, 327(4):1273–1278, Nov 2001. doi: 10.1046/j.1365-8711.2001.04821.x.

L. Strüder, U. Briel, K. Dennerl, R. Hartmann, E. Kendziorra, N. Meidinger, E. Pfeffermann, C. Reppin, B. Aschenbach, and W. Bornemann. The European Photon Imaging Camera on XMM-Newton: The pn-CCD camera. *A&A*, 365:L18–L26, Jan 2001. doi: 10.1051/0004-6361:20000066.

Annapurni Subramaniam, Shyam N. Tandon, John Hutchings, Swarna K. Ghosh, Koshy George, V. Girish, P. U. Kamath, S. Kathiravan, Amit Kumar, and J. Paul Lancelot. In-orbit performance of UVIT on ASTROSAT. In *Space Telescopes and Instrumentation 2016: Ultraviolet to Gamma Ray*, volume 9905 of *Society of Photo-Optical Instrumentation Engineers (SPIE) Conference Series*, page 99051F, Jul 2016. doi: 10.1117/12.2235271.

S. Suchy, K. Pottschmidt, J. Wilms, I. Kreykenbohm, G. Schönherr, P. Kretschmar, V. McBride, I. Caballero, R. E. Rothschild, and V. Grinberg. Pulse Phase-Resolved Analysis of the High-Mass X-Ray Binary Centaurus X-3 over Two Binary Orbits. *ApJ*, 675:1487–1498, March 2008. doi: 10.1086/527042.

M. Sugizaki, K. Mitsuda, H. Kaneda, K. Matsuzaki, S. Yamauchi, and K. Koyama. Faint X-Ray Sources Resolved in the ASCA Galactic Plane Survey and Their Contribution to the Galactic Ridge X-Ray Emission. *ApJS*, 134:77–102, May 2001. doi: 10.1086/320358.

Cindy R. Tam, Fotis P. Gavriil, Rim Dib, Victoria M. Kaspi, Peter M. Woods, and Cees Bassa. X-Ray and Near-IR Variability of the Anomalous X-Ray Pulsar 1E 1048.1-5937: From Quiescence Back to Activity. *ApJ*, 677(1):503–514, Apr 2008. doi: 10.1086/528368.

Y Tanaka. . In *Lecture Notes in Physics, Berlin Springer Verlag, Vol. 255, IAU colloq 89: Radiation Hydrodynamics in Stars and Compact Objects*, 1986.

S. N. Tandon, J. B. Hutchings, S. K. Ghosh, A. Subramaniam, G. Koshy, V. Girish, P. U. Kamath, S. Kathiravan, A. Kumar, J. P. Lancelot, P. K. Mahesh, R. Mohan, J. Murthy, S. Nagabhushana, A. K. Pati, J. Postma, N. K. Rao, K. Sankarasubramanian, P. Sreekumar, S. Sriram, C. S. Stalin, F. Sutaria, Y. H. Sreedhar, I. V. Barve, C. Mondal, and S. Sahu. In-orbit Performance of UVIT and First Results. *Journal of Astrophysics and Astronomy*, 38:28, June 2017. doi: 10.1007/s12036-017-9445-x.

Lev Titarchuk. Generalized Comptonization Models and Application to the Recent High-Energy Observations. *ApJ*, 434:570, Oct 1994. doi: 10.1086/174760.

Lev Titarchuk and Xin-Min Hua. A Comparison of Thermal Comptonization Models. *ApJ*, 452:226, Oct 1995. doi: 10.1086/176293.

Lev Titarchuk and Yurij Lyubarskij. Power-Law Spectra as a Result of Comptonization of the Soft Radiation in a Plasma Cloud. *ApJ*, 450:876, Sep 1995. doi: 10.1086/176191.

J. A. Tomsick, R. Lingenfelter, R. Walter, J. Rodriguez, A. Goldwurm, S. Corbel, and P. Kaaret. Igr J16320-4751. *IAU Circ.*, 8076, February 2003.

J. M. Torrejón, N. S. Schulz, M. A. Nowak, and T. R. Kallman. A Chandra Survey of Fluorescence Fe Lines in X-ray Binaries at High Resolution. *ApJ*, 715:947–958, June 2010. doi: 10.1088/0004-637X/715/2/947.

V. Trimble. The Distance to the Crab Nebula and NP 0532. *PASP*, 85:579, October 1973. doi: 10.1086/129507.

J. Truemper, W. Pietsch, C. Reppin, W. Voges, R. Staubert, and E. Kendziorra. Evidence for strong cyclotron line emission in the hard X-ray spectrum of Hercules X-1. *ApJ*, 219:L105–L110, Feb 1978. doi: 10.1086/182617.

J. E. Trümper, A. Zezas, Ü. Ertan, and N. D. Kylafis. The energy spectrum of anomalous X-ray pulsars and soft gamma-ray repeaters. *A&A*, 518:A46, Jul 2010. doi: 10.1051/0004-6361/200911834.

E. Trussoni, W. Brinkmann, H. Ogelman, G. Hasinger, B. Aschenbach, and A. Ferrari. EXOSAT observation of the supernova remnant MSH 15-52. *A&A*, 234:403, Aug 1990.

S. S. Tsygankov, A. A. Lutovinov, E. M. Churazov, and R. A. Sunyaev. V0332+53 in the outburst of 2004-2005: luminosity dependence of the cyclotron line and pulse profile. *MNRAS*, 371:19–28, September 2006. doi: 10.1111/j.1365-2966.2006.10610.x.

M. J. L. Turner, A. Abbey, M. Arnaud, M. Balasini, M. Barbera, E. Belsole, P. J. Bennie, J. P. Bernard, G. F. Bignami, and M. Boer. The European Photon Imaging Camera on XMM-Newton: The MOS cameras : The MOS cameras. *A&A*, 365: L27–L35, Jan 2001. doi: 10.1051/0004-6361:20000087.

S. V. Vadawale, T. Chattopadhyay, A. R. Rao, D. Bhattacharya, V. B. Bhalerao, N. Vagshette, P. Pawar, and S. Sreekumar. Hard X-ray polarimetry with Astrosat-CZTI. *A&A*, 578:A73, Jun 2015. doi: 10.1051/0004-6361/201525686.

S. V. Vadawale, T. Chattopadhyay, N. P. S. Mithun, A. R. Rao, D. Bhattacharya, A. Vibhute, V. B. Bhalerao, G. C. Dewangan, R. Misra, B. Paul, A. Basu, B. C. Joshi, S. Sreekumar, E. Samuel, P. Priya, P. Vinod, and S. Seetha. Phase-resolved X-ray polarimetry of the Crab pulsar with the AstroSat CZT Imager. *Nature Astronomy*, 2:50–55, Nov 2018. doi: 10.1038/s41550-017-0293-z.

Santosh V. Vadawale, A. R. Rao, Dipankar Bhattacharya, Varun B. Bhalerao, Gulab C. Dewangan, Ajay M. Vibhute, N. P. S. Mithun, Tanmoy Chattopadhyay, and S. Sreekumar. In-orbit performance AstroSat CZTI. In *Proc. SPIE*, volume 9905 of *Society of Photo-Optical Instrumentation Engineers (SPIE) Conference Series*, page 99051G, Jul 2016. doi: 10.1117/12.2235373.

A. Valinia and F. E. Marshall. RXTE Measurement of the Diffuse X-Ray Emission from the Galactic Ridge: Implications for the Energetics of the Interstellar Medium. *ApJ*, 505:134–147, September 1998. doi: 10.1086/306155.

M. H. van Kerkwijk, J. G. J. van Oijen, and E. P. J. van den Heuvel. Extended optical spectroscopy of the massive companion of 4U 1907+09. *A&A*, 209:173–182, January 1989.

M. H. van Kerkwijk, J. van Paradijs, and E. J. Zuiderwijk. On the masses of neutron stars. *A&A*, 303:497, November 1995.

Maitra Varun, Chandreyee, Pradhan Pragati, Raichur Harsha, and Paul Biswajit. Probing the Cyclotron line characteristics of 4U 1538-522 using AstroSat-LAXPC. *MNRAS*, 484(1):L1–L6, Mar 2019. doi: 10.1093/mnrasl/sly234.

K. Viironen and J. Poutanen. Light curves and polarization of accretion- and nuclear-powered millisecond pulsars. *A&A*, 426:985–997, Nov 2004. doi: 10.1051/0004-6361:20041084.

Jacco Vink. Supernova remnants: the X-ray perspective. *A&ARv*, 20:49, Dec 2012. doi: 10.1007/s00159-011-0049-1.

Julia K. Vogel, Romain Hascoët, Victoria M. Kaspi, Hongjun An, Robert Archibald, Andrei M. Beloborodov, Steven E. Boggs, Finn E. Christensen, William W. Craig, Eric V. Gotthelf, Brian W. Grefenstette, Charles J. Hailey, Fiona A. Harrison, Jamie A. Kennea, Kristin K. Madsen, Michael J. Pivovaroff, Daniel Stern, and William W. Zhang. NuSTAR Observations of the Magnetar 1E 2259+586. *ApJ*, 789 (1):75, Jul 2014. doi: 10.1088/0004-637X/789/1/75.

V. Vybornov, D. Klochkov, M. Gornostaev, K. Postnov, E. Sokolova-Lapa, R. Staubert, K. Pottschmidt, and A. Santangelo. Luminosity-dependent changes of the cyclotron line energy and spectral hardness in Cepheus X-4. *A&A*, 601:A126, May 2017. doi: 10.1051/0004-6361/201630275.

M. C. Weisskopf, G. G. Cohen, H. L. Kestenbaum, K. S. Long, R. Novick, and R. S. Wolff. Measurement of the X-ray polarization of the Crab nebula. *ApJ*, 208:L125–L128, Sep 1976. doi: 10.1086/182247.

M. C. Weisskopf, E. H. Silver, H. L. Kestenbaum, K. S. Long, R. Novick, and R. S. Wolff. Search for X-ray polarization in Cygnus X-1. *ApJ*, 215:L65–L68, Jul 1977. doi: 10.1086/182479.

M. C. Weisskopf, H. L. Kestenbaum, K. S. Long, R. Novick, and E. H. Silver. An upper limit to the linear X-ray polarization of Scorpius X-1. *ApJ*, 221:L13–L16, Apr 1978a. doi: 10.1086/182655.

M. C. Weisskopf, E. H. Silver, H. L. Kestenbaum, K. S. Long, and R. Novick. A precision measurement of the X-ray polarization of the Crab Nebula without pulsar contamination. *ApJ*, 220:L117–L121, Mar 1978b. doi: 10.1086/182648.

M. C. Weisskopf, R. F. Elsner, W. Darbo, D. Leahy, S. Naranan, P. G. Sutherland, J. E. Grindlay, Jr. Harnden, F. R., and F. D. Seward. The period history of the X-ray pulsar in MSH 15-52. *ApJ*, 267:711–712, Apr 1983. doi: 10.1086/160908.

N. E. White, J. H. Swank, and S. S. Holt. Accretion powered X-ray pulsars. *ApJ*, 270: 711–734, Jul 1983. doi: 10.1086/161162.

P. Wojdowski, G. W. Clark, A. M. Levine, J. W. Woo, and S. N. Zhang. Quasi-periodic Occultation by a Precessing Accretion Disk and Other Variabilities of SMC X-1. *ApJ*, 502:253–264, July 1998. doi: 10.1086/305893.

J. W. Woo, G. W. Clark, A. M. Levine, R. H. D. Corbet, and F. Nagase. Orbital Decay, Spin-down, and Pulse-Phase–resolved Spectroscopy of LMC X-4 from GINGA and ROSAT Observations. *ApJ*, 467:811, August 1996. doi: 10.1086/177655.

P. M. Woods, V. M. Kaspi, C. Thompson, F. P. Gavriil, H. L. Marshall, D. Chakrabarty, K. Flanagan, J. Heyl, and L. Hernquist. Changes in the X-ray Emission from the Magnetar Candidate 1E 2259+586 during its 2002 Outburst. In Philip Kaaret, Frederick K. Lamb, and Jean H. Swank, editors, *X-ray Timing 2003: Rossi and Beyond*, volume 714 of *American Institute of Physics Conference Series*, pages 298–301, Jul 2004. doi: 10.1063/1.1781044.

C. Yang, R. F. Archibald, J. K. Vogel, H. An, V. M. Kaspi, S. Guillot, A. M. Beloborodov, and M. Pivovaroff. NuSTAR Observations of Magnetar 1E 1048.1-5937. *ApJ*, 831(1):80, Nov 2016. doi: 10.3847/0004-637X/831/1/80.

J. Yokogawa, B. Paul, M. Ozaki, F. Nagase, D. Chakrabarty, and T. Takeshima. ASCA Observation of the New Transient X-Ray Pulsar XTE J0111.2-7317 in the Small Magellanic Cloud. *ApJ*, 539:191–196, August 2000. doi: 10.1086/309202.

Weiping Zhang, Alan B. Giles, K. Jahoda, Yang Soong, Jean H. Swank, and Edward H. Morgan. Laboratory performance of the proportional counter array experiment for the X-ray Timing Explorer. In Oswald H. Siegmund, editor, *EUV, X-Ray, and Gamma-Ray Instrumentation for Astronomy IV*, volume 2006 of *Society of Photo-Optical Instrumentation Engineers (SPIE) Conference Series*, pages 324–333, Nov 1993. doi: 10.1117/12.162845.

V. V. Zharkova, A. A. Kuznetsov, and T. V. Siversky. Diagnostics of energetic electrons with anisotropic distributions in solar flares. I. Hard X-rays bremsstrahlung emission. *A&A*, 512:A8, Mar 2010. doi: 10.1051/0004-6361/200811486.